Science with Integral Field Spectrographs Present and Future

Simon Zieleniewski
Hertford College
University of Oxford

A thesis submitted for the degree of
Doctor of Philosophy

Hilary 2016

Science with Integral Field Spectrographs Present and Future

Simon Zieleniewski

Hertford College, University of Oxford

A thesis submitted for the degree of
Doctor of Philosophy

Hilary 2016

In the first part of this thesis we use the Oxford Short Wavelength Integral Field specTrograph (SWIFT) to trace radial variations of initial mass function (IMF) sensitive stellar absorption features in several galaxies. We observe M31 and M32, the two massive Coma brightest cluster galaxies (BCGs), NGC4889 and NGC4874, and the BCG in the Coma south-west cluster NGC4839. We measure equivalent widths of the sodium NaI λ8190 doublet, calcium triplet CaT λ8498, 8542, 8662 and Wing-Ford band FeH λ9916. In M31 we find a strong NaI gradient within the central 10 arcsec (38 pc) in contrast to a *flat* FeH profile. M32 displays flat profiles for all three indices, with similar FeH but lower NaI strengths compared with M31. Using stellar population synthesis (SPS) models we find that M31 and M32 are well described by a Chabrier IMF throughout, although M31 displays a strong negative gradient in Na abundance within the inner 30 pc reaching [Na/Fe] $\sim +1.0$ at the centre. Within NGC4889 we again find a strong NaI gradient and *flat* FeH profile and derive a Chabrier, or even bottom-light IMF, with a strong Na abundance gradient. This suggests conflict with recent evidence for an increased IMF slope with increased velocity dispersion in early type galaxies. We also infer a Chabrier IMF for NGC4874. However, for NGC4839 we measure both strong NaI *and* strong FeH, which may be evidence for a bottom-heavy IMF. The IMFs we infer for the BCGs are supported by optical index measurements and dynamical modelling results from the literature. Our galaxies cover a wide range of central velocity dispersions (60–400 $\mathrm{km\,s^{-1}}$) and we find no IMF variation at both lowest and highest masses, with only one galaxy showing evidence for a bottom-heavy IMF.

In the second part we present HSIM: a dedicated pipeline for simulating observations with HARMONI on the European ELT. HSIM takes high spectral and spatial resolution input data cubes, encoding physical descriptions of astrophysical sources, and incorporates detailed models of the sky, telescope and instrument to produce realistic mock data cubes. We employ a new method of incorporating the strongly wavelength dependent adaptive optics point spread functions. HSIM provides an advancement upon traditional exposure time calculators and allows us to predict the feasibility of a given observing programme with HARMONI through the full analysis of mock data. We use HSIM to predict the performance of the current HARMONI design, through point source sensitivities and noise regimes for each operating mode. We find that HARMONI will be predominately read-out noise limited in the R- and H-bands, but heavily background-limited for the majority of K-band modes. The coarsest 30×60 mas spatial scale offers background-limited observations in all bands. We compare the visible wavelength AO performance between HARMONI and MUSE, finding that HARMONI offers improved sensitivity at Hα, and longer, wavelengths. Lastly, we perform a suite of HSIM simulations of star-forming emission-line galaxies at $z \sim 2$–3. We detail the construction of input data cubes using two separate generation methods. We show that HARMONI will provide exquisite resolved spectroscopy of these objects, probing and deriving properties of individual star forming complexes down to at least $\sim$ 350 pc in size. It will be possible to spatially resolve the sub-kpc star-forming complexes of multiple bright galaxies in a single night, which represents a large increase in observing efficiency over current telescopes and instruments.

Declaration

The work in this thesis is based on research carried out by me at the University of Oxford between October 2012 and March 2016, under the supervision of Prof. Niranjan Thatte and Dr. Ryan Houghton. I was supported by funding from the Science and Technology Facilities Council (grant numbers ST/J002216/1, ST/M007650/1, ST/N002717/1). I declare that no part of this thesis has been accepted, or is currently being submitted, for any degree or diploma or certificate or any other qualification in this University or elsewhere. Except where explicit reference is made to the work of others, the work contained in this thesis is my own.

The research carried out in Chapter 2 has been published as a refereed paper,

- S. Zieleniewski, R. Houghton, N. Thatte, R. Davies, 2015, MNRAS, 452, 597,

and the research carried out in Chapter 3 has been submitted to the Monthly Notices of the Royal Astronomical Society for publication. In these chapters the kinematic fitting using PPXF was primarily performed by Dr. Ryan Houghton.

Chapters 4, 5 and 6 are based on work I led as part of a collaboration with Dr. Sarah Kendrew of Oxford University, Dr. Mark Swinbank of Durham University, and Dr. Thierry Fusco of Laboratoire d'Astrophysique de Marseille. The production of simulated E-ELT point spread functions was done by Thierry Fusco, and the production of some input data cubes was done by Mark Swinbank. Parts of each chapter have been published as conference proceedings,

- S. Zieleniewski, N. Thatte, 2013, Proc. of AO4ELT3
- S. Zieleniewski, N. Thatte, S. Kendrew, R. Houghton, M. Tecza, F. Clarke, T. Fusco, M. Swinbank, 2014, Proc. of SPIE, 9147, 93,

and a refereed paper,

- S. Zieleniewski, N. Thatte, S. Kendrew, R. Houghton, M. Swinbank, M. Tecza, F. Clarke, T. Fusco, 2015, MNRAS, 453, 3754.

Simon Zieleniewski

(*March 2016*)

Acknowledgements

Firstly a tremendous thank you to my supervisors Niranjan Thatte and Ryan Houghton. You have tirelessly supported and guided me through my studies, given me wonderful opportunities to travel, and displayed great patience as I stumbled my way through the world of research. Together you have taught me an immeasurable amount and I am eternally grateful to both of you for the last three and a half years of intellectual adventure.

To the wider HARMONI group of Matthias, Sarah, Fraser, Kieran, Vanessa and Jim, I thank you all for being a great team, developing my interest in and understanding of instrumentation, and being there to help when I came calling. I couldn't have done this without any of you. A grateful thanks also to Mark Swinbank for being a fantastic collaborator, providing constant motivation and ideas, and to Roger Davies for being a wonderful supervisor in spirit.

To my office mates past and present; Jamie, Rob, Kimon and Jack from the dark days in the dungeon of 367; Rupert, Holly, Marisa, Macarena, (Jamie again), and Ben in 512 - it's been a blast. Also the Abingdon Massive of Alfie and Andre. Thank you for the mad and the mundane; cricket, tea and biscuits, Friday breakfasts, late night documentaries, the occasional astronomy discussion, and most importantly cricket! I wish you all the best for the future. And of course, no Oxford Astrophysics D.Phil is complete without thanking the legend that is; Ashling Morris.

Even before Oxford, a thank you to my friends and supervisors in Durham; Carlton Baugh, you were a great inspiration and ignited my desire to pursue astronomy. Also the scholar pugilists of DUABC, you made Durham an incredible four years of my life.

Outside astronomy I have been fortunate to have had the company and support from many friends over the years. The gentlemen of HCBC, HCBCCC and HCBCCCAoEC thank you: Benedict, Chris's N and H, Crabbster, Matt, Thomas, Callum - "No fielders in the sky!" The ladies and gents of OUABC for an intense season in the gym and the ring, and especially my sparring partner Elliott for pugilism and political discourse in equal measure. Thanks to Timmy Rose for being a constant source of Aussie banter and a great brief roommate. To my good friends CJ and Kevin, thank you for helping me find my feet in Oxford and for shaping my experience always for the better. Also to the scholar-soldier Dr Burgess, the last eight years have been a real adventure - thank you for always being there through the highs and lows.

Thank you Katie for your constant love, support, and supply of Daisy photos that has added so much these last six years. Lastly to my family. Mum, Granny, John, Dave and Nick, you have supported me my entire life, nurturing my myriad of interests and always encouraging me onwards. I owe everything to you.

To Nick, Ed and Oli

Contents

List of Figures

List of Tables

Chapter 1

Introduction

In this chapter we review the two main themes of this thesis and place our work within a broader scientific context. We first introduce the instrumentation part of this work. The technique of integral field spectroscopy as an advancement upon traditional long-slit spectroscopy is a central component to this thesis. We introduce the two instruments on which this work is based, the Oxford SWIFT on the Hale 200 inch telescope at Palomar Observatory, and HARMONI on the future 39 m European Extremely Large Telescope. We also introduce the principles of adaptive optics as a method for correcting the effects of atmospheric turbulence on ground-based observations. We then cover the astrophysics aspects of this work. We first review the field of galaxy stellar populations through spectroscopic methods. The main scientific themes of this thesis concern star formation and constraining the stellar initial mass function. The stellar initial mass function is a fundamental property of galaxies and we discuss historic and recent attempts to constrain it. We then briefly review studies of star formation at high redshift using adaptive optics-fed ground-based telescopes.

1.1 Integral field spectroscopy and adaptive optics

Astronomers have been studying astronomical spectra ever since the use of a prism by Newton to disperse the light from the Sun into a spectrum (Newton, 1704). Alongside imaging, the technique of long-slit spectroscopy has been of fundamental importance to astronomy throughout the 20th century. Traditionally, the light from a telescope illuminates a slit, which is aligned within the field of view (FoV) along the astronomical object. The light is then dispersed through one of several methods (e.g. diffraction grating or prism) onto a detector. This results in a set of spectra along one spatial axis of the object. While this technique has been instrumental in the advancement of astronomy, it suffers from several drawbacks, namely a) the use of a slit means most of the light collected by the telescope is wasted, and b) only a single spatial dimension is probed per observation, so the slit must be scanned across an object to obtain 2D information, which is costly for telescope time and is susceptible to inhomogeneities in the resulting data.

Integral field spectroscopy (IFS) is a relatively new technique in astronomy, which has been developed since the early 1980s (first prototype by Vanderriest, 1980), and is an advancement upon long-slit spectroscopy. The technique collects spectra simultaneously over a 2D field, overcoming the two key problems with long-slit spectroscopy. Through the data reduction stage, the product of an IFS observation is usually a data cube with axes (x, y, λ) containing two spatial axes and one spectral axis. It can be thought of either as a cube containing images at many different wavelengths, or an image whereby every pixel contains a spectrum. An example of the entire integral field observation process is shown in Figure 1.1. An important challenge in the development of IFS was packing the three dimensions of information (two spatial and one spectral) onto a two dimensional detector. With modern computing techniques, rearranging the data from the detector into a 3D product has become relatively straightforward.

1.1.1 IFS techniques

The key to IFS is the method of splitting up and dispersing a 2D field onto a detector in order to pack three dimensions of information within a 2D space. Several techniques have been developed for integral field units (IFUs) to achieve this as shown in Figure 1.2. These are:

a) **The lenslet or microlens** method whereby an array of small lenses in the focal plane produces an array of small images of the telescope pupil, which is then dispersed onto a detector creating a spectrum for each lenslet. This method was pioneered by TIGER on the

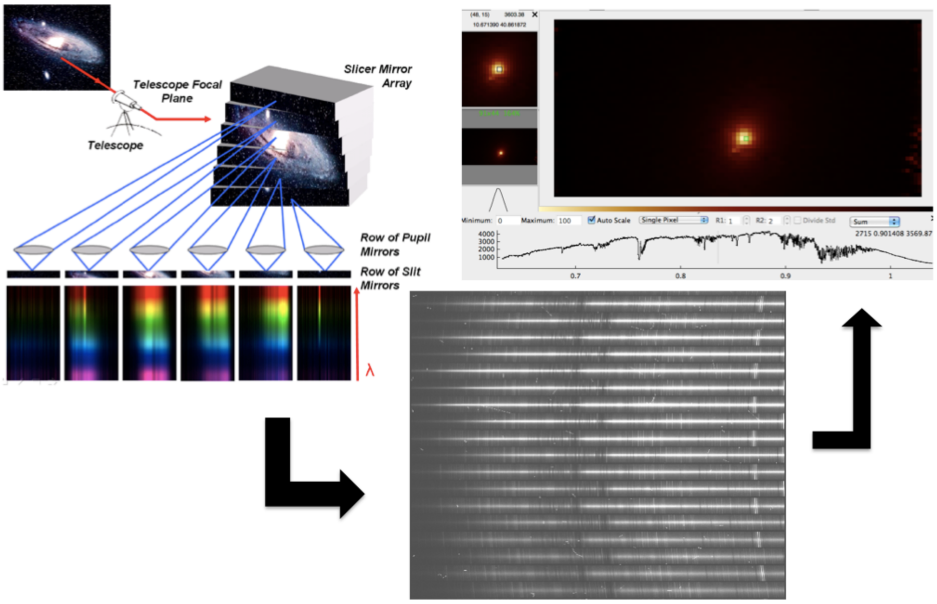

Figure 1.1: Diagram showing the processes involved in an integral field spectrograph observation. The telescope light is split (here shown using a mirror stack) and rearranged into a pseudo long-slit. This is then dispersed onto a detector. Data reduction converts the raw detector frames into data cubes with two spatial and one spectral dimension. *Image credit: adapted from Figure 1 in Vivès & Prieto (2006).*

Canada-France-Hawaii 3.6 m telescope (CFHT, Bacon et al., 1995). It is conceptually the simplest design so offers the greatest throughput. However it suffers from inefficient use of detector real estate due to requiring space between the spectra from each lenslet to prevent overlap. Other IFUs to successfully utilise this technique include OASIS (Emsellem, 1999) and SAURON (Bacon et al., 2001).

b) **The optical fibre** method where the field is split up using a bundle of optical fibres, which are then rearranged to form a one dimensional row of points to be dispersed akin to a long-slit. Fibres have been used for IFUs since Vanderriest (1980) and Hill et al. (1980), and continue to be employed in many instruments (e.g. SAMI, Croom et al., 2012). There are two main disadvantages of this technique. Firstly, optical fibres are circular with an outer layer of protective cladding, thus they under fill a field when in a close-packed array. Secondly they suffer from focal ratio degradation (FRD) whereby light entering the fibre at an angle departs from the other end at a range of angles around the input (e.g. Heacox, 1986; Clayton, 1989). An instrument with a faster focal ratio than the telescope can reduce the effect of FRD, otherwise losses can be significant. A recent example of a fibre-based IFU is the SAMI instrument (Bryant et al., 2012; Croom et al., 2012).

Optical fibres have been combined with lenslets to substantially improve the overall performance. The lenslet array allows for a much greater fill factor and can also feed the fibres with lower focal ratio beams to minimise FRD. This method has been employed by the GMOS instruments on the Gemini telescopes (Allington-Smith et al., 2002).

c) **The image slicer** method consists of a stack of mirrors each aligned at slightly different angles to the incoming light (see e.g. Figure 1.1). This optically splits the field into thin slices which diverge along different paths and are optically aligned into a long slit by a second set of mirrors. The resulting pseudo long-slit is dispersed akin to a traditional 1D spectrograph. Image slicers offer the advantage of being easy to cool down to cryogenic temperatures, thus being able to extend to near-infrared (NIR) wavelengths where thermal background emission becomes prominent. They also offer extremely efficient use of detector space with a near perfect fill factor. The optics are however expensive to manufacture and they can be substantially larger instruments than those employing the alternate methods, which creates additional challenges for instrument design. Examples of slicer-based IFUs are SINFONI (Eisenhauer et al., 2003) and MUSE (Bacon et al., 2010) on the VLT.

IFS has become a standard technology on many of the world's largest ground-based optical and NIR telescopes. Whereas the first IFUs were designed predominately as proof of technology (e.g. TIGER; Bacon et al., 1995), several different types of IFU instruments are now in operation, which are tailored towards specific scientific goals. These include:

- Multi-object spectroscopy (MOS) instruments, consisting of multiple mini-IFUs for the simultaneous observation of several objects, and total sample sizes in the thousands (e.g. KMOS with 24 image-slicer IFUs, Sharples et al. 2013; SAMI with 13 optical fibre 'hexabundles', Croom et al. 2012; MaNGA with 17 optical fibre bundles, Bundy et al. 2015; Drory et al. 2015).

- Large, single FoV IFUs for observations including extended nearby objects, resolved stellar populations, and deep field surveys (e.g. MUSE with a 1×1 arcmin FoV, Bacon et al., 2010).

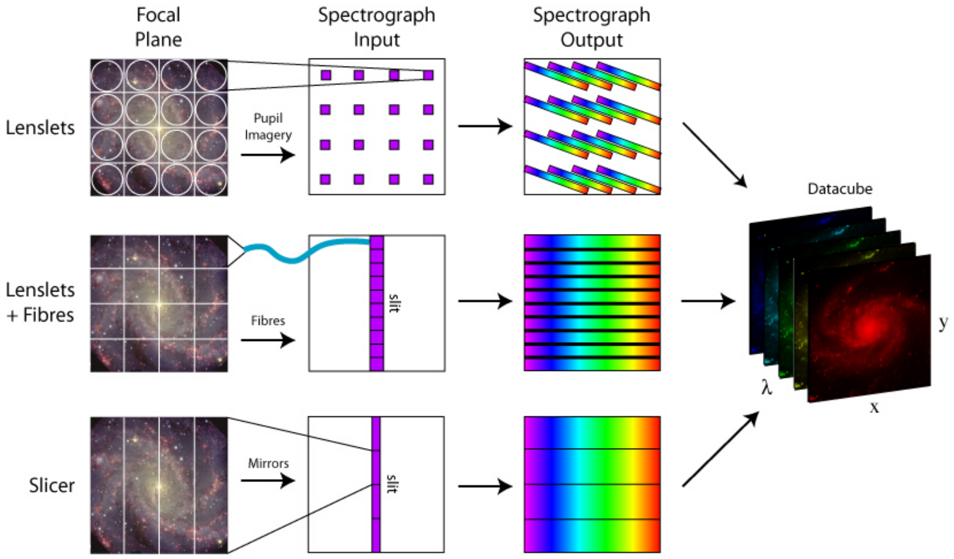

Figure 1.2: Different design methods of integral field units to split the light from a 2D field and disperse onto a detector. These are, from top to bottom, the lenslet array, the optical fibre+lenslet method, and the image-slicer method. The final product (after data reduction) in each case is a 3D data cube. *Image credit: Figure 1 in Westmoquette et al. (2009) adapted from Figure 5 from Allington-Smith et al. (1998).*

- High contrast IFUs using extreme adaptive optics and coronagraphs for exoplanet imaging and low resolution spectroscopy (e.g. SPHERE on the VLT, Beuzit et al., 2008).

This thesis concerns two integral field spectrographs, which both utilise the image slicer technique. These are the Oxford SWIFT instrument on the Hale 200 inch telescope at Palomar Observatory, and the first-light HARMONI instrument for the European ELT. We give a brief overview of each instrument here.

1.1.2 Oxford Short Wavelength Integral Field specTrograph (SWIFT)

The Oxford Short Wavelength Integral Field specTrograph (SWIFT: Thatte et al. 2006) is an instrument built for the Hale 200 inch telescope at Palomar Observatory. SWIFT is a slicer-based integral field spectrograph covering the wavelength range $0.63 - 1.04\,\mu$m at a resolution of $\sim 2\,\text{Å}$ with a spectral sampling of $1\,\text{Å}\,\text{pix}^{-1}$. It offers several spatial pixel (spaxel) scales, ranging from seeing limited observations at $235\,\text{mas}\,\text{spaxel}^{-1}$ with a FoV of $21 \times 10\,$arcsec, to 80 mas and 16 mas scales for use with the PALM 3K single conjugate

Table 1.1: Design parameters for SWIFT.

Wavelength range	0.63 - 1.04 μm
Spatial scales (FoV)	16 mas ($1.42'' \times 0.7''$), 80 mas ($7.1'' \times 3.5''$) 235×235 mas ($20.9'' \times 10.3''$)
Resolving Power	3250 at 0.65 μm 4400 at 1.0 μm
Temperature	155 K detectors
Detector	2× LBNL 250 μm, fully depleted, 4k × 2k CCDs
Throughput	23% (avg. inc. tel. & det.)
AO modes	SCAO, seeing-limited

adaptive optics (SCAO) system (Bouchez et al., 2008). The thick, 250 μm silicon CCD detectors used are cryogenically cooled using liquid nitrogen and offer greater quantum efficiency (QE) at red wavelengths compared to normal CCDs. The full design parameters of SWIFT are shown in Table 1.1.

SWIFT has been utilised for numerous science programmes, ranging from studies of Solar system bodies (Clarke et al., 2013), to resolved studies of ring galaxy systems (Fogarty et al., 2011), kinematic surveys of galaxy clusters (Scott et al., 2012; Houghton et al., 2013), and stellar populations analysis of nearby galaxies (Zieleniewski et al., 2015a). It is optimised to take advantage of the calcium triplet (CaT) absorption feature for measuring galaxy kinematics, but the wavelength coverage includes several important NIR absorption features, which enable the study of stellar populations of nearby galaxies.

In the first part of this thesis we use SWIFT in seeing-limited mode to undertake studies of the stellar populations in nearby galaxies, with the aim of constraining the low-mass end of the initial mass function. We introduce the field of galaxy stellar populations and the initial mass function in Section 1.2.2.

1.1.3 HARMONI on the European ELT

The High Angular Resolution Monolithic Optical and Near-infrared Integral field spectrograph (HARMONI: Thatte et al. 2010) is the first-light integral field spectrograph for the European Extremely Large Telescope (E-ELT), a 39 m optical/NIR telescope currently being constructed by the European Southern Observatory (ESO) on Cerro Armazones, Chile.

Table 1.2: Current design parameters for HARMONI.

Wavelength range	0.47 - 2.45 μm
Spatial scales (FoV)	4 mas ($0.61'' \times 0.86''$), 10 mas ($1.52'' \times 2.14''$) 20 mas ($3.04'' \times 4.28''$), 60×30 mas ($6.42'' \times 9.12''$)
Resolving Power	3500 ($V+R$; $Iz+J$; $H+K$) 7500 (Iz; J; H; K) 20000 (half of each NIR band)
Temperature	120 K cryostat, 40 K detectors
Detectors	Teledyne HgCdTe 4k × 4k for NIR 4k × 4k CCD for visible
Throughput	$\geq 30\%$ avg.
AO modes	SCAO, LTAO, seeing-limited

Upon completion the E-ELT will boast greater light gathering power than all current optical/NIR telescopes combined. It will be a fully-adaptive telescope providing two flavours of adaptive optics (AO) correction: SCAO, which uses a single natural guide star to provide high level correction only in the vicinity of stars of $M_V \lesssim 13\,\mathrm{mag}$, and laser-tomography adaptive optics (LTAO), which will use six laser guide stars in combination with several natural guide stars to provide high-level correction over the entire sky. It will also be able to operate in seeing-limited mode.

HARMONI will provide core spectroscopic capability for the E-ELT at visible and NIR wavelengths. It will most likely provide $152 \times 214 = 32528$ simultaneous spectra arranged in a $\sqrt{2}$:1 aspect ratio contiguous field made up from four separate IFU optical channels. The instrument is currently in preliminary design phase with construction planned for later this decade. First light for the E-ELT and HARMONI is currently around 2025. The current design parameters of HARMONI are shown in Table 1.2. It is being designed as a single-field, visible and NIR integral field spectrograph, and will provide a range of spaxel scales and spectral resolving powers, which permit the user to optimally configure the instrument for a wide range of science programmes; from ultra-sensitive to diffraction-limited, spatially resolved, physical (through morphology), chemical (via abundances and line ratios) and kinematic (through line-of-sight velocities) studies of astrophysical sources. HARMONI will be compatible with both SCAO and LTAO, allowing it to tackle a broad range of astrophysical problems, including: a) the physics of mass assembly of galaxies at high redshifts, b) resolved studies of stellar populations in distant galaxies, c) detecting and weighing intermediate mass black holes in nearby galaxies or globular clusters, and d) characterising known extra-solar planets.

The contract to build HARMONI between ESO and the HARMONI consortium was signed in September 2015. During the design stage of such a large instrumentation project, it is of vital importance to accurately quantify the expected instrument performance, and assess the feasibility of future scientific programmes, prior to construction. The second part of this thesis involves the development of the instrument simulation pipeline HSIM for HARMONI, and its use for predicting instrument performance and simulating specific science cases.

1.1.4 Principles of adaptive optics

Most modern IFU instruments are coupled to AO systems, so here we give an overview of the basic principles of AO.

In the absence of any phase distortions, light enters a telescope as a flat wavefront and is focussed to a diffraction-limited point spread function (PSF). For a circular aperture of diameter D with a central obscuration the full width at half maximum (FWHM) of the PSF in radians for a wavelength λ is given by

$$\mathrm{FWHM} = A\frac{\lambda}{D}, \tag{1.1}$$

where A depends on the size of the central obscuration but is very close to unity. The Raleigh criterion states that the angular resolution in radians is given by

$$\theta = 1.22\frac{\lambda}{D}. \tag{1.2}$$

However, in practice ground-based observations are limited by atmospheric turbulence or *seeing*. Light travelling through the Earth's atmosphere suffers random aberrations as it passes through regions where there is turbulent mixing of air of different temperatures and therefore different refractive indices. The energy entering the atmosphere on large scales, for example through heating from sunlight, transfers down to successively smaller scales, leading to the changes in temperature and refractive index. These temporal changes cause the flat wavefronts of light to be perturbed as they travel through the atmosphere, creating phase differences across the telescope aperture. The resulting short exposure image is a large collection of individual diffraction-limited images known as a *speckle* pattern. Observing for much longer than the *coherence timescale* of the turbulence τ_0, integrates the speckle patterns to a large seeing disc or halo.

In the Kolmogorov (1941) turbulence model, energy enters the atmosphere on infinite scales, and so the atmospheric turbulence power spectrum is described by a power law on infinite scales. The PSF full width at half maximum (FWHM) in radians of a long-exposure seeing-limited observation is given by,

$$\mathrm{FWHM} = A\frac{\lambda}{r_0}, \tag{1.3}$$

where r_0 is the Fried parameter, which characterises the scale of atmospheric turbulence (e.g. Roddier, 1981; Sarazin & Roddier, 1990) and is usually around 10–20 cm[1]. The phase variance across the aperture is given from Fried (1965) as,

$$\sigma^2 = 1.03\left(\frac{D}{r_0}\right)^{5/3}, \tag{1.4}$$

so for a telescope with $D < r_0$ the variance will be small and thus it will still be diffraction-limited. For a telescope with $D > r_0$ the long-exposure resolution is limited to[2],

$$\theta = 1.22\frac{\lambda}{r_0}. \tag{1.5}$$

AO systems operate on the principle of measuring the incoming wavefront phases across the telescope pupil, using a *wavefront sensor*, and relaying commands via a *real time control*

---

[1] r_0 is defined as the diameter of a circular aperture over which the wavefront phase variance is equal to one radian.

[2] The more recent von Kármán model also includes a finite outer scale L_0, which reduces the variance of turbulence on large scales (e.g. Tokovinin, 2002; Martinez et al., 2010). This results in an improvement in seeing-limited performance for telescopes with $D > r_0$ (Tokovinin, 2002).

system to a *deformable mirror*, which changes shape to correct for the phase changes. A schematic of an AO system is shown in Figure 1.3. The distorted wavefronts of light entering the AO system are incident upon the DM and are split by the beamsplitter, which sends the light of scientific interest to the science instrument, and the remaining wavelengths to the AO-loop. We describe the three key components of an AO system.

Wave front sensor (WFS): The WFS samples the phase differences across the pupil. Several types of WFS exist; the most common is the Shack-Hartmann (SH) WFS, which uses an array of lenslets to split the pupil into several sub-pupils, which are each focussed onto a detector. Any phase distortions across the wavefront cause the positions of the sub-images to move relative to the positions from a flat wavefront. Thus, the SH WFS measures the gradient of the wavefronts across the aperture. Other methods include the curvature WFS (Roddier & Roddier, 1988) and pyramid WFS (e.g. Ragazzoni et al., 2000).

Deformable mirror (DM): The DM comprises a mirror with individual (but not necessarily separate) sections that are able to move up and down via actuators, allowing the DM to take the required shape to correct for wavefront distortions. The actuator density (number of actuators across a DM) indicates the level of correction possible. Several types of DM exist including segmented, ferrofluid, and biomorph DMs.

Real time control (RTC) system: An RTC system is required to relay phase measurements from the WFS into actuator commands for the DM. For accurate correction the AO loop must operate at high speed, usually hundreds of Hz. The RTC creates an *interaction matrix* from the WFS measurements, of which the inverse is the *reconstructor matrix*, which gives the actuator commands to the DM to perform the correction.

The performance of an AO system is encoded in the resulting PSF. The ability of an AO system to correct the PSF can be quantified using the Strehl ratio (SR),

$$\mathrm{SR} = \frac{\mathrm{Max}(\mathrm{PSF}_{\mathrm{AO}})}{\mathrm{Max}(\mathrm{PSF}_{\mathrm{DL}})}, \tag{1.6}$$

where $\mathrm{PSF}_{\mathrm{DL}}$ is the PSF of a perfectly diffraction-limited system. An example performance comparison between a seeing-limited and AO-corrected observation is shown in Figure 1.4.

AO systems are complex and operate at high frequencies, so the performance is limited

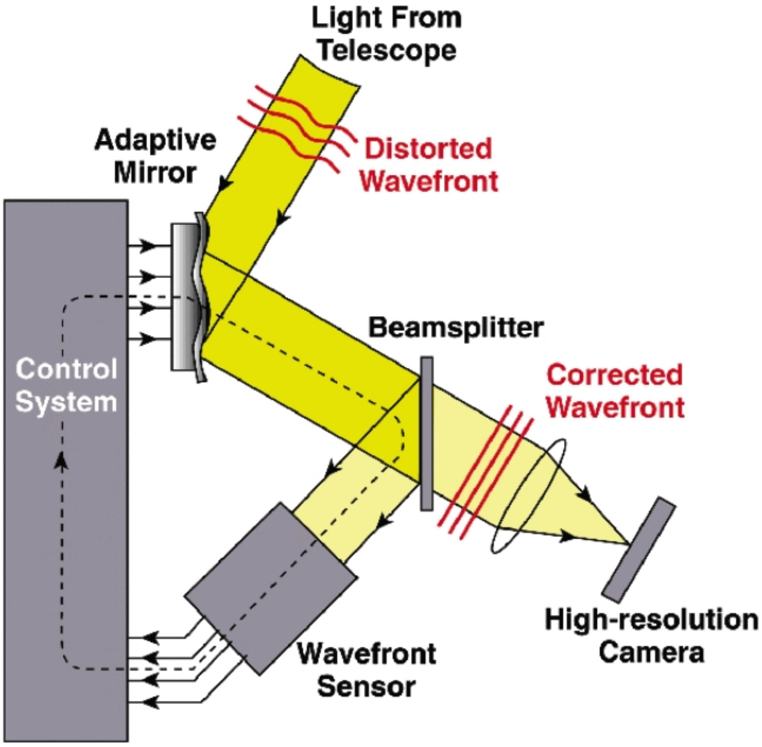

Figure 1.3: A basic schematic of an AO system. The wavefronts of light entering the telescope are distorted by atmospheric turbulence. The light is incident onto a deformable mirror (DM) and is then split by a beamsplitter. The wavelengths of scientific interest are sent to the instrument while the other part is incident onto a WFS. The WFS measures the incoming phase fronts and relays inverse commands to the DM to correct for the distortions. The control loop between the WFS and DM is usually run at speeds of hundreds of Hz. Successive wavefronts are partially corrected by the DM and thus yield better angular resolution PSFs. *Image credit: NSF Center for Adaptive Optics.*

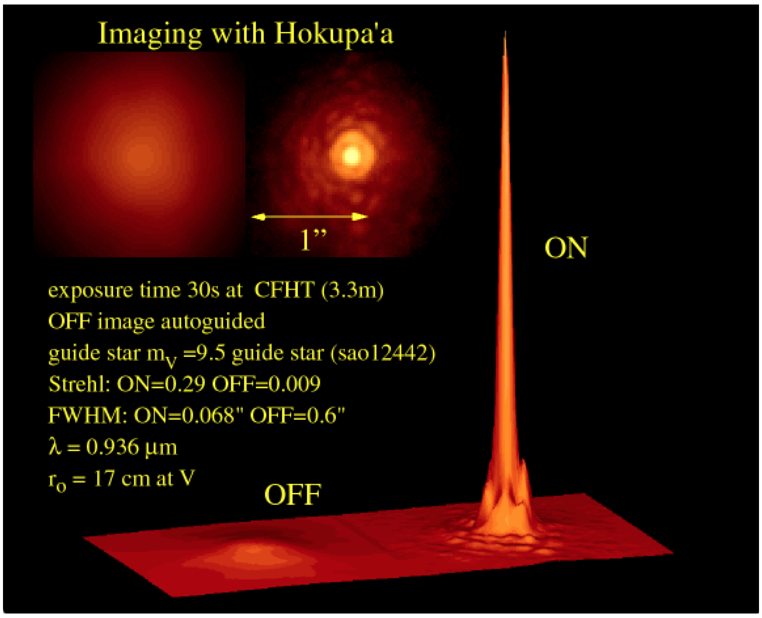

Figure 1.4: Observation of a star at 0.94 μm with (right) and without (left) AO using the Hokupa'a AO system on the Canada-France-Hawaii 3.6 m telescope (CFHT) . The improvement in FHWM and SR of the AO-corrected PSF compared to the seeing-limited PSF is stark, with a factor ~ 10 decrease in the PSF FWHM. *Image credit: L. Close and University of Hawaii, Institute for Astronomy.*

by many variables. The main sources of error are:

Fitting error: The level of AO correction is limited by how accurately the DM can form the shape of the incoming phase fronts. The fitting error is proportional to the size of the actuators; decreasing the actuator size allows the correction of higher spatial frequencies. Moreover, smaller actuator sizes allow for better correction at shorter wavelengths. As $r_0 \propto \lambda^{6/5}$ (e.g. Davies, 2008), the wavefront distortions are to first-order achromatic, so for longer wavelengths, phase distortions are a smaller fraction of the wavelength and AO correction is better for a given actuator size. Shorter wavelengths need smaller actuators as phase distortions are a larger fraction of the wavelength.

WFS error: The ability of the WFS to determine the wavefront phases is limited by the signal-to-noise of the wavefront measurements. Observing a brighter reference object reduces the WFS error, as does reducing the AO-loop frequency but this must be traded against the Servo error.

Servo error: The time delay between measuring the wavefront aberrations and changing the DM introduces an error due to the short coherence time of the turbulence (on the order of milliseconds). Running the system at higher frequency reduces this error but this must be traded off agains the resulting increase in WFS error.

Isoplanatic error: Light from a correcting source off-axis to a science object (or vice versa) passes through a slightly different section of atmosphere, and due to the small coherence length of the atmosphere this introduces an error, which increases with increasing angular separation between the objects.

Non-common path (NCP) errors: Any optical aberrations introduced downstream of the WFS will not be seen by the AO system and thus not corrected. It is possible to correct for some NCP errors using post-processing techniques (e.g. kernel phase; Pope et al., 2016).

Several types of AO system exist and an overview of the two systems mentioned within this thesis are given here (see Figure 1.5):

- **SCAO:** the most common AO type using a single bright natural guide star to perform high level correction on-axis. A single DM is conjugate to the telescope pupil giving high order correction but in a very limited FoV. SCAO is useful for science where the correcting object is also the object of scientific interest, e.g. extrasolar planet imaging or studies of binary stars. Due to the relative rarity of bright stars, SCAO operation is generally limited to only a few per cent of the sky area.

- **LTAO:** The use of laser guide stars alleviates problem of limited sky coverage[3]. Laser tomography involves the use of multiple laser guide stars in a specific asterism shape, combined with the same number of WFSs, to provide full reconstruction of the atmospheric profile within the area of observation. It will therefore offer correction for extended objects and over a much larger percentage of the sky compared with SCAO. LTAO is a new technology but is being actively pursued by pathfinder instruments including CANARY on the William Herschel Telescope (Morris et al., 2014).

---

[3] Laser guide stars include specific sources of error, for example: the *cone effect* due to the finite height of a laser guide star above the ground, and spot elongation on the SH-WFS detector, which limits centroid accuracy.

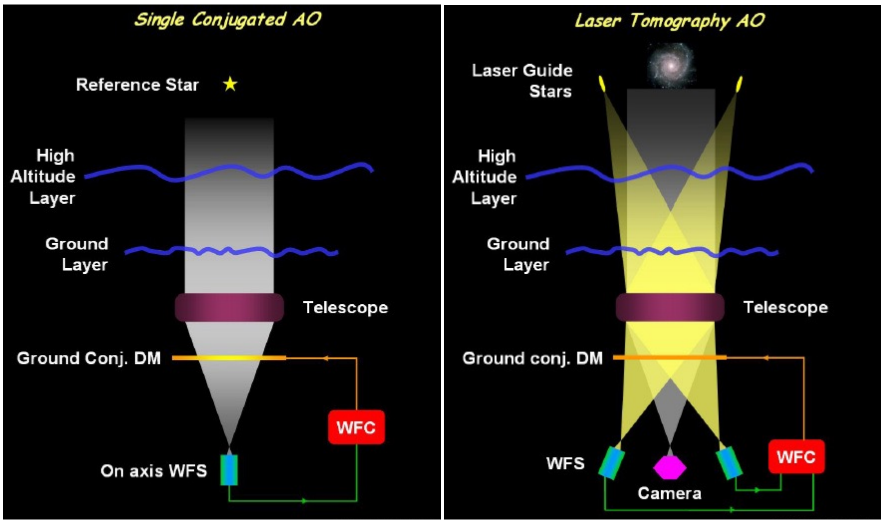

Figure 1.5: Diagrams of SCAO (left) and LTAO (right) systems. SCAO provides good on-axis correction by correcting on a single natural guide star, but is limited by the rarity of bright stars in the sky. LTAO uses an asterism of multiple laser guide stars to give tomographic reconstruction of the complete turbulence profile within the asterism area on the sky. It offers much greater sky coverage but with reduced performance due to the complexity of the system compared with SCAO. *Image credit: European Southern Observatory.*

1.1.5 Signal and noise

In this section we introduce some useful equations for quantifying basic instrument performance. In astronomy we seek to measure the *signal* from an object on a CCD or NIR detector above additional noise sources. The total *counts* on a detector resulting from an observation can be decomposed into four contributions,

$$counts = signal + background + dark + read, \tag{1.7}$$

where the *background* consists of sky emission and telescope/instrument thermal emission, *dark* is the detector dark current, and *read* is the read-out noise introduced whenever the detectors convert the accumulated electrons to voltage. We assume that the first three terms are governed by Poisson statistics so that their variances V equal their mean values,

$$\langle signal \rangle = V_{signal}, \;\; \langle background \rangle = V_{bg}, \;\; \langle dark \rangle = V_{dark}, \tag{1.8}$$

Table 1.3: List of parameters required to calculate the S/N of an IFS observation

Parameter	Symbol	Example units
Object flux (point source)	F_λ	$\mathrm{erg\,s^{-1}\,cm^{-2}\,\AA^{-1}}$
Object flux (extended source)	F_λ	$\mathrm{erg\,s^{-1}\,cm^{-2}\,\AA^{-1}\,arcsec^{-2}}$
Background flux	F_{bg}	$\mathrm{erg\,s^{-1}\,cm^{-2}\,\AA^{-1}\,arcsec^{-2}}$
Photon energy	E_λ	erg
Telescope area	A	$\mathrm{cm^2}$
Resolution element	$\Delta\lambda$	Å
Number of spaxels	N_{spax}	
Number of (spectral) pixels	N_{pix}	
Number of exposures	N_{exp}	
Exposure time	T_{exp}	s
Detector dark current	D_{c}	$\mathrm{e^-\,s^{-1}\,pixel^{-1}}$
Detector read-out noise	σ_{R}	$\mathrm{e^-\,pixel^{-1}}$
Spaxel scale	r_{spax}	arcsec
Ensquared energy (fraction of PSF)	$E_{\mathrm{PSF}}(N_{\mathrm{spax}} r_{\mathrm{spax}}^2)$	
Atmospheric transmission	T_{atm}	
Telescope transmission	T_{tel}	
Instrument transmission	T_{ins}	
Detector quantum efficiency	Q_{det}	
Total transmission	$T_{\mathrm{tot}} = T_{\mathrm{atm}} T_{\mathrm{tel}} T_{\mathrm{ins}} Q_{\mathrm{det}}$	

and that the read-out noise has a mean of zero and variance of σ_{R}^2. We further assume that the four contributions are uncorrelated so that their variances add,

$$V_{data} = V_{signal} + V_{bg} + V_{dark} + \sigma_{\mathrm{R}}^2. \tag{1.9}$$

Thus we define the standard signal-to-noise (S/N) equation as,

$$\mathrm{S/N} = \frac{\langle signal \rangle}{\sqrt{V_{data}}} = \frac{\langle signal \rangle}{\sqrt{\langle signal \rangle + \langle background \rangle + \langle dark \rangle + \sigma_{\mathrm{R}}^2}}. \tag{1.10}$$

Calculating the S/N of an observation of a source with flux F_λ requires many parameters, which are listed in Table 1.3.

The number of electrons N_{obj} stored in an area of the detector $N_{\mathrm{spax}} r_{\mathrm{spax}}^2$ each second from a spectroscopic observation of an object, is given by,

$$N_{\text{obj}} = \frac{F_\lambda\, T_{\text{tot}}\, A\, \Delta\lambda\, E_{\text{PSF}}(N_{\text{spax}} r_{\text{spax}}^2)}{E_\lambda} \quad \text{(point sources)}, \tag{1.11}$$

$$= \frac{F_\lambda\, T_{\text{tot}}\, A\, \Delta\lambda\, N_{\text{spax}} r_{\text{spax}}^2}{E_\lambda} \quad \text{(extended sources)}, \tag{1.12}$$

where, for point source observations, E_{PSF} is dependent on the point spread function (PSF) and the area over which we integrate. The number of background electrons from sky/telescope/instrument emission arriving over the same area each second is given by,[4]

$$N_{\text{bg}} = \frac{F_{\text{bg}}\, T_{\text{tot}}\, A\, \Delta\lambda\, N_{\text{spax}} r_{\text{spax}}^2}{E_\lambda}. \tag{1.13}$$

If the resolution element $\Delta\lambda$ is sampled by N_{pix} spectral pixels (where for $N_{\text{pix}} = 2$ we are Nyquist sampling), then the S/N per resolution element of an observation of duration $T_{\text{exp}} N_{\text{exp}}$, is given by,

$$\text{S/N} = \frac{N_{\text{obj}}\, T_{\text{exp}} \sqrt{N_{\text{exp}}}}{\sqrt{(N_{\text{obj}} + N_{\text{bg}} + N_{\text{spax}} N_{\text{pix}} D_{\text{c}}) T_{\text{exp}} + N_{\text{spax}} N_{\text{pix}} \sigma_{\text{R}}^2}}. \tag{1.14}$$

In the far red and NIR where the sky becomes brighter with many prominent sky lines it is usual to subtract a separate sky exposure, which adds additional noise terms,

$$\text{S/N} = \frac{N_{\text{obj}}\, T_{\text{exp}} \sqrt{N_{\text{exp}}}}{\sqrt{(N_{\text{obj}} + 2N_{\text{bg}} + 2N_{\text{spax}} N_{\text{pix}} D_{\text{c}}) T_{\text{exp}} + 2N_{\text{spax}} N_{\text{pix}} \sigma_{\text{R}}^2}}. \tag{1.15}$$

It is now useful to look at the limiting situations. For the *source*-limited case where $N_{\text{obj}} >> N_{\text{bg}}$, $N_{\text{spax}} N_{\text{pix}} D_{\text{c}}$, $N_{\text{spax}} N_{\text{pix}} \sigma_{\text{R}}^2$ we find that $\text{S/N} \propto \sqrt{N_{\text{obj}} T_{\text{exp}} N_{\text{exp}}}$. One can increase the total exposure time, either by increasing T_{exp} or N_{exp}, or observe a brighter source to increase the S/N. In reality, T_{exp} is usually limited either by the saturation level of the detector, or by the number of cosmic rays incident on the detector.

More commonly, for faint observations the background dominates such that $N_{\text{bg}} >>$

---

[4] Strictly speaking the transmission will be different for each background component as, for example, the telescope thermal emission is only transmitted through the instrument and onto the detector. Even within the telescope the emission from individual mirrors goes through one less subsequent mirror along the light path. We account for these factors within this thesis.

N_{obj}, $N_{\mathrm{spax}}N_{\mathrm{pix}}D_{\mathrm{c}}$, $N_{\mathrm{spax}}N_{\mathrm{pix}}\sigma_{\mathrm{R}}^2$ and we find that,

$$\mathrm{S/N} = \frac{N_{\mathrm{obj}}\sqrt{T_{\mathrm{exp}}N_{\mathrm{exp}}}}{\sqrt{N_{\mathrm{bg}}}} \tag{1.16}$$

$$\propto \frac{D\sqrt{T_{\mathrm{exp}}N_{\mathrm{exp}}}}{\sqrt{N_{\mathrm{spax}}r_{\mathrm{spax}}^2}} \quad \text{(point sources)}, \tag{1.17}$$

$$\propto D\sqrt{N_{\mathrm{spax}}r_{\mathrm{spax}}^2T_{\mathrm{exp}}N_{\mathrm{exp}}} \quad \text{(extended sources)}, \tag{1.18}$$

where we have substituted in Equations 1.11 and 1.13, and the telescope area A scales with the square of the diameter D.

Similar relations can be found in the dark-limited case,

$$\mathrm{S/N} \propto D^2\sqrt{T_{\mathrm{exp}}N_{\mathrm{exp}}} \quad \text{(point sources)}, \tag{1.19}$$

$$\propto D^2\sqrt{N_{\mathrm{spax}}r_{\mathrm{spax}}^2T_{\mathrm{exp}}N_{\mathrm{exp}}} \quad \text{(extended sources)}, \tag{1.20}$$

and the read-limited case,

$$\mathrm{S/N} \propto D^2T_{\mathrm{exp}}\sqrt{N_{\mathrm{exp}}} \quad \text{(point sources)}, \tag{1.21}$$

$$\propto D^2T_{\mathrm{exp}}\sqrt{N_{\mathrm{spax}}r_{\mathrm{spax}}^2N_{\mathrm{exp}}} \quad \text{(extended sources)}, \tag{1.22}$$

For seeing-limited observations, the PSF is independent of D and so the S/N scales as $\mathrm{S/N} \propto D$ for the source- and background-limited cases, and $\propto D^2$ for the dark- and read-limited cases, for both point and extended sources. If an instrument Nyquist samples the near diffraction-limited AO-corrected PSF so that,

$$r_{\mathrm{spax}} = \frac{\lambda}{2D}, \tag{1.23}$$

then for the background-limited case, the point source $\mathrm{S/N} \propto D^2$. This can also be represented in terms of the observing efficiency, or inverse time to achieve a required S/N. As $\mathrm{S/N} \propto \sqrt{T_{\mathrm{exp}}}$ then it can be seen that the observing efficiency scales as D^4. Thus, the 4 mas spaxel scale of HARMONI is designed to Nyquist sample the PSF at NIR wavelengths and exploit the huge gain in sensitivity and efficiency offered by the E-ELT operating with

AO.

The equations shown here do not include systematic effects, which in reality limit how the S/N scales in the various regimes. However, the S/N equation is the principle on which exposure time calculators are based, and these offer vital insight into the feasibility of observations. We use this as a basis for the HSIM pipeline presented in the second part of this thesis.

1.2 Galaxy stellar populations and star formation

1.2.1 Galaxy formation: a brief overview

That we inhabit an expanding universe consisting predominately of dark energy (Λ) and cold mark matter (CDM), which started out from the Big Bang, has become the well-established cosmological model. Recent results from the Planck satellite have shown that dark energy constitutes around 68 % of the energy-density of the Universe, with dark matter comprising around 27 % (Planck Collaboration et al., 2014, 2015). The remaining 5 % is in the form of baryonic matter, which makes up the stars, gas and galaxies that we can directly observe. The ΛCDM framework has been successful in explaining many observed properties of our universe including the existence and distribution of the cosmic microwave background, the large-scale structure of space through the distributions of galaxies, the expansion of the Universe, and the abundances of the light elements hydrogen, helium, and lithium.

In this framework, initial density perturbations were inflated in the early Universe and then grew through gravity to form increasingly large structures. Dark matter comprises the majority of the *cosmic web* of filaments and voids that makes up the large scale structure. The baryonic matter traced the dark matter and formed stars and galaxies within the large gravitational potential wells of dark matter haloes. The galaxies then evolved through complex non-linear processes such as gas cooling and accretion, star formation with stellar feedback, and mergers, to form the complex distribution of galaxies we now see at the present day (e.g. Cole et al., 2000).

When we observe nearby galaxies, we see a rich diversity of morphologies, colours and sizes, ranging from giant red ellipticals to blue spiral galaxies with complex secular structures (e.g. bars). Understanding the evolution of galaxies from the first stars to the vast diversity seen at the present day is an immense challenge for modern astronomy. The physical processes governing how galaxies form their stars are still far from fully understood. Processes such as the inhibition of gas cooling through stellar or active galactic nuclei (AGN) feedback, or minor and major merging of galaxies, are actively studied to try and understand their effects on the galaxy population, using both observational and theoretical approaches.

Two important and complementary observational threads that exist to try to better understand the processes involved in star formation are: studying the *fossil record* of nearby galaxies through their old stellar populations, and probing star formation in the high redshift universe.

1.2.2 Galaxy stellar populations

Studying the stellar populations in nearby galaxies is akin to archeology. The stars are the directly observable baryonic component of galaxies and harbour much information about their formation and evolution over billions of years. This information must be teased out from the stars that we see shining today. Stars vary in mass from the faintest and smallest, which are fractions of the mass of the Sun, up to the brightest and most massive, each constituting around 100 solar masses. Stellar evolution theories predict the energy emitted by a star as a function of time, given its initial mass and chemistry, giving a spectral energy distribution (SED). Light from a galaxy is therefore a complex superposition of SEDs from every star integrated along the line of sight. A great advance in our understanding of stellar populations within galaxies arrived with the advent of stellar population synthesis (SPS) modelling (e.g. Tinsley, 1968, 1972; Faber, 1973; Searle et al., 1973). This method utilised stellar evolution theory to generate models according to possible spectral types for a given age and chemical composition. With advances in evolutionary theory throughout the second half of the 20th century, SPS modelling has become the standard approach to understanding the SEDs of galaxies, with many different models now existing (e.g. Bruzual & Charlot, 1993; Worthey et al., 1994; Vazdekis et al., 1996; Bruzual & Charlot, 2003; Vazdekis et al., 2003; Maraston, 2005).

SPS models utilise the *simple stellar population* (SSP), which is defined as the SED of an instantaneously birthed group of stars as a function of certain key parameters such as:
a) the formation epoch or *age*,
b) the *metallicity* or abundance of elements heavier than helium relative to that in the Sun [Z/H],
c) abundance ratios of α*-process* elements[5] relative to iron [α/Fe],
d) abundance ratios of individual elements relative to iron, e.g. sodium [Na/Fe], magnesium [Mg/Fe],
e) the *initial mass function* $\xi(m)$, which sets the distribution of stellar masses.

These components are usually combined in the following way to create the SED of an SSP,

$$F_{\mathrm{SSP}}(t, Z, \xi) = \int_{m_{\mathrm{l}}}^{m_{\mathrm{u}}(t)} F_{\mathrm{star}}[T_{\mathrm{eff}}, \log g(m)|t,\ Z]\,\xi(m)\,\mathrm{d}m, \tag{1.24}$$

where F_{star} is a stellar spectrum, m_{l} is the low mass cut-off, and $m_{\mathrm{u}}(t)$ is the age-dependent upper mass limit. The low and high (at birth) mass limits are usually set to around $0.1\,\mathrm{M}_{\odot}$ and $100\,\mathrm{M}_{\odot}$ respectively. The input stellar spectra vary according to temperature T_{eff} and surface gravity $\log g(m)$ for a given age and chemical composition. Stellar spectral libraries, either empirical or theoretical (or both), are combined with *isochrones*[6] to generate F_{star} for any given parameters, thus allowing the generation of a full SSP. The challenges facing SPS model generation are large. There is no one set of isochrones which completely describe all phases of stellar evolution, and a wide number exist (e.g. Padova models cover a range of ages, metallicities and stellar phases: Bertelli et al. 1994; Girardi et al. 2000; Marigo et al. 2008; Geneva models follow high mass stars through post-main sequence stages: Schaller et al. 1992; Meynet & Maeder 2000; Lyon models cover very low mass stars: Chabrier & Baraffe 1997; Baraffe et al. 1998), and the treatment of certain evolutionary phases is still a topic of debate (e.g. thermally pulsating (TP)-AGB stars Maraston, 2005). Furthermore, stellar spectral libraries suffer from certain deficiencies. Theoretical libraries can fully cover the T_{eff}, $\log g(m)$, Z parameter space but require stellar modelling assumptions and have

---

[5] O, Ne, Mg, Si, S, Ar, Ca, and Ti are elements built up with α-particle nuclei.

[6] These set the distribution of stars of the same age and metallicity on the Hertzsprung-Russell diagram according to evolutionary theory.

incomplete atomic and molecular line lists, whereas empirical libraries poorly cover the parameter space due to the rarity of stars of certain evolutionary phases. Recent reviews by Peletier (2013) and Conroy (2013) overview SPS modelling, highlighting the challenges involved but also demonstrating the huge progress being made and the power of the approach.

Galaxies are actually a complex ensemble of different stellar populations, each amassed over a specific star formation history (SFH) and formed under different chemical and environmental conditions. However, despite the model limitations there is still power in comparing SSPs against integrated galaxy spectra to derive *SSP-equivalent* properties of a galaxy's stellar populations, through various analyses including broadband colours, spectral absorption feature indices, or full spectrum fitting. The SED of a galaxy contains many absorption features corresponding to specific atomic or molecular species. These features vary in strength depending on the ages, metallicities, chemical abundances and IMF of the stellar populations. Absorption feature indices have been extensively studied within individual stars (e.g. Spinrad & Taylor, 1969, 1971; Faber et al., 1985; Bressan et al., 1996; Cardiel et al., 1998; Cenarro et al., 2001, 2009) and used to calibrate stellar evolutionary theories and their resulting SEDs.

Spectral indices are usually defined with two pseudo-continuum bandpass regions either side of a feature bandpass region. Then the spectral index equivalent width is measured as,

$$I(\text{Å}) = \int_{\lambda_{c_1}}^{\lambda_{c_2}} \left[1 - \frac{\mathrm{S}(\lambda)}{\mathrm{C}(\lambda)}\right] \mathrm{d}\lambda, \tag{1.25}$$

where λ_{c_1} and λ_{c_2} are the limits of the central bandpass, $S(\lambda)$ is the observed spectrum, and $C(\lambda)$ is the local pseudo-continuum, which is derived as a error-weighted linear fit between the two continuum bandpass regions, one either side of the feature bandpass.

The Lick/IDS index system (Burstein et al., 1984, 1986; Faber et al., 1985; Gorgas et al., 1993; Worthey et al., 1994; Trager et al., 1998) has become a standard set of optical index definitions utilised for inferring galaxy stellar populations over the last thirty years. Other features have been defined at longer wavelengths (e.g. calcium triplet at $\sim 8500\,\text{Å}$: Cenarro et al., 2001) and now a comprehensive set of well studied indices that have different responses to SSP parameters is available between ∼0.4–1.0 μm.

However, a well known problem is the existence of numerous degeneracies between SSP parameters (e.g. the well known age-metallicity degeneracy; Worthey et al., 1994)[7], which heavily complicates the interpretation of observations. Solutions involve using so called *index-index* plots to break degeneracies between SSP parameters, and combining with other data like broadband colours. Despite the challenges, major developments in the quantitative understanding of galaxy stellar populations have been made through analysis of integrated SEDs (e.g. Faber, 1973; Burstein et al., 1984; Trager et al., 1998, 2008).

The most studied galaxy population has been elliptical *early type galaxies* (ETGs), along with *classical bulges* within some spiral galaxies, which share similar properties. Together these count for over half of the total stellar mass in the Universe (e.g. Bell et al., 2003; Gallazzi et al., 2008; Bernardi et al., 2010). ETGs are generally the most massive galaxies and tend to reside in the densest environments, such as the centres of galaxy clusters (Dressler, 1980). They have smooth brightness profiles and generally redder colours with little evidence of star formation (e.g. Renzini, 2006). The basic observable properties of ETGs, the effective radius R_e, the surface brightness within the effective radius, $\langle I \rangle$, and the central stellar velocity dispersion σ_*, have been found to form a very tight correlation known as the *fundamental plane (FP)* (Dressler et al., 1987; Djorgovski & Davis, 1987). The FP is a consequence of virial theory for the stellar dynamics of ETGs, but observations have shown that the FP is actually slightly tilted with respect to that derived from pure virialisation (e.g. Bender et al., 1992).

Using the age-sensitive Hβ and metallicity sensitive Mgb indices, Peletier (1989) and Worthey et al. (1992) showed that ETGs are generally enhanced in [α/Fe]. As the α-elements are predominately produced by the deaths of massive stars in type II supernovae, whereas iron-peak elements are generated by type Ia supernovae, the [α/Fe] ratio become an important estimator of the star formation timescale of ETGs. Thomas et al. (2005) showed that [α/Fe] correlated with σ_* and thus derived the picture of the most massive

---

[7] Galaxies become redder as they age because more massive, bluer stars move off the main sequence earlier, and they also become redder with increasing metallicity, as effective temperatures of most stars decrease because of increasing opacities in the stellar photosphere. Thus a change in stellar age can be compensated by a change in metallicity to give a near identical SED.

ETGs forming at earlier times, with higher star formation rates and shorter star formation periods.

The overall similarities in the properties of ETGs implies a common formation mechanism. Two main formation scenarios have been proposed in the last fifty years:
monolithic collapse where galaxies formed in very rapid, intense star formation bursts in the early universe and then passively evolved to the present day (e.g. Larson, 1974; Carlberg, 1984; Bressan et al., 1994);
hierarchical formation where galaxies grow through successive merging of smaller objects (e.g. Toomre & Toomre, 1972; Toomre, 1977; Frenk, 1988; Cole & Lacey, 1996; Cole et al., 2000).
While hierarchical formation is favoured by the ΛCDM model, massive ETGs have been observed at redshifts of around $z \sim 1$–3 (e.e. Cimatti et al., 2004), and so the picture cannot be as simple as smaller systems merging to form increasingly larger galaxies. Thus, understanding how these competing formation mechanisms leave imprints on the stellar populations of nearby ETGs is a vital task, and one key approach is in trying to discern the form of the initial mass function for these objects.

1.2.3 The stellar initial mass function

The IMF is one of the most important parameters to help constrain our understanding of galaxy formation. This function sets the mass distribution in stars, which in turn sets the stellar mass-to-light ratio of the galaxy. It subsequently affects the amount of hot gas and chemical enrichment returned to the inter-stellar medium (ISM) through supernova feedback, as well as the numbers of stellar remnants, directly affecting observable properties including colour and metallicity. Thus, the IMF provides the link between the galaxy light we observe and the stellar mass, a fundamental property of galaxies which we wish to measure.

The IMF was first defined by Salpeter (1955) as the number of stars N in a volume V per logarithmic mass interval $\log m$ formed at one time,

$$\xi(\log m) = \frac{\mathrm{d}(N/V)}{\mathrm{d}\log m} = \frac{\mathrm{d}n}{\mathrm{d}\log m}, \tag{1.26}$$

where n is the number density of stars. Through direct star counts within the Milky Way (MW) Salpeter 1955 determined that the IMF takes a simple power-law form,

$$\xi(\log m) = km^{-\mu}, \tag{1.27}$$

where $\mu = 1.35$ for $m > 1\,\mathrm{M}_{\odot}$.

Later, Scalo (1986) defined the IMF per mass bin as,

$$\xi(m) = \frac{\mathrm{d}n}{\mathrm{d}m} = \frac{1}{m\ \ln 10}\xi(\log m), \tag{1.28}$$

so that,

$$\xi(m) = k'm^{-x}, \tag{1.29}$$

where equations 1.27 and 1.29 are related as $x = \mu + 1$. Below $1\,M_{\odot}$ the IMF becomes increasingly difficult to constrain as less massive stars are much fainter (luminosity L scales as $L \propto m^{3.5}$ on the main sequence). However, work by several groups showed either a flattening-off of the slope (Miller & Scalo, 1979; Kroupa, 2001) or even a turnover around $1\,\mathrm{M}_{\odot}$ (Chabrier, 2003). The MW IMF is now generally accepted as the Kroupa or Chabrier forms, which use $x = 2.35$ for $m > 1\,\mathrm{M}_{\odot}$, and utilise a broken power law flattening-off and exponential turnover respectively for sub-solar masses, as shown in Figure 1.6 (Kroupa et al., 2013).

1.2.4 A universal IMF?

It has generally been assumed that the form of the IMF is universal for all galaxy types, masses and epochs. Indeed, most galaxy formation and large scale structure simulations simply invoke a single form of the IMF for all simulations. Historical arguments for IMF variations have generally not had substantial observational support; the review by Bastian et al. (2010) suggests that there is no compelling evidence for variation in the IMF for stars of masses above 1–2 $\mathrm{M}_{\odot}$. However, IMF variations have been postulated as possible explanations for several observed phenomena including, the large sodium absorption features present in the centre of M31 (e.g. Spinrad & Taylor, 1971), the observed [α/Fe] enhancement

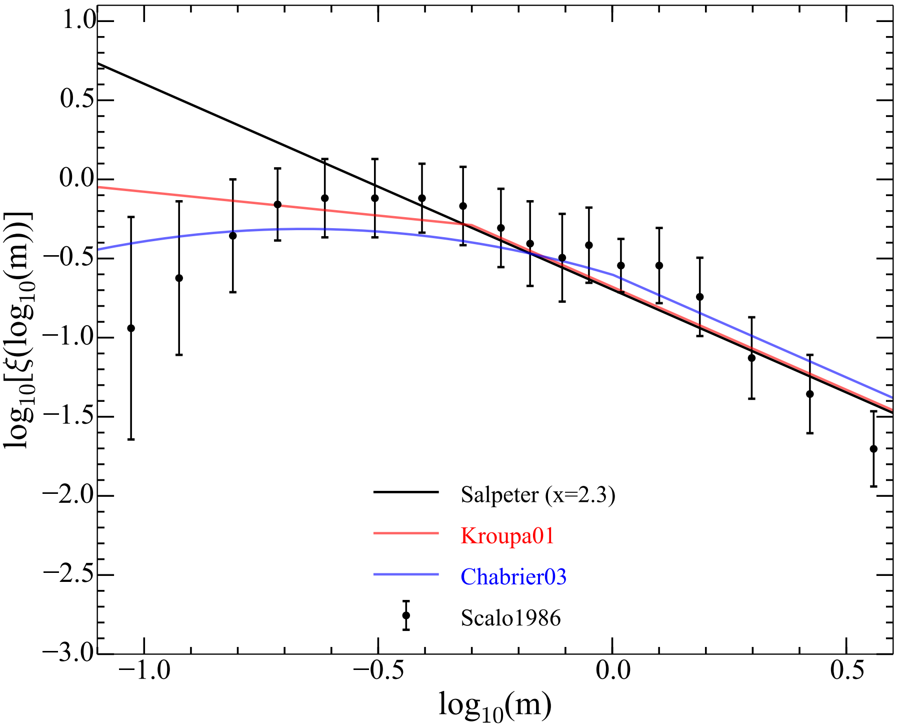

Figure 1.6: Various forms of the MW initial mass function against data from Scalo (1986). The data has been vertically shifted to account for different normalisations. The Salpeter (1955) IMF was determined only for stars of $m > 1\,\mathrm{M}_{\odot}$. The later work by Miller & Scalo (1979); Kroupa (2001) and Chabrier (2003) showed a flattening and even turn-over of the MW IMF at sub-solar masses.

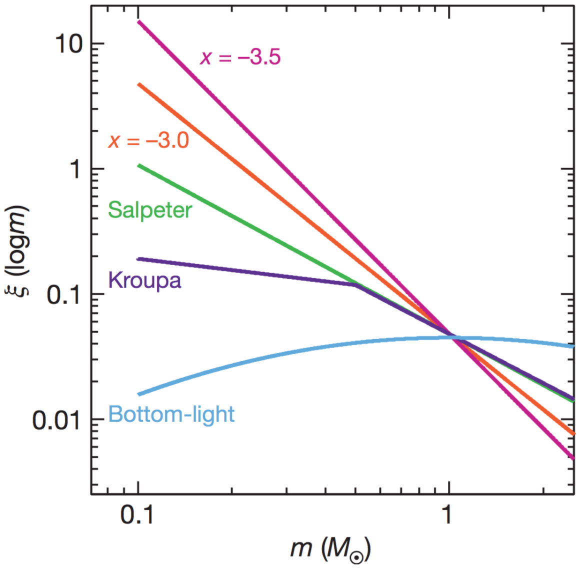

Figure 1.7: Different forms of the low-mass end of the IMF, varying from ‘bottom-light’ to extremely bottom-heavy $x = 3$. IMFs are normalised at $1\,\mathrm{M}_{\odot}$. *Image credit: Figure 2 from van Dokkum & Conroy (2010).*

in the centres of massive ETGs (e.g. Worthey et al., 1992), and to explain the observed tilt in the fundamental plane of elliptical galaxies (Renzini & Ciotti, 1993). The low mass end of the IMF ($< 1\,\mathrm{M}_{\odot}$) has been one of the most difficult functions to constrain for external galaxies, as direct star counts are not possible with current telescopes and low mass stars only contribute a few per cent of the total luminosity of a galaxy (see e.g. Figure 2 from Conroy & van Dokkum, 2012a). Thus, techniques must be developed to interpret the kinematics, dynamics and integrated stellar light on scales of a few to hundreds of parsecs. Several independent methods have been developed to constrain the IMF in external galaxies.

Dynamical modelling: Mapping the 2D stellar kinematics of galaxies using IFS allows dynamical models to be constructed, which can constrain the total mass-to-light ratio M/L. This approach constrains all mass within a given radius and thus includes dark- as well as luminous matter. This technique has been used extensively on ETGs, which are generally gas-poor and thus weak in emission lines. By accounting for the dark matter halo it is possible to derive the stellar M_{*}/L. One can then compare to the M_{*}/L for a given SSP

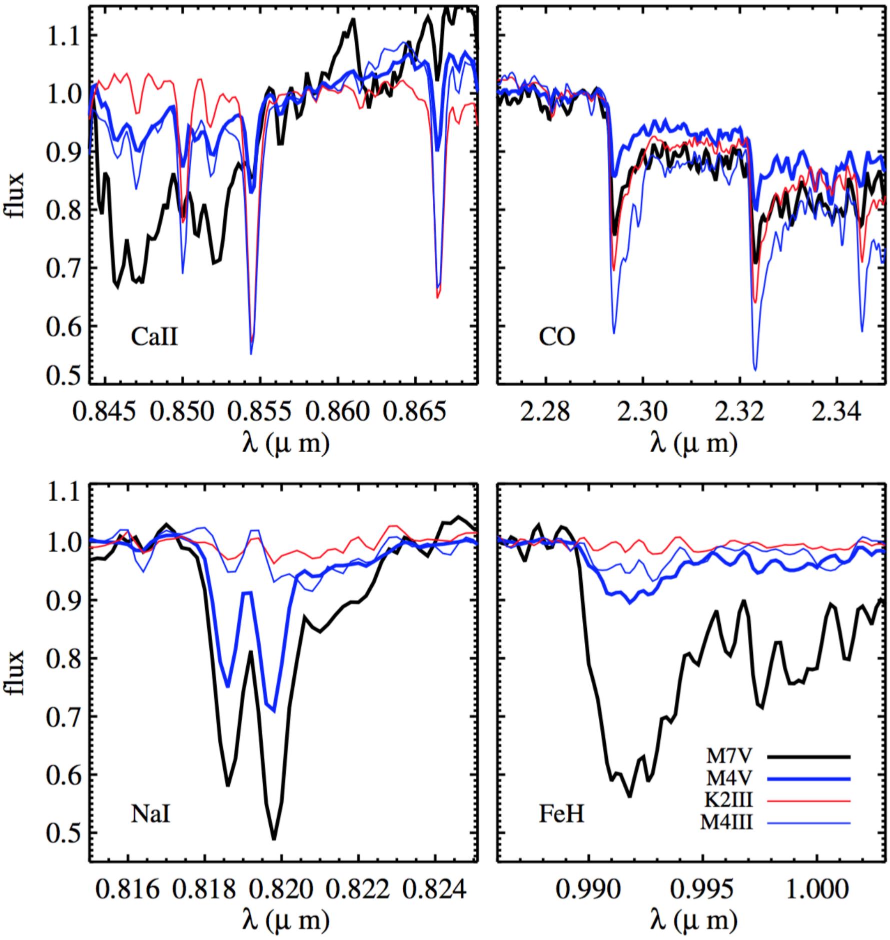

Figure 1.8: NASA IRTF spectra for stars of different luminosity and spectral types around gravity- and temperature-sensitive absorption features. The top row shows the calcium triplet CaT around 8500 Å (left) and CO2.30 feature (right), which are both strong in giants and weak in dwarfs. The bottom row shows the sodium doublet NaI0.82 (left) and the Wing-Ford band FeH (right), which are both strong in dwarfs and weak in giants. The physical scenario of these features is a consequence of ionisation equilibrium: for atoms, as the electron pressure increases at fixed temperature due to the increased surface gravity, the ratio of singly ionised to neutral species of the same atom decreases. For molecules, molecular dissociation equilibrium implies that an increase in pressure generates more molecules on the side of the chemical reaction with fewer moles of gas. *Image credit: Figure 6 from Conroy & van Dokkum (2012a).*

model with a fixed (universal) IMF and find a mismatch parameter,

$$\alpha = \frac{(M_*/L)_{\rm dyn}}{(M_*/L)_{\rm ssp}} \tag{1.30}$$

Recent dynamical modelling results have shown a systematic increase in α as a function of galaxy velocity dispersion σ (e.g. Thomas et al., 2011; Cappellari et al., 2012, 2013). One challenge with this approach is accurately accounting for the dark matter, as an increase in dark matter is degenerate with a small decrease in the low-mass IMF (Bundy et al., 2015). Thus, dynamical measurements should be viewed as upper limits on the M_*/L.

Gravitationally lensed galaxies: Similarly to dynamical modelling, the total mass in a system can be constrained using strong gravitational lensing. This method offers very accurate (total) mass measurements as they are not affected by the dynamics or thermal state of systems, and only require geometrical knowledge of the lensing system (e.g. distances to objects), which can obtained from spectroscopy. Results (e.g. Treu et al., 2010; Auger et al., 2010; Spiniello et al., 2011) have shown agreement with the dynamical result of an increase of α with velocity dispersion. Further results by Smith & Lucey (2013) and Smith et al. (2015b) have shown four massive ETGs favouring a MW-like IMF.

Gravity sensitive stellar absorption features: Throughout the second half of the 20th century, numerous groups detected and highlighted specific stellar absorption features that are prominent in the spectra of low mass *dwarf* stars, but absent in high mass *giants*. These included the sodium doublet NaI at 8190 Å (Faber & French, 1980; Schiavon et al., 1997a) and the iron-hydride Wing-Ford band FeH at 9920 Å (Wing & Ford, 1969; Schiavon et al., 1997b; Cushing et al., 2003). Giant-sensitive features like the calcium triplet CaT (Cenarro et al., 2001) also exist and Figure 1.8 shows several key features in individual stellar spectra. These and other features have been used to try and infer the numbers of dwarf stars present and thus the IMF in the centres of both spiral and elliptical galaxies (e.g. Faber & French, 1980; Carter et al., 1986; Hardy & Couture, 1988; Delisle & Hardy, 1992; Couture & Hardy, 1993). However, a lack of both high S/N data and detailed SPS models, coupled with the challenges of spectroscopy in the far red and NIR, meant that arguments for a varying IMF were inconclusive. As $L \propto m^{3.5}$ on the main sequence, integrated light is dominated by the most massive stars at the tip of the main sequence turn-off. Therefore these features are only of the order of several per cent relative to the continuum in an integrated spectrum. However, recent progress by van Dokkum & Conroy (2010) and Conroy & van Dokkum (2012b) has shown that it is possible to detect and model these absorption features in integrated light from massive ETGs with very high S/N spectra obtained using modern NIR detectors. They detected the NaI doublet, the calcium triplet CaT, and FeH in spectra from the centres of 38 giant ETGs. Using SPS models specially crafted for studying low mass populations, they found both an IMF-σ relation in agreement with the dynamical studies, and also a correlation with [α/Fe]. Further work using a variety of optical and far red indices has reinforced the IMF-σ relation in ETGs (e.g. Ferreras et al., 2013; La Barbera et al., 2013; Spiniello et al., 2014), however there has been some evidence to weaken the correlation with α-enhancement (La Barbera et al., 2013).

This potentially emerging picture of more massive galaxies having greater abundances of dwarf stars poses interesting questions for our understanding of galaxy formation. One implication is that star formation occurs under different conditions in higher mass galaxies. Recent work has suggested that the processes of fragmentation via supersonic turbulence in molecular clouds as a possible physical model (e.g. Hennebelle & Chabrier, 2008; Hopkins, 2012a,b; Chabrier et al., 2014). The most massive ETGs are α-enhanced, which can be inferred as higher star formation rates (SFRs) over a shorter formation timescale (e.g. Thomas et al., 2005). It is possible that higher Mach numbers caused by high type II supernovae rates drives the IMF to lower characteristic masses (Conroy & van Dokkum, 2012a). In this picture the IMF is driven by the conditions under which the stars form in a galaxy. Therefore, in the centres of massive ETGs one might expect a deeper potential and thus, a higher concentration of gas, higher star formation densities, higher Mach numbers and therefore a more bottom-heavy IMF. As one moves towards the outskirts of the galaxies, the star formation densities will presumably fall and the IMF will become less bottom-heavy. However, the physical interpretation of the recent IMF results is still an open question, and even the notion of a varying IMF is still not a universally accepted concept.

1.2.5 Radial gradients in the IMF

While the recent IMF work suggests a paradigm shift is required from the assumption of a universal IMF for all galaxies, these results are only representative of the central regions of each galaxy. The centres of regular galaxies are the most dense and turbulent regions where one might expect to see large dwarf star abundances. If the dwarf sensitive features are present out to further radii this would have large implications for the total stellar mass of galaxies, and a radial gradient of these features could imply that the IMF is a *local* property within a galaxy and thus stars form differently within different environments, and that galaxies grow their stellar structure from the inside outwards.

Searching for IMF radial gradients will therefore provide more conclusive results for use in galaxy formation and evolution modelling. Detecting radial gradients in IMF-sensitive features has previously been investigated by Boroson & Thompson (1991), who were able to see such a gradient in the NaI index for three ellipticals in Virgo out to around $30''$, but unable to confirm that it was an IMF effect. Also, Delisle & Hardy (1992) measured radial gradients in a range of far red indices, including NaI and FeH, for several spiral bulges and elliptical galaxies, concluding that radial trends were more likely due to metallicity rather than a varying IMF. However, recent results by Martín-Navarro et al. (2015a) have indicated a gradient to the IMF slope, ranging from very bottom-heavy in the centre, to Salpeter-like at the effective radius, in a massive ETG with central velocity dispersion of $\sigma \sim 300\,\mathrm{km\,s^{-1}}$. A further work by Martín-Navarro et al. (2015b) has presented measurements for another massive ETG suggesting a flat, bottom-heavy IMF profile throughout the galaxy. These recent results by Martín-Navarro et al. were also derived from strong sodium index gradients. If they do represent IMF gradients then other IMF-sensitive features, including FeH which was not covered in these studies, should also show gradients.

The form of the low-mass end of the IMF in external galaxies has been a contentious topic for several decades. However, the hunt for evidence of IMF radial gradients is a more recent and compelling avenue of exploration. The first part of this thesis is a contribution to these areas. In Chapters 2 and 3 we present radial measurements of several far red absorption features within a small sample of galaxies, and use SPS modelling to:

(a) constrain the low-mass end of the IMF,

(b) hunt for radial gradients and determine whether they represent IMF gradients or are driven by other factors.

IFS provides a powerful advancement upon long-slit spectroscopy for detecting the faint IMF-sensitive absorption features. The spatial coverage allows the binning of data over a 2D field so we can achieve a desired S/N with much greater efficiency. As an example, if we want to measure the NaI feature in a galaxy, Conroy & van Dokkum (2012a) state that S/N $\geq 100\,\text{Å}^{-1}$ is necessary to distinguish between a Chabrier and Salpeter IMF at the 2σ level in their SPS models. We can estimate the required observing time for the Coma ETG NGC4839 (a target in Chapter 3) as follows:

the i-band surface brightness of the Coma ETG NGC4839 at the centre is

$F_{\lambda,i} = 18\,\mathrm{mag\,arcsec^{-2}} = 7.74\,\mathrm{erg\,s^{-1}\,cm^{-2}\,Å^{-1}\,arcsec^{-2}}$ (Ali et al., 2014);

the sky background is $F_{\mathrm{bg},i} = 19.7\,\mathrm{mag\,arcsec^{-2}} = 1.66\,\mathrm{erg\,s^{-1}\,cm^{-2}\,Å^{-1}\,arcsec^{-2}}$ (Patat, 2004)[8];

and the required parameters for SWIFT are:

$D_{\mathrm{c}} = 0.0022\,\mathrm{e^{-}\,s^{-1}\,pixel^{-1}}$,

$\sigma_{\mathrm{R}} = 4.0\,\mathrm{e^{-}\,pixel^{-1}}$,

$T_{\mathrm{tot}} = 0.23$,

$\Delta\lambda = 1\,\text{Å}$ ($N_{\mathrm{pix}} = 1$ in this case as SWIFT sampled at $1\,\text{Å}\,\mathrm{pixel^{-1}}$),

$r_{\mathrm{spax}} = 0.235\,\mathrm{arcsec\,spaxel^{-1}}$,

$A = 20\,\mathrm{m^2}$.

From Equations 1.12 and 1.13 we find,

$$\mathrm{N_{obj}} = 0.08161\,\mathrm{e^{-}\,s^{-1}\,Å^{-1}\,spaxel^{-1}}, \tag{1.31}$$

$$\mathrm{N_{bg}} = 0.01753\,\mathrm{e^{-}\,s^{-1}\,Å^{-1}\,spaxel^{-1}}, \tag{1.32}$$

and so from Equation 1.15 we find that for one hour on-source ($T_{\mathrm{exp}} = 900\,\mathrm{s}$, $N_{\mathrm{exp}} = 4$) the

---

[8] Using an i-band zeropoint (Vega system) of $1.226 \times 10^{-9}\,\mathrm{erg\,s^{-1}\,cm^{-2}\,Å^{-1}}$ given for the ESO ETCs: `http://www.eso.org/observing/etc/doc/formulabook/node12.html`

S/N per Å in a single spaxel is,

$$\mathrm{S/N} = \frac{0.08161 \times 900 \times \sqrt{4}}{\sqrt{(0.08161 + 2 \times 0.01753 + 2 \times 0.0022) \times 900 + 2 \times 4^2}}, \tag{1.33}$$

$$= 12.4\,\text{Å}^{-1}\,\mathrm{spaxel}^{-1}. \tag{1.34}$$

Importantly, as $\mathrm{S/N} \propto \sqrt{N_{\mathrm{spax}}}$, we find that by binning over 70 spaxels we achieve $\mathrm{S/N} > 100\,\text{Å}^{-1}$. This represents a circular aperture of 5 spaxels in radius. This would not be possible with a long-slit spectrograph without a much longer integration time, or integrating along a much larger radial extent, thereby reducing the spatial resolution of the data; 70 SWIFT spaxels along one dimension corresponds to 16 arcsec. This demonstrates several advantages of IFS over long-slit spectroscopy:

a) S/N can be improved by both increasing observing time and by summing over a larger spatial extent in the FoV. These can be traded off against each other to maximise observing efficiency (minimise telescope time).

b) for very extended objects an IFU can be used as a *light-bucket* where one bins over the entire FoV for a large gain in S/N. Using SWIFT, an observer can gain in S/N by a factor of up to $\sim \sqrt{3500} = 60$.

c) resolved studies like absorption feature gradients can be undertaken using the full radial extent of the galaxy, rather than along the single radial vector covered by a long-slit spectrograph observation.

For the first part of this thesis, we utilise SWIFT to gain from all three advantages. We use the 2D spatial coverage for annular binning to perform resolved studies of the centres of galaxies, and make use of it as a light-bucket when integrating over low surface brightness fields.

1.2.6 Star formation in high redshift galaxies

From studying local galaxies, we know that the formation of stars occurs in cold, giant molecular clouds (GMCs) of neutral molecular hydrogen, which are subject to gravitational collapse when perturbed by gravitational instabilities to exceed the characteristic Jeans mass. Turbulence and self-gravity cause fragmentation of the GMCs across a range of masses, within which stars form through further collapse. Within each of these fragments the collapsing gas radiates away the energy gained by the release of gravitational potential energy. As the density increases, the fragments become opaque and are thus less efficient at radiating away their energy. This raises the temperature of the cloud and inhibits further fragmentation, leading to the generation of a rotating proto-star (e.g. McKee & Ostriker, 2007).

Newly-formed, massive O and B type stars have huge UV photon fluxes and ionise the surrounding neutral atomic hydrogen to form HII regions. As hydrogen recombines, electrons cascade down to the $n = 1$ level and prominent Hα emission corresponding to the $n = 3 \rightarrow 2$ transition is emitted at 6562.8 Å. HII regions are therefore strong tracers of underlying star formation in galaxies, and SFRs have been well calibrated from Hα emission (e.g. Kennicutt, 1983; Kennicutt et al., 1994). These calibrations have also offered constraints on the high mass end of the IMF slope, which are generally consistent with the Salpeter $x = 2.35$ slope. Characteristic sizes of HII regions range from $\sim$ 40–100 pc (González Delgado & Pérez, 1997; Sánchez et al., 2012) in local galaxies.

However, the specifics of the many mechanisms which influence star formation in galaxies at high redshift are still a challenge to fully understand. Using large, wide- and deep-field surveys, astronomers have probed the Universe back to when it was less than 1 Gyr old and traced how galaxy star formation varied throughout cosmic time (see Figure 1.9). Observations have shown that the star formation density has increased from early times to a peak at $z \sim 1.5$–3 and since decreased to the present day. Thus, $z \sim 1.5$–3 has been heralded as the peak epoch of star formation when most of today's massive galaxies formed the bulk of their stellar mass (Madau & Dickinson, 2014). At these early times galaxies appear to be undergoing significant changes to their morphologies and stellar populations. The gas content of galaxies is also much higher at high redshift, with more intense feedback mechanisms in place (e.g. Bower et al., 2006), so the conditions of star formation in these galaxies is very different to locally.

Over the past decade major advances have been made in measuring the kinematics and dynamics of galaxies at these early epochs using integral field spectroscopy (e.g. SINS

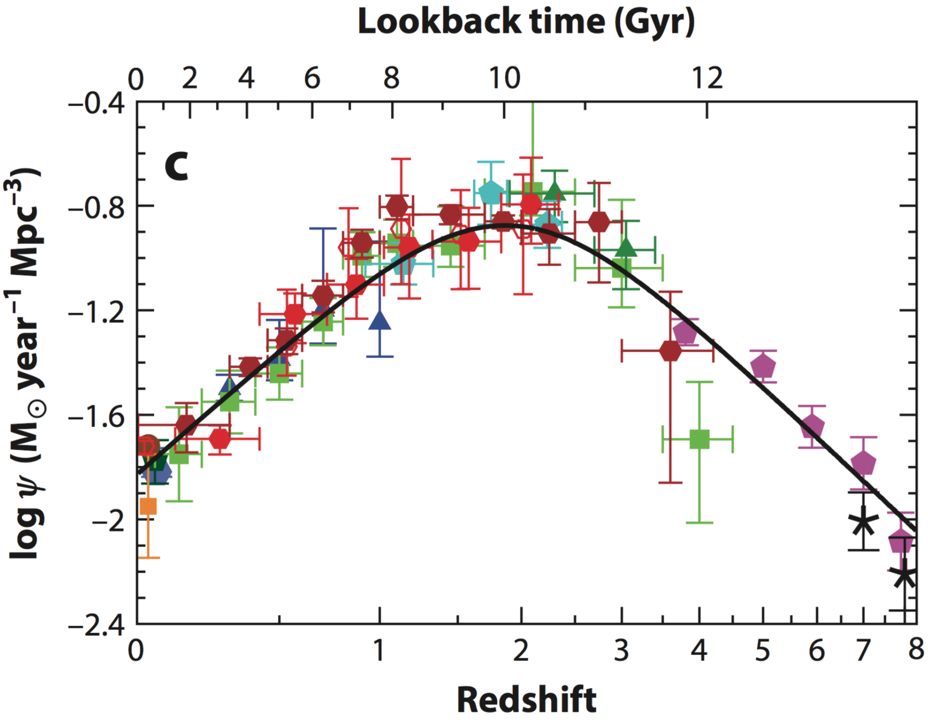

Figure 1.9: Star formation density as a function of redshift or age of the Universe, derived through large, wide- and deep-field, ground- and space-based surveys. Star formation rose steadily to a peak around z ∼2–4 and has since declined to the present day. The data are derived from a combination of ultra-violet (UV) and NIR observations, where the observed galaxy luminosities are converted to SFRs assuming a Salpeter IMF. The Universe created the bulk of its stellar mass around 10 Gyr in the past. *Image credit: Figure 9 from Madau & Dickinson (2014).*

using SINFONI on the VLT: Genzel et al. 2006, Förster Schreiber et al. 2006, 2009; OSIRIS on Keck II: Law et al. 2007, 2009; KMOS on the VLT: Wisnioski et al. 2015; see also Glazebrook 2013 review). Many galaxies show regular rotation at these early times, even when the morphologies appear irregular. The general picture is of turbulent disc galaxies, rich in molecular gas and containing large $\sim 1\,\mathrm{kpc}$ star-forming complexes.

However, due to the photon-starved nature of the observations, deriving the dynamics of high redshift galaxies requires long integration times on 8–10 m telescopes, which only offer limited spatial resolution. From Equation 1.2, we see that the diffraction limit of 8–10 m telescopes is 50–70 mas in the K-band ($2.2\,\mu$m). However, except in the most stable conditions, current AO systems usually only achieve angular resolutions of around $\sim 100\,\mathrm{mas}$, which corresponds to $\sim 1\,\mathrm{kpc}$ at $z = 2$ (e.g. Förster Schreiber et al., 2011a,b; Swinbank et al., 2012b,a). Gravitationally-lensed star-forming galaxies do provide the unique ability to resolve regions at scales of $\sim$ 60–200 pc (Jones et al., 2010; Livermore et al., 2012, 2015), however these are notable rare exceptions limited to a handful of objects. Therefore, current constraints on star formation, chemical abundance evolution and stellar/AGN feedback are only possible from statistical studies of the high redshift population as a whole, and neglect the complex physics of star formation within clumps, merging, supernovae and AGN activity of individual galaxies.

One of the main scientific goals of HARMONI on the E-ELT will be to spatially resolve the interstellar medium (ISM) at $z \sim$ 2–3. The increased light-gathering power and spatial resolution of the E-ELT combined with AO will provide exquisite resolution of galaxies at the sub-kpc level. The theoretical angular resolution of the E-ELT is 15 mas in the K-band ($2.2\,\mu$m), which corresponds to $\sim 125\,\mathrm{pc}$ at $z = 2$, around the size of the largest individual star-forming HII complexes. The properties (e.g. sizes, luminosities, velocity dispersions, chemical make-up and spatial distribution) of these regions reflect the underlying ISM (such as gas density and pressure), which in turn reflect the dominant route by which galaxies accrete the bulk of their gas.

During the development stage of HARMONI we assess the feasibility of these observations by undertaking simulations of high redshift galaxies, with an aim to set simple limits on the SFRs, kinematics and clump sizes detectable in reasonable observing periods. This work is presented in Chapter 6.

1.3 Thesis outline

This thesis begins with two projects using observations taken with the SWIFT instrument. We have explored radial gradients of IMF-sensitive far red spectral absorption features in two sets of galaxies, utilising the advantages of IFS for its 2D spatial coverage for resolved studies, and as a light-bucket. Chapter 2 presents the spiral M31 alongside its dwarf elliptical M32; Chapter 3 presents three ETGs in the Coma cluster, the two massive Coma brightest cluster galaxies (BCGs), NGC4889 and NGC4874, and the BCG in the Coma south-west cluster NGC4839. For each project we detail the data reduction process, the measurements, analysis using SPS models and our derived conclusions regarding the IMF of the stellar populations.

The second part of this thesis presents the development and use of a simulation pipeline for the HARMONI instrument on the E-ELT. Chapter 4 presents our HARMONI simulation pipeline HSIM, detailing the individual stages incorporated to create accurate IFS mock data. As part of this we describe our implementation of a wavelength-dependent AO PSF model into the pipeline.

In Chapter 5 we present predicted instrument performance through point source sensitivity calculations using HSIM. We explore the noise regimes of the various instrument operating configurations. We also perform a comparison of the expected AO performance at visible wavelengths between HARMONI and the MUSE narrow field mode.

In Chapter 6 we present simulations undertaken using HSIM of $z \sim$2–3 emission-line galaxies. We describe the procedures for generating realistic input data cubes and present simulations of disc-like and clumpy galaxies. We then present resolved kinematics of these galaxies and explore HARMONI's potential for probing star-forming regions at sub-kpc scales in galaxies at these redshifts.

Finally, a summary of conclusions and brief overview of future directions is given in Chapter 7.

Part I

Science with the Oxford SWIFT

Chapter 2

The initial mass functions of M31 and M32 through far red stellar absorption features

In this chapter we use the Oxford SWIFT to detect and measure radial gradients in IMF-sensitive absorption features within M31 and M32. While all of the recent IMF work has looked at early type galaxies (ETGs, e.g. Conroy & van Dokkum, 2012b; Ferreras et al., 2013; Spiniello et al., 2014), it is interesting to compare to the bulges of spiral galaxies. M31 is an ideal target for high S/N resolved spectroscopy due to its proximity. It is an archetypal spiral galaxy and the central bulge has had its stellar populations extensively studied, both using spectroscopy (e.g. Davidge, 1997; Saglia et al., 2010) and photometry (e.g. Stephens et al., 2003; Sarajedini & Jablonka, 2005). Determining the presence of IMF gradients will help provide a more comprehensive understanding of spiral bulges and the process behind IMF variations.

The form of the IMF in the nuclear region of M31 has been the subject of much debate throughout the second half of the 20th century (see Conroy & van Dokkum, 2012b, Section 4.2). The core has been known to have prominent sodium absorption and this has been interpreted as an increased dwarf abundance by some (e.g. Faber & French, 1980) and sodium enhancement by others (e.g. Alloin & Bica, 1989).

In this chapter we present three studies on:

a) the variations of the IMF-sensitive features NaI, CaT and FeH in M31 through the bulge out to the old disc at $\sim 700''$ (2.7 kpc);

b) the variations of these features through the inner bulge to the nuclear region of M31 where there has been much historic debate;

c) these features in the central $8''$ (30 pc) of M32.

We use the definitions from Kormendy & Bender (1999) and Tempel et al. (2011) to describe the components of M31. The nuclear region is defined as $r < 4''$ (15 pc), the bulge as $4 < r < 450''$ (1.7 kpc), and the disc as $r > 450''$. We also refer to the region between $4 < r < 10''$ as the inner bulge.

We analyse our results using the latest stellar population synthesis models from Conroy & van Dokkum (2012a, hereafter CvD12) and Vazdekis et al. (2012, hereafter V12). We further investigate a method of disentangling the degeneracies in age and metallicity by using colour as a proxy for age, in the absence of the standard Hβ absorption line.

We adopt a distance to M31 of 785 kpc as measured by McConnachie et al. (2005), which gives a scale of 3.8 pc arcsec^{-1}. We further adopt the IMF naming convention used by CvD12, namely a Chabrier IMF corresponding to that defined in Chabrier (2003) for the disc of the Milky Way; a Salpeter IMF defined as $x = 2.3$ for V12 and $x = 2.35$ for CvD12; and a bottom-light IMF as defined in van Dokkum (2008).

2.1 Observations and data reduction

2.1.1 Overview

Observations of M31 and M32 were obtained over the nights of 2011 December 3 and 5; 2012 September 23 and 24; and 2014 October 2 using the SWIFT instrument (Thatte et al., 2006) on the Palomar 200 inch (5.1 m) telescope. Figure 2.1 shows the position of each pointing. Observations were taken at the 235 mas spaxel^{-1} spatial scale covering a field of $10'' \times 21''$. The spectra cover the wavelength range $6300 - 10400$ Å with a dispersion of ~ 2 Å FWHM and a sampling of 1 Å pix^{-1}. Table 2.1 lists the pointings and dates of the observations. The seeing was around $1.5''$ full width half maximum (FWHM) for all

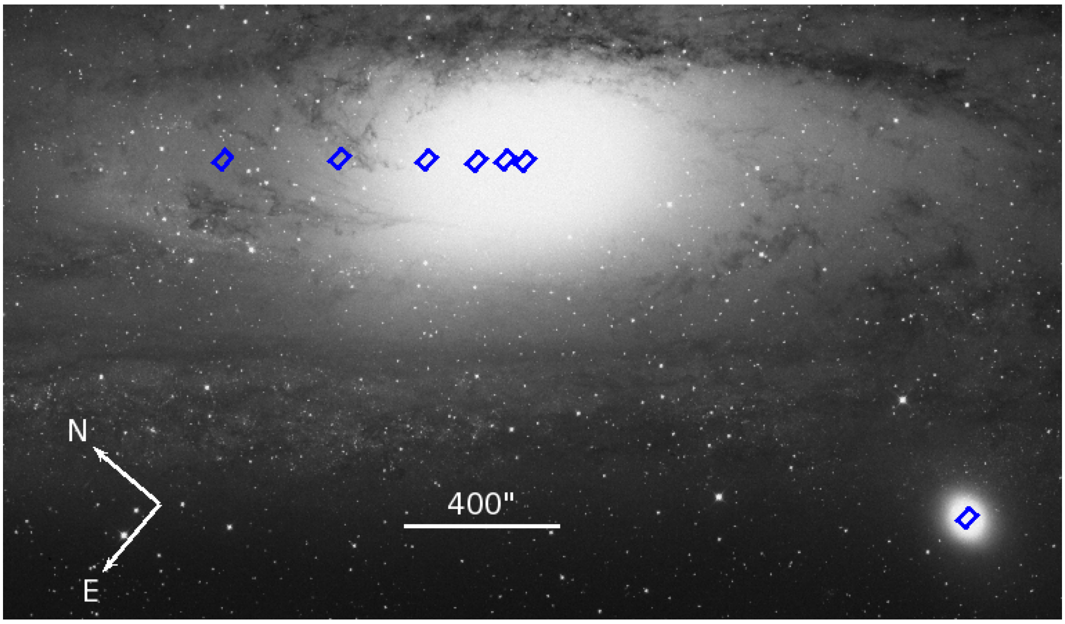

Figure 2.1: STScI/Digital Sky Survey (DSS) image of M31 and M32 showing the locations of the SWIFT fields (blue boxes). The M31 fields are named in order of increasing radius from M31_1 through to M31_6. Note that the boxes only show the locations of the fields, and are not representative of the size of the SWIFT field of view.

observations.

The data were reduced using the SWIFT data reduction pipeline, written in IRAF. The pipeline handles all the standard reduction processes of bias subtraction, flat fielding, wavelength calibration, error propagation as well as IFS specific features of illumination correction and cube reconstruction. Cosmic rays were detected and removed using the LACOSMIC routine (van Dokkum, 2001).

We obtained Sloan Digital Sky Survey (SDSS) $g-r$ colour data from Saglia et al. (2010) and Tempel et al. (2011). Saglia et al. covered all M31 pointings except M31_6 for which we used Tempel et al. (2011). Sodium D (NaD λ5893) index measurements for M31 and M32 were obtained from Davidge (1991, 1997). We applied corrections to the Davidge NaD data based upon the CvD12 models to account for the measurements being at a lower resolution than $\sigma = 200\,\mathrm{km\,s^{-1}}$ (see Section 2.1.5).

Table 2.1: Observational fields of M31 and M32 along with dates and total exposure times. Observations of M31 are labelled as M31_1 through to M31_6 in increasing radii from the centre. We also give the positions of the sky fields.

Field	RA	DEC	Date	T_{exp} (s)
M31_1	00:42:44.57	+41:16:05.7	03-12-2011	3600
M31_2	00:42:46.82	+41:16:41.3	23-09-2012	1800
M31_3	00:42:51.04	+41:17:38.3	23-09-2012	1800
M31_4	00:42:58.19	+41:19:17.8	02-10-2014	1800
M31_5	00:43:10.80	+41:22:03.7	23-09-2012	3600
M31_6	00:43:28.30	+41:25:52.8	23-09-2012	3600
M32	00:42:41.86	+40:51:57.0	23-09-2012	3600
SKY_M31	00:44:12.04	+40:48:05.6		
SKY_M32	00:46:15.27	+41:01:28.3		

2.1.2 Sky subtraction and spectra extraction

Sky subtraction was performed to first order by subtracting sky frames observed adjacent in time to each science frame. We were careful to choose sky fields sufficiently far away so as to avoid contamination from M31. The positions are given in Table 2.1. We extracted spectra in two ways.

For fields M31_2 to M31_6 we summed up all spaxels within the field to obtain a median spectrum of maximal S/N; in this case we first normalised by the median image to remove the increased weighting of brighter regions over fainter ones.

For M31_1 and M32 fields we performed sector binning (Houghton et al., 2013) to obtain a 2D map of spectra with S/N $\sim 100\,\text{pixel}^{-1}$ (in the central wavelength region). This gave ~ 200 individual spectra within a radius of $10''$ for M31_1 and ~ 170 spectra within $8''$ for M32. The numbers are slightly lower for the FeH optimised spectra due to more demanding S/N requirements for that region of the spectrum. The final median S/N around each spectral feature is shown in Table 2.2.

2.1.3 Telluric correction

Atmospheric telluric absorption is prominent in both the NaI and FeH regions. We observed A0V stars during the observations to act as telluric standards. These stars have strong Paschen lines around 8500 Å which we remove using a dedicated routine written in

Table 2.2: Median S/N of spectra around each index for M31 and M32. For $R < 8''$ the S/N is a median of all the individual binned spectra from the sector binning (see Section 2.1.2).

Field	R ($''$)	NaI	CaT	FeH
		M31		
M31_1	< 8	123	122	90
M31_2	40	321	320	213
M31_3	100	273	273	191
M31_4	230	192	195	135
M31_5	415	104	106	94
M31_6	710	78	80	66
		M32		
M32	< 8	89	89	59

IDL. The telluric spectra are divided out by model A0V spectra provided by R. Kurucz[1], using a version of the amoeba algorithm allowing for velocity shifts and stellar rotation. Our corrected telluric spectra are accurate to around the 0.5–1 % level (see Figure A.1 in Appendix A).

2.1.4 Kinematic fitting and second-order sky subtraction

We fit the kinematics of the spectra with the penalised pixel fitting routine (PPXF, Cappellari & Emsellem, 2004) using, as template spectra, the stellar population models from CvD12. Due to the presence of skyline residuals in the spectra, we found it necessary to perform a *simultaneous* second-order sky subtraction while extracting the kinematics (Weijmans et al., 2009). This was accomplished using the techniques described in Davies (2007): rather than scaling a single sky spectrum covering multiple OH vibrational transitions, we divide the spectrum into separate regions covering each OH vibrational transition. This allows independent scaling of each transition. We also scale the O_2 emission around $0.864\,\mu$m separately. Furthermore, to account for flexure (error in the wavelength calibration) we interpolate the spectrum of each transition (OH & O_2) forward and backwards by one pixel. The sky spectra are extracted from the matching spaxels, or bins, as their respective science spectra. All these spectra are then passed to PPXF which finds the best-fit linear summation that reproduces the skyline residuals while also finding the best fit kinematics[2]. For each

---

[1] Spectra available at `http://kurucz.harvard.edu/stars.html` - last accessed 09-02-16

[2] We manually altered the internal limits in PPXF to allow negative sky spectrum weights.

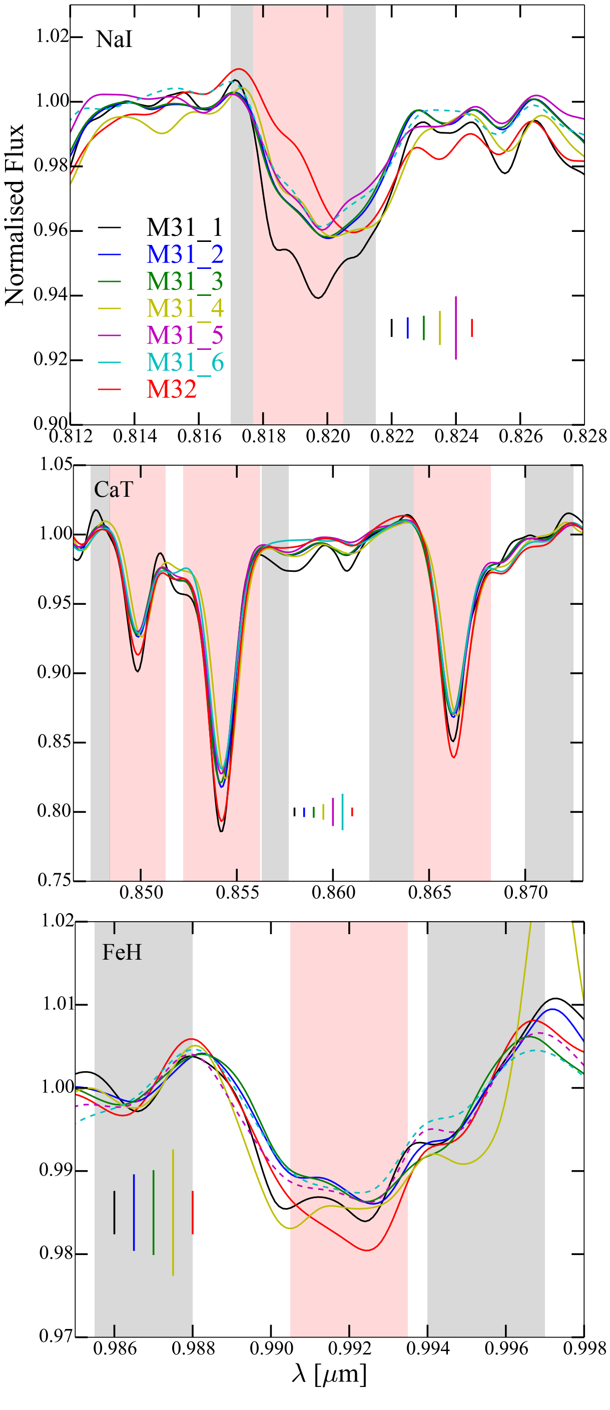

Figure 2.2: Plots of the three IMF-sensitive spectral features, NaI (top), CaT (middle) and FeH (bottom) for each pointing in M31 and M32. The feature and pseudo continuum definitions (Table 2.3) are shown in each subplot by the red and grey shaded regions respectively. The spectra have been normalised to the continuum bands either side of the feature. M31_1 and M32 correspond to median spectra obtained over the entire M31_1 and M32 fields. For M31_6 in the NaI plot, and for M31_5 and M31_6 in the FeH plot, we show the best fit kinematic template spectra (coloured dashed lines) instead of the science data due to contamination from the sky background. Typical $\pm 1\sigma$ error bars are denoted by the vertical lines at the bottom of each subplot.

galaxy spectrum (whether it be from a single bin or a median of the entire field-of-view), we measure the intrinsic instrument dispersion from the skylines in the same wavelength range as the principal absorption features.

The resolution of a galaxy spectrum as observed by SWIFT is $\sigma_{*,\mathrm{obs}}$ and is given by,

$$\sigma_{*,\mathrm{obs}} = \sqrt{\sigma_*^2 + \sigma_{\mathrm{inst}}^2}, \tag{2.1}$$

where σ_* is the intrinsic galaxy stellar velocity dispersion and σ_{inst} is the instrument resolution. PPXF measures the galaxy resolution by fitting with template spectra of intrinsic resolution σ_{temp}. When the template resolution used in PPXF is finer than the instrument resolution ($\sigma_{\mathrm{temp}} < \sigma_{\mathrm{inst}}$), we convolve the template library to the same resolution as the instrument, so $\sigma_{\mathrm{temp,n}} = \sigma_{\mathrm{inst}}$, and then PPXF measures,

$$\sigma_{\mathrm{ppxf}} \approx \sigma_* = \sqrt{\sigma_{*,\mathrm{obs}}^2 - \sigma_{\mathrm{temp,n}}^2}. \tag{2.2}$$

However, the SWIFT spectral resolution varies from $40\,\mathrm{km\,s^{-1}}$ (R $\sim$ 3100) to $65\,\mathrm{km\,s^{-1}}$ (R $\sim$ 2000) across the field of view and the resolution of the CvD12 models is R=2000 beyond $0.75\,\mu$m. In this case we cannot convolve the template library to the instrument resolution and PPXF instead underestimates the galaxy dispersion by measuring,

$$\sigma'_{\mathrm{ppxf}} = \sqrt{\sigma_{*,\mathrm{obs}}^2 - \sigma_{\mathrm{temp}}^2}. \tag{2.3}$$

Therefore, when $\sigma_{\mathrm{temp}} > \sigma_{\mathrm{inst}}$, it is necessary to correct the dispersions found by PPXF for the difference between instrument and template resolutions: to all PPXF dispersions we added in quadrature the difference between the template resolution in that wavelength range and the instrument resolution,

$$\sigma_* \approx \sqrt{\sigma'^2_{\mathrm{ppxf}} + (\sigma_{\mathrm{temp}}^2 - \sigma_{\mathrm{inst}}^2)}. \tag{2.4}$$

In practice this only significantly affects dispersions less than $100\,\mathrm{km\,s^{-1}}$ (M31_6 and M32).

Using this technique, we are able to clean sky residuals from the galaxy spectra (prior to calculating element abundances) using the best-fit ‘second-order’ sky spectrum generated by PPXF. However, the sky spectrum contains both continuum and line emission, and scaling to remove the line residuals also scales the continuum. This may be a source of bias: adding or subtracting a constant continuum level from the galaxy spectrum will alter subsequent equivalent width measurements. As there is no reason to believe continuum and line emission scale in the same way (unless the continuum is composed primarily of unresolved faint OH lines from the same transition, Davies, 2007), we subtracted the continuum from the second-order sky spectrum before using it to remove the skyline residuals in the galaxy spectra. Typically, the effect of this in equivalent width measurements is only a few per cent, but it can be as large as 10 %.

For all fields, we fit the kinematics (and second-order sky spectra) separately for the NaI–CaT ($0.785\,\mu$m to $0.90\,\mu$m) and FeH ($0.97\,\mu$m to $1.02\,\mu$m) regions. For the FeH fit, we find it necessary to mask the region between $1.002\,\mu$m and $1.008\,\mu$m due to a significant template mismatch between the CvD12 and M31 spectra. For template spectra, we use only the solar metallicity SSPs covering a range of ages and IMFs. We do not include spectra for different element abundances as these are only available for a 13.5 Gyr Chabrier IMF SSP.

We tried masking the NaI and FeH absorption features during the kinematic fitting to test whether fitting the second-order sky spectrum affects the strength of these absorption features; no significant difference was found for data presented here.

2.1.5 Index measurements

Before making index measurements, we de-redshift each spectrum to correct for its velocity as determined from the kinematic fit, and convolve all our spectra up to a common resolution of $200\,\mathrm{km\,s^{-1}}$ using a Gaussian of width given by

$$\sigma_{\mathrm{conv}} = \sqrt{200^2 - \sigma_*^2}, \tag{2.5}$$

where σ_* in the stellar velocity dispersion measured by PPXF. Table 2.3 gives the index and continuum definitions for the indices used in this chapter.

Table 2.3: Index bandpass and continuum definitions from Cenarro et al. (2001) and Conroy & van Dokkum (2012a). Wavelengths are in vacuum. We note several different definitions of NaI exist in the literature, including Vazdekis et al. (2012) and La Barbera et al. (2013).

Index	Blue Continuum (Å)	Feature (Å)	Red Continuum (Å)
NaD	5862.2-5877.2	5878.5-5911.0	5923.7-5949.7
NaI	8170.0-8177.0	8177.0-8205.0	8205.0-8215.0
CaT	8474.0-8484.0	8484.0-8513.0	8563.0-8577.0
	8474.0-8484.0	8522.0-8562.0	8563.0-8577.0
	8619.0-8642.0	8642.0-8682.0	8700.0-8725.0
PaT	8474.0-8484.0	8461.0-8474.0	8563.0-8577.0
	8563.0-8577.0	8577.0-8619.0	8619.0-8642.0
	8700.0-8725.0	8730.0-8772.0	8776.0-8792.0
FeH	9855.0-9880.0	9905.0-9935.0	9940.0-9970.0

The spectra around the NaI, CaT and FeH features are plotted in Figure 2.2. For our resolved data of M31_1 and M32, we plot a median spectrum from the entire field. We include the positions of the spectral index definitions from Table 2.3 in each subplot. Figure 2.2 shows the high quality of our measured spectra. Note that we have omitted the science spectra for M31_6 in the NaI plot, and for M31_5 and M31_6 in the FeH plot. This is due to strong residual sky lines after optimisation during the sky subtraction stage discussed in Section 2.1.4. We have instead plotted the best fit kinematic template spectra and we show a comparison between the data and templates in the appendix. We also note the definition of NaI appearing slightly blue-ward of the feature. The feature definition is over the Na doublet but there is a TiO band next to it, giving the appearance of a larger feature (van Dokkum & Conroy, 2012).

We measure the index equivalent widths using the formalism for generic indices given in Cenarro et al. (2001), which includes an error-weighted least-squares fit to the pseudo-continuum. We propagate individual pixel photon errors through the data reduction pipeline as variance spectra for each science spectrum. For M31_1 and M32 we calculate radially binned average index values and standard errors on the mean from the individual spectra in the resolved fields. For M31_2 to M31_6 we combine the index uncertainty in quadrature with a conservative factor accounting for the uncertainty in telluric correction.

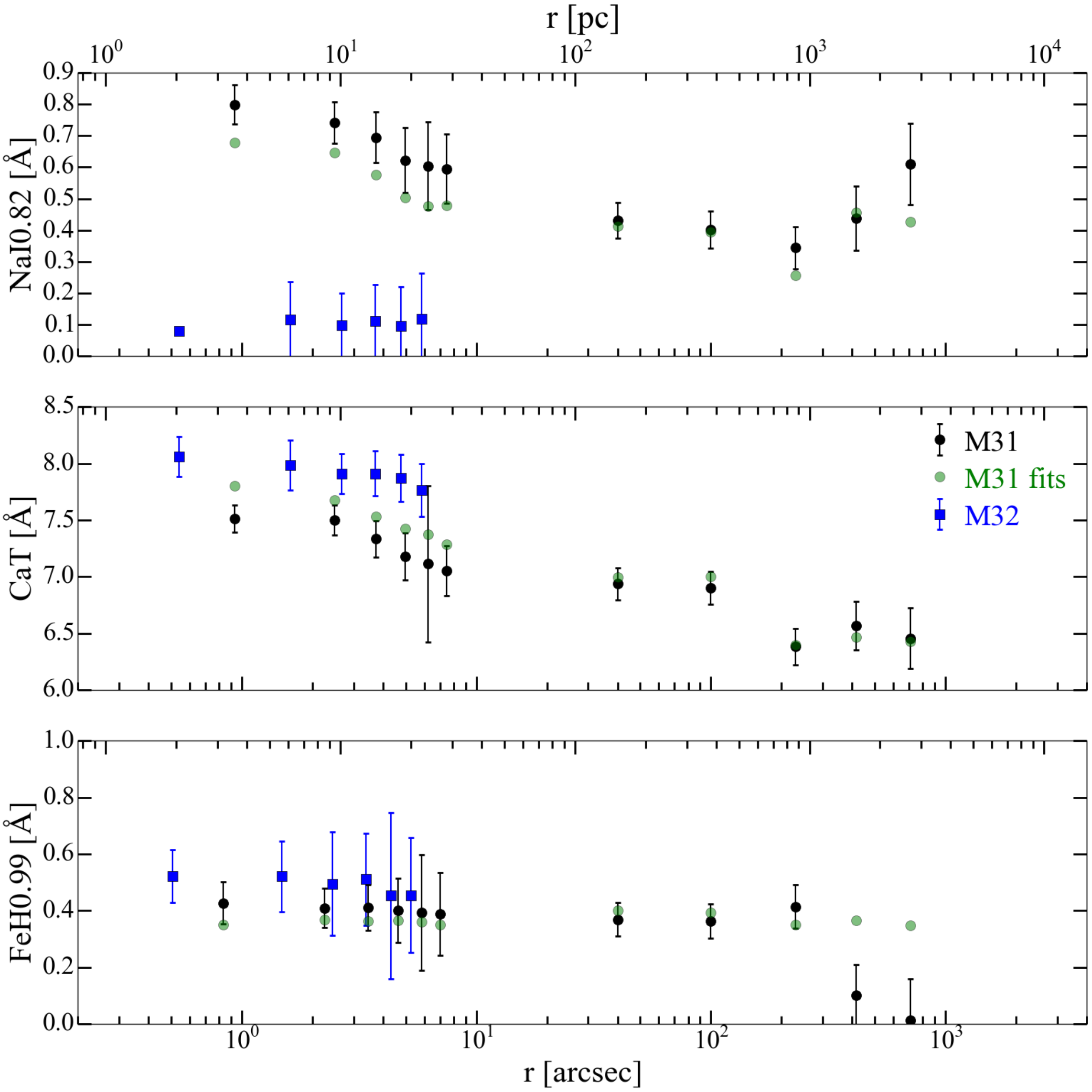

Figure 2.3: Plots of radial gradients for each index for M31 (black circles) and M32 (blue squares). Shown are the NaI (top), CaT (middle) and FeH (bottom) indices as a function of radial distance. Our measurements of the best fit kinematic template spectra for M31 are shown as the green circles.

2.2 Results

Our measurements of the three absorption features as a function of radius are shown in Figure 2.3 and we discuss each feature in turn for both galaxies.

The top panel in Figure 2.3 shows our measurements of the IMF sensitive index NaI. A clear negative gradient is visible in the central $\sim 10''$ of M31, which becomes flat towards the edge of the bulge. Our measurement nearest the nucleus is a factor of two greater than the average for the bulge. In contrast, M32 displays a flat profile of low absorption. It is clear from Figure 2.3 that, for M31, our best fit template spectra have systematically lower values in the central $\sim 10''$ compared to the observed spectra. However, in the outer bulge the two index measurements are in strong agreement (with the exception of M31_6, which we show in the appendix). We believe the discrepancy in the central $10''$ originates from our input template spectra for PPXF not including the SSPs with varying element abundances (as these spectra have a fixed age and IMF, see Section 2.3.1).

CaT is shown in the second panel in Figure 2.3. M31 displays a negative gradient throughout the bulge, dropping from 7.5 Å in the nuclear region down to 6.4 Å in the disc. The kinematic templates show a small systematic increase of ~ 0.25 Å compared to the measurements within $10''$, but are in very good agreement for the outer bulge measurements. The central discrepancy can be partly attributed to differences in the continuum measurements between the real and fitted spectra - the kinematic fits do not display as strong hydrogen absorption in the continuum. Residual telluric absorption could also be affecting the continuum level in the observed data. M32 displays very high calcium absorption of ~ 8.0 Å with a slight negative radial gradient.

Our measurements of FeH are shown in the bottom panel of Figure 2.3. For both M31 and M32 FeH has a flat profile. The absorption strength is 0.4 Å for M31, and between $0.45 - 0.50$ Å for M32.

2.3 Analysis

2.3.1 Stellar population synthesis models

We analyse our measurements of the far red absorption features in M31 and M32 using the SPS models of CvD12 and V12, which both allow for variations in the IMF slope and age. However other SSP parameters are specific to each set. CvD12 explore α-element enhancement [α/Fe], as well as variations in individual elemental abundance ratios [X/Fe] for 17 different elements (for fixed 13.5 Gyr age and fixed Chabrier IMF). V12 explore variations in the total metallicity [Z/H] for all IMFs and ages. Note that the V12 models do not cover the FeH feature. Our spectra do not cover the commonly-used age indicator Hβ, so we instead use SDSS $g-r$ colour. Figure 2.4 shows NaI (top) and FeH (bottom) against $g-r$ for the CvD12 models with the M31 data overplotted. The colour bar indicates the radial distance. Using these index maps, we now discuss our measurements in the context of our three goals: investigating the disc, bulge and nuclear region of M31, and the central region of M32. We show model variation plots for the CvD12 and V12 models in Appendix A.

2.3.2 M31

Figure 2.4 shows NaI (left) and FeH (right) index measurements plotted against SDSS $g-r$ colour as a function of radius. We over plot our data onto CvD12 model predictions for both indices. NaI appears to suggest an IMF slope around $x = 3$ for the central $10''$ with the bulge values also in a region of steepened IMF slope. In contrast, the FeH data follow the CvD12 predictions for a Chabrier IMF at solar metallicity closely. The discrepancy between NaI and FeH predictions can be explained by Na enhancement within the bulge of M31. The left plot in Figure 2.4 shows that a Chabrier IMF with Na enhancement of $[\mathrm{Na/Fe}] = +0.3$ dex could cover the outer bulge measurements. The inner bulge and nuclear region would require even stronger Na enhancement, with linear extrapolation of the models suggesting up to an order of magnitude above solar. The $g-r$ data indicate a decreasing age between inner and outer bulge along the major axis, although the large errors of ±0.03 mag do not allow for any stronger conclusions. However, this is in general agreement with best fit ages derived by Saglia et al. (2010).

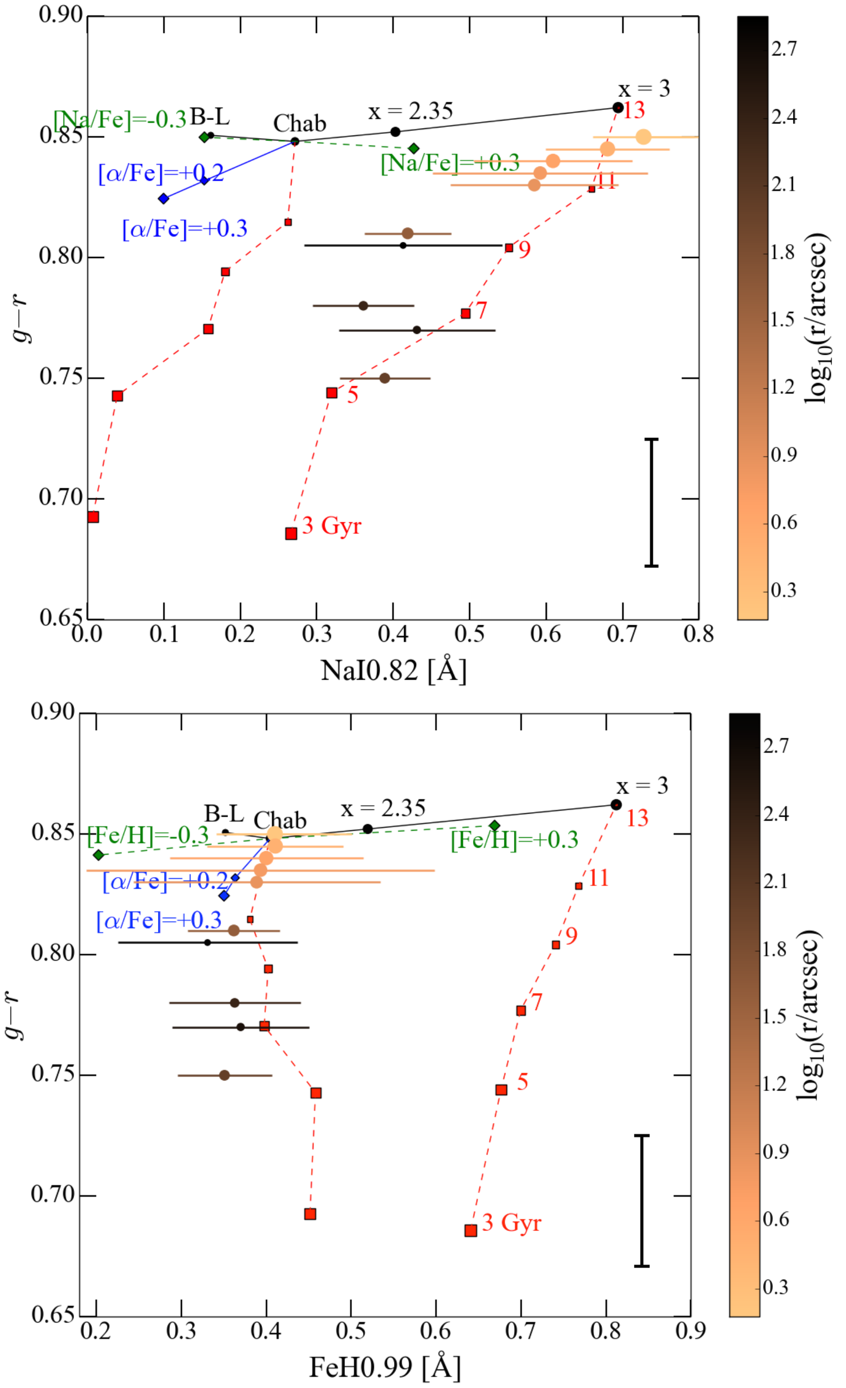

Figure 2.4: Plots of NaI (top) and FeH (bottom) against SDSS $g-r$ colour showing CvD12 models with M31 data overplotted. B-L corresponds to a bottom-light IMF from van Dokkum (2008), and Chab to a Chabrier (2003) IMF. The colour bar corresponds to the radial distance of each pointing to the centre of M31. Symbol sizes also decrease with increasing radial distance. Vertical colour error bars are omitted from the points for clarity and are shown in the bottom right of each plot.

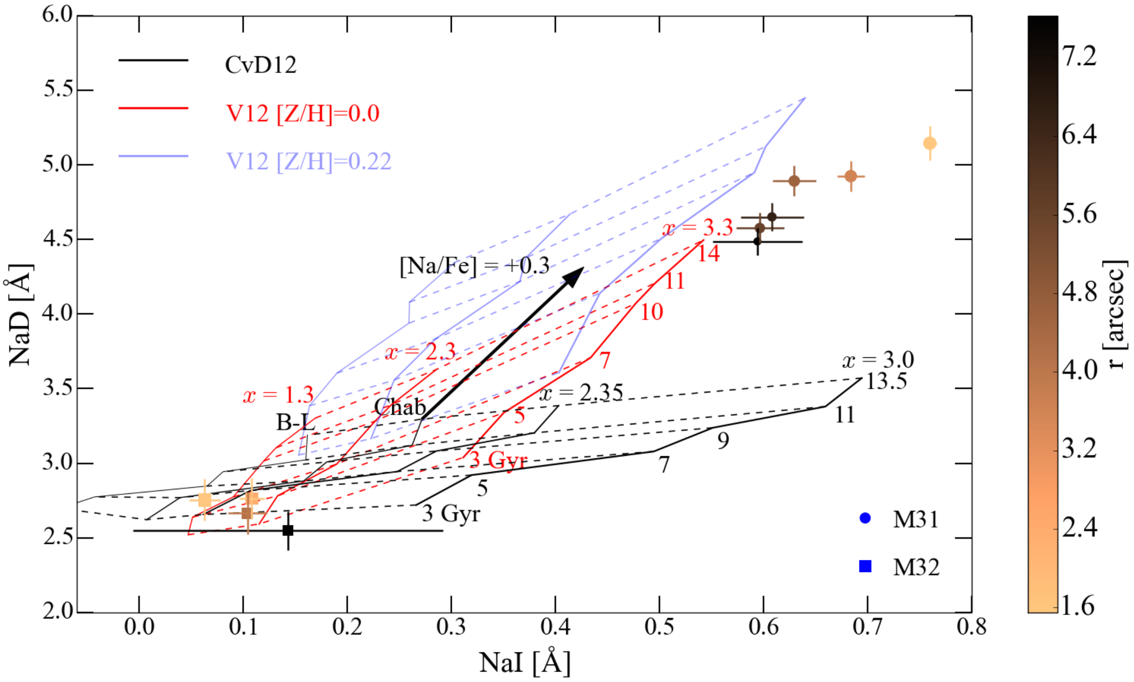

Figure 2.5: SSP model grids for CvD12 (black) and V12 (red and blue) showing variations in NaI against NaD. The CvD12 models are at solar metallicity, whereas the V12 models are at both solar (red, for M32) and metal enhanced with [Z/H]=+0.22 (blue, for M31). Note that the varying age vectors from the V12 models are parallel to the [Na/Fe] vector from the CvD12 models (black arrow). The central $10''$ of M31 (circles) and M32 (squares) are plotted. Symbol sizes decrease with increasing radial distance. We use the NaD measurements of Davidge (1991, 1997) that cover $r \leq 10''$. IMF labels are the same as in Figure 2.4.

CaT is known to be inversely proportional to IMF slope (see e.g. Cenarro et al., 2003). However, it is much more strongly influenced by [α/Fe] and Ca abundance than by IMF. The CvD12 models suggest an order of magnitude increase in the sensitivity of CaT to changes in [α/Fe] compared to changes in IMF (see Figure A.4). The gradient we measure is indicative of a steepening IMF slope with radius. Furthermore, this is in contrast to the FeH measurements. CvD12 note that Na enhancement can change the CaT strength. Thus, the flat profile of FeH leads us to conclude that the bulge of M31 holds a Chabrier IMF and is Na enhanced throughout, more so in the central $10''$.

Figure 2.5 shows the central $10''$ of M31 on an index-index plot of the two sodium features, NaI and NaD. Model grids for CvD12 are fixed at solar metallicity (black), whereas those of V12 are at both solar (red) for M32 (Rose et al., 2005) and [Z/H] = +0.22 (blue) for M31 (Saglia et al., 2010). The radial measurements of the M31 inner bulge and nuclear region follow the V12 model lines of varying age at a very bottom-heavy $x > 3.3$ IMF exponent. Thus the V12 models suggest a bottom-heavy IMF in this region, which would become Salpeter-like through the rest of the bulge as NaI approaches 0.4 Å. However, also plotted is a CvD12 SSP at 13.5 Gyr, with a Chabrier IMF and sodium enhanced by +0.3 dex. It is clear from this SSP that the CvD12 models attribute a stronger dependence of NaD on [Na/Fe] than the IMF slope, and further it is indicative that the CvD12 models suggest the level of Na enhancement seen in the central $10''$ of M31 is consistent with a normal (between Chabrier and Salpeter) IMF. It is not possible to resolve the differences between the two model predictions without coverage of the FeH feature and elemental abundance variations in the V12 models.

2.3.3 M32

M32 displays flat profiles for both NaI and FeH, with a slightly negative gradient in CaT. NaI is markedly lower than in M31 with values around 0.1 Å. From Figure 2.5 both the CvD12 and V12 models suggest this is consistent with a Chabrier IMF at solar metallicity around 3–5 Gyr in age. The stellar populations of M32 are younger than M31 (see e.g. O'Connell, 1980) and the model predictions for the age from both CvD12 and V12 are in reasonable agreement with long-slit spectroscopy measurements by Rose et al. (2005), who measure an age gradient from 3–4 Gyr in the centre to 6–7 Gyr at 30″. A younger stellar population with Chabrier IMF is further supported by the FeH index, which is slightly stronger than in M31.

A striking difference is the much higher CaT values compared to M31. This has previously been noted by Kormendy & Bender (1999) and Cenarro et al. (2008). Thomas et al. (2003) suggest this can be explained by the fact that M32 is younger than M31, and the younger stars contaminate the CaT index, which is known to be affected by Paschen lines. However, the CaT* index is defined by Cenarro et al. (2001) as $\mathrm{CaT}^* = \mathrm{CaT} - 0.93 \times \mathrm{PaT}$, where PaT is an index defined over several Paschen lines next to CaT, in order to calibrate out the hydrogen lines. We measured the CaT* index within the central 2″ of M32 as CaT* $= 7.39 \pm 0.22$ Å and within the same aperture of M31 as CaT* $= 6.75 \pm 0.16$ Å, which still shows greater absorption for M32. It would be an interesting test to see whether other dwarf galaxies of the same age as M32 also display strong calcium absorption. Overall our measurements of M32 are fully consistent with a Chabrier IMF.

2.4 Discussion

The form of the IMF in the nuclear region of M31 has been of intense historical debate. The main factor driving the idea of a bottom heavy IMF has been the prominent NaI feature in the central $\sim 3''$. Spinrad & Taylor (1971) interpreted this as the presence of a large number of dwarf stars. Further observations by many groups (see e.g. Whitford, 1977; Frogel et al., 1978; Cohen, 1978; Faber & French, 1980; Carter et al., 1986; Alloin & Bica, 1989; Delisle & Hardy, 1992) have led to conflicting results. Conroy & van Dokkum (2012b) observed the central 15 pc of M31 (4″) and inferred a mass-to-light ratio consistent with an IMF slope between Chabrier and Salpeter. They concluded that the central region is entirely consistent with a Milky Way IMF, albeit requiring very large sodium enhancement of the order [Na/Fe]~ 1.0.

All current work suggesting increasing IMF slopes with velocity dispersion in the centres of galaxies has been for massive early-types, which generally have large dispersions, upwards of 300 km s^{-1}. Ferreras et al. (2013), La Barbera et al. (2013) and Spiniello et al. (2014)

find similar empirical relations between the IMF slope and velocity dispersion. M31 has a dispersion of $\sigma \sim 160\,\mathrm{km\,s^{-1}}$ (out to 0.4 kpc which we adopt as a typical central dispersion), which gives an IMF slope of $x \sim 1.9$ from all three relations and is consistent with a normal (i.e. not bottom-heavy) IMF. We measure a Chabrier IMF throughout M31 even at the largest radius which has a dispersion of $\sigma \sim 90\,\mathrm{km\,s^{-1}}$, and also in the centre of M32 which has a central dispersion of $\sim 60\,\mathrm{km\,s^{-1}}$; this suggests that the relations linking IMF to velocity dispersion should become fixed at Chabrier IMF for $\sigma < 150\,\mathrm{km\,s^{-1}}$. Chabrier et al. (2014) have presented a theoretical scenario for dwarf enrichment and a steepening of the IMF within the framework of gravitationally collapsing turbulent molecular clouds. They deduce an upper limit to the IMF slope of $x \sim 2.8$ in extremely high density and turbulent systems. We note that the centres of M31 and M32 have very high stellar density and yet we measure a Chabrier IMF.

The physical size scales here are also worth considering. The central $8''$ of M31 corresponds to 30 pc, which is a very small region of space in which to create and maintain an overabundance of dwarf stars (or in fact, a population with [Na/Fe]$\sim +1.0$). Furthermore, sodium excess in stars (Briley et al., 1996) and in galaxies (Jeong et al., 2013) is not particularly rare, suggesting that M31 may not be peculiar. In fact, Jeong et al. (2013) measure NaD absorption as high as $\sim 7\,\text{Å}$ in some ETGs and late type galaxies (LTGs); much higher than seen in M31. They conclude that the NaD index in most Na enhanced LTGs is strongly contaminated by the interstellar medium (ISM) and/or dust. These findings caution against using sodium as a sole IMF indicator, especially for late type galaxies. Most importantly, our measurements of the FeH absorption reject the possibility of a dwarf-dominated nuclear region. Conroy & van Dokkum (2012b) also reached this conclusion for the central $4''$ and our results have extended that conclusion throughout the bulge and into the disc.

It is an important point that the two SSP models give different predictions when considering the sodium indices as highlighted by Spiniello et al. (2015). Specifically V12 attribute a much stronger dependence of NaD on the IMF slope than the CvD12 models. This is clear in Figure 2.5 and gives apparently discrepant predictions for the IMF slope in M31. We conclude with Spiniello et al. (2015) that sodium is complex and poorly understood. However, the V12 models do not cover the FeH wavelength range so no constraint on the

IMF can be made using this feature with the V12 models.

2.5 Conclusions

Using the Oxford SWIFT instrument we have undertaken a study of M31 and M32 with the aim of discerning possible gradients in IMF-sensitive far red absorption features. We obtained high S/N integral field spectroscopy of M31, covering the nuclear region, bulge and old disc at $\sim 700''(2.7\,\mathrm{kpc})$, as well as for the central $10''(38\,\mathrm{pc})$ of M32. We conclude the following:

1. In M31, the NaI index shows a flat equivalent width profile at ~ 0.4 Å through the majority of the bulge, with a strong gradient up to 0.8 Å in the central $10''$. FeH is measured to be flat at 0.4 Å on all scales. CaT shows a gradual positive gradient inwards through the bulge. M32 displays flat profiles for all three indices: slightly stronger FeH absorption than M31, anomalously strong CaT absorption in agreement with other studies, and very weak NaI absorption.

2. M31 is consistent with a Chabrier IMF throughout the central region, bulge and old disc from analysis of the flat FeH index using the CvD12 models. We also infer a gradient in sodium enhancement of [Na/Fe] $\sim +0.3$ dex in the disc and outer bulge, rising up to [Na/Fe] $\sim +1.0$ dex in the nuclear region.

3. Our measurements of NaI and FeH for M32 are consistent with a Chabrier IMF for ages $\sim$3–5 Gyr using the CvD12 and V12 models.

4. The use of sodium indices alone is a poor method for investigating IMF variations as it is susceptible to sodium enhancement and [α/Fe] variations. Sodium is a poorly understood element as highlighted by the discrepant predictions of the CvD12 and V12 models.

5. The centres of M31 and M32 have very high stellar densities and yet we measure a Chabrier IMF in both regions.

Chapter 3

Radial gradients of far red stellar absorption features in Coma brightest cluster galaxies

In this chapter we add to the small but growing amount of literature regarding radial gradients in IMF-sensitive stellar absorption features of massive ETGs, by presenting results from four galaxies in the Coma cluster. We use the Oxford SWIFT to target the two massive, slow-rotator, brightest cluster galaxies (BCGs) within the main cluster: NGC4889 and NGC4874 ($\epsilon = 0.36, \lambda_{\mathrm{R}} = 0.04$ and $\epsilon = 0.12, \lambda_{\mathrm{R}} = 0.08$ respectively, Houghton et al. 2013. ϵ is the ellipticity and λ_{R} is the specific angular momentum; slow rotators are defined as having $\lambda_{\mathrm{R}} < 0.31\sqrt{\epsilon}$, see Emsellem et al. 2011); as well as the BCG NGC4839 within the Coma south-west cluster. We also obtain unresolved spectroscopy for the fast rotator NGC4873 ($\epsilon = 0.23, \lambda_{\mathrm{R}} = 0.41$) as a low-$\sigma$ comparison galaxy. These galaxies cover a range of central velocity dispersions and derived ages, metallicities and α-abundances (Trager et al., 2008; Loubser et al., 2009). The IMF of Coma galaxies has been previously studied by Smith et al. (2012) using spectra stacked by velocity dispersion. However, their results only concerned the central 0.6 kpc. In this study for each galaxy we present radial measurements of the far red features covered by the SWIFT instrument, NaI, CaT, MgI, TiO, and FeH, out to $10''$ (5 kpc). We then utilise the latest stellar population synthesis (SPS) models to

Table 3.1: Our sample of Coma galaxies with positions, effective radii R_e taken from Loubser et al. (2008) and Houghton et al. (2013), and total on-source exposure times. The R_e column shows the fraction of R_e covered by our observations in parentheses.

Galaxy	RA	DEC	R_e ($''$)	T_exp (s)
NGC4889 (GMP2921)	13:00:08.1	+27:58:37	38.0 (0.2)	5400
NGC4874 (GMP3329)	12:59:35.7	+27:57:33	50.4 (0.2)	6300
NGC4839 (GMP4928)	12:57:24.3	+27:29:52	17.2 (0.5)	3600
NGC4873 (GMP3367)	12:59:32.8	+27:59:01	5.9 (0.5)	2700

analyse our results in the context of a possible variable IMF.

This chapter is organised as follows: Section 3.1 details our observations and data reduction procedures. In Section 3.2 we present the absorption feature strengths, and Section 3.3 contains our analysis using index-index maps and comparing to SPS model predictions for simple stellar population (SSP) spectra. We discuss our results in Section 3.4 and conclude our work in Section 3.5. In this chapter we adopt the IMF naming convention used by Conroy & van Dokkum (2012a, hereafter CvD12), namely a Chabrier IMF corresponding to that defined in Chabrier (2003) for the disc of the Milky Way; a Salpeter (1955) IMF defined as $x = 2.35$; and a bottom-light IMF as defined in van Dokkum (2008). We adopt a flat ΛCDM cosmology with $H_0 = 68\,\mathrm{km\,s^{-1}\,Mpc^{-1}}$, $\Omega_m = 0.3$ and $\Omega_\Lambda = 0.7$. This gives a distance to the Coma cluster ($z = 0.024$, Han & Mould, 1992) of 108 Mpc.

3.1 Observations and data reduction

Observations were obtained over the nights of 2009 May 4; 2012 May 11; 2013 April 17, 20 and 22 using the SWIFT instrument (Thatte et al., 2006) on the Palomar 200 inch (5.1 m) telescope. Observations were taken at the 235 mas spaxel^{-1} spatial scale covering a field of $10'' \times 21''$. The spectra cover the wavelength range $6300 - 10400\,\text{Å}$ with a dispersion of $\sim 2\,\text{Å}$ FWHM and a sampling of $1\,\text{Å}\,\mathrm{pix}^{-1}$. Table 3.1 lists our galaxy sample and total exposure time for each galaxy. The seeing was around $1.5''$ for all observations.

The data were reduced using the SWIFT data reduction pipeline, written in IRAF. The pipeline handles all the standard reduction processes of bias subtraction, flat fielding, wavelength calibration, error propagation as well as IFS specific features of illumination correction and cube reconstruction. Cosmic rays were detected and removed using the LACOSMIC routine (van Dokkum, 2001). First order sky subtraction was performed by subtracting sky frames observed adjacent in time to each science frame. We were careful to choose sky fields sufficiently far away as to avoid contamination from other galaxies in the cluster.

Residual sky lines and telluric absorption are two effects that significantly hamper accurate measurement of the faint far red absorption features of interest, especially the FeH index. The next two sub-sections detail our efforts to minimise these effects and ensure high quality spectra with which to make robust index measurements.

3.1.1 Telluric correction

Due to the redshift of the Coma cluster ($z = 0.024$) the IMF-sensitive absorption features are redshifted relative to the main regions affected by telluric absorption. Figure 3.1 shows an example telluric absorption spectrum (from the ESO Skycalc tool; Noll et al. 2012) convolved to the SWIFT spectral resolution and scaled by a factor of 0.5. Also plotted is an example model spectrum (red: CvD12 13.5 Gyr Chabrier IMF SSP) redshifted to $z = 0.024$, as well as an example telluric standard A0V spectrum (blue: after division by a polynomial fit to the continuum) showing the positions of the prominent Paschen absorption lines. This illustrates the regions affected by both, atmospheric absorption and telluric star features, relative to the positions of the key far red absorption features in the science spectra (shaded regions). Atmospheric telluric absorption is prominent in the blue pseudo-continuum of $\mathrm{NaI_{SDSS}}$ and across the MgI and TiO features. The furthest red pseudo-continuum region of CaT also falls into a telluric region, but FeH is in a region of negligible telluric absorption. However the SWIFT throughput is a strong function of wavelength at the red end, which must be corrected for. Furthermore, residuals from correcting the prominent Paschen feature are present around 1.01 μm, which may affect our measurements of the FeH feature. Figure 3.2 shows an example telluric spectrum along with a fit to the continuum. Also shown are the FeH bandpass definitions redshifted to the redshift of NGC4873 ($z = 0.0193$, Trager et al., 2008). This clearly shows that our FeH measurements would be susceptible to residuals from poor fitting of the Paschen lines. We therefore pursue two separate methods to correct for telluric absorption.

Firstly, we use A0V stars observed alongside the galaxies to act as telluric standards. We remove the prominent Paschen absorption lines using a dedicated routine written in IDL. The telluric spectra are divided out by model A0V spectra provided by R. Kurucz, using a version of the amoeba algorithm allowing for velocity shifts and stellar rotation. Figures B.1, B.2 and B.3 show examples of our telluric correction around the MgI feature for NGC4889 (∼ best case), NGC4874 and NGC4839 (∼ worst case). In each plot we use our kinematic template fits (see section 3.1.2) as an assumed 'telluric free' galaxy spectrum. We compute the rms residuals after telluric correction around each feature (NaI$_{\mathrm{SDSS}}$, CaT, MgI, TiO) for each galaxy. We find that MgI has the highest residuals of $\sigma \sim 0.01$ (see Figures B.1, B.2, B.3) and all other features have residuals lower than 1 %.

Secondly, we fit a high order polynomial to the continuum of each telluric star spectrum (after division by the best fitting A0V model) to represent a relative throughput curve without residual hydrogen features. We then divide the galaxy by this fit to correct for only the smooth throughput variation of SWIFT at the far red end. Thus we create two separate spectra for each galaxy, one corrected by the telluric spectrum and one corrected by a continuum fit to the (A0V divided) telluric spectrum. We use the telluric corrected spectrum to measure the NaI, CaT, MgI and TiO features, and we use the 'throughput-divided' spectrum to measure the FeH feature. However, we do compare our FeH measurements from the telluric divided spectrum (see Figure B.4 in Appendix B).

3.1.2 Second-order sky subtraction, binning and kinematics

Residual sky lines are still prominent at red wavelengths due to time-dependent variations of the sky emission on the scale of minutes. These are the dominant source of systematic error around $1\,\mu$m and so must be accurately removed to measure the FeH feature of only a few per cent strength relative to the continuum. We employ two separate methods to try and remove these residual lines. The first method involves fitting and removing the skylines while fitting the kinematics, and the second method involves fitting each wavelength spatial channel (image) of the data cube with a Sérsic function to separate the galaxy light from sky light.

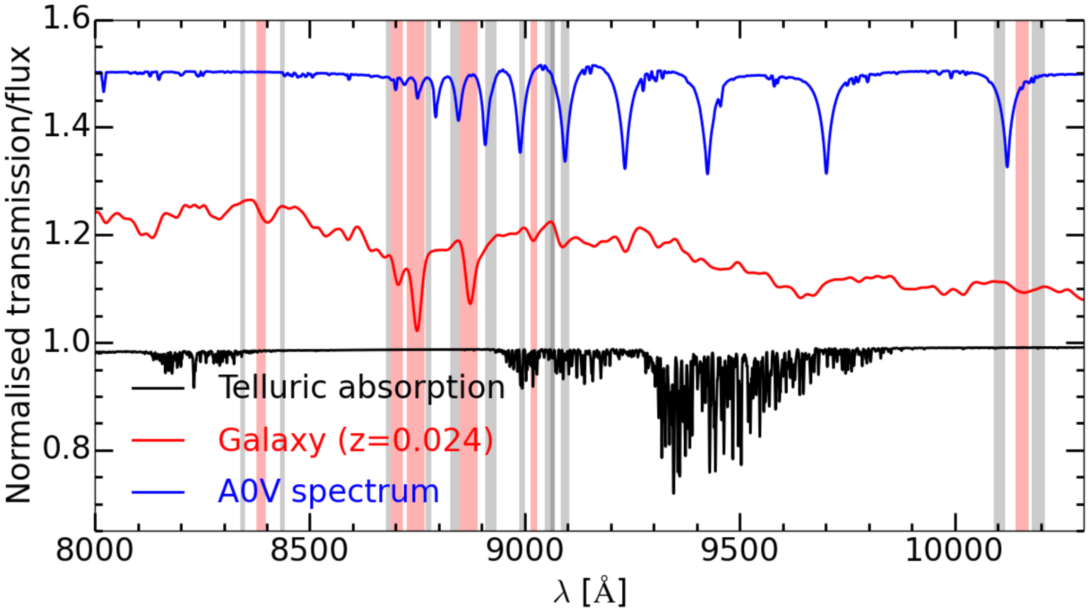

Figure 3.1: Plot showing atmospheric absorption spectrum (black; scaled by 0.5 and plotted at $y = 0.98$), SSP model spectrum (red; plotted at $y = 1.2$) redshifted to the nominal redshift of the Coma cluster $z = 0.024$ (Han & Mould, 1992), and a model A0V spectrum (blue; continuum divided and plotted at 1.5). The telluric spectrum is convolved to the SWIFT resolution and the 'galaxy' spectrum is a CvD12 13.5 Gyr, Chabrier IMF SSP that has been smoothed to $\sigma = 300\,\mathrm{km\,s^{-1}}$. The redshifted (to $z = 0.024$) positions of the key absorption feature bandpasses are denoted by the shaded regions. They are, from left to right, $\mathrm{NaI_{SDSS}}$, CaT, MgI, TiO and FeH.

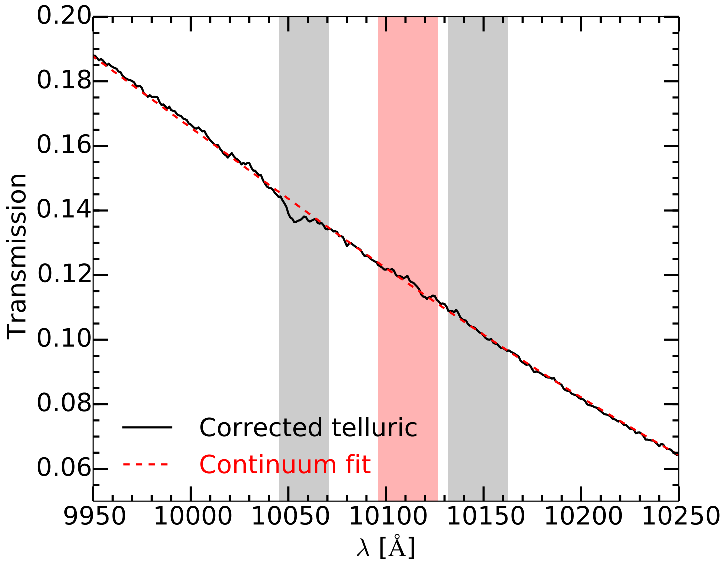

Figure 3.2: Plot showing a corrected (A0V divided) telluric spectrum around the FeH feature (black solid line) and a polynomial fit to the continuum (red dashed line). The fit removes the residual features left over from dividing out the A0V absorption. The shaded regions show the FeH pseudo-continuum and feature bandpass definitions redshifted to $z = 0.0193$ of NGC4873 (Trager et al., 2008). The blue continuum would be affected by residuals in the telluric spectrum, but these are removed by the continuum fit.

For the first method we perform a simultaneous second-order sky subtraction while extracting the kinematics (Weijmans et al., 2009). We fit the kinematics of the spectra with the penalised pixel fitting routine (PPXF, Cappellari & Emsellem, 2004) using, as template spectra, the stellar population models from CvD12. We compute the kinematics in annular bins of increasing radii from the centres of each galaxy to achieve a target S/N $> 100\,\mathrm{pixel}^{-1}$ in the central part of the spectra (around CaT, MgI and TiO features). Sky subtraction was accomplished using a variation of the techniques described in Davies (2007): rather than scaling a single sky spectrum covering multiple OH vibrational transitions, we divide the spectrum into separate regions covering each OH vibrational transition. This allows independent scaling of each transition. We also scale the O_2 emission around $0.864\,\mu$m separately. Furthermore, to account for flexure (error in the wavelength calibration) we interpolate each spectrum forward and backwards by one pixel. The sky spectra are extracted, using the identical annular apertures as the science spectra, from a separate sky cube shifted and combined in the same way to match the spaxel positions. All these spectra are then passed to PPXF which finds the best-fit linear combination (including scaling) that reproduces the skyline residuals while also finding the best fit kinematics[1]. For each galaxy spectrum, we measure the intrinsic instrument dispersion from the skylines at the same wavelength as the principal galaxy absorption features (NaI/CaT/FeH) and independently for each azimuthal bin.

The SWIFT spectral resolution varies from $40\,\mathrm{km\,s^{-1}}$ (R $\sim$ 3100) to $65\,\mathrm{km\,s^{-1}}$ (R $\sim$ 2000) across the field of view and the resolution of the CvD12 models is R=2000 beyond $0.75\,\mu$m. In this case it is necessary to correct the dispersions found by PPXF σ'_{ppxf}, for the difference between instrument and template resolutions to find the galaxy stellar velocity dispersion σ_*: to all PPXF dispersions we added in quadrature the difference between the template resolution in that wavelength range σ_{temp}, and the instrument resolution σ_{inst},

$$\sigma_* \approx \sqrt{\sigma'^2_{\mathrm{ppxf}} + (\sigma^2_{\mathrm{temp}} - \sigma^2_{\mathrm{inst}})}. \tag{3.1}$$

In practice this only significantly affects dispersions less than $100\,\mathrm{km\,s^{-1}}$ so has little effect with the high dispersion galaxies presented in this study.

Using this technique, we are able to clean sky residuals from the galaxy spectra (prior to calculating element abundances) by subtracting the best-fit ‘second-order’ sky spectrum generated by PPXF. However, the sky spectrum contains both continuum and line emission, and scaling to remove the line residuals also scales the continuum. We check whether this can be a source of bias by adding and subtracting a constant continuum level from the galaxy spectrum and checking subsequent equivalent width measurements. We use the CvD12 Chabrier and $x = 3$ IMF models and measure the indices after convolving to $400\,\mathrm{km\,s^{-1}}$ and adding or subtracting a constant level of 1, 5 and 10 %. Trivially and as expected we find that the index value changes by $\sim$ 1, 5 and 10 % respectively for both IMFs. We also find that adding a first-order gradient across a feature has minor affect, on the order of 1 % for a 20 % gradient across the feature. However, we do find that a higher-order differential change in the continuum across a feature can alter the measured index more substantially; we create a high-order polynomial fit to a 10 % step function offset from the central feature

---

[1] We manually altered the internal limits in PPXF to allow negative sky spectrum weights.

wavelength, and adding this changes the measured indices by around 30 %. As there is no reason to believe continuum and line emission scale in the same way (unless the continuum is composed primarily of unresolved faint OH lines from the same transition or scattered light from bright OH lines, Davies, 2007), we subtracted the continuum from the second-order sky spectrum before using it to remove the skyline residuals in the galaxy spectra. Typically, the effect of this in equivalent width measurements is only a few per cent, but it can be as large as 10 %. We use a high order Legendre polynomial fit with sigma-clipping to smoothly follow the continuum and minimise bias from the sky lines. Examples of this sky subtraction routine are shown in Figures B.1, B.2 and B.3.

For each galaxy we also obtain an *optimally extracted 'global' spectrum* extracted over all radii. We use a method of optimal extraction based on Horne (1986) and Robertson (1986) to achieve maximal S/N. We analyse the optimally extracted global spectra (hereafter referred to as global spectra) along with the resolved data.

3.1.3 Galaxy profile fitting

Due to the difficulty of removing residual skylines we pursue a separate, independent sky subtraction method to compare with the PPXF method. In each galaxy object-minus-sky (O-S) data cube the galaxy light and sky light contribute to the total light differently; sky light I_S corresponds to an additive shift up or down (assuming uniform sky across data cube), whereas galaxy light can be modelled as a Sérsic function,

$$I(R) = I_0 e^{-kR^{\frac{1}{n}}}, \tag{3.2}$$

where I is the intensity, R is the radius, and n is the Sérsic index (Sérsic, 1963), and an increase in galaxy light causes a steepening of the light profile towards the centre. Thus by fitting a Sérsic profile to each wavelength channel (spatial image) of the data cube we can separate the two contributions of galaxy and sky. This profile fitting relies on the galaxy light *not* being uniform across the SWIFT field of view - the steeper the variation in galaxy light the better our ability to disentangle sky and galaxy. We perform this procedure for each O-S data cube. We iterate over all wavelengths and first perform a ‘free’ fit of,

$$I(R) + I_S, \tag{3.3}$$

using the amoeba algorithm and allowing all parameters to vary. Then we fit a ‘fixed’ Sérsic to each wavelength channel, varying only I_0 and I_S with the other variables fixed at the mean values from the ‘free’ fit. Finally we perform another fixed fit after masking out any bad IFU slices where the fixed fit varies from the science data cube by over two standard deviations.

We are left with sky-subtracted O-S data cubes, which we combine to create an alternative sky-subtracted data cube for each galaxy. We compute the binning and kinematics using PPXF as before but without performing second-order sky subtraction described in Section 3.1.2. Thus we are left with three different spectra for each galaxy radial bin (and three different global spectra), which we summarise here:

(a) spectra telluric corrected and sky-subtracted using PPXF,

(b) spectra corrected by a fit to the telluric profile and sky-subtracted using PPXF,

(c) spectra corrected by a fit to the telluric profile and sky-subtracted using O-S spatial fitting.

Spectra (a) are used for measuring $\mathrm{NaI_{SDSS}}$, CaT, MgI and TiO features. Spectra (b) are used for measuring the FeH feature and we compare to measurements from spectra (a) and (c) to see the effects of telluric correction and sky-subtraction methods on the FeH index.

3.1.4 Masking

After the telluric correction and sky-subtraction routines a small number of the resolved spectra still contain narrow bad pixel regions near to the index feature or continuum definitions. We mask these regions out and replace with values from our best fit kinematic template spectra. No masking is required for any NGC4889 or NGC4873 spectra. NGC4874 has two narrow bad pixel regions around CaT and a bad region in the blue continuum of MgI. The outermost spectrum of NGC4839 suffers from a large number of bad regions around $\mathrm{NaI_{SDSS}}$ and CaT and we treat these index measurements with some caution. No

Table 3.2: Median S/N of spectra around each index for each galaxy. Global refers to the optimally extracted spectrum extracted over all radii for each galaxy.

R ($''$)	$\mathrm{NaI_{SDSS}}$	CaT	MgI	TiO	FeH
		NGC4889			
0.0	121	123	124	124	65
1.7	155	159	160	160	83
2.6	156	160	163	164	82
3.6	144	147	152	154	76
4.5	127	133	141	144	67
5.4	112	116	123	127	58
6.3	91	95	101	105	48
7.5	90	92	99	102	48
Global	349	355	368	372	200
		NGC4874			
0.0	66	67	70	70	33
1.8	96	99	103	104	49
2.8	94	96	102	104	48
3.7	93	96	102	104	47
4.8	90	94	100	103	45
6.8	100	105	114	118	51
Global	213	215	226	231	115
		NGC4839			
0.0	63	64	66	67	35
2.0	99	101	107	108	55
5.7	67	67	75	76	44
Global	142	145	154	155	85
		NGC4873			
Global	96	95	105	105	54

masking is required for the global spectra.

3.1.5 Index measurements

The S/N of our spectra around each index are shown in Table 3.2. Before making index measurements, we de-redshift each spectrum to correct for its velocity as determined from the kinematic fit. In order to equally compare the spectra at each radius within a galaxy we convolve the spectrum of each radial position up to a common resolution of σ_{out} using a Gaussian of width given by

$$\sigma_{\mathrm{conv}} = \sqrt{\sigma_{\mathrm{out}}^2 - \sigma_*^2}, \tag{3.4}$$

Table 3.3: Index bandpass and continuum definitions from Cenarro et al. (2001) and Conroy & van Dokkum (2012a). In this work we use the $\mathrm{NaI_{SDSS}}$ index as defined in La Barbera et al. (2013). The TiO index is defined as the ratio between the blue and red pseudo-continua and is therefore dimensionless. Wavelengths are in vacuum.

Index	Blue Continuum (Å)	Feature (Å)	Red Continuum (Å)
$\mathrm{NaI_{SDSS}}$	8145.2-8155.2	8182.3-8202.3	8235.3-8246.3
CaT	8474.0-8484.0	8484.0-8513.0	8563.0-8577.0
	8474.0-8484.0	8522.0-8562.0	8563.0-8577.0
	8619.0-8642.0	8642.0-8682.0	8700.0-8725.0
MgI	8777.4-8789.4	8801.9-8816.9	8847.4-8857.4
TiO	8835.0-8855.0		8870.0-8890.0
FeH	9855.0-9880.0	9905.0-9935.0	9940.0-9970.0

where σ_* is the stellar velocity dispersion measured by PPXF. For each galaxy we convolve the radial spectra to match the central velocity dispersion of that galaxy. These correspond to, $400\,\mathrm{km\,s^{-1}}$ for NGC4889, $270\,\mathrm{km\,s^{-1}}$ for NGC4874 and NGC4839, and $200\,\mathrm{km\,s^{-1}}$ for NGC4873. Note we do not convolve all galaxies up to the same common resolution as this would involve large convolutions and blending of sky line residuals. Rather, we aim to equally compare the spectra at different radial positions within each galaxy, and then compare each galaxy individually against SPS model predictions. Table 3.3 gives the index and continuum definitions for the indices used in this chapter. These are the same as in Chapter 2 except for the sodium index for which we use the $\mathrm{NaI_{SDSS}}$ index definition given in La Barbera et al. (2013) due to the larger velocity dispersions in the galaxies we are studying in this chapter. We also measure the MgI and TiO indices covered by the SWIFT wavelength range.

The global galaxy spectra are shown in Figure 3.3. The global and resolved spectra around the NaI, CaT and FeH features are plotted for each of the BCGs in Figures 3.4, 3.5, and 3.6, and the for global spectra of NGC4873 in Figure 3.7.

We measure the index equivalent widths using the formalism for generic indices given in Cenarro et al. (2001), which includes an error-weighted least-squares fit to the pseudo-continuum. We propagate individual pixel photon errors through the data reduction pipeline as variance spectra for each science spectrum, and present our index measurements with formal 1σ uncertainties.

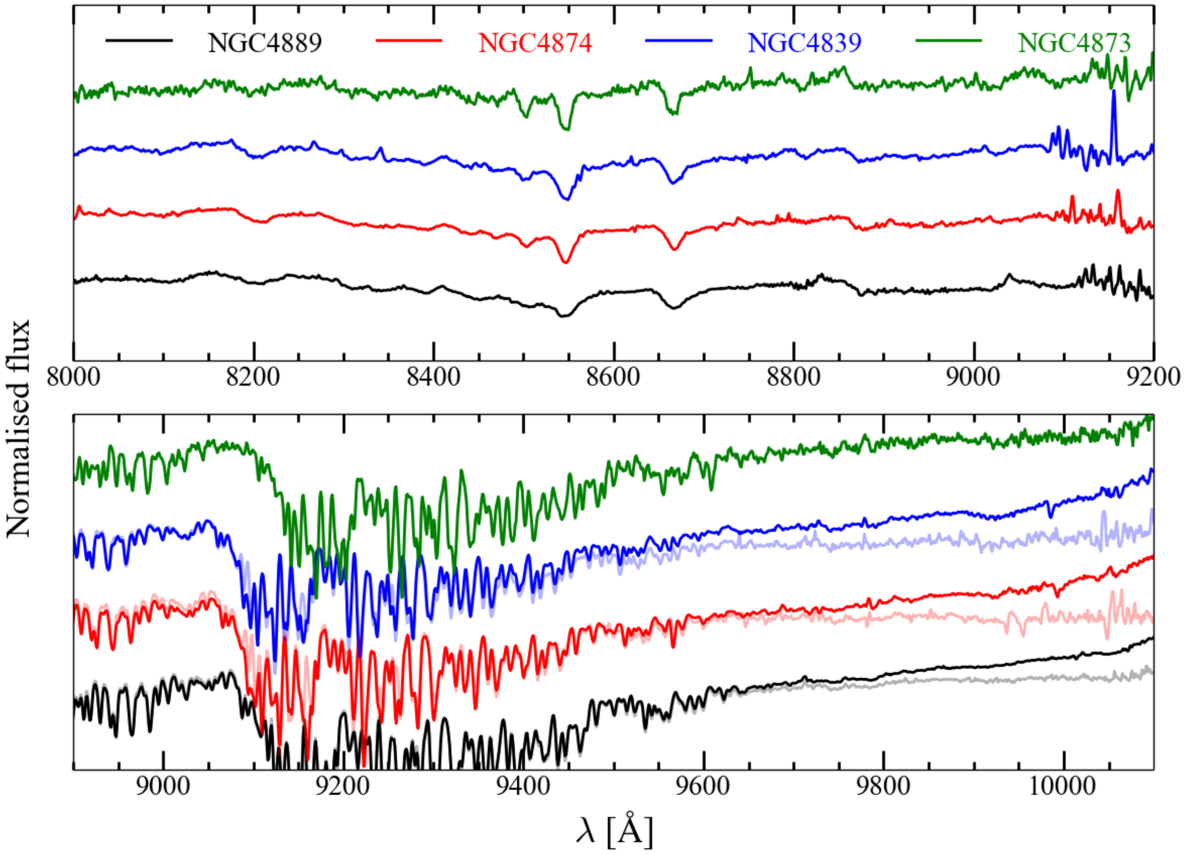

Figure 3.3: Global (optimally extracted) spectra of the four Coma galaxies NGC4889 (black), NGC4874 (red), NGC4839 (blue) and NGC4873 (green). Spectra have been normalised by the median continuum level and are spaced for presentation purposes. In the lower panel the fainter coloured lines show the global spectra obtained using the O-S cube Sérsic profile fitting discussed in section 3.1.3.

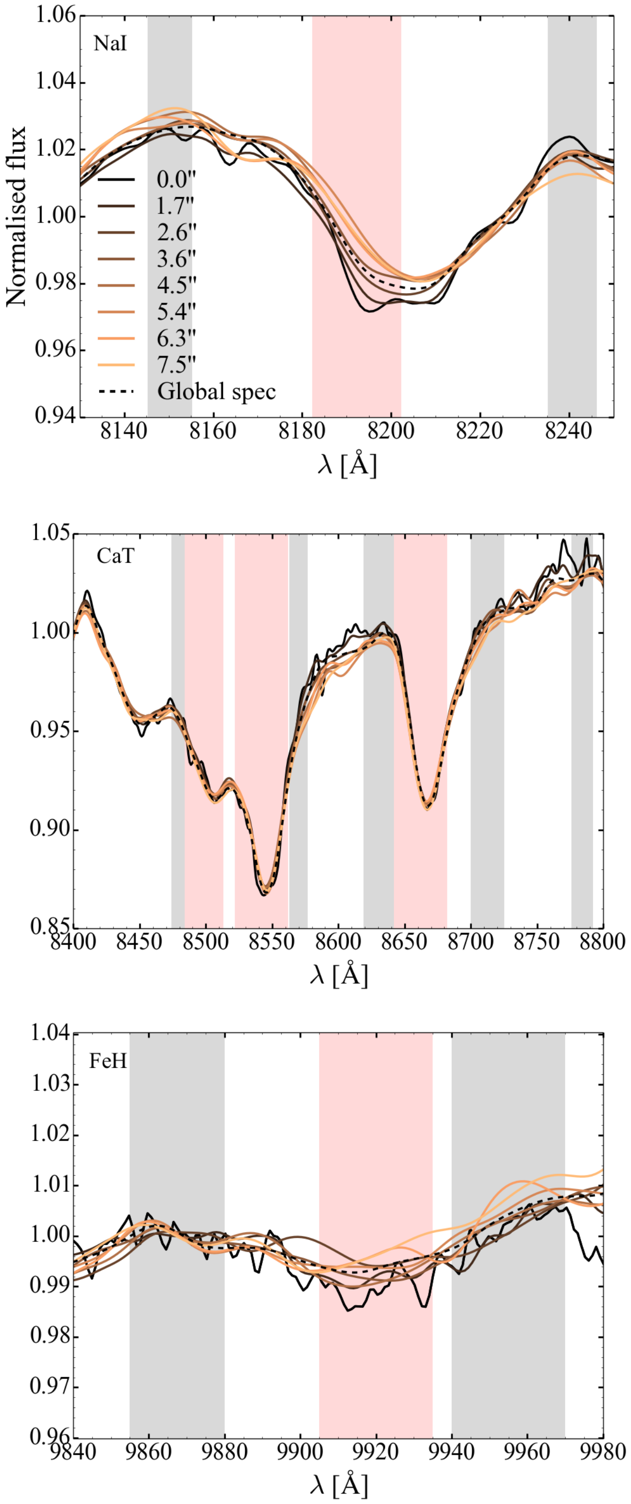

Figure 3.4: Spectra showing the three IMF-sensitive features in NGC4889: from top to bottom: $\mathrm{NaI_{SDSS}}$, CaT and FeH. The spectra have been convolved to a common velocity dispersion of $400\,\mathrm{km\,s^{-1}}$. The spectra are coloured by radial distance in arcsec from the galaxy centre. Also plotted is the optimally extracted global spectrum (black dashed line). The limits of the feature and pseudo-continua band definitions are shown as the shaded red and grey regions respectively.

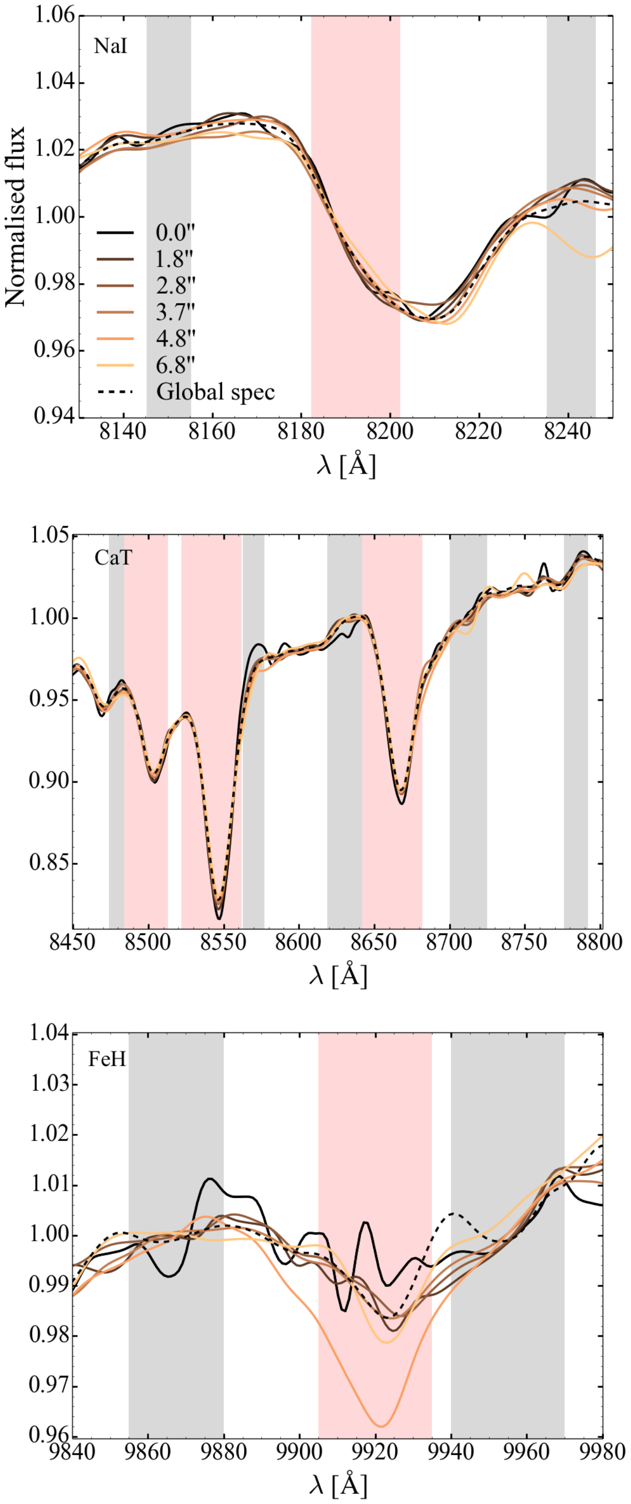

Figure 3.5: Same as Figure 3.4 but for NGC4874. These spectra are convolved to 270 km s^{-1}.

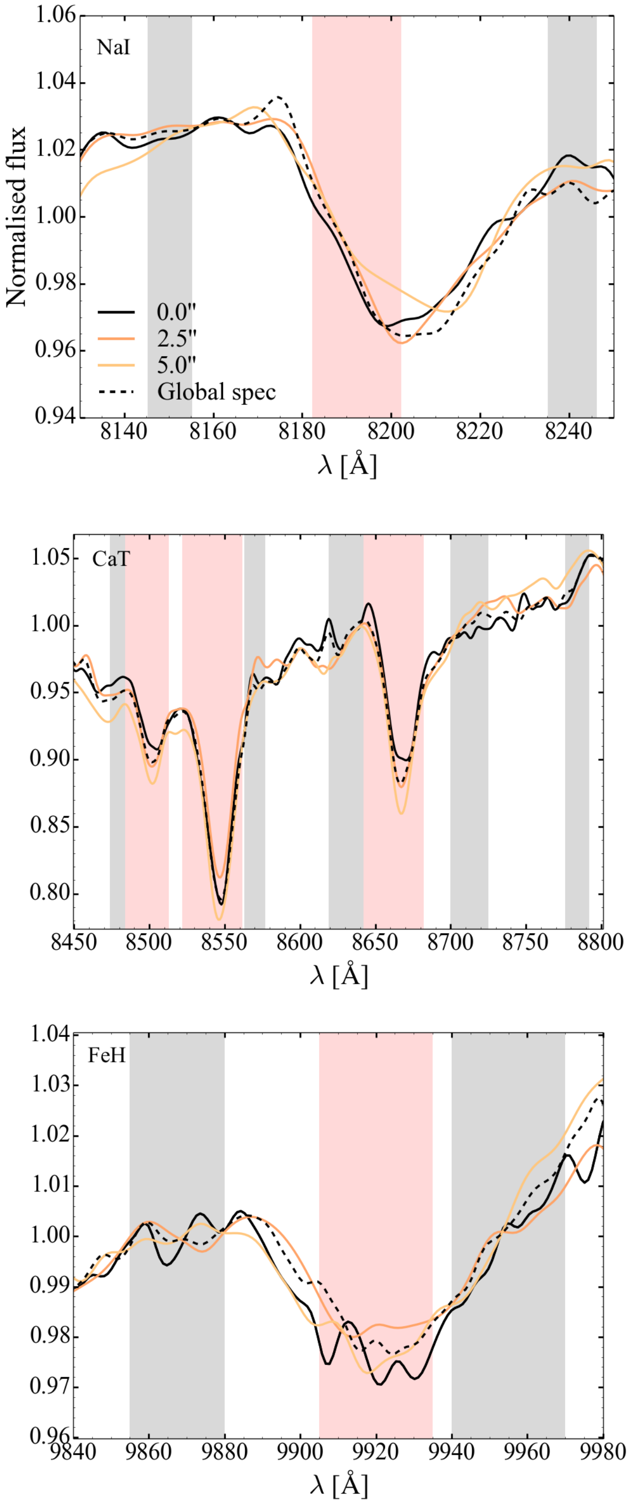

Figure 3.6: Same as Figure 3.4 but for NGC4839. These spectra are convolved to 270 km s^{-1}.

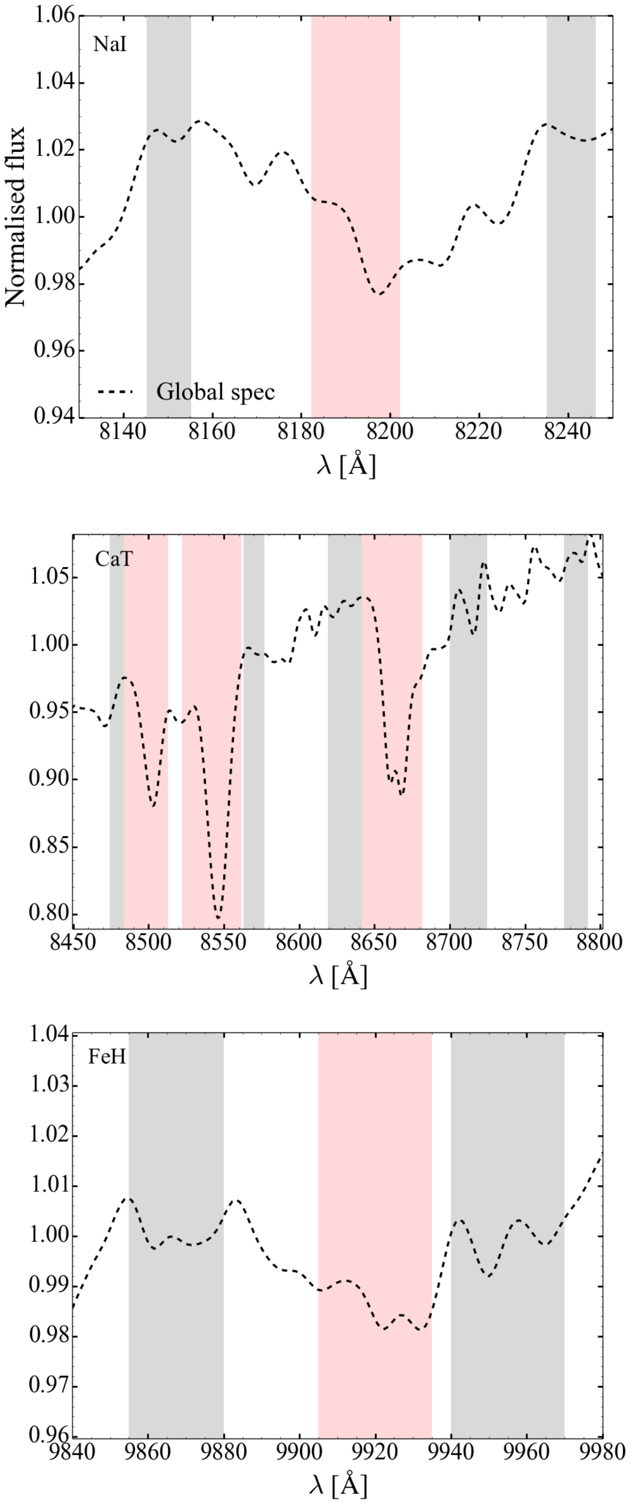

Figure 3.7: Same as Figure 3.4 but for NGC4873. These spectra are convolved to 200 km s^{-1}.

Table 3.4: Index equivalent widths (ratio for TiO) from the optimally extracted global spectra for each galaxy, measured at the velocity dispersion given in the second column.

Galaxy	σ ($\mathrm{km\,s^{-1}}$)	$\mathrm{NaI_{SDSS}}$ (Å)	CaT (Å)	MgI (Å)	TiO	FeH (Å)
NGC4889	400	0.64 ± 0.02	5.59 ± 0.05	0.17 ± 0.01	1.063 ± 0.001	0.24 ± 0.04
NGC4874	270	0.49 ± 0.03	6.24 ± 0.09	0.15 ± 0.02	1.055 ± 0.001	0.36 ± 0.07
NGC4839	270	0.65 ± 0.04	6.75 ± 0.13	0.26 ± 0.03	1.055 ± 0.002	0.61 ± 0.10
NGC4873	200	0.63 ± 0.07	7.62 ± 0.12	0.64 ± 0.03	1.073 ± 0.002	0.41 ± 0.14

3.2 Results

3.2.1 Global spectra

For each galaxy we have a global spectrum optimally extracted over all radii. Figure 3.8 shows the index measurement from these global spectra as white-filled symbols located at $4''$, along with the resolved spectra at different radii (colour filled symbols). For NGC4873 we only measure indices from the global spectra. We present the global index measurements in Table 3.4 and we discuss the measurements for each index in turn.

Strong sodium $\mathrm{NaI_{SDSS}}$ absorption is present in NGC4889, NGC4839 and NGC4873 of ~ 0.64 Å. NGC4874 shows distinctly weaker $\mathrm{NaI_{SDSS}}$ absorption at 0.49 ± 0.03 Å.

NGC4889 shows the weakest level of calcium CaT absorption at 5.59 ± 0.05 Å. NGC4874 and NGC4839 show stronger levels at 6.24 ± 0.09 and 6.75 ± 0.123 Å respectively. NGC4873 shows the strongest CaT absorption of 7.62 ± 0.12 Å.

NGC4889 and NGC4874 display very similar levels of magnesium MgI absorption around 0.16 Å. NGC4839 shows slighter stronger MgI absorption at 0.26 ± 0.03 Å. NGC4873 shows the strongest MgI absorption of 0.64 ± 0.03 Å.

We measure identical titanium oxide TiO absorption strengths in NGC4874 and NGC4839 of 1.055. NGC4889 displays stronger TiO absorption at 1.063 ± 0.001 and NGC4873 displays even stronger TiO absorption at 1.073 ± 0.002.

NGC4889 shows the weakest level of iron-hydride FeH absorption at 0.23 ± 0.04 Å. NGC4874 and NGC4873 display slightly stronger absorption at 0.29 ± 0.08 Å and 0.27 ± 0.14 Å respectively. NGC4839 shows the strongest FeH absorption at 0.56 ± 0.10 Å.

3.2.2 Resolved spectra

Our measurements of the absorption features as a function of radius are shown in Figure 3.8 and we discuss the trends for each galaxy in turn. For NGC4873 our data did not have sufficient S/N to create resolved spectra, so this section covers only the three BCGs.

3.2.2.1 NGC4889

Strong negative gradients are evident for $\mathrm{NaI_{SDSS}}$ and CaT. Sodium ranges from ~ 0.8 Å in the central bin (0.5 kpc) to ~ 0.5 Å at $8''$ (4 kpc). Calcium ranges from 6.1 Å in the central bin to flat at ~ 5.2 Å from $5''$ (2.5 kpc) outwards. Weak negative gradients in MgI and TiO are evident. Magnesium ranges from ~ 0.23 Å in the central $2''$ (1 kpc) to ~ 0.1 Å at $8''$. TiO varies from 1.065 in the central $3''$ (1.5 kpc) to 1.060 from $6''$ (3 kpc). Finally, FeH shows a flat profile throughout of around 0.30 Å, although the 1σ error bars place it anywhere between $0.2 - 0.4$ Å.

3.2.2.2 NGC4874

A strong negative gradient is evident in CaT with a weaker gradient in MgI and flat profiles for $\mathrm{NaI_{SDSS}}$, TiO and FeH. Calcium ranges from 6.8 Å in the central bin to 5.8 Å at $8''$. Magnesium is very weak throughout and ranges from ~ 0.16 Å in the central $\sim 3''$ to 0.05 Å at $8''$. Sodium absorption is flat at ~ 0.5 Å throughout the central $6''$ with the outermost bin showing lower absorption at 0.3 Å, although we see from Figure 3.5 that the red continuum of the outermost spectrum has been strongly affected by residual sky oversubtraction. TiO shows similar behaviour with a flat profile at 1.055 to $5''$ and a slight decrease to 1.050 at $\sim 7''$. FeH absorption scatters around 0.4 Å at all radii but carries a large uncertainty. We also note one clear anomalous FeH measurement at $5''$ showing very strong absorption.

3.2.2.3 NGC4839

Due to the shorter total exposure time on this galaxy we only create three radial bins with sufficient S/N to make measurements. The outermost bin spectrum is also strongly affected by residual sky features, which are marked on Figure 3.8 with dashed error bar lines for

NaI$_{\mathrm{SDSS}}$ and CaT. The NaI$_{\mathrm{SDSS}}$ feature shows strong central absorption of ~ 0.75 Å with a negative gradient to 0.65 Å at $3''$ (1.5 kpc). CaT displays flat absorption of ~ 6.5 Å out to $3''$. MgI shows flat absorption at 0.2 Å in the central $3''$ and the second and third bins suggest a positive gradient up to ~ 0.35 Å around $6''$. TiO displays a flat profile at a similar level to NGC4874 of ~ 1.055. FeH shows a flat profile of between 0.5–0.7 Å, which is the strongest absorption out of the four galaxies. We note the larger FeH error bars for this galaxy, which place the resolved measurements anywhere between 0.5–0.9 Å but we find consistency between these and the global measurement.

3.2.3 Index measurement robustness

Figure B.4 shows our measurements of the FeH index for each BCG from the three different spectra discussed in Section 3.1.3, namely: spectra telluric corrected and sky-subtracted using PPXF (a); spectra corrected by a fit to the telluric profile and sky-subtracted using PPXF (b); spectra corrected by a fit to the telluric profile and sky-subtracted using O-S spatial fitting (c). For NGC4889, all three measurements generally agree, with the O-S fitting giving slightly lower index values. For NGC4874 there is a systematic offset with the telluric corrected spectra producing substantially higher FeH values, whereas the PPXF and O-S sky-subtraction methods are in close agreement. For NGC4839 we again see general agreement with high FeH values from all three spectra.

We also check to see whether convolving the spectra within each galaxy up to a common resolution (corresponding to the peak dispersion value of that galaxy) causes any changes in the measured indices. We measure each index as a function of dispersion in the CvD12 models and derive a multiplicative correction factor to correct each index value for the difference in dispersion between the peak value and the value at the given radius. A comparison of measurements for NGC4889 is shown in Figure B.5. We find the indices only change by up to a few per cent for all galaxies and thus trust our measurements from the convolved spectra.

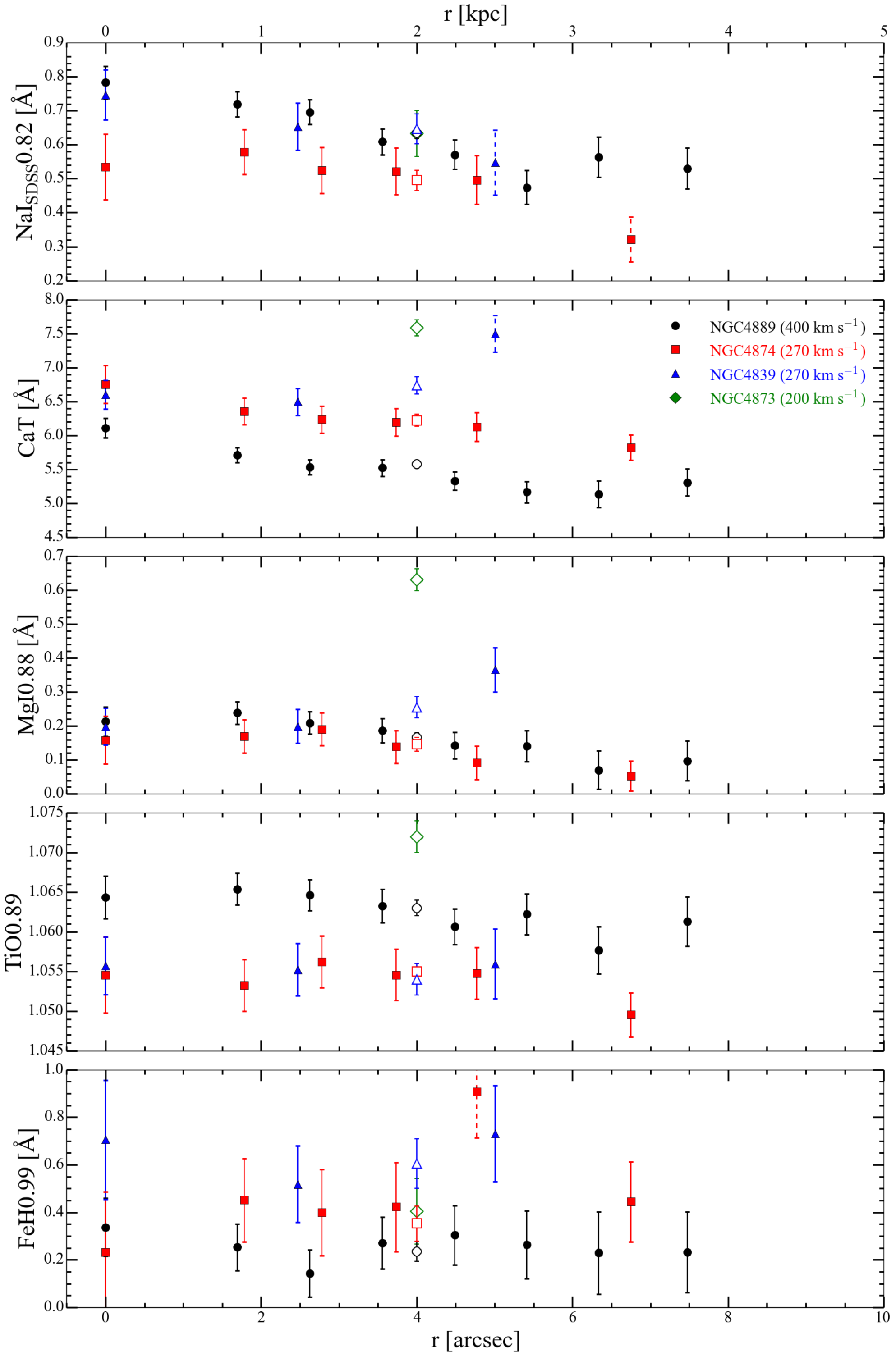

Figure 3.8: Plots of radial gradients for each index for NGC4889 (black circles), NGC4874 (red squares), NGC4839 (blue triangles), and NGC4873 (green diamonds). The measurements have been made at the peak velocity dispersion of each galaxy shown in the legend. Plotted in white-filled symbols at 4″ are the values from the optimally extracted global spectra. The points with dashed error bar lines have been affected by prominent residual sky.

3.3 Analysis

3.3.1 Stellar population synthesis models

In this section we compare our results with SPS model predictions of CvD12. For each galaxy we compare our index measurements with measurements from the SSPs convolved to the matching resolution. The CvD12 models provide SSP spectra with variations in the IMF slope ('bottom-light' through to $x = 3$ 'bottom-heavy'), age (3–13.5 Gyr), α-element enhancement [α/Fe] (solar, +0.2, +0.3), and variations in individual elemental abundance ratios [X/Fe] for 17 different elements (for fixed 13.5 Gyr age and fixed Chabrier IMF). We also make use of the models from Vazdekis et al. (2012, hereafter V12), which allow for variations in the IMF slope, age and total metallicity.

The stellar populations of the three Coma BCGs have been well studied using optical spectra (e.g. Jørgensen, 1999; Mehlert et al., 2000; Moore et al., 2002; Mehlert et al., 2003; Nelan et al., 2005; Sánchez-Blázquez et al., 2006; Trager et al., 2008; Loubser et al., 2009; Coccato et al., 2010; Loubser & Sánchez-Blázquez, 2012; Groenewald & Loubser, 2014). Trager et al. (2008) and Loubser et al. (2009) summarise the derived ages, metallicities and α-enhancements for each galaxy from the literature. The values are derived using $2.7''$ diameter equivalent apertures and thus represent the central regions of each galaxy. An age-metallicity degeneracy is present in the derived SSP parameters for NGC4889 and NGC4874, which complicates the analysis. The more recent investigations (post-2005) generally agree that all three BCGs consist of old ($\sim$ 10 Gyr), metal- and α-enhanced populations, with NGC4889 being the most α-enhanced ($\sim$ +0.3). The compiled parameters on NGC4873 agree that it is younger ($\sim$ 4.9 Gyr) and also metal- and α-enhanced.

3.3.2 NGC4889

In Figure 3.9 we plot FeH–TiO (top) and $\mathrm{NaI_{SDSS}}$–MgI (bottom) index-index maps against CvD12 model predictions at a common resolution of $400\,\mathrm{km\,s^{-1}}$. From the FeH–TiO map we see from the CvD12 models that these indices work in orthogonal directions; FeH positively correlates with IMF slope and [Fe/H], whereas TiO increases with decreasing age or increasing [α/Fe]. The NGC4889 measurements scatter around the [α/Fe] = +0.3, 13 Gyr

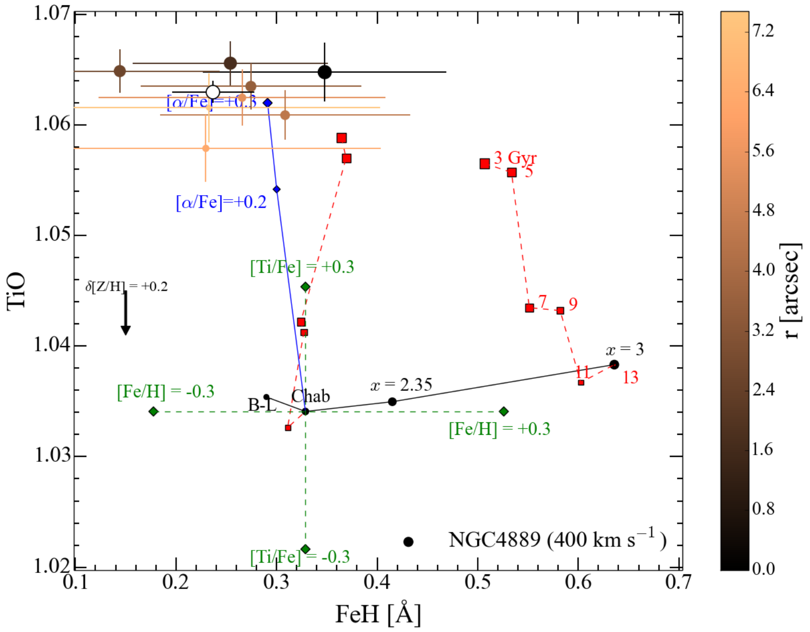

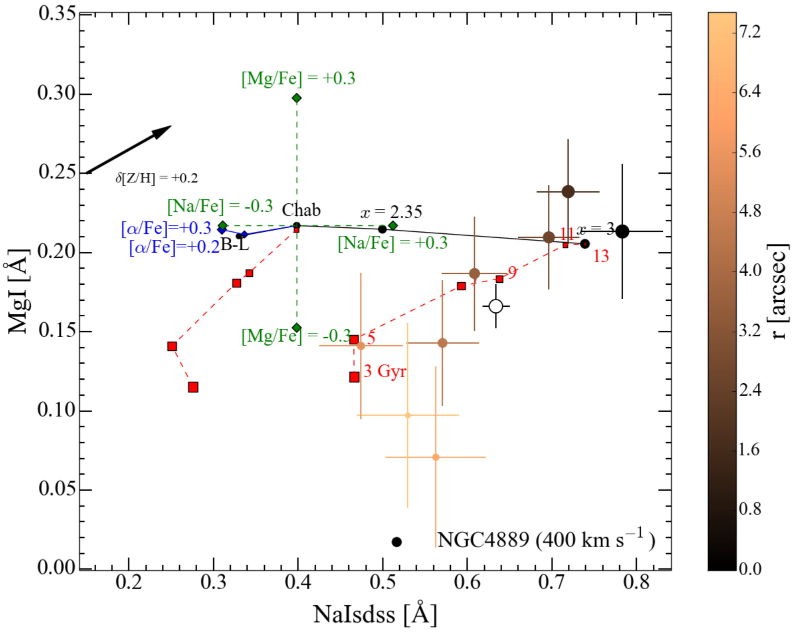

Figure 3.9: Index maps for FeH–TiO (top) and $\mathrm{NaI_{SDSS}}$–MgI (bottom) showing radial variation in NGC4889 compared with model predictions of CvD12. The colour bar and marker sizes indicate the radial position from the centre of the galaxy; size decreases and colour lightens with increasing radial distance. The white filled circle shows the optimally extracted global spectrum measurements. The CvD12 models show variation in IMF slope (black circles with each IMF labelled; B-L for bottom-light, and Chab for Chabrier), age (red squares), [α/Fe] (blue diamonds), and individual elemental abundance variations for a 13 Gyr Chabrier IMF (green diamonds). The black arrow shows the index responses to a change in total metallicity as derived from the V12 models. From the FeH–TiO map we infer an old, α-enhanced population with a Chabrier, or bottom-light, IMF. We then infer from the $\mathrm{NaI_{SDSS}}$–MgI map strong gradients in the relative abundances of sodium and magnesium, rather than a bottom-heavy $x = 3$ IMF with a decreasing age gradient.

Chabrier IMF SSP, with no radial trends. The FeH measurements reject a bottom-heavy $x = 3$ IMF slope and the global spectrum measurement places FeH closer to a bottom-light IMF, strongly rejecting a bottom-heavy IMF. Our measurements therefore suggest that either NGC4889 has a Chabrier IMF and a solar iron abundance, or is largely iron deficient with a bottom-heavy IMF.

The $\mathrm{NaI_{SDSS}}$–MgI map shows the radial gradients of these two indices in NGC4889. The model predictions show that MgI is independent of IMF and $[\alpha/\mathrm{Fe}]$, and positively correlates with age and magnesium abundance. $\mathrm{NaI_{SDSS}}$ is mostly sensitive to IMF, age and sodium abundance. As we take the age, $[\alpha/\mathrm{Fe}]$ and IMF to be fixed from the FeH–TiO map, we infer strong negative gradients in the sodium and magnesium abundances, rather than the interpretation of a bottom-heavy $x = 3$ IMF with decreasing age gradient.

The most striking behaviour from the radial index measurements is the discrepancy between the large $\mathrm{NaI_{SDSS}}$ gradient and the flat FeH profile. Zieleniewski et al. (2015a) and McConnell et al. (2015) have both measured the same discrepant behaviour, in M31 and two massive ETGs respectively. These galaxies have lower central velocity dispersions, between $200 < \sigma < 250\,\mathrm{km\,s^{-1}}$, and so NGC4889 represents a much higher dispersion and more massive galaxy where bottom-heavy IMFs have been recently proposed (e.g. Cappellari et al., 2012; Conroy & van Dokkum, 2012b; La Barbera et al., 2013; Ferreras et al., 2013; Spiniello et al., 2014). Furthermore, van Dokkum & Conroy (2010) presented a stacked spectrum around NaI from four galaxies in the Coma cluster, which included NGC4889, and they concluded a bottom-heavy IMF. However, they did not present the stacked Coma spectrum around FeH. Thus, the flat FeH profile we measure presents tension with the notion of increased IMF slope in this galaxy and with the general IMF-σ relation (see Section 3.4.1). Assuming the IMF is Chabrier we see that this gives a sodium enhancement in the centre of $[\mathrm{Na/Fe}]\sim +1.0$, which decreases to $\sim +0.3$ at $5''$ (2.5 kpc).

We see a magnesium gradient of $[\mathrm{Mg/Fe}]\sim +0.1$ in the centre down to $[\mathrm{Mg/Fe}]\sim -0.5$ at $5''$, assuming that the age is constant. This then discourages the notion of iron deficiency within NGC4889 as any lack of iron would show up as an enhanced [Mg/Fe] unless this galaxy is extremely deficient in magnesium. Thus we are led to the conclusion of a ‘light’ IMF, between the bottom-light and Chabrier forms.

3.3.3 NGC4874

Figure 3.10 shows FeH–TiO (top) and $\mathrm{NaI_{SDSS}}$–MgI (bottom) index-index maps against CvD12 model predictions at a common resolution of $\sigma = 270\,\mathrm{km\,s^{-1}}$. NGC4874 is shown with the circle points. We exclude the anomalously high FeH datapoint at $r = 5''$. The remaining points scatter around the Chabrier IMF slope with a bottom-heavy $x = 3$ IMF excluded. The TiO index places the galaxy at around [α/Fe]$\sim +0.1$ for an old (13 Gyr) population. Similarly to NGC4889 we find from the FeH index that NGC4874 would need either iron deficiency with a dwarf-dominated IMF, or a Chabrier IMF and solar iron abundance. The $\mathrm{NaI_{SDSS}}$–MgI map suggests weak gradients in magnesium and sodium, although we measure very weak MgI compared with the CvD12 predictions. We do not find a conflicting radial gradient between iron and sodium for NGC4874 and the flat $\mathrm{NaI_{SDSS}}$ profile at $\sim 0.4\,\text{Å}$ (except the outermost point which has a bad continuum region) strengthens the case for a Chabrier IMF in this galaxy.

3.3.4 NGC4839

Figure 3.10 shows our measurements for NGC4839 as square markers on the FeH–TiO (left) and $\mathrm{NaI_{SDSS}}$–MgI (right) maps, compared to the CvD12 models at a common resolution of $\sigma = 270\,\mathrm{km\,s^{-1}}$. The FeH measurements scatter around a bottom-heavy $x > 2.35$ IMF slope and the TiO measurements place the galaxy around [α/Fe] $\sim +0.1$ for a 13 Gyr population, or a solar $\sim 9\,$Gyr population. The TiO measurements are very similar to NGC4874. The most striking difference for this galaxy is the deeper FeH absorption compared with the other two BCGs. The global spectrum FeH measurement places the galaxy at either an IMF slope of $x \sim 2.6$ with solar iron abundance, or a Chabrier IMF with [Fe/H]~ 0.3. From the $\mathrm{NaI_{SDSS}}$–MgI map we infer that NGC4839 is also weak in MgI, but the strong $\mathrm{NaI_{SDSS}}$ index with no gradient also supports a steeper IMF slope.

3.3.5 NGC4873

Figure 3.11 shows our global measurements for NGC4873 on the FeH–TiO (top) and $\mathrm{NaI_{SDSS}}$–MgI (bottom) maps, compared with the CvD12 models at a common resolution

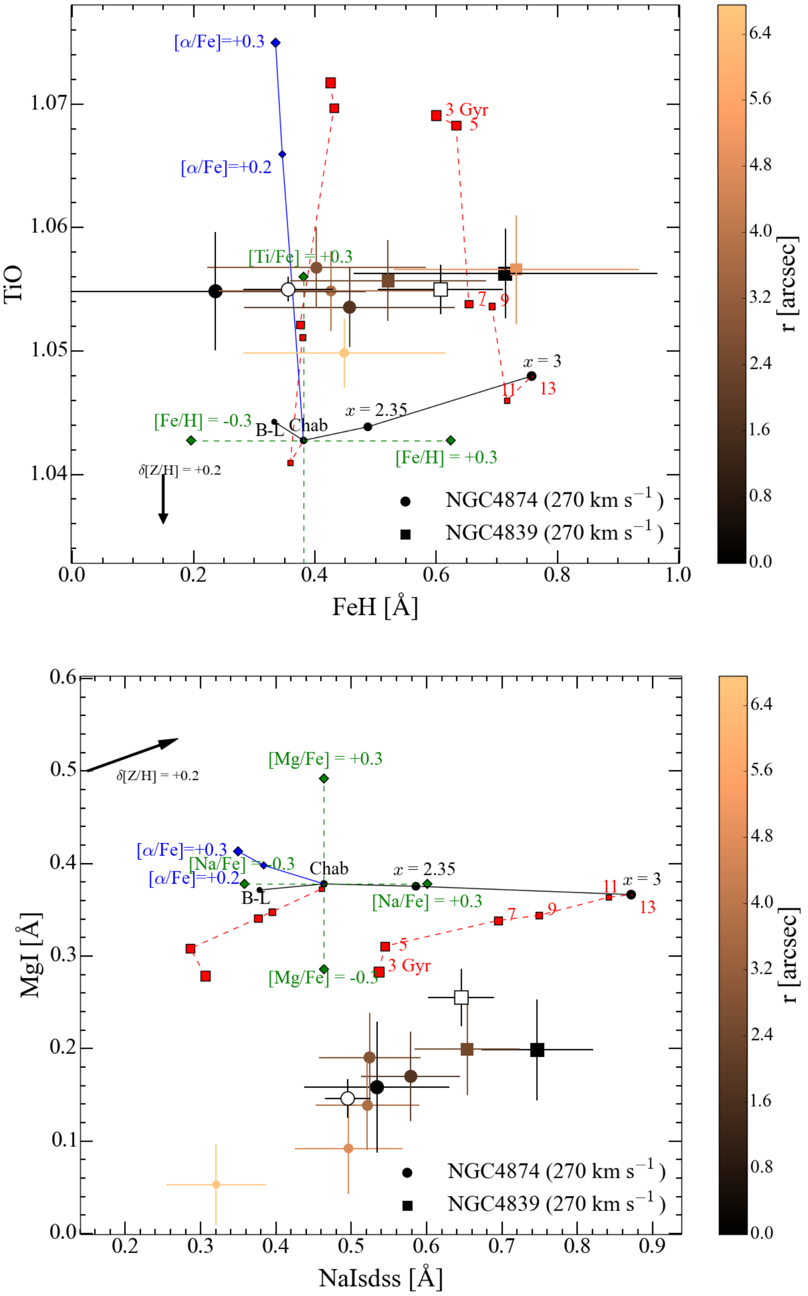

Figure 3.10: FeH–TiO (top) and NaI$_{\mathrm{SDSS}}$–MgI (bottom) index maps showing radial variation in NGC4874 (circles) and NGC4839 (squares), compared with model predictions of CvD12 at a common resolution of $\sigma = 270\,\mathrm{km\,s^{-1}}$. The colour bar indicates the radial position from the centre of the galaxy. The white circle and square show the optimally extracted global spectrum measurements for NGC4874 and NGC4839 respectively. The CvD12 model labels are the same as in Figure 3.9.

of $\sigma = 200\,\mathrm{km\,s^{-1}}$. Our measurements are consistent with NGC4873 being younger and α-enhanced through a strong magnesium enhancement. We infer a Chabrier IMF from FeH, which is further supported by the $\mathrm{NaI_{SDSS}}$ measurement suggesting a small Na-enhancement for a Chabrier IMF.

3.3.6 Breaking degeneracies using optical index measures

Trager et al. (2008) and Loubser et al. (2009) have presented Lick index measurements for the centres of the galaxies in our sample, derived from apertures of $2.7''$ and $R_\mathrm{e}/8$ in diameter respectively. Their complete samples both cover cluster environments, with Trager et al. (2008) presenting collated measurements for 187 ETGs in the Coma cluster, and Loubser et al. (2009) presenting measurements for 49 nearby BCGs. Figure 3.12 shows the measurements of the Mg*b* and <Fe> indices[2] for the sample of BCGs from Loubser et al. (2009), with the Coma BCGs denoted by coloured symbols. We see that NGC4889 shows the strongest absorption in both indices. NGC4874 and NGC4839 have similar, lower levels of <Fe> compared to NGC4889, and NGC4839 shows slightly weaker Mg*b* absorption compared to NGC4874.

These optical indices, especially <Fe>, are strong tracers of the relative atomic abundances rather than the IMF (see e.g. Conroy & van Dokkum, 2012a). It is clear from these published measurements that NGC4889 is the most iron-enhanced compared to the other two Coma BCGs. If we assume from Figure 3.9 that the $\mathrm{NaI_{SDSS}}$ gradient in NGC4889 traces a steep IMF gradient from very bottom-heavy in the centre to Chabrier at 5 kpc, then the flat FeH profile can only be explained by an iron gradient ranging from [Fe/H] ~ -0.5 in the centre to [Fe/H] ~ 0.0 at 5 kpc. This is not supported by the central <Fe> index strength. Similarly, NGC4839 has the weakest <Fe> strength of the three Coma BCGs, but is relatively 'normal' compared to other galaxies and so the strong FeH is not supported by iron-enhancement. We therefore conclude that our observations of the FeH feature are tracing the underlying IMF of these galaxies. Our measurements suggest a Chabrier or bottom-light IMF for NGC4889, a Chabrier IMF for NGC4874 and NGC4873, and a bottom-heavy (heavier than Salpeter) IMF for NGC4839.

---

[2] <Fe> is a combination of the Fe5270 and Fe5335 indices, defined as <Fe> = (Fe5270 + Fe5335)/2.

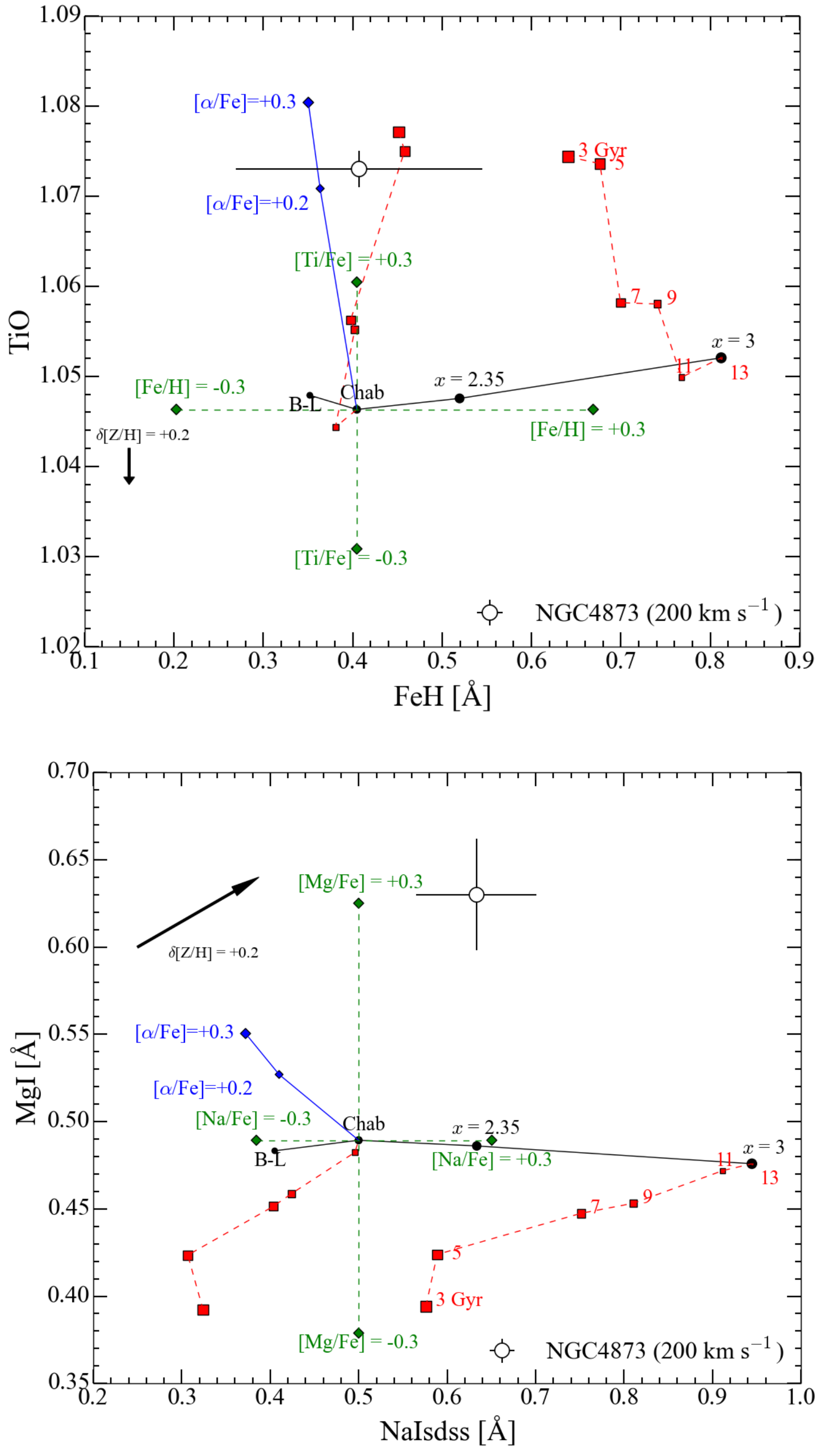

Figure 3.11: FeH–TiO (top) and NaI$_{\mathrm{SDSS}}$–MgI (bottom) maps showing NGC4873 (white circle), compared with model predictions of CvD12 at a common resolution of $\sigma = 200\,\mathrm{km\,s^{-1}}$. The CvD12 model labels are the same as in Figure 3.9.

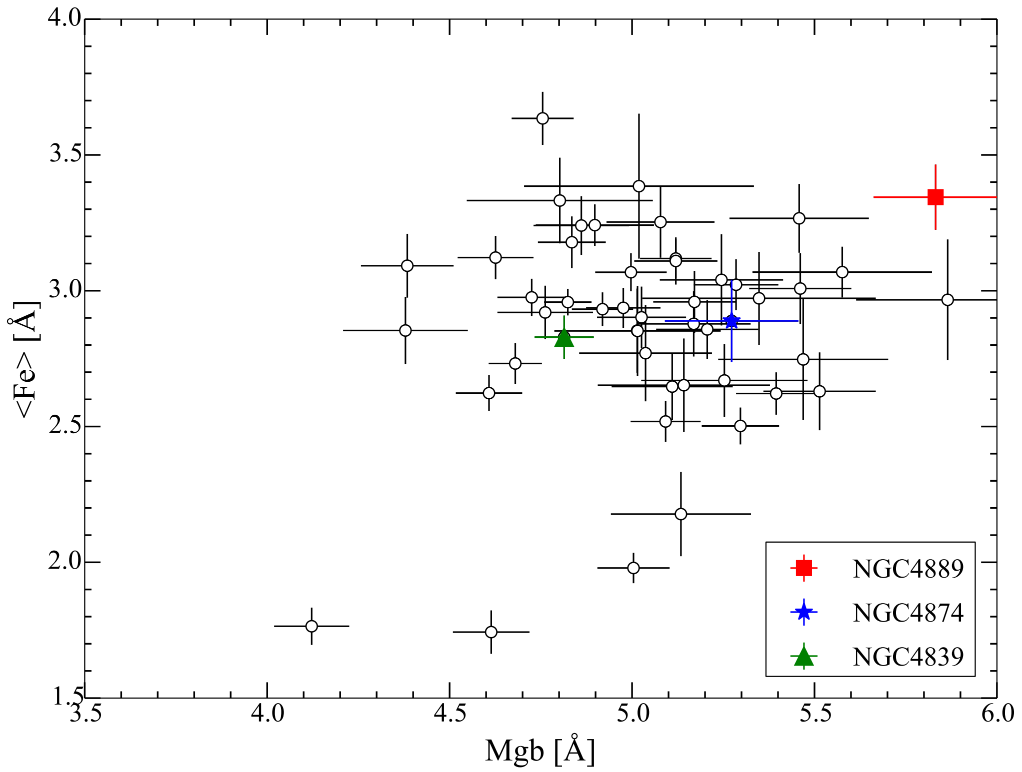

Figure 3.12: Mg*b*–<Fe> index map for a sample of 49 nearby BCGs and two ellipticals from Loubser et al. (2009). The Coma BCGs are shown in the coloured symbols, NGC4889 (red square), NGC4874 (blue star), and NGC4839 (green triangle). This map shows that NGC4889 has the strongest <Fe> and Mg*b* strengths of the three Coma BCGs, and NGC4839 has the weakest <Fe> strength of the three; as these indices predominately trace relative abundances it suggests that NGC4889 cannot be iron-deficient (compared to the other two BCGs), and NGC4839 cannot be iron-enhanced compared to the other two.

3.4 Discussion

3.4.1 The IMF-σ relation

Ferreras et al. (2013), La Barbera et al. (2013) and Spiniello et al. (2014) have all published IMF-σ relations for ETGs showing that an increase in σ corresponds to an increase in IMF slope. These relations are all derived using galaxies covering a range of velocity dispersions from $\sim$ 150–320 $\mathrm{km\,s^{-1}}$, and so NGC4874, NGC4839 and NGC4873 fall well within this range. While there is some variation between the relations, the general conclusion is that galaxies with $\sigma > 200\,\mathrm{km\,s^{-1}}$ (for LB13 and F13; $\sigma > 250\,\mathrm{km\,s^{-1}}$ for S14) have IMFs steeper than Salpeter, and galaxies with $\sigma < 200\,\mathrm{km\,s^{-1}}$ have IMFs approaching Chabrier. Therefore our qualitative analysis for NGC4873 ($\sigma \sim 200\,\mathrm{km\,s^{-1}}$) having a normal IMF agrees well with these relations. NGC4874 and NGC4839 have $\sigma \sim 270\,\mathrm{km\,s^{-1}}$ and the index interpretation of NGC4839 having a steeper (than Salpeter) IMF slope also agrees. However, our global measurements for NGC4874 are not consistent with an IMF slope steeper than Salpeter. Finally, NGC4889 ($\sigma \sim 400\,\mathrm{km\,s^{-1}}$) has a central dispersion much larger than the galaxies used to derive the IMF-σ relations, but our inferred Chabrier IMF from the flat FeH profile is in conflict with the relations, which predict a very bottom-heavy IMF slope ($x > 3$).

To quantitatively compare our results to the published IMF-σ relations we derive single power-law IMF slopes for our full sample of galaxies. We take published ages, metallicities and α-enhancements for each galaxy as priors and infer the response of the FeH index to variations of each parameter using the CvD12 SPS models. Our derived IMF slopes for each galaxy are shown in Figure 3.13. We find consistency with a Chabrier IMF for each galaxy across the σ range, except for NGC4839 where we find evidence of an IMF slightly steeper than Salpeter.

Ferreras et al. (2013) and La Barbera et al. (2013) have also invoked a bimodal form of the IMF and fitted it to observational data to derive $\mathrm{IMF_b} - \sigma$ relations. The bimodal IMF is defined in Vazdekis et al. (1996) with a slope of x for $M > 0.6\,\mathrm{M_\odot}$ and flattening below $0.6\,\mathrm{M_\odot}$. For an exponent of $x = 2.3$ it very closely maps the Kroupa (2001) universal IMF. La Barbera et al. (2015) recently used the FeH index to distinguish between bottom-heavy

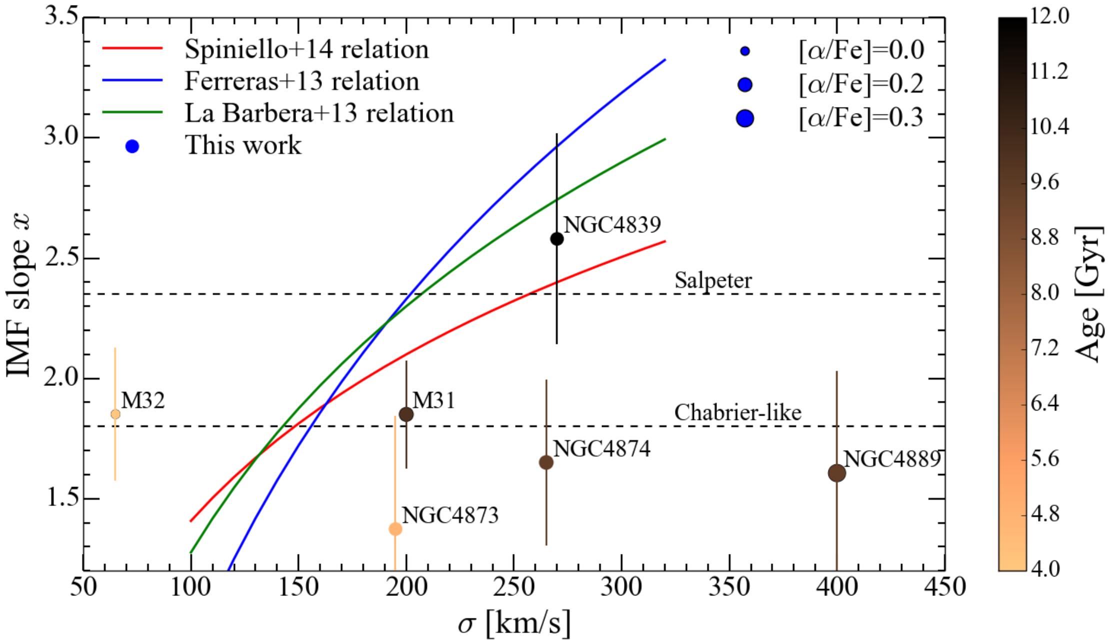

Figure 3.13: Derived IMF slope x against central velocity dispersion for our sample of galaxies. The IMF slope has been derived from our *global* FeH measurements accounting for CvD12 model responses to age, [α/Fe] and [Fe/H] variations using published values in the literature for each galaxy (Rose et al., 2005; Trager et al., 2008; Loubser et al., 2009; Saglia et al., 2010; Coccato et al., 2010; Loubser & Sánchez-Blázquez, 2012). For our data, the colour of each point indicates the age and the marker size indicates the level of [α/Fe] enhancement for each galaxy. The coloured lines show IMF-σ relations from the previous works of Ferreras et al. (2013); La Barbera et al. (2013) and Spiniello et al. (2014), derived using central 2.7″ SDSS spectra and several optical/NIR features, including NaD/NaI but excluding FeH. The dashed horizontal lines show the Salpeter (upper) and Chabrier-equivalent (lower) slopes. Our results show consistency with a universal Chabrier IMF across a large range of velocity dispersions, with the exception of the single galaxy NGC4839, for which we derive an IMF slightly heavier than Salpeter.

unimodal and bimodal IMFs in a massive ETG ($\sigma \sim 300\,\mathrm{km\,s^{-1}}$). FeH is most sensitive to $M \leq 0.3M_\odot$ and thus can constrain the very low mass end of the IMF. From La Barbera et al. (2015) the FeH index is predicted to vary much more weakly with increased bimodal IMF slope compared to the unimodal IMF. In fact a bottom-heavy bimodal IMF with $x = 4$ gives a similar FeH strength to the Salpeter IMF (at $\sigma = 300\,\mathrm{km\,s^{-1}}$; see figure 10 in La Barbera et al., 2015) of ~ 0.45 Å. However, NGC4889 has an even weaker FeH feature at a larger σ and seems to be incompatible with even a bimodal bottom-heavy IMF.

3.4.2 Comparison with dynamical modelling and lensing results

Stellar M_*/L_R have been published for each of the BCGs by Thomas et al. (2007, 2011) and for NGC4889 by McConnell et al. (2012). For NGC4889, the independent results by Thomas et al. (2007) of $M_*/L_R = 6.5\,\mathrm{M_\odot\,L_\odot}^{-1}$ (Thomas et al. do not quote 1σ uncertainties) and by McConnell et al. (2012) of $M_*/L_R = 5.9 \pm 1.7\,\mathrm{M_\odot\,L_\odot}^{-1}$ are in good agreement. For NGC4874 and NGC4839, Thomas et al. (2007, 2011) measured $M_*/L_R = 7.0\,\mathrm{M_\odot\,L_\odot}^{-1}$ and $M_*/L_R = 8.5 \pm 2.0\,\mathrm{M_\odot\,L_\odot}^{-1}$ respectively. It should be noted that these represent upper limits on M_*/L due to the uncertainties of incorporating a dark matter component in the models (e.g. Thomas et al., 2011; Bundy et al., 2015).

The order of increasing M_*/L_R between NGC4889, NGC4874 and NGC4839 is echoed by the IMFs we infer from the FeH measurements within these galaxies. A simple comparison can be made with the V12 published M_*/L_R values. For a 12.5 Gyr [Z/H] = +0.22 SSP, we find that a bottom-light $x = 1.8$ IMF gives $M_*/L_R = 6.4$, a Kroupa IMF gives $M_*/L_R = 4.2$, and a $x = 2.5$ IMF slightly steeper than Salpeter gives $M_*/L_R = 7.6$. These mass-to-light ratios from SPS models are in general agreement with the dynamical measurements of NGC4889 and NGC4839.

Mass-to-light ratios measured from gravitationally lensed galaxies also provide an interesting comparison. Smith & Lucey (2013) have presented a massive lensed ETG ($\sigma \approx 330\,\mathrm{km\,s^{-1}}$) with a mass excess factor $\alpha = (M/L)_{\mathrm{lens}}/(M/L)_{\mathrm{kroup}} = 1.04 \pm 0.15$, which strongly favours a Kroupa or Chabrier IMF and rejects even a Salpeter IMF. Furthermore, Smith et al. (2015b) have presented an average mass excess factor derived from three gravitationally lensed massive ETGs ($\sigma > 300\,\mathrm{km\,s^{-1}}$). They find $\langle\alpha\rangle = 1.1$, which again rejects a Salpeter IMF and strongly rejects bottom-heavy IMFs in these galaxies. Thus, our results should not be considered particularly discrepant in comparison with other recent IMF determinations.

3.4.3 IMF or abundance gradients and implications for the stellar populations of BCGs

Strong radial absorption feature gradients have now been documented within the centres of some ETGs by several authors, most notably for sodium (e.g. Faber & French, 1980; Boroson & Thompson, 1991; Martín-Navarro et al., 2015a,b; Zieleniewski et al., 2015a; McConnell et al., 2015). Furthermore, the discrepancy between the strengths of sodium and iron 'IMF' indices has also been noted by numerous authors (e.g. Smith et al., 2012; Conroy & van Dokkum, 2012a; Smith & Lucey, 2013; Zieleniewski et al., 2015a; McConnell et al., 2015). This poses interesting questions for understanding the physical context of these gradients. The general scenario is that BCGs form in the deepest potential wells in short, intense star formation bursts, with successive growth through small-scale mergers around the outskirts (e.g. Larson, 1974; Carlberg, 1984; Naab et al., 2009; Hopkins et al., 2010; Cappellari, 2016). This inside-out formation scenario predicts metallicity gradients, as the central stellar populations enrich in-falling gas sustaining the ongoing star formation. For NGC4889 and NGC4874 we infer magnesium and sodium abundance gradients. Tracing the radial behaviour of the NaD feature would help constrain the underlying physical driver behind the $\mathrm{NaI}_{\mathrm{SDSS}}$ gradient. However, sodium is not an α-element and is generally poorly understood in the context of galaxy stellar populations (e.g. Jeong et al., 2013; Spiniello et al., 2014; Smith et al., 2015a), so further study of sodium-enhancement in galaxies is required.

The recent study of IMF variations has shown correlations with both [α/Fe] and central velocity dispersion (Cappellari et al., 2012; Conroy & van Dokkum, 2012b; Ferreras et al., 2013; La Barbera et al., 2013; Spiniello et al., 2014). One physical model is that larger mass and α-enhanced systems have more type II supernovae driven turbulence, leading to greater fragmentation of star forming gas clouds (Conroy & van Dokkum, 2012b). Chabrier et al. (2014) highlights that the IMF slope should correlate with *density* rather than velocity dispersion. Therefore, galaxies that underwent more rapid formation periods via mergers or intense gas inflows should have more bottom-heavy IMFs. NGC4839 distinguishes itself from the other two BCGs as sitting in a smaller cluster located to the south west of the main Coma cluster, and contains the oldest stellar populations of the BCGs (Trager et al., 2008; Loubser et al., 2009; Groenewald & Loubser, 2014). Our results therefore suggest the possibility of different formation periods for each of the Coma BCGs, with NGC4389 forming in the shortest timescale with the highest gas inflow and highest central density, leading to a more dwarf-rich IMF.

The very low FeH measured in NGC4889 could be consistent with a bottom-light IMF dominated by remnants rather than low-mass stars. This form has been proposed by studies of sub-millimetre (submm) galaxies with extremely high star formation rates (e.g. Baugh et al., 2005; Narayanan & Davé, 2012, 2013, c.f. Hayward et al. 2013) which have been thought to be the progenitors of BCGs. Indeed the dynamical modelling of Cappellari et al. (2012, 2013) shows a systematic increase of the M_*/L with velocity dispersion, but cannot distinguish between bottom-light or bottom-heavy forms.

Our work, and other studies using independent methods (e.g. gravitational lensing, Smith & Lucey, 2013; Smith et al., 2015b), points to the notion that careful mass determinations of individual galaxies should be taken on a galaxy-by-galaxy basis. High S/N optical spectroscopy of these objects covering other known IMF-sensitive features (see e.g. Spiniello et al., 2014) would help elucidate the stellar component of these galaxies. Our results show that the Coma BCGs present an exciting target for IFS surveys like MaNGA (Bundy et al., 2015), which would be able to provide mass constraints using both, visible to far red spectral coverage, and dynamical modelling techniques.

3.5 Conclusions

Using the Oxford SWIFT instrument we have undertaken a study of the three brightest cluster galaxies in the Coma cluster with the aim of discerning possible gradients in IMF-sensitive far red stellar absorption features. We obtained high S/N resolved spectroscopy of NGC4889, NGC4874 and NGC4839, covering the central $\sim 10''\,(5\,\mathrm{kpc})$ of each galaxy, as well as unresolved data for the fast rotator NGC4873. We utilised two separate sky subtraction methods to minimise sky line residuals in our spectra and validate our results. We measured the far red NaI doublet, calcium triplet CaT, magnesium MgI, titanium oxide TiO and iron hydride Wing-Ford band FeH as functions of radius. We conclude the following:

1. NGC4889 shows strong negative gradients in $\mathrm{NaI_{SDSS}}$ and CaT, mild negative gradients in MgI and TiO, and a flat profile of low FeH absorption. The strong $\mathrm{NaI_{SDSS}}$ gradient is in tension with the flat FeH profile in the context of a bottom-heavy IMF. Comparing FeH and TiO indices to stellar population models we infer a Chabrier or possibly bottom-light IMF and old, α-enhanced population, in agreement with optical stellar population studies. This result is especially interesting due to the large central velocity dispersion of $\sim 400\,\mathrm{km\,s^{-1}}$ in the centre of NGC4889, which from previous IMF-σ relations would infer a very bottom-heavy IMF.

2. NGC4874 shows weak negative gradients in CaT, MgI and TiO. $\mathrm{NaI_{SDSS}}$ and FeH profiles are both flat and do not show strong absorption. Comparing to models we again find a Chabrier IMF with slight α-enhancement compared to NGC4889 and in agreement with optical stellar population studies.

3. NGC4873 displays strong CaT, MgI and TiO absorption. We measure low FeH absorption suggesting a Chabrier IMF, which is what we expect for a galaxy of this velocity dispersion.

4. Within NGC4839 we measure strong $\mathrm{NaI_{SDSS}}$ *and* strong FeH absorption. This may be evidence of a dwarf-heavy population in the centre and from optical indices suggests it is not caused by iron-enhancement. We compare to dynamical modelling results, which suggest an IMF ~ 2.5 times heavier than Kroupa is required, which is in agreement with a bottom-heavy IMF.

5. These galaxies span a large range of velocity dispersions and we find tension with the notion of a simple IMF-σ relation compared to the interpretation from the IMF-sensitive features. Specifically, NGC4889 has a very high central dispersion ($\sim 400\,\mathrm{km\,s^{-1}}$) and we only detect low levels of FeH compared with a strong $\mathrm{NaI_{SDSS}}$ gradient. The IMFs we infer for these galaxies are supported by published optical index measurements. We conclude

that interpretations of dwarf-dominated stellar populations should be treated on a galaxy-by-galaxy basis. Combining NIR and optical IMF-sensitive indices with dynamical models should give strong constraints on the dwarf-abundance in individual galaxies.

Part II

Science with HARMONI on the European ELT

Chapter 4

HSIM: a simulation pipeline for HARMONI on the European ELT

The European Extremely Large Telescope (E-ELT) is a 39 m diameter, optical and near-infrared (NIR) telescope being constructed by the European Southern Observatory (ESO) for operations commencing within the next decade. Upon completion, this facility will provide the angular resolution and light-gathering power to revolutionise our current understanding in many areas of astrophysics. However, as telescope and instrumentation projects enter such ambitious scales of size and complexity of design, it is becoming imperative to accurately quantify performance prior to construction.

Consequently, several recent integral field spectrograph instrumentation projects have developed detailed instrument simulation models, including KMOS (Lorente et al., 2008), MUSE (Jarno et al., 2008), JWST/NIRSpec (Piquéras et al., 2010; Dorner et al., 2011), and EAGLE/ELT-MOS (Puech et al., 2008, 2010a,b). The most rigorous simulation method involves using the full optical design of the instrument to propagate photons to the detector plane, before using data reduction software to reduce the simulations akin to real data. While this full end-to-end technique is possible for currently operational instruments and those at an advanced stage of design, it is a level above what is possible at an early stage of development.

As part of the concept design for an ELT multi-object spectrograph (MOS), Puech et al.

(2010b) developed an IFS instrument simulator that processed input data cubes, generating mock observation cubes assuming a perfect data reduction process. The simulator encoded all the sky, telescope and adaptive optics (AO; through the point spread function) and instrument parameters, returning mock observations containing source and background flux as well as noise contributions. They were able to analyse the feasibility of a key MOS program to observe star forming galaxies at $z \sim 6$.

This chapter presents the development of the instrument simulation pipeline HSIM for the HARMONI instrument that will be used to quantify the performance. HSIM improves on the method developed by Puech et al. in several key areas, including spectral line spread convolutions, and a wavelength dependent telescope and adaptive optics point spread function (PSF) model. We detail the components of HSIM and show the importance of the key stages and their effects on observations.

The chapter is organised as follows: Sections 4.1 and 4.2 detail the motivation, goals and methodology of the simulations; in Section 4.3 we present an overview of the pipeline stages; in Section 4.4 we present our point spread function parameterisation and demonstrate its importance; Section 4.5 shows our verification crosschecks against existing software. In Section 4.6 we discuss the pipeline and current simulation efforts.

Throughout this chapter we adopt a flat ΛCDM cosmology with $H_0 = 70\,\mathrm{km\,s^{-1}\ Mpc^{-1}}$, $\Omega_m = 0.3$ and $\Omega_\Lambda = 0.7$. We use AB magnitudes throughout unless otherwise stated.

4.1 Motivation and goals

Developing an instrument simulation pipeline serves several important purposes:

a) it gives a quantitative understanding of the feasibility of observing programs, characterising both the capabilities and limitations of an instrument,

b) it allows for performance trade-offs between differing instrument designs or configurations.

The first point is important since it will allow observing time on the E-ELT to be more efficiently utilised. Quantifying performance usually consists of determining the exposure time required to achieve a particular signal-to-noise ratio (S/N) for a given target. However, an instrument simulation pipeline allows us to go one step beyond exposure time calculators and ascertain the precision with which we can derive a number of key physical parameters for particular science cases. The input data cubes can be built to encode as many physical characteristics as desired. The mock output data represents that of real observations and so it is possible to use identical analysis methods as used on real data (or permits users to develop and verify analysis methods prior to taking the real data). This allows the user to specifically determine the feasibility of their science goal, for example: how coarsely data needs to be spatially binned to extract resolved kinematics; what the uncertainty on a final black hole mass measurement may be; how sky absorption and emission lines may hamper absorption line equivalent width measurements and associated chemical abundances. It also provides a direct comparison between the scientific capabilities of current generation instrumentation and those of the ELT era.

Designing a self-contained and modular pipeline means that all simulations are kept consistent within the current design of the instrument. The pipeline can easily be modified to reflect any changes in the instrument design (e.g. changing spaxel scales, spectral resolving power etc), thus allowing exploration of the second goal above. It will also be possible to explore instrument effects such as imperfect sky subtraction and spectrograph throughput variations, and give quantitive constraints on such calibration issues.

4.2 Simulation methodology

The procedure for performing simulations can be broken down into three parts:

a) An input data cube encoding the spatial and spectral properties of the object such as size, shape, morphology, absorption/emission lines and associated kinematics, dynamics, chemical abundances etc;

b) A simulation pipeline that takes the input and adds all the first-order sky, telescope, instrument, and detector effects, as well as random and systematic noise, creating an output mock-observed data cube. The user is able to choose suitable observing parameters to be able to explore the instrument and telescope modes;

c) The analysis of the output mock-observed data to enable an understanding of what information may be extracted from a real HARMONI observation, i.e. how well can the properties of the input data cube be recovered in the output cube.

Within this framework there are two areas of parameter space to be explored: the physical characteristics of the objects (e.g. morphology, mass, redshift, magnitude, line strengths) as well as the observational characteristics of the telescope, and instrument (e.g. spatial scale, exposure time, resolving power, emissivity, AO correction). Consequently the combined parameter space is vast, and a full exploration is simply not possible. For the purposes of this part of the thesis, we have firstly pursued point source sensitivity calculations for all current instrument configurations in Chapter 5, which gives a general overview of the performance of the instrument design. We then present simulations of a representative case of $z \sim 2$–3 emission-line galaxies in Chapter 6.

4.3 Simulation pipeline overview

We have presented the simulation pipeline in Zieleniewski et al. (2014, 2015b). The overall process is presented in Figure 4.1. HSIM is written in PYTHON and makes use of the ASTROPY (Astropy Collaboration et al., 2013), NUMPY, SCIPY, WX, and PPROCESS packages. It handles input and output data in FITS format, as this is the usual file format for 3D spectrographs. The input data cube is uploaded as a 3D array with two spatial and one spectral dimension. The FITS headers contain all the relevant information about the object (e.g. spatial and spectral sampling, flux units, spectral resolution). Figure 4.2 shows the HSIM graphical user interface. The user chooses suitable observing parameters and the data cube is then processed through several steps. We provide a general user's guide to the HSIM code with details of input parameters and data cube requirements in Appendix C.

4.3.1 Line spread function convolution

The spectral resolution of the input cube is degraded to the output resolution depending on the chosen grating. This is achieved by convolving the spectral dimension with a

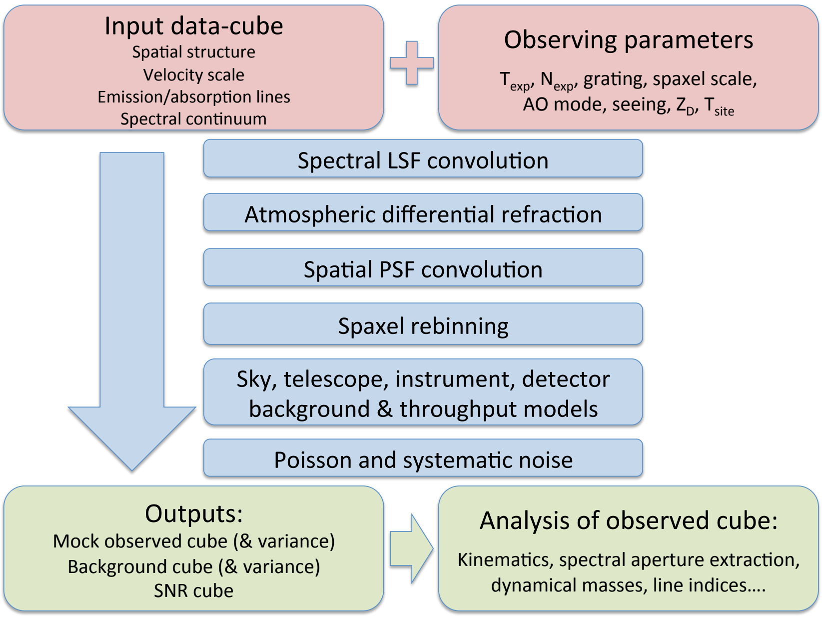

Figure 4.1: Flowchart of the simulation process. Input data cubes provide all the physical details of the object. The cube is then 'observed' for given instrument, telescope and site parameters. The observing process adds all first-order telescope and instrument effects, as well as random and systematic noise. The output cube represents a perfectly reduced data cube, and can be analysed exactly like real data.

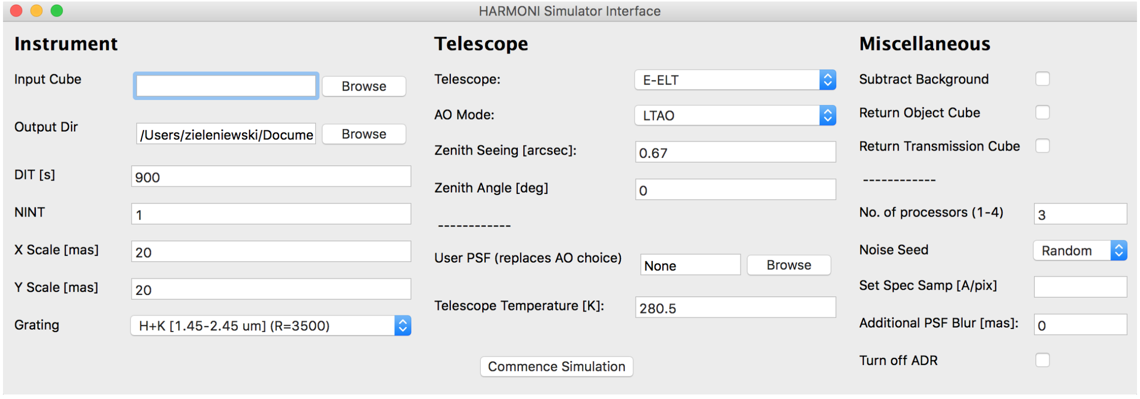
HARMONI Simulator Interface

Instrument

Input Cube:
Output Dir: /Users/zieleniewski/Docume
DIT [s]: 900
NINT: 1
X Scale [mas]: 20
Y Scale [mas]: 20
Grating: H+K [1.45-2.45 um] (R=3500)

Telescope

Telescope: E-ELT
AO Mode: LTAO
Zenith Seeing [arcsec]: 0.67
Zenith Angle [deg]: 0

User PSF (replaces AO choice): None
Telescope Temperature [K]: 280.5

Miscellaneous

Subtract Background ☐
Return Object Cube ☐
Return Transmission Cube ☐

No. of processors (1-4): 3
Noise Seed: Random
Set Spec Samp [A/pix]:
Additional PSF Blur [mas]: 0
Turn off ADR ☐

Figure 4.2: The HSIM pipeline graphical user interface where the input data cube and observing parameters are entered.

Gaussian line spread function (LSF). We use a Gaussian of constant full width half maximum (FHWM) in wavelength units as a reasonable approximation for the resolution of a slit-width limited grating spectrometer. We ensure the output resolution of the cube is consistent by generating a LSF of width $\Delta\lambda_{\mathrm{conv}}$ given by,

$$\Delta\lambda_{\mathrm{conv}} = \sqrt{(\Delta\lambda_{\mathrm{out}})^2 - (\Delta\lambda_{\mathrm{in}})^2}, \tag{4.1}$$

where $\Delta\lambda_{\mathrm{in}}$ is the spectral resolution of the input cube specified in the FITS header (by the user), and $\Delta\lambda_{\mathrm{out}}$ is the output resolution given by the chosen grating. This assumes that the input data cube has a Gaussian LSF of FWHM $\Delta\lambda_{\mathrm{in}}$. The spectral dimension of the cube is then sampled (with a minimum of two pixels per FWHM to satisfy the Nyquist criteria). If the input spectral resolution is coarser than the grating resolution ($\Delta\lambda_{\mathrm{in}} > \Delta\lambda_{\mathrm{out}}$) then the user can choose to either convolve with a LSF of width $\Delta\lambda_{\mathrm{out}}$ or perform no spectral convolution. The former option is useful in situations where the input data cube contains a spectrum where the resolution is limited by e.g. stellar velocity dispersion in galaxies, and the spectrum still needs to incorporate the instrumental effect. The option to ignore the spectral convolution is always available if it is not required (e.g. if the input data cube has been pre-formatted spectrally, or makes use of real spectra observed at coarser resolution).

4.3.2 Atmospheric refraction

The effect of atmospheric refraction (AR) is added according to the equations of Schubert & Walterscheid (2000) and Roe (2002). The angle in radians between the true zenith distance Z_D and the apparent zenith distance Z_a is approximated by,

$$R = Z_D - Z_a \simeq \left(\frac{n^2 - 1}{2n^2}\right) \tan Z_D, \tag{4.2}$$

where the refractive index n is a function of wavelength, pressure, temperature and humidity[1]. Thus the angular change $R_1 - R_2$, between two wavelengths is given by,

$$R_1 - R_2 = \left(\frac{n_1^2 - 1}{2n_1^2} - \frac{n_2^2 - 1}{2n_2^2} \right) \tan(Z_D). \tag{4.3}$$

This effect is prominent at both visible wavelengths, where the refractive index varies the most strongly with wavelength, and at the smallest spatial scales. Figure 4.3 illustrates the effect of AR as a function of wavelength. Each wavelength channel (spatial image at a given wavelength in the 3D cube) is shifted relative to an optimal wavelength, which is calculated to give equal maximal shift at each end wavelength of the data cube. The shift is made along the longest spatial dimension of the output data cube (this assumes the user aligns the longest spatial axis of the instrument field of view along the parallactic angle). After the data cube is rebinned to the chosen spaxel scale, the AR is 'corrected' by shifting the wavelength channels back again to emulate the correction achieved by a data reduction pipeline. This stage reduces the common field of view of the data cube. The differential effect whereby the axis of AR moves throughout an exposure causing the object to blur in the data cube, is not included.

4.3.3 Point spread function convolution and spatial rebinning

Each wavelength channel is convolved with a spatial PSF. We have developed a novel method for parameterising the E-ELT AO PSFs first presented in Zieleniewski & Thatte (2013) allowing us to generate PSFs at any wavelength within the HARMONI range. The PSF parameterisation is described in more detail in Section 4.4. We also include the option of a Gaussian model to approximate a seeing-limited PSF. We use the wavelength- and seeing-dependent FWHM from Tokovinin (2002) and Martinez et al. (2010), which includes the turbulence outer-scale L_0 set to the generally accepted value at Paranal of $L_0 = 23\,\mathrm{m}$

---

[1] We use site characteristics for Paranal from Kendrew et al. (2008), namely a pressure of 760 mbar and relative humidity of 10 %.

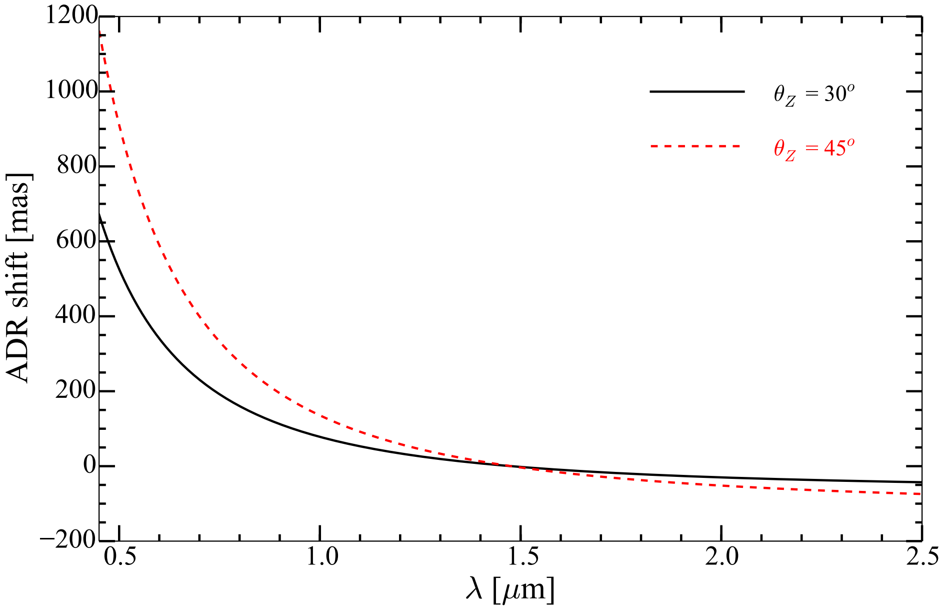

Figure 4.3: Atmospheric refraction as a function of wavelength for zenith angles of 30° (black solid line) and 45° (red dashed line). The shift shown here is relative to the central wavelength of the full HARMONI wavelength range at $\sim 1.5\,\mu$m. AR has been calculated using a site temperature of 280.5 K and other characteristics for Paranal from Kendrew et al. (2008), namely a pressure of 760 mbar and relative humidity of 10 %.

(e.g. Martin et al., 2000; Martinez et al., 2010),

$$\mathrm{FWHM}_{\mathrm{PSF,seeing}} = 0.976\frac{\lambda}{r_0}\sqrt{1 - 2.183\left(\frac{r_0}{L_0}\right)^{0.356}} \text{ radians,} \tag{4.4}$$

where for a seeing FWHM of $0.67''$ at $\lambda = 500\,\mathrm{nm}$, $r_0 = 0.15\,\mathrm{m}$ and scales as $r_0 \propto \lambda^{6/5}$. This is the standard seeing-limited PSF as used by ESO exposure time calculators (ETCs).

HSIM generates PSFs at 1 mas sampling and performs the PSF convolution at a scale of $1/10^{\mathrm{th}}$ of the output spatial scale in order to minimise convolution effects due to the finite sampling of the input cube and PSF. This is conceptually different to the spectral dimension convolution where we use Gaussian functions; in the spatial dimension we have a spatially complex AO PSF (or large seeing PSF) and therefore cannot define a convolving kernel to convolve the spatial channel up to a specific resolution. If the input data cube is coarser than $1/10^{\mathrm{th}}$ of the output scale then it is interpolated up to $1/10^{\mathrm{th}}$, ensuring flux conservation.

The data cube is rebinned to the chosen output spatial scale ensuring flux conservation.

4.3.4 Background and throughput

Total background and throughput cubes are generated incorporating the effects of sky, telescope, instrument and detector. We use the ESO Skycalc sky model described by Noll et al. (2012) and Jones et al. (2013) for both emission and transmission. We model the telescope as a grey-body whereby a thermal black-body curve for the given site temperature T_{site} is multiplied by a constant emissivity ϵ,

$$B(T,\lambda) = \epsilon\frac{2hc^2}{\lambda^5}\frac{1}{e^{\frac{hc}{\lambda k_B T_{\mathrm{site}}}} - 1}, \tag{4.5}$$

where h is Planck's constant, k_B is Boltzmann's constant, λ is the wavelength, and $c = 2.998 \times 10^8\,\mathrm{m\,s^{-1}}$. We assume a uniform throughput value for the instrument. The NIR detector quantum efficiency (QE) is based on the KMOS HAWAII-2RG detectors (Finger et al., 2008) and the CCD QE is based on MUSE calibration data (D. Ives, priv. comm.).

4.3.5 Noise

Poisson noise from the object, sky and telescope background, and detector dark current is added along with detector read-out noise. We use separate statistics to represent the use of CCDs for visible wavelengths and NIR arrays for longer wavelengths. Again, the NIR detector statistics are modelled on the KMOS HAWAII-2RG detectors (Finger et al., 2008) and the CCD statistics are based on the MUSE calibration data (D. Ives, priv. comm.). The wavelength cut between visible CCDs and NIR detectors is set at 0.8 μm.

4.3.6 Outputs

The final outputs of HSIM are:

1. A mock observed cube: the main product of the simulation containing flux from the source and background, detector dark current, and all associated noise for each (x, y, λ) pixel of the cube (with an associated variance cube as first extension);

2. A background cube containing all background flux (with an associated variance cube as first extension);

3. A S/N cube giving the signal-to-noise ratio for each pixel calculated as,

$$\mathrm{S/N} = \frac{N_{\mathrm{obj}}(x,y,\lambda)T_{\mathrm{exp}}\sqrt{N_{\mathrm{exp}}}}{\sqrt{N_{\mathrm{obj}}(x,y,\lambda)T_{\mathrm{exp}} + N_{\mathrm{bg}}(x,y,\lambda)T_{\mathrm{exp}} + D_{\mathrm{c}}\,T_{\mathrm{exp}} + \sigma_{\mathrm{R}}^{2}}}, \tag{4.6}$$

with the terms defined as in Table 1.3 but per pixel rather than per resolution element. There are also options to return a noiseless object cube containing only source flux, return a transmission cube allowing perfect telluric absorption correction, and perform automatic perfect sky subtraction (observed cube - background cube).

4.4 Incorporating AO point spread functions

The effects of the telescope and AO system on observations are encoded in the spatial PSF. The E-ELT PSF is predicted to be a strong function of wavelength as well as other parameters including seeing, off-axis distance from reference AO star, and guide star magnitude. Its complex form means it needs to be incorporated carefully into the simulations not simply modelled as a simple Gaussian or Moffat function. We have incorporated a continuously varying AO PSF as a function of wavelength and seeing, for both LTAO and SCAO, in our simulation pipeline, using the ELTPSFFIT program developed by J. Liske[2]. We use a set of simulated, high resolution, long-exposure LTAO and SCAO PSFs (provided by T. Fusco), covering the HARMONI wavelength range at $0.1\,\mu$m intervals. The simulation parameters of these input PSFs are shown in Table 4.1. Using ELTPSFFIT we are able to fit the azimuthally averaged radial profile of each PSF using several analytical functions,

$$A(R) = \frac{I_A}{(1-\epsilon^2)^2}\left(\frac{2J_1(R) - 2\epsilon J_1(\epsilon R)}{R}\right)^2, \quad R(r) = \frac{\sin(r)}{w_A}, \tag{4.7}$$

$$L(r) = \frac{I_L}{\left(\frac{r-p_L}{w_L}\right)^2 + 1} \tag{4.8}$$

$$M(r) = \frac{I_M}{\left(\left(\frac{r}{w_M}\right)^2 + 1\right)^{\beta}}. \tag{4.9}$$

Eq. 4.7 is a form of the obscured Airy function which represents the diffraction limited core, where I_A is the intensity, $J_1(R)$ is the first Bessel function of the first kind, $w_A = \lambda/(\pi D)$ gives the HWHM where D is the telescope diameter, and $\epsilon = 0.3$ is the obscuration ratio for the E-ELT. The Lorentzian function in Eq. 4.8 models the AO correction cutoff point[3] where I_L is intensity, w_L is the HWHM and p_L is the radial position of the peak. The seeing halo is modelled by the Moffat function (Eq. 4.9) where I_M is intensity, w_M is the HWHM and β is the *shape* parameter. The full radial profile of the PSF is given by,

$$PSF(r) = A(r) + M_s(r) + L(r) + M_c(r). \tag{4.10}$$

The second Moffat function $M_c(r)$ is used only for visible PSFs to represent the non-diffraction limited core and becomes negligible in the NIR. The analytic profile can then be sampled at any radius or wavelength by interpolating the smoothly varying model parameters. This allows the generation of a PSF data cube that can be used to convolve

---

[2] `https://www.eso.org/sci/facilities/eelt/science/drm/tech_data/ao/psf_fitting/` - last accessed 01-06-15

[3] This is caused due to the finite number of the DM actuators. There exists a maximum spatial frequency that can be corrected by the DM; all higher spatial frequencies form a seeing halo.

Table 4.1: Simulation parameters for input high resolution PSFs used in HSIM.

	PSFs
$\lambda\,(\mu\mathrm{m})$	0.4–2.5
Seeing FWHM (arcsec)	0.67, 0.85, 0.95, 1.10
Zenith angle (deg)	30
Off-axis distance (arcsec)	0
rms jitter (mas)	3 (LTAO), 2 (SCAO)
AO WFS	SH
LTAO laser guide stars	6
LTAO asterism radius (arcsec)	60
SCAO NGS mag (V-band)	12
Telescope diameter (m)	37 fully-filled

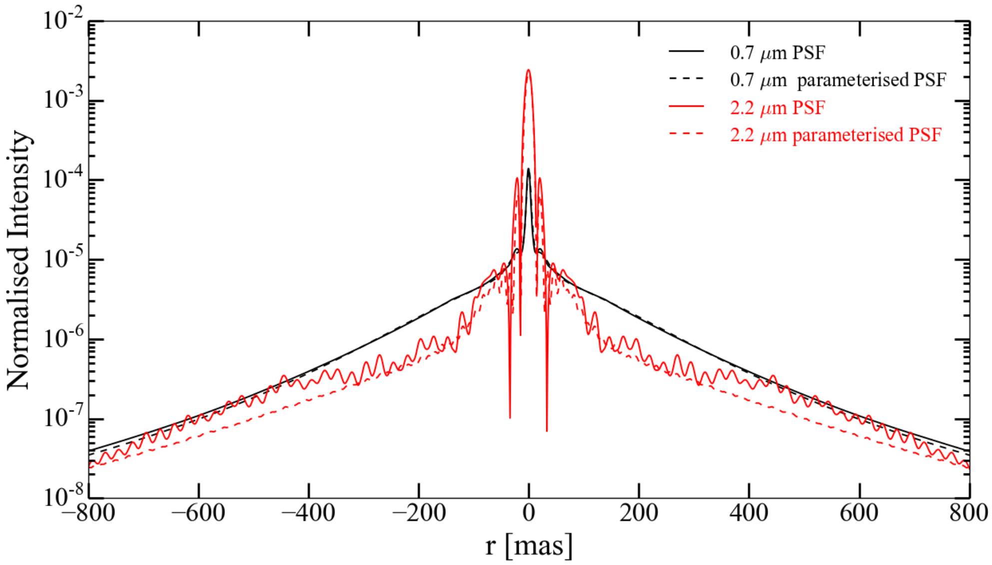

Figure 4.4: Comparison of radial profiles between input (solid lines) and parameterised (dashed lines) LTAO PSFs for R- and K-bands. PSFs are generated at a seeing FWHM of $0.67''$ at $0.5\,\mu$m, and zenith angle of 30°.

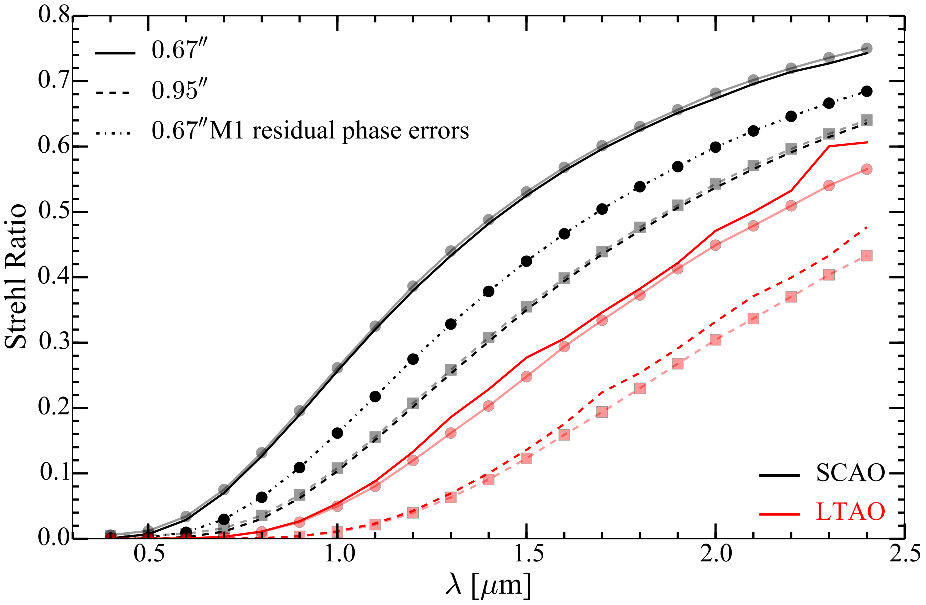

Figure 4.5: Strehl ratios of parameterised PSFs used in HSIM as a function of wavelength for SCAO (black) and LTAO (red) for two seeing values of 0.67″ (solid) and 0.95″ (dashed) FWHM at 0.5 μm. For each line, the fainter points (and lines of the same colour and type) show the equivalent values for the input, high resolution on-axis PSFs (see Table 4.1 for details). For the SCAO PSFs the input lines have been moved up by 0.005 for clarity. We also show the Strehl ratio for 0.67″ SCAO PSFs with residual M1 phase errors (dot-dashed line) for comparison with our parameterisation method.

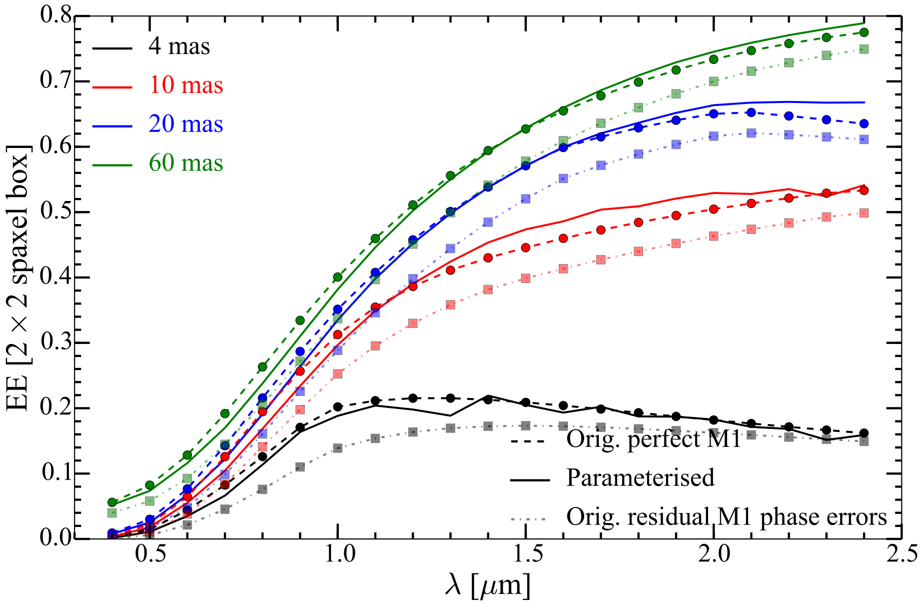

Figure 4.6: Ensquared energies (EEs) of parameterised SCAO PSFs used in HSIM as a function of wavelength for SCAO at 0.67″ FWHM seeing at 0.5 μm. EEs are extracted from a 2×2 spaxel aperture for each of the output HARMONI spaxel scales. We also show the EE from SCAO PSFs with residual M1 phase errors (dot-dashed lines) for comparison with our parameterisation method.

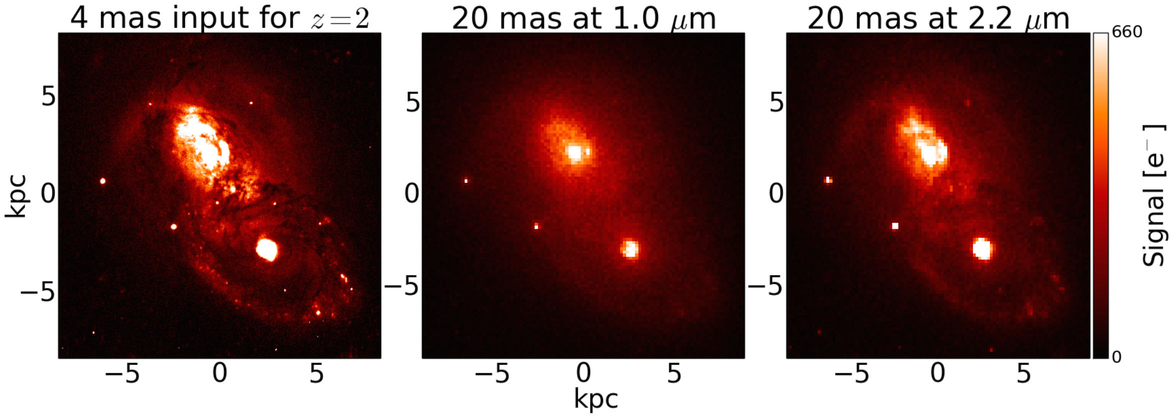

Figure 4.7: Integrated continuum maps from an HSIM simulation of a ULIRG observed with LTAO. Left panel shows the input map at a sampling of 4 mas after scaling an HST WCS image of a local galaxy (50 mas sampling) to the correct spatial extent at $z = 2$. Centre panel shows a 20 mas continuum map at 1.0 μm in the Iz-band. Right panel shows a 20 mas continuum map at 2.2 μm in the K-band. The observed maps are shown at S/N = 10. We assume identical intensity and spatial distribution for both continuum maps. The improved PSF performance at longer wavelengths is clearly evident, although the small diffraction-limited core at 1.0 μm is evident in the middle panel.

each spectral channel of a HARMONI data cube with the correct PSF. We have only used on-axis PSFs without M1 residual errors, and we assume the PSF does not vary spatially within the field of view. Figure 4.4 shows a comparison of radial profiles between input and parameterised LTAO PSFs. Good agreement in the shape is evident at both wavelengths. Figure 4.5 shows the measured Strehl ratios (SR) of our parameterised PSFs for both LTAO and SCAO compared with the input PSFs. Generally good agreement is evident between the two sets of input and output PSFs. We also plot the SR for SCAO PSFs with residual M1 phase errors as a comparison with our parameterisation method. Figure 4.6 shows the EE for SCAO PSFs as a function of wavelength. The EE is calculated from a 2×2 spaxel aperture for each of the HARMONI output spaxel scales. Again, we see generally good agreement between input and parameterised PSFs, and we also show the EE for PSFs with M1 residual phase errors as a comparison. The smooth variation of AO performance with wavelength in our parameterised PSFs is clear and our parameterisation does not introduce a dominant source of error.

The importance of the wavelength variation is worth emphasising. Whilst the diffraction limit of a telescope increases from visible to NIR wavelengths, AO performance vastly improves at longer wavelengths because the atmospheric turbulence becomes relatively less disruptive. This large improvement, as seen in Figure 4.5, more than compensates for the increasing diffraction limit at longer wavelengths. We demonstrate this qualitatively in Figure 4.7, which shows continuum maps for a simulated HARMONI observation of an ultra luminous infra-red galaxy (ULIRG) at a redshift of $z = 2$. The input HST ACS image at a resolution of 50 mas (IRAS06076-2139: from Armus et al., 2009) has been cosmologically scaled and sampled to 4 mas at $z = 2$. The central image shows the object as observed in the Iz-band at 1.0 μm. The right image shows the object as observed in the K-band at 2.2 μm. For easier comparison we assume equal flux at both wavelengths and we ignored the increased thermal background in the K-band. It is clear from the two maps that the overall spatial resolution in the K-band is much improved over the Iz-band due to the higher SR, providing exquisite detail of the underlying star-forming morphology of the ULIRG. We do note that the Iz-band actually has a narrower diffraction-limited core compared to the K-band.

The AO PSFs that we used for the parameterisation also include a small amount of intrinsic jitter or blur, which estimates the effect of wind-shake on the telescope structure. This corresponds to 2 and 3 mas rms for the SCAO and LTAO PSFs respectively. We include the ability to add additional amounts of PSF blur to approximate reduced AO performance. We model this by convolving the AO PSF with a Gaussian of chosen rms width, so any additional blurring adds in quadrature.

4.5 Verification runs

To test the results of HSIM we compare to two separate tools. Firstly, we compared to the pipeline of Puech et al. (2010a), which has itself been verified using real SINFONI observations from Genzel et al. (2006). As part of the E-ELT design reference mission (DRM) science case C10: *The physics and mass assembly of galaxies out to* $z \sim 6$, Puech et al. undertook simulations of which some examples are publicly available[4]. We took the example data cube UGC5253, a rotating disc galaxy with prominent Hα emission. We converted the cube for compatibility with HSIM using the description from the DRM. We then ran simulations using identical parameters as used by Puech et al. including the identical spatial PSF. Puech et al. do not specify the sky transmission spectrum they use, so we manually convolved one from the E-ELT DRM to match the spectral resolution of the data cube.

The outputs of the comparison are shown in Figure 4.8. HSIM computes the total signal of $N_{\rm exp}$ combined exposures, so we have divided our output cube by $N_{\rm exp}$ to get a mean value for each pixel (cf. Puech et al. who determine the median value of each pixel from $N_{\rm exp}$ cubes). It is clear from both the signal and S/N plots that we are computing consistent values within the uncertainty of different transmission functions, and can be confident that HSIM is working correctly.

For the second crosscheck we compared HSIM with the ESO SINFONI ETC. We ran the ETC for an extended object with an A0V spectrum at a K-band Vega magnitude of 14, observed in seeing-limited mode for two hours (8×900 s). The ETC returns the input

---

[4] `https://www.eso.org/sci/facilities/eelt/science/drm/C10/` - last accessed 01-06-15

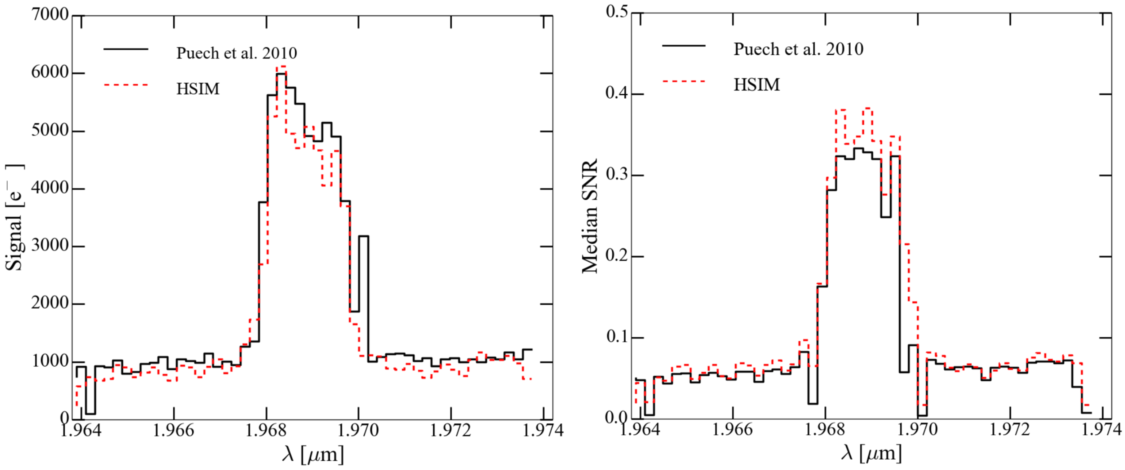

Figure 4.8: Left: comparison of the signal extracted from a 10 spaxel radius aperture centred on the galaxy between Puech et al. simulation and HSIM. Right: comparison of the median S/N over every spaxel in each wavelength channel. The HSIM and Puech et al. simulations are consistent to within the noise realisations.

spectrum which we used to create an input cube. We simulated an identical observation with HSIM, using a seeing-limited PSF and the relevant VLT telescope parameters. We were careful to calculate our object flux over two spatial pixels as done by the ETC. We note that we approximated the output resolution of our spectrum using the central wavelength value of the spectrum divided by the resolving power of the SINFONI grating, as it is unclear exactly how the LSF convolution is performed in the ETC. Figure 4.9 shows the total S/N and object signal within two spaxels (main panels), and the respective residuals after median smoothing by 10 spectral pixels to account for potential differences in LSF convolution (sub panels). Our results show extremely good agreement with the ETC with sub 5 % residuals over the majority of the spectrum We conclude that the HSIM procedures are working correctly and it is producing realistic signal and noise values.

4.6 Discussion and conclusions

HSIM is a standalone simulation pipeline that offers a capability far exceeding that of a simple ETC. The pipeline takes input data cubes and simulates observations, folding in realistic sky, telescope, instrument and detector models to create output mock data, which can be analysed akin to real data. Thus it can make quantitative predictions about the

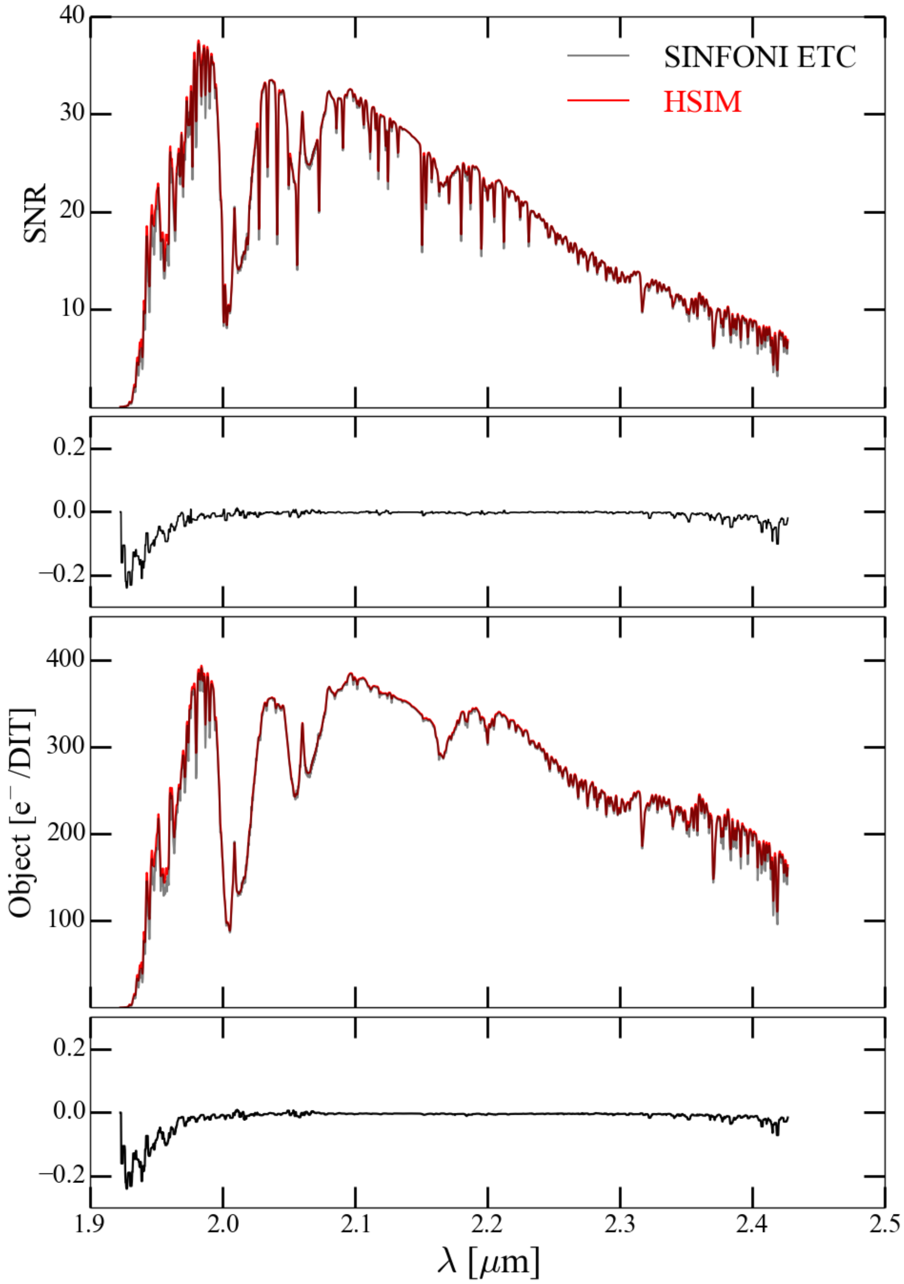

Figure 4.9: Comparison of the total S/N and object signal between HSIM (red) and the SINFONI ETC (grey). The two main panels show the total S/N and object signal within two spaxels. The two smaller panels show the respective residuals after median smoothing by 10 spectral pixels.

feasibility of particular science goals, which presents a step beyond simple S/N predictions.

There are some caveats and limitations to the simulations, which we describe here. Firstly, the predictive power of a particular simulation is dependent on the complexity and accuracy of the physical prescriptions incorporated within the input data cube. While the basic method of utilising the pipeline is to compare mock-observed output with input, this only offers physical meaning if the input physics is accurate. Designing input data cubes for science simulations requires specific tailoring for each individual case. We briefly discuss some examples of input data cube generation below and provide further details in Appendix C.

A second factor is the accuracy of the telescope PSF model. Our parameterisation method allows for accurate circularly-symmetric, wavelength-dependent PSFs to be produced at little computational expense. However, it is currently only capable of parameterising on-axis PSFs of point-like reference sources. More complex PSFs formed by referencing on extended objects would be difficult to parameterise, which limits science cases where the object of interest, e.g. a Jovian moon, is also used as the SCAO reference. An alternative method could be to use principal component analysis which has been used extensively for modelling spatial variations (e.g. for HST, see Jee et al., 2007). However, for the purposes of providing general PSFs for different AO types, our parameterisation method holds merit. The AO parameters are held as a data file in HSIM. As the HARMONI and AO module designs develop the simulated PSFs will become closer to what is expected at the telescope. Thus HSIM can be easily updated with refined PSFs.

We also do not include various systematic effects such as bad detector pixels/columns, or throughput variations between the different IFU optical paths. Adding these effects into HSIM before the instrument design is fully defined would have to be done on an arbitrary basis. Once the instrument design is fixed higher order systematics can be incorporated as necessary. In the next chapters, we use reasonably conservative instrument parameter values when predicting the instrument performance using HSIM.

HSIM is currently being used to explore a wide range of scientific simulations and we briefly summarise some examples here.

- Studies of high redshift, emission-line galaxies: we use HSIM to explore limits on HARMONI's ability to obtain resolved kinematics of galaxies at redshifts from $z = 2$–3 (see Chapter 6).

- Integrated and resolved absorption-line kinematics of high redshift galaxies, generated from high resolution cosmological simulations: we have used an output of the adaptive mesh refinement (AMR) hydrodynamical code RAMSES (Teyssier, 2002) to create an input galaxy data cube at $z = 3$ for which we know the exact input physics. We have simulated the galaxy using HSIM and compared measured kinematics to the inputs (Kendrew et al., 2016). This work will be expanded to explore the possibility of being able to observationally distinguish between different physical prescriptions involved in galaxy formation.

- Supermassive black hole (SMBH) mass measurements: we are exploring the distance at which HARMONI will be able to obtain an accurate SMBH mass within a typical L_* galaxy. This will enable limits to be set on the numbers of galaxies that can have SMBH mass constraints. We are using a multi Gaussian expansion (MGE) code (Emsellem et al., 1994; Cappellari, 2002) to create input data cubes that contain detailed kinematics of the galaxy nuclear region.

- Detection and characterisation of type Ia supernova (SN) in distant galaxies: expanding the distance to which we can observe type Ia SN will help constrain models of dark energy. We are using the galaxy data cube generated from the RAMSES code as above, with a SN spectrum inserted and scaled to the correct redshift. We can then produce mock observations and determine limits on detecting characteristic absorption features, with the added challenge of discerning the SN against the galaxy background.

Chapter 5

Sensitivity predictions with HSIM

In this chapter we utilise HSIM to explore the capabilities of HARMONI for observing point sources. A standard method of demonstrating the performance of an instrument is through limiting magnitudes for a specific observing time within a set aperture. As HSIM outputs mock-observed data cubes and variances from simulations, it is possible to explore sensitivity predictions for the observing configurations of HARMONI as a function of aperture size. This is important in order to determine optimal aperture sizes for each grating owing to the wavelength dependent PSF. It is also possible to explore optimal extraction methods as we have full knowledge of the PSF and we can determine the theoretical gain over standard extraction for the HARMONI observing configurations. Complementary to this, it is also possible and useful to explore noise predictions to understand which noise terms dominate for each observing configuration. This helps astronomers plan observing time more efficiently and understand the limitations on their data.

In this chapter we first present point source sensitivity predictions using HSIM to determine limiting magnitudes. We then present predictions of the noise contributions for these limiting magnitude calculations, which show the noise regimes for each observing configuration of HARMONI. We explore how the extracted S/N depends on aperture size and wavelength and compare standard extraction methods to optimal extraction to quantify the theoretical performance gain from optimal extraction. Lastly, we perform a comparison of visible wavelength performance between HARMONI and the AO-fed narrow field mode of MUSE on the VLT.

5.1 Sensitivity predictions

In this section we present instrument point source sensitivities for several operating configurations of HARMONI as computed using HSIM. We compute the limiting AB magnitude M_{AB} to achieve S/N = 5 per spectral resolution element (2 pixels) after five hours on-source ($T_{\mathrm{exp}} = 900\,\mathrm{s}$, $N_{\mathrm{exp}} = 20$) from a 2 × 2 spaxel aperture. We assume sky subtraction with no penalty to on-source exposure time, using 'nodding-on' or similar techniques. To do this we calculate the S/N for a given M_{AB} after five hours on-source, then compute the multiplicative factor f required to give a M_{AB} that yields S/N = 5. Adding this factor along with $N_{\mathrm{pix}} = 2$ and $N_{\mathrm{spax}} = 4$, Equation 1.15 becomes,

$$\mathrm{S/N} = \frac{f\,N_{\mathrm{obj}}\,T_{\mathrm{exp}}\sqrt{N_{\mathrm{exp}}}}{\sqrt{(f\,N_{\mathrm{obj}} + 2N_{\mathrm{bg}} + 16D_{\mathrm{c}})T_{\mathrm{exp}} + 16\sigma_{\mathrm{R}}^2}}, \tag{5.1}$$

and this is solved for f using the standard quadratic equation where the negative solution is discarded. The S/N is calculated within a 2 × 2 spaxel extraction aperture, although for the 30 × 60 mas scale we upsize to a 120 × 120 mas (4 × 4 spaxel) box. We compare *R*-, *H*- and *K*-bands. For each band we create an input cube containing a point source with a flat spectrum (constant M_{AB}) F_λ,

$$F_\lambda = F_\nu \frac{c}{\lambda^2} \quad \mathrm{erg\,s^{-1}\,cm^{-2}\,\AA^{-1}}, \tag{5.2}$$

where,

$$F_\nu = 10^{-(M_{\mathrm{AB}}+48.6)/2.5} \quad \mathrm{erg\,s^{-1}\,cm^{-2}\,Hz^{-1}}. \tag{5.3}$$

The input cubes are generated with a spatial sampling of 0.4 mas for the 4 × 4 mas output scale and at 1 mas for the 10 × 10, 20 × 20 and 30 × 60 mas output scales. The input cube is generated with ∼ 30 wavelength channels so as to be computationally efficient. The S/N is an average value over all the wavelength channels in the spectrum extracted from the 2 × 2 spaxel box. For each grating we choose wavelength regions minimally affected by sky lines and telluric absorption. The central wavelengths for each input cube are 0.677 μm for *R*-band, 1.76 μm for *H*-band, and 2.145 μm for *K*-band.

These sensitivity calculations are intended to provide a general indication of the performance of the current instrument design. Whilst the instrument parameters (e.g. throughput, dark current, read-out noise) are not set at the minimum specification, we use simple 2×2 spaxel aperture extraction to present reasonably conservative performance estimates. Improved S/N would be obtained using the more rigorous method of optimal extraction (Horne, 1986; Robertson, 1986, also see Section 5.3).

5.1.1 Simulation parameters

We set the following instrument and site parameters so as to provide conservative estimates for the resulting performance.

Site and telescope: We use a Paranal-like site (and telescope) temperature of 280.5 K. Seeing is set to the Cerro Armazones median value of $0.67''$ FWHM at $0.5\,\mu$m. We use the official 39 m E-ELT model, which has a maximum all-glass diameter of 37 m, an obscuration ratio of 0.3, and six spider arms each 0.5 m wide, giving a total collecting area of $A = 932.5\,\mathrm{m}^2$.

For the telescope transmission we have two sets of values available: the per surface reflectivity R for an MgF_2 on Ag/Al coating (B:0.968, V:0971, R:0973, I:0976, z:0.98, J:0985, H:0.988, K:0.99)[1], and the telescope K-band emissivity $\epsilon(= 1 - R)$ for five reflections (M1 through M5), which is set to be no worse than 15 %[2]. Using the $\epsilon_{K,5} = 0.15$ for the total emissivity, and assuming the emissivity fraction is the same for all five surfaces, we get $\epsilon = 1 - (1 - 0.15)^{1/5} = 0.032$ per surface. A model where a fraction f_d of the mirror area is covered with dust (unit emissivity) and the rest is a reflective surface of $R = 0.99$, yields a dust area fraction of $f_\mathrm{d} = 0.032 - 0.01 = 0.022$ per surface. The dust both reduces the reflective area and contributes emissivity in the K-band, whilst only reducing reflectivity at other wavelengths. Thus, for all bands other than K, the actual reflectivity is the coating reflectivity multiplied by $0.99 - 0.022 = 0.978$. Given that HARMONI has two additional mirrors (M6, and the dichroic above the cryostat M7) in its path, and assuming that these two mirrors have the same characteristics as the other telescope mirrors, we get a total K-

---

[1] E-ELT Design Reference Mission technical data - `http://www.eso.org/sci/facilities/eelt/science/drm/tech_data/telescope/`

[2] E-ELT Observatory Top Level Requirements document - Section 5.6

band throughput of $(0.99 \times 0.978)^7 = 79.8$ % for the telescope. The wavelength dependence is then characterised by multiplying the coating reflectivity by the dust free fraction.

The telescope emissivity is related to the transmission as above, assuming that there is no absorptivity at any point in the system. In addition, we have the emissivity from the spiders, which we assume to be unity. The area covered by the spiders is 38.5 m^2 ($\epsilon = 1$), out of the all-glass area of 971 m^2 ($\epsilon = 0.202$), to yield a total reflective area of 932.5 m^2, with an emissivity of 24.4 %, if no attempt is made to mask the emission from the spiders within the instrument. If the spiders were to be masked with a perfectly aligned (rotating) cold pupil stop, the emissivity would drop to 20.2 % (i.e. only that of the seven reflections before the cryostat window). Thus, a cold mask matched to the spiders improves the background by ∼one part in five, for a similar gain in exposure time for K-band observations. However, given that there is likely to be some residual pupil wander, we cannot align a cold pupil mask precisely to the image of the spider arms. If we assume that we have ±1 % pupil wander (fraction of the pupil diameter), then the oversized cold pupil mask reduces the telescope's effective area by an additional 56.9 m^2. Thus, the two realistic options are emissivity of 24.4 % with an area of 932.5 m^2, or an emissivity of 20.2 % with an area of 875.6 m^2. The corresponding sensitivity gain from using an oversized cold pupil mask for K-band observations is typically ~ 0.06 mag in limiting magnitude, while the corresponding hit in transmission for other bands (where emissivity is not an issue) is ~ 0.12 mag. Thus, we conclude that masking the spiders does not provide a large enough benefit, and assume the higher emissivity number in our sensitivity computation.

Instrument: We use a uniform instrument throughput of 35 %. The operating temperature of 120 K means the instrument contributes negligible thermal background.

Detector model: To accurately model the NIR detector noise properties, we have investigated the properties of the KMOS HAWAII-2RG detectors, which are similar to the ones proposed for HARMONI. We use 10 dark frames downloaded from the ESO data archive[3] and calculate the mean and variance for each pixel on the detector. We measure a mean

---

[3] `archive.eso.org`

dark current value of $0.0053\,\mathrm{e^-\,s^{-1}\,pix^{-1}}$. The variance σ^2 encodes the read noise σ_R,

$$\sigma^2 = \sigma^2_\mathrm{dark} + \sigma^2_\mathrm{R}, \tag{5.4}$$

where σ_dark is the noise on the dark current. We compute a read noise of $\sigma_\mathrm{R} = 2.845\,\mathrm{e^-pix^{-1}}$ rms. For the visible CCD detector statistics we adopt a dark current of $0.00042\,\mathrm{e^-\,s^{-1}\,pix^{-1}}$ and read-out noise of $2.0\,\mathrm{e^-\,pix^{-1}}$ based on the MUSE CCDs (D. Ives priv. comm.).

5.1.2 Results

We present the results of sensitivities for LTAO, SCAO, and seeing-limited observations in Tables 5.1, 5.2, and 5.3 respectively. These tables give the estimated limiting magnitudes to achieve S/N $=$ 5 measured from a 2×2 spaxel aperture (4×2 for the 30×60 mas scale). These are separated into visible R-band, and NIR H- and K-bands and for each resolving power. We note that in the current HARMONI design, SCAO does not offer R-band observations as the visible light ($\lambda < 0.8\,\mu$m) is sent to the WFS and used for AO correction.

From Table 5.1 it is clear that in the R-band sensitivity increases with spaxel size. LTAO performance at visible wavelengths is poor, with Strehl ratios of ~ 1 %, so larger spaxels incorporate more object flux. In the H-band the 20×20 mas scale offers slightly improved sensitivity compared to the 10×10 mas scale and $\sim$ 1 mag greater sensitivity compared to the 4×4 mas scale. However, in the K-band, the 10×10 mas is ~ 0.4 mag more sensitive than the 20×20 mas scale. This is due to the increased thermal background in K-band, which penalises the larger spaxel scales.

From Table 5.2 we find that SCAO results in $\sim$ 0.5–0.6 mag improved sensitivity in H-band and $\sim$ 0.3–0.4 mag improvement in K-band over LTAO. Table 5.3 shows that the seeing-limited observation limiting magnitudes are $\sim$ 1.5 mag brighter than LTAO for R-band at the 30×60 mas scale and $\sim$ 2.5 mag brighter for H- and K-bands.

From Tables 5.1 and 5.2 we see that the sensitivity increases from the 4 mas and 30×60 mas scales towards the intermediate 10 mas and 20 mas scales for AO observations. This leads us to determine whether a 15 mas scale would provide the best sensitivity and therefore

Table 5.1: Point source sensitivity predictions for HARMONI with LTAO calculated from a 2×2 spaxel aperture centred on the object. Limiting AB magnitudes to achieve S/N = 5 per spectral resolution element for five hours on-source ($T_{\rm exp} = 900\,{\rm s}$, $N_{\rm exp} = 20$). We assume sky subtraction with no penalty to on-source exposure time. Band column gives the bandpass region, R is the resolving power and the remaining columns give the limiting magnitude for each HARMONI spaxel scale. 4×2 spaxel aperture for 30×60 mas scale.

2 × 2 spaxel aperture (LTAO)

Band	R	4 × 4	10 × 10	20 × 20	30 × 60
R	3500	22.7	23.6	24.3	25.1
H	3500	26.2	27.0	27.0	26.4
	7500	25.2	26.0	26.1	25.7
	20000	24.1	25.0	25.1	24.9
K	3500	25.7	26.3	25.8	24.8
	7500	25.2	25.8	25.4	24.5
	20000	24.2	25.1	24.8	23.9

if the two intermediate scales could be amalgamated to simplify instrument design. We perform the identical calculations for 15 mas and plot the sensitivity as a function of spaxel scale in Figure 5.1. We see that there is no clear gain in sensitivity offered by using 15 mas spaxels and the limiting magnitude in *H*-band plateaus between the 10 mas and 20 mas scales. Therefore there is no motivation for a 15 × 15 mas scale option.

Table 5.4 shows magnitudes for identical LTAO observations to Table 5.1 but after extracting the spectrum from an aperture containing 50 % of the ensquared energy (EE) of the PSF. For the *R*-, *H*- and *K*-bands these correspond to 400 × 400, 140 × 140 and 80×80 mas respectively. We omit values for the 30×60 mas spaxel scale in *K*-band because the 4 × 2 spaxel aperture already contains greater than 50 % of the EE. This table shows that a greater S/N can be achieved in the *R*-band by increasing the aperture size. For the 4×4 and 10×10 mas scales, a factor of ~ 1 mag improvement is gained. However, for both *H*- and *K*-bands, the limiting magnitudes are brighter because the extra spaxels from the larger extraction aperture contribute more detector and background noise for each band respectively, as can be seen from Figures 5.3 and 5.4.

Table 5.2: Point source sensitivity predictions for HARMONI with SCAO calculated from a 2×2 spaxel aperture centred on the object. Limiting AB magnitudes to achieve $\mathrm{S/N} = 5$ per spectral resolution element for five hours on-source ($T_{\mathrm{exp}} = 900\,\mathrm{s}$, $N_{\mathrm{exp}} = 20$). We assume sky subtraction with no penalty to on-source exposure time. Band column gives the bandpass region, R is the resolving power and the remaining columns give the limiting magnitude for each HARMONI spaxel scale. 4×2 spaxel aperture for 30×60 mas scale. Note that there is no *R*-band for SCAO as the visible light is used for AO correction.

2×2 spaxel aperture (SCAO)

Band	R	4 × 4	10 × 10	20 × 20	30 × 60
H	3500	26.8	27.6	27.6	26.8
	7500	25.8	26.6	26.7	26.1
	20000	24.7	25.6	25.7	25.3
K	3500	26.1	26.6	26.2	25.2
	7500	25.6	26.2	25.8	24.8
	20000	24.6	25.4	25.2	24.3

Table 5.3: Point source sensitivity predictions for HARMONI seeing-limited observations calculated from a 4×2 spaxel aperture centred on the object in the 30×60 mas scale. Limiting AB magnitudes to achieve $\mathrm{S/N} = 5$ per spectral resolution element for five hours on-source ($T_{\mathrm{exp}} = 900\,\mathrm{s}$, $N_{\mathrm{exp}} = 20$). We assume sky subtraction with no penalty to on-source exposure time. Band column gives the bandpass region and R is the resolving power.

2×2 spaxel aperture (Seeing-limited)

Band	R	30 × 60
R	3500	23.7
H	3500	23.9
	7500	23.2
	20000	22.4
K	3500	22.2
	7500	21.9
	20000	21.3

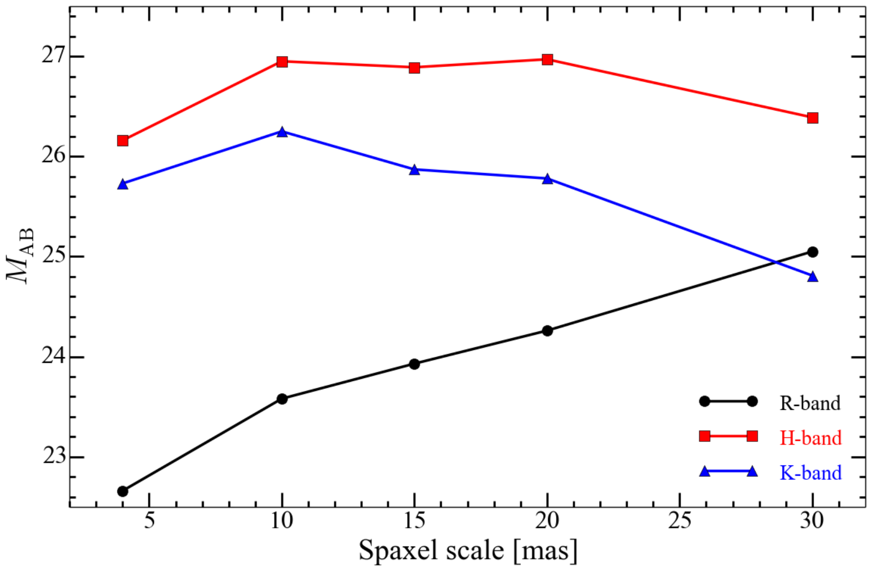

Figure 5.1: Point source sensitivity predictions for HARMONI with LTAO as a function of spaxel scale, for five hours on-source from a 2 × 2 spaxel aperture at $R = 3500$. 30 mas on the x-axis corresponds to the 30 × 60 mas scale. Sensitivity is defined as limiting AB magnitude to achieve S/N = 5 per resolution element for five hours on-source ($T_{\rm exp} = 900\,$s, $N_{\rm exp} = 20$). We also compute the sensitivity at a spaxel scale of 15 mas, between the two current intermediate scales. 15 mas offers no significant gain over 10 or 20 mas spaxels.

Table 5.4: Point source sensitivity predictions for HARMONI with LTAO calculated from a square aperture that encloses 50 % of the ensquared energy (EE) for each band. Limiting AB magnitudes to achieve S/N = 5 per spectral resolution element for five hours on-source ($T_{\rm exp} = 900\,$s, $N_{\rm exp} = 20$). We assume sky subtraction with no penalty to on-source exposure time. Band column gives the bandpass region, R is the resolving power, Aperture column gives the 50 % EE aperture sizes, and the remaining columns give the limiting magnitude for each HARMONI spaxel scale.

50 % EE square aperture (LTAO)

Band	R	Aperture (mas)	4 × 4	10 × 10	20 × 20	30 × 60
R	3500	400 × 400	23.6	24.6	25.1	25.4
H	3500	140 × 140	24.5	25.4	26.0	26.2
	7500		23.5	24.5	25.1	25.6
	20000		22.5	23.4	24.1	24.7
K	3500	80 × 80	24.7	25.1	25.1	-
	7500		24.1	24.6	24.8	-
	20000		23.1	23.9	24.2	-

5.2 Noise regimes

To illustrate the different noise regimes, Figures 5.2, 5.3 and 5.4 show heat maps representing the contributions to the total variance from each source: sky, telescope, dark current, and read-out noise, when observing with LTAO in the R-band, H-band and K-band respectively. Each observing configuration is represented by a single box. Light colours show small contribution and dark colours show larger contribution. For each observing configuration, the boxes show the percentage of the total variance from each source. It is clear from these figures that in the R- and H-bands HARMONI is generally detector read-out noise dominated, except for the 30×60 mas scale combined with the two lowest resolving powers, which are sky dominated. However, in the K-band observations are telescope (thermal) background dominated, except for the finest spaxel scale and highest resolving powers.

5.3 Varying aperture sizes and optimal extraction

The previous sections have shown that a 2×2 spaxel aperture does not necessarily provide the best S/N spectrum when using standard extraction techniques. This is due to the strongly wavelength dependent AO PSFs predicted for the E-ELT. It is particularly evident when comparing Tables 5.1 and 5.4, which show that the R-band limiting magnitude increases when using a larger aperture. Therefore it is useful to determine how the aperture size to obtain peak S/N spectra varies with wavelength. Applying various aperture extraction techniques demonstrates the versatility of HSIM over traditional ETCs.

Naylor (1998) shows that for a background-limited 2D Gaussian source, the ‘best’ aperture size for standard extraction is $\frac{2}{3} \times$ FWHM. The predicted LTAO PSF for the E-ELT has a very small diffraction-limited peak at visible wavelengths, which increases with wavelength, so it is different to a Gaussian. From Figures 5.2, 5.3 and 5.4 only the coarsest scale is normally background limited.

As part of this we also investigate the use of ‘optimal’ extraction methods on IFS data cubes. Optimal extraction for long-slit spectra was first presented by Horne (1986) and Robertson (1986). Naylor (1998) extended the principle to photometry and in principle IFS can be thought of as iterative optimal photometry over many wavelengths. With HSIM we

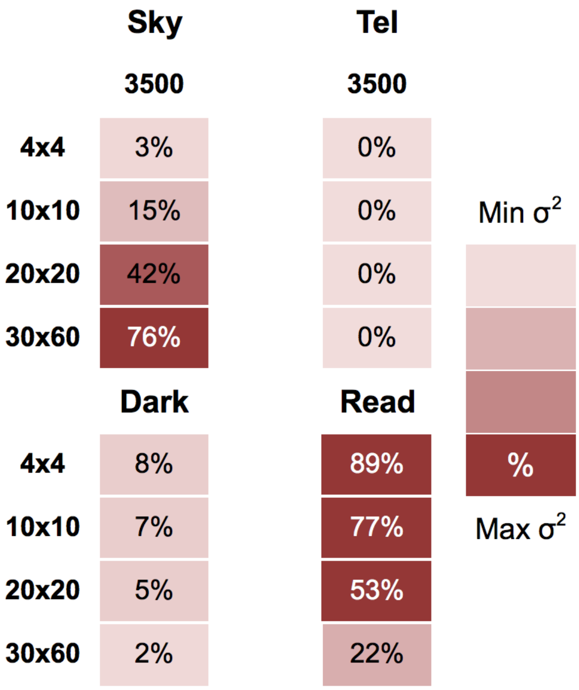

	Sky	Tel
	3500	3500
4x4	3%	0%
10x10	15%	0%
20x20	42%	0%
30x60	76%	0%

	Dark	Read
4x4	8%	89%
10x10	7%	77%
20x20	5%	53%
30x60	2%	22%

Figure 5.2: Heat map showing contributions to the variance for LTAO point source observations in R-band for five hours on-source ($T_{\mathrm{exp}} = 900\,\mathrm{s}$, $N_{\mathrm{exp}} = 20$) after extracting in a 2×2 (4×2 for 30×60 mas scale) spaxel aperture centred on the object. The four quadrants show the contributions to the variance from (clockwise from top left) sky, telescope, read-out noise and dark current respectively for each observing mode of the instrument (spaxel scale and resolving power). The instrument thermal background is assumed to be negligible. Dark colours show a greater contribution and light colours show a smaller contribution. For each instrument configuration, the boxes show the percentage contribution to the total variance. Observations in R-band vary from read-out noise limited at the finest spatial scales to sky limited at the coarsest scale.

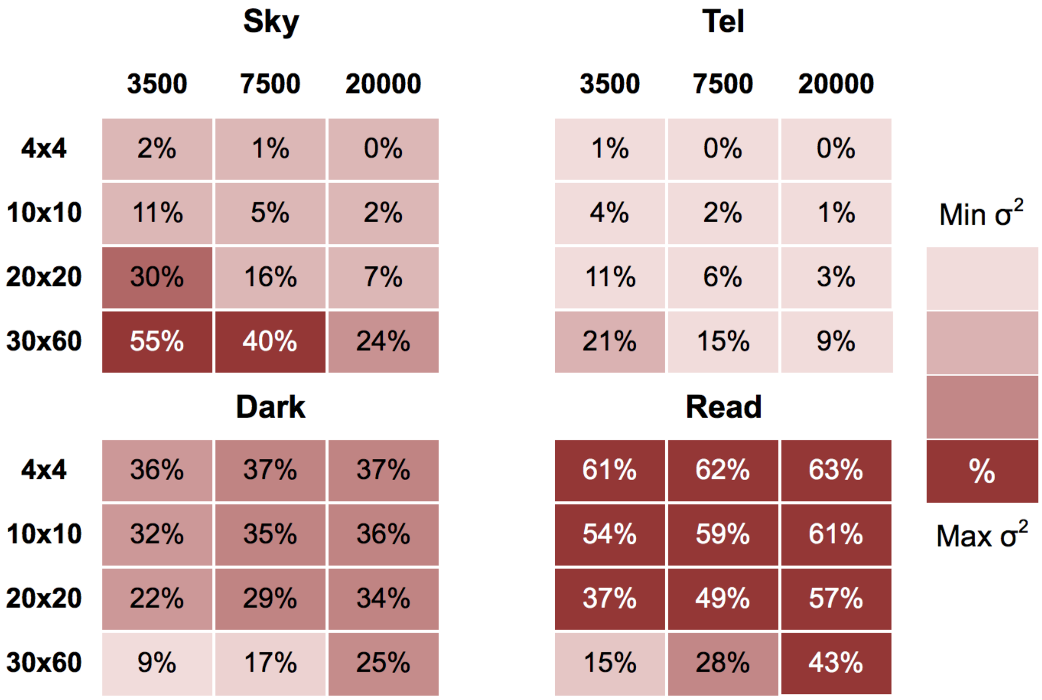

	Sky			Tel		
	3500	7500	20000	3500	7500	20000
4x4	2%	1%	0%	1%	0%	0%
10x10	11%	5%	2%	4%	2%	1%
20x20	30%	16%	7%	11%	6%	3%
30x60	55%	40%	24%	21%	15%	9%

	Dark			Read		
4x4	36%	37%	37%	61%	62%	63%
10x10	32%	35%	36%	54%	59%	61%
20x20	22%	29%	34%	37%	49%	57%
30x60	9%	17%	25%	15%	28%	43%

Figure 5.3: Same as Figure 5.2 but for H-band observations: heat map showing contributions to the variance for LTAO point source observations in H-band for five hours on-source ($T_{\rm exp} = 900\,$s, $N_{\rm exp} = 20$) after extracting in a 2×2 spaxel aperture centred on the object. Observations in H-band are predominately read-out noise limited except at the coarsest spaxel scale and lowest resolving powers which are sky limited.

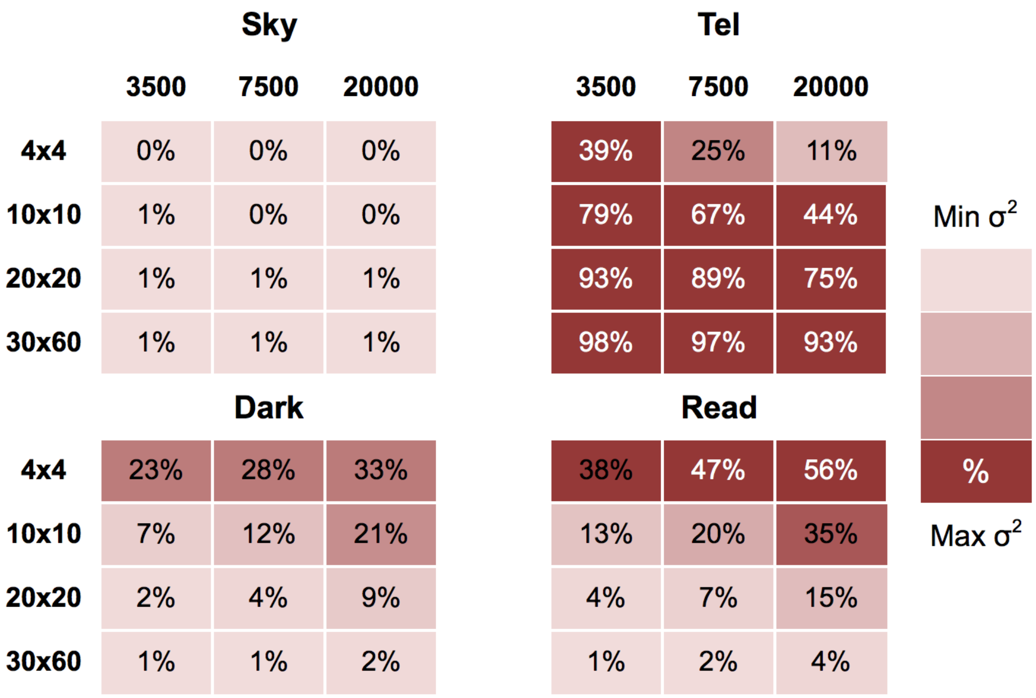

Sky

	3500	7500	20000
4x4	0%	0%	0%
10x10	1%	0%	0%
20x20	1%	1%	1%
30x60	1%	1%	1%

Tel

	3500	7500	20000
4x4	39%	25%	11%
10x10	79%	67%	44%
20x20	93%	89%	75%
30x60	98%	97%	93%

Dark

	3500	7500	20000
4x4	23%	28%	33%
10x10	7%	12%	21%
20x20	2%	4%	9%
30x60	1%	1%	2%

Read

	3500	7500	20000
4x4	38%	47%	56%
10x10	13%	20%	35%
20x20	4%	7%	15%
30x60	1%	2%	4%

Figure 5.4: Same as Figure 5.3 but for K-band observations: heat map showing contributions to the variance for LTAO point source observations in K-band for five hours on-source ($T_{\rm exp} = 900\,$s, $N_{\rm exp} = 20$) after extracting in a 2×2 spaxel aperture centred on the object. Comparing to Figure 5.3 the K-band observations are dominated by the telescope thermal background, except at finest spaxel scale and highest resolving powers which are read-out noise limited.

know the exact PSF, so can create a 'perfect' model with which to scale the image at each wavelength. Naylor (1998) state that optimal photometry offers ~ 10 % gain over standard techniques (for a background-limited 2D Gaussian source). Thus, we are interested to see what level of improvement is offered for HARMONI.

To determine the optimal S/N aperture sizes we generate input data cubes containing a $M_{\mathrm{AB}} = 25$ point source. We again use narrow wavelength regions in-between sky lines. We simulate the cubes for five hours on-source ($T_{\mathrm{exp}} = 900\,\mathrm{s}$, $N_{\mathrm{exp}} = 20$) as before. In the visible wavelength range we use the 30 × 60 mas scale and in the NIR we use the 20 mas, 10 mas and 4 mas scales. We then determine the S/N for different square aperture sizes by calculating the average over all wavelength channels in each narrow data cube.

Figure 5.5 shows the S/N as a function of square aperture size in the $V+R$ band for both LTAO and seeing-limited observations. It is clear that the AO offers a small improvement in S/N for wavelengths $>\sim 0.65\,\mu$m ($\sim \lambda_{\mathrm{H}\alpha}$). At $\lambda = 0.77\,\mu$m this is ~ 6 %. The peak aperture sizes for LTAO are around 400 mas, which corresponds to the 50 % EE aperture used for Table 5.4. Figures 5.6, 5.7 and 5.8 show standard versus optimal extraction for three regions in the $H + K$ band for the 20 mas, 10 mas and 4 mas scales respectively. It is clear that for standard extraction in the NIR, a 2 × 2 spaxel aperture gives the peak S/N, except in the 4 mas scale for which a 4 × 4 spaxel aperture gives peak S/N. We also see that optimal extraction gives ~ 10 % improvement in S/N in agreement with Naylor (1998). The maximal S/N falls as a function of wavelength in the $H + K$ band due to the increasing telescope thermal background.

5.4 Comparison with MUSE narrow field mode

in this section a comparison is made between the AO performance of MUSE narrow field mode (NFM) on the VLT and HARMONI with LTAO on the E-ELT at visible wavelengths. The MUSE AO system on the VLT has an actuator spacing (as projected onto M1) of 20 cm compared to the E-ELT's 50 cm spacing, so MUSE is predicted to offer better AO performance at visible wavelengths. However, the E-ELT has a factor of ~ 18 greater collecting area and ~ 5 greater diffraction limited angular resolution. We use simulated PSFs and

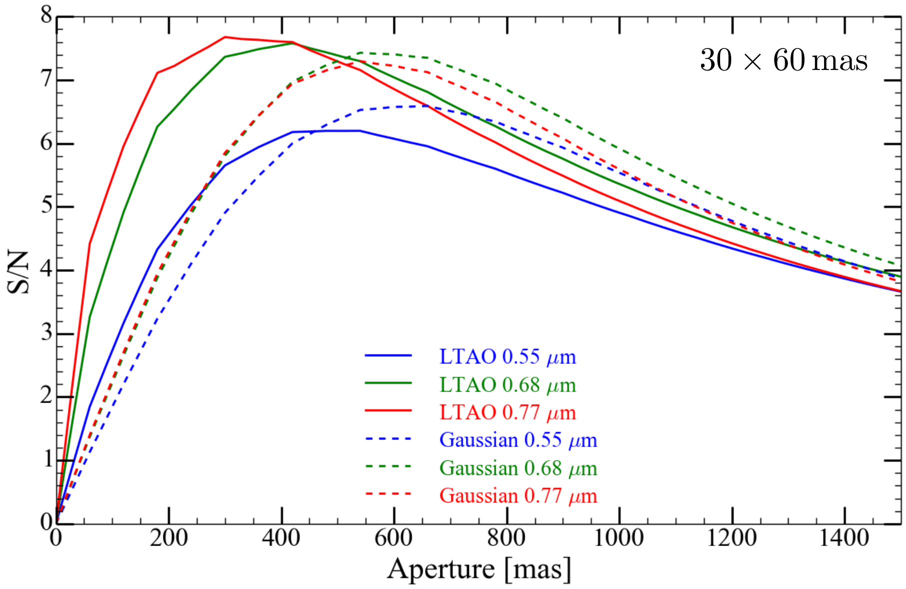

Figure 5.5: S/N as a function of aperture size for LTAO (solid lines) and seeing-limited (dashed lines) observations at three visible wavelengths in 30 × 60 mas scale. Wavelengths are 0.55 μm (blue), 0.68 μm (green), and 0.77 μm (red).

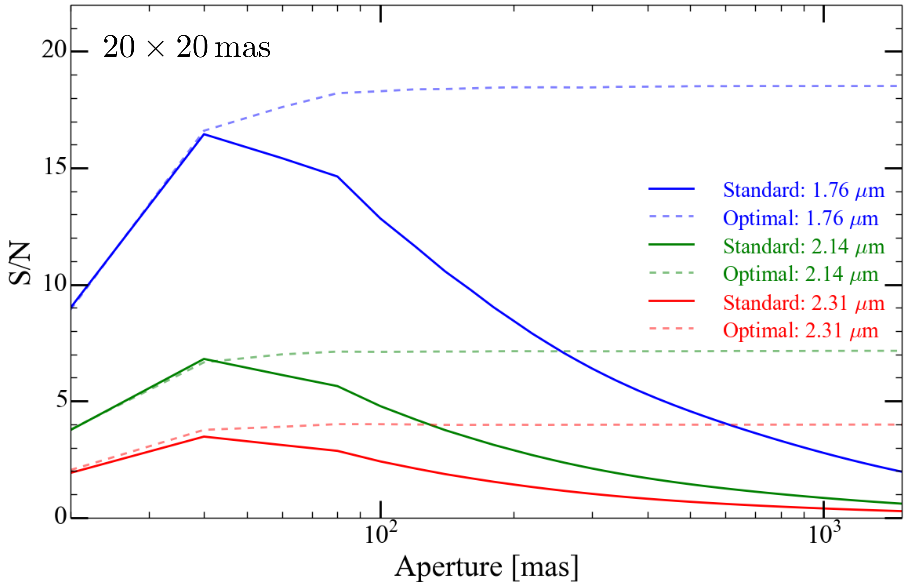

Figure 5.6: S/N as a function of aperture size for LTAO observations in the $H + K$ wavelength range using both standard (solid lines) and optimal extraction (dashed lines) in 20 mas scale. The three wavelengths are 1.76 μm (blue), 2.14 μm (green), and 2.31 μm (red).

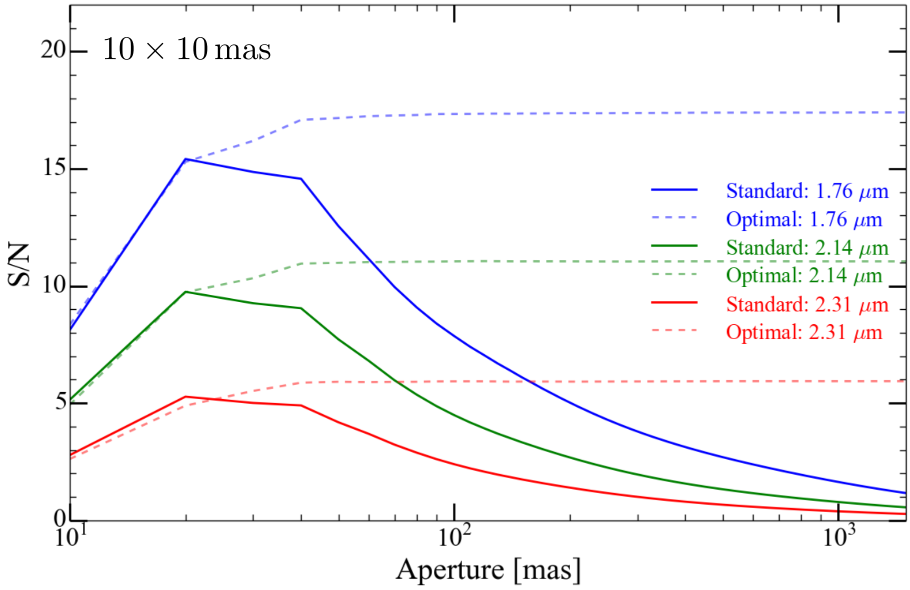

Figure 5.7: S/N as a function of aperture size for LTAO observations in the $H + K$ wavelength range using both standard (solid lines) and optimal extraction (dashed lines) in 10 mas scale. The three wavelengths are 1.76 μm (blue), 2.14 μm (green), and 2.31 μm (red).

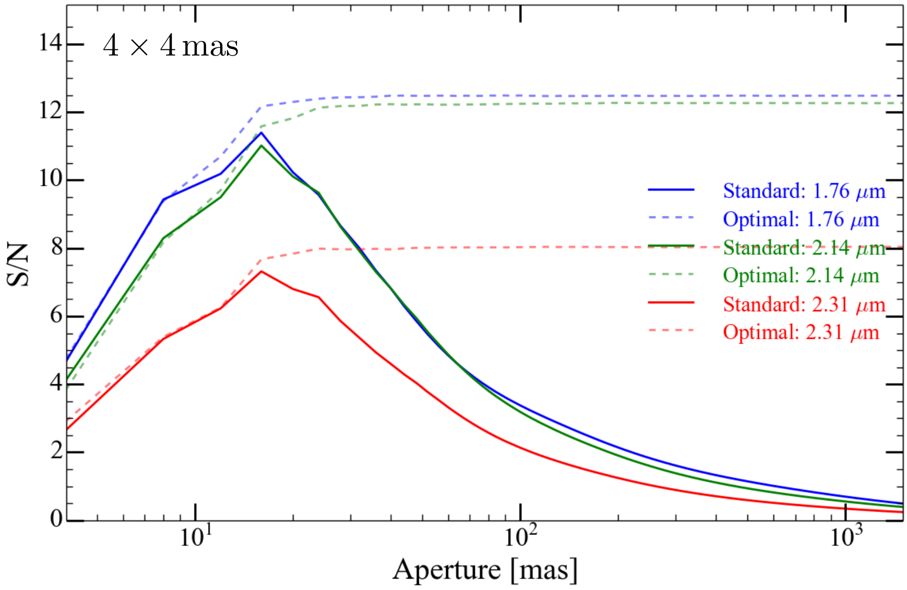

Figure 5.8: S/N as a function of aperture size for LTAO observations in the $H + K$ wavelength range using both standard (solid lines) and optimal extraction (dashed lines) in 4 mas scale. The three wavelengths are 1.76 μm (blue), 2.14 μm (green), and 2.31 μm (red).

Table 5.5: Details of the MUSE-NFM and HARMONI-LTAO PSFs used for visible performance comparison.

	MUSE	HARMONI (HSIM)	HARMONI (05-11-15)
AO	LTAO	LTAO	LTAO
$\lambda\,(\mu$m)	0.5, 0.65, 0.9	0.5, 0.65, 0.9	0.66
Seeing (arcsec)	0.6	0.73	0.70
r_0 at 0.5 μm (cm)	17	15	15
Off-axis distance (arcsec)	0	0	0
rms jitter (mas)	-	3	2
#LGS	4	6	6
Asterism radius (arcsec)	10	60	30

compare their properties, before utilising these to make predictions on point source sensitivities. We refer to the VLT-MUSE-NFM PSFs as MUSE and E-ELT-HARMONI-LTAO PSFs as HARMONI throughout this section.

We use three sets of PSFs: one set of MUSE PSFs generated by M. Le Louarn (21-01-2009) covering three wavelengths ($0.5, 0.65, 0.9\,\mu$m), one set of HARMONI PSFs generated by T. Fusco as used for HSIM covering the same three wavelengths, and a new HARMONI PSF generated at Hα ($0.66\,\mu$m) by T. Fusco (05-11-2015). The full details of the three sets of PSFs are shown in Table 5.4.

One dimensional radial profiles of the PSFs are shown in Figure 5.9. Each PSF is normalised so the sum is unity and the PSFs are sampled at 5.03, 6.54 and 9.06 mas for 0.5, 0.65/0.66 and 0.9 μm respectively. It is clear that the MUSE PSFs have greater energy in the diffraction-limited core and smaller seeing halo compared to the HARMONI PSFs. However, the diffraction-limited cores of the HARMONI PSFs have much smaller FWHMs compared to the MUSE PSFs. Our measurements of the FWHM are shown in Table 5.6. We also show SRs in Figure 5.10 and EEs within different box sizes in Figure 5.11. MUSE PSFs have higher EE and SR for every wavelength, except at 0.9 μm and 4 mas spaxels when the HARMONI PSF yields the same EE.

5.4.1 Results

We use the EEs to predict point source limiting AB magnitudes for the two instruments. We use the same values for the sky and thermal backgrounds, and telescope, instrument and

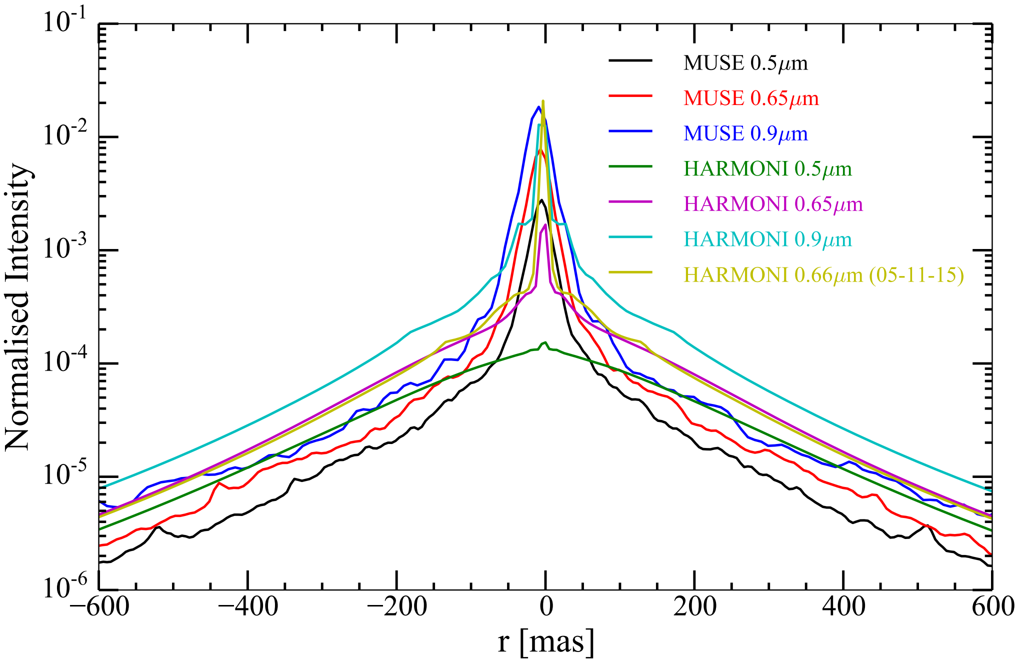

Figure 5.9: Radial profiles of HARMONI and MUSE visible LTAO PSFs. All PSFs are normalised so the sum is unity and are sampled so that PSFs of the same wavelength have the same sampling. These correspond to 5.03, 6.54 and 9.06 mas for 0.5, 0.65/0.66 and 0.9 μm respectively.

Table 5.6: FWHM in mas of the diffraction-limited cores of HARMONI and MUSE visible LTAO PSFs.

λ (μm)	MUSE	HARMONI (HSIM)	HARMONI (05-11-15)
0.5	26.7	6.3	
0.65/0.66	27.2	6.8	4.9
0.9	30.3	7.0	

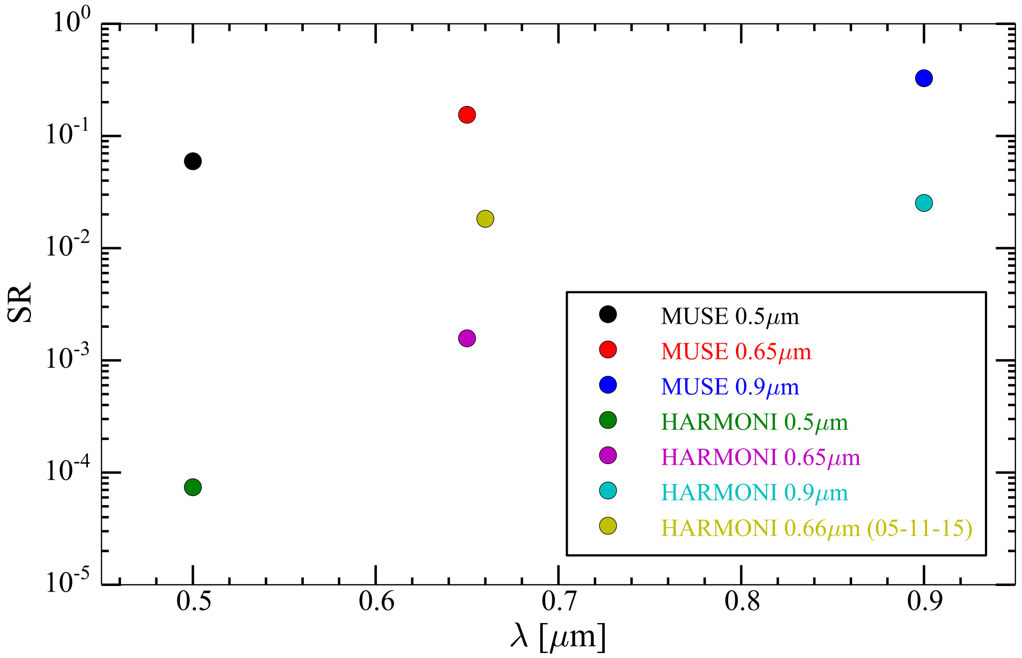

Figure 5.10: Strehl ratios of HARMONI and MUSE visible PSFs. All PSFs are normalised so the sum is unity and are sampled so that PSFs of the same wavelength have the same sampling as in Figure 5.9.

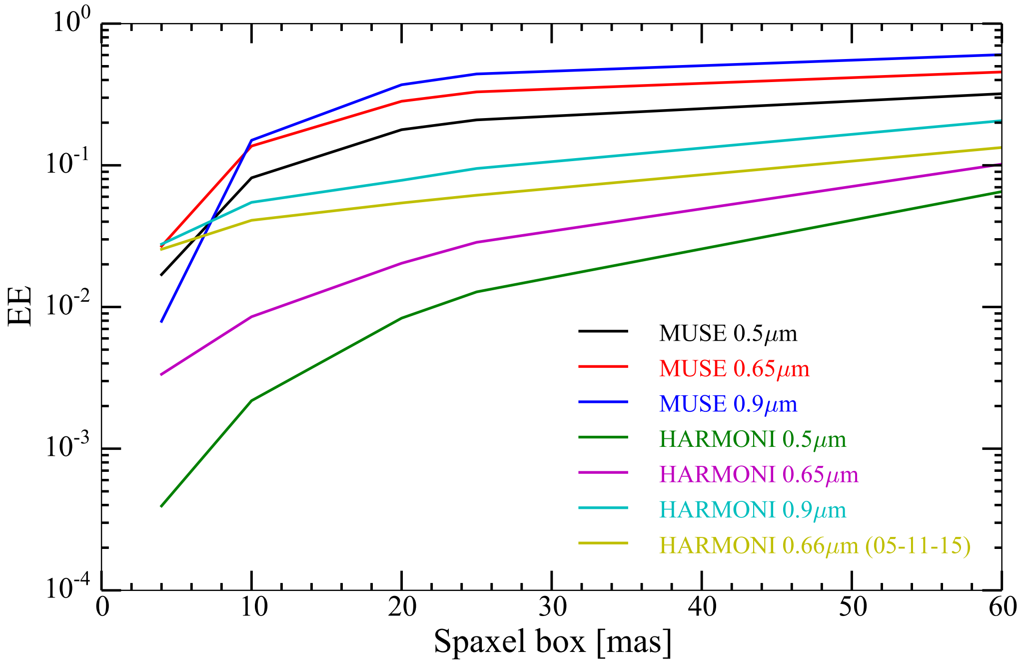

Figure 5.11: Ensquared energies of HARMONI and MUSE visible PSFs. All PSFs are normalised so the sum is unity and are sampled so that PSFs of the same wavelength have the same sampling as in Figure 5.9.

detector throughputs as used in HSIM (Section 5.1.1). We assume these are the same for both VLT-MUSE and ELT-HARMONI and we assume both instruments operate at a spectral resolving power of R = 3500. We use a telescope mirror area of 52.1 m^2 for the VLT. For MUSE, and HARMONI for $\lambda < 0.8\,\mu$m, we use a dark current of $0.00028\,\mathrm{e}^-\,\mathrm{s}^{-1}\,\mathrm{pix}^{-1}$ and read-out noise of $2.0\,\mathrm{e}^-\,\mathrm{pix}^{-1}$ for all wavelengths[4]. We compute the point source limiting AB magnitude to achieve S/N = 5 in five hours on-source with $T_{\mathrm{exp}} = 900\,\mathrm{s}$ and $N_{\mathrm{exp}} = 20$. Figure 5.12 shows the results for each wavelength/PSF as function of the aperture box size in mas. For MUSE we use 25 mas spaxel steps and for HARMONI 20 mas steps to emulate the spaxel scales of both of these instruments.

From Figure 5.12 it can be seen that in a 2 × 2 spaxel box, the HSIM HARMONI PSFs only start to win at wavelengths longer than $0.65\,\mu$m. However, it is possible to integrate over a larger aperture size to achieve a much fainter limiting magnitude with the shorter wavelengths. However, the new HARMONI Hα PSF with slightly smaller windshake jitter and smaller laser asterism radius (and simulated in better seeing) presents a large improvement over the old HARMONI PSFs and the MUSE PSFs for all aperture sizes. Within a 2 × 2 spaxel box, it gains a magnitude extra sensitivity over MUSE.

5.5 Discussion and conclusions

We have used HSIM to predict the point source sensitivity of HARMONI using a standard metric of limiting magnitude to achieve a S/N = 5 in five hours observing on-source from a 2 × 2 spaxel aperture. For LTAO and SCAO observing, the 10 and 20 mas scales offer the best sensitivity except in the visible, which is best at the coarsest scale. We show that the sensitivity in the visible range can be improved by using a larger aperture than 2 × 2 spaxels. We check to see whether a 15 mas scale offers optimum sensitivity in-between the 10 and 20 mas scales, but find no evidence for this.

We investigate the dominating noise source for each of the instrument's operating modes. We find that in the *R*- and *H*-bands, observations are predominately read-out noise limited, except at the coarsest spaxel scale and lowest resolving powers, which are sky limited.

---

[4] The lower dark current represents a slightly more optimistic value of the MUSE CCDs compared with the value we have used in the earlier HARMONI sensitivity predictions (D. Ives priv. comm.).

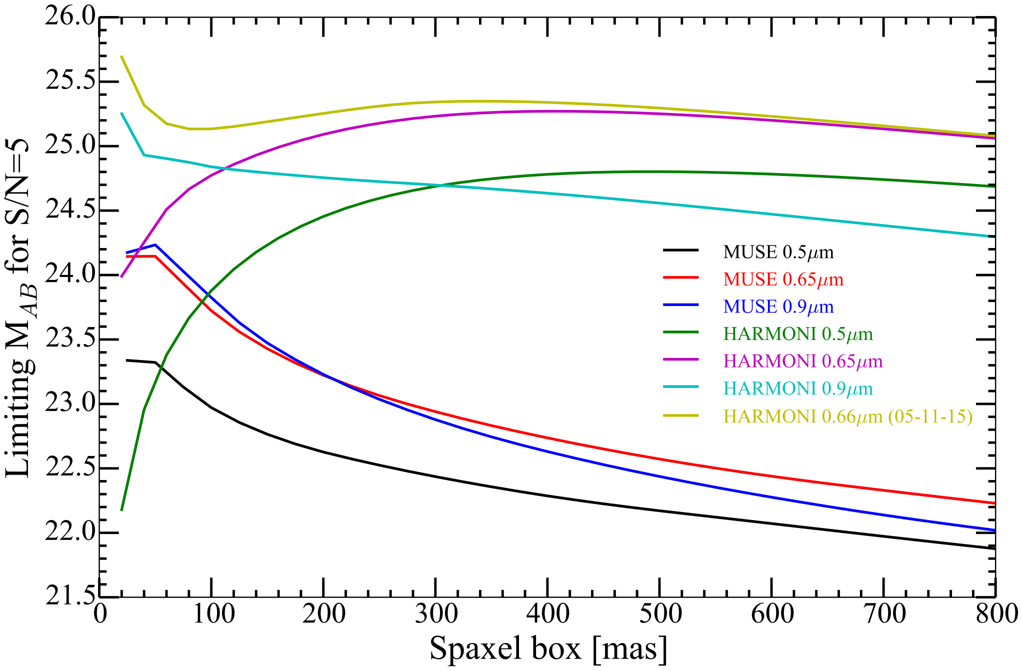

Figure 5.12: Limiting AB magnitudes to achieve S/N = 5 in five hours on-source exposure time ($T_{\mathrm{exp}} = 900\,\mathrm{s}$, $N_{\mathrm{exp}} = 20$) as a function of aperture box size in mas, for both HARMONI and MUSE in the visible.

However, the K-band is dominated by the telescope thermal background, except at the finest spaxel scale and highest resolving powers, which are read-out noise limited. As the majority of operating configurations are read-out noise limited, this result demonstrates that the choice of detectors will play a role in the capabilities offered by HARMONI. An improved read-out noise will improve the sensitivity for the majority of operating modes. However, the coarsest scale is currently sky-limited so a reduction in the size of the coarsest spaxels would move it towards the read-out limited regime and consequently reduce the sensitivity of that mode. This has implications for any potential change in detectors for HARMONI.

We then investigate varying aperture sizes for LTAO observations and a comparison with optimal extraction methods. We find that LTAO offers an improvement for visible wavelengths $> \lambda_{\mathrm{H}\alpha}$ ($0.65\,\mu$m), and the aperture size to achieve the highest S/N for standard extraction is around 400×400 mas. At NIR wavelengths we find that a 2×2 spaxel aperture offers the highest S/N for standard extraction at the 10 mas and 20 mas scales (4×4 spaxel for 4 mas scale) and we find a ~ 10 % improvement in S/N from using optimal extraction, in agreement with previous studies.

Lastly, we compare the AO performance of MUSE-NFM on the VLT with HARMONI and LTAO on the E-ELT, at visible wavelengths. Below $\lambda_{\mathrm{H}\alpha}$ there is no predicted gain from HARMONI over MUSE due to the poor performance of the LTAO. At $\lambda_{\mathrm{H}\alpha}$ and longer HARMONI starts to win against MUSE both with greater diffraction-limited resolution in the core of the PSFs and with better point source sensitivity, due to the much greater mirror diameter. A new HARMONI-LTAO PSF with a smaller laser guide star asterism radius presents a large improvement over the original PSFs (although simulated in lower seeing and with lower windshake jitter) and gives at least a magnitude gain in sensitivity at $H\alpha$ compared to MUSE. Therefore, HARMONI holds a strong advantage over MUSE at Hα and longer wavelengths and thus should offer capability in this wavelength region.

Chapter 6

Simulations of high redshift emission-line galaxies

6.1 Goals and methodology

In this chapter we present a set of HSIM simulations to investigate HARMONI's ability to detect and measure kinematics of emission-line galaxies at redshifts of $z \sim 2$–3, which represents the peak epoch of star formation. Our goals are to:
(i) determine how well the global kinematics (e.g. rotation curves) can be derived as a function of star formation rate (SFR), size and morphology for galaxies at $2 \leq z \leq 3$;
(ii) determine the smallest physical scales for which physical properties can be derived, including identifying/measuring the properties of individual star-forming regions.

To demonstrate the use of our simulation pipeline in this area, we present results from a set of simulated observations of a sample of emission-line galaxies at $2 \leq z \leq 3$. We focus on galaxies with prominent Hα emission, which falls into the K-band at these redshifts, although we also use [OII] as a tracer of star formation at higher redshifts. We highlight that our simulations are not designed to test galaxy formation models; rather they are designed to test how well-measured properties (e.g. rotation curves, clump properties) can be derived for a given line flux and exposure time (and at a given spatial resolution) using a reasonable input galaxy image/spectrum with a set of disc and clump scaling relations.

In the rest of this chapter, we discuss how we construct mock data cubes, our simulation runs, analysis methods and derived conclusions for this science case.

6.2 Input data cubes

Generating realistic input data cubes is a vital component for gaining useful output information from a simulation. In order to obtain quantitative predictions from simulations of galaxies at high redshifts, we need to ensure that the morphologies and kinematic distributions are reasonably realistic up to the resolutions that current instruments can achieve. As HARMONI on the E-ELT is expected to reach far higher spatial resolutions, some assumptions do need to be made on sub-kpc scales.

In order to minimise bias in our results, we pursue two methods for generating the input data cubes. The first method, led by M. Swinbank, uses analytical models for generating the morphology of the galaxies and the second method uses Hα maps of local galaxies as morphological templates. We describe both approaches here.

6.2.1 Analytical models

We generate a sample of input galaxy data cubes covering a range of star formation rates, redshifts and morphologies ranging from smooth exponential discs of gas and stars to ‘clumpier’ galaxies (gas follows stars in each case). Each galaxy data cube is generated with values randomly picked from a range of uniformly distributed physical parameters: redshift z (2.0–3.0), total disc SFR (1–200 $\mathrm{M}_\odot\,\mathrm{yr}^{-1}$), gas fraction (0.1–0.9), inclination (20–70 deg), position angle (0–360 deg), reddening A_v (0–1.5 mag), half-light radius r_{hl} (0.5–2.5 kpc), disc intrinsic velocity dispersion (15–40 $\mathrm{km\,s}^{-1}$) and metallicity ($Z = 0.05$–$1\,Z_\odot$). The underlying light profile of the galaxy disc follows an exponential profile, and the velocity field follows a simple *arctan* model (Courteau, 1997),

$$v(r) = v_{\mathrm{max}} \frac{2}{\pi} \arctan\left(\frac{r}{r_{\mathrm{p}}}\right), \tag{6.1}$$

where $v_{\max}$ is the asymptotic maximum velocity and $r_{\rm p}$ defines the transition between the rising and flat parts of the curve. To relate SFR to Hα luminosity we use the star formation law of Kennicutt (1998b),

$$\mathrm{SFR}\,[\mathrm{M}_\odot\,\mathrm{yr}^{-1}] = \frac{7.9\times10^{42}}{1.7}\mathrm{L}_{\mathrm{H}\alpha}, \tag{6.2}$$

where $L_{\mathrm{H}\alpha}$ is the luminosity of Hα in erg s^{-1} and the factor of 1.7 converts to a Chabrier (2003) IMF from the Salpeter (1955) form.

We also add a number of star-forming regions using scaling relations inferred from observations of lensed star-forming galaxies at $z \sim 1$–3 (e.g. Jones et al., 2010; Livermore et al., 2012, 2015). The number of star-forming clumps is set using the redshift dependent clump luminosity function from Livermore et al. (2012, 2015), where the normalisation is a function of the disc gas fraction and ranges from 0.01–2. The clump gas velocity dispersions σ, radii r and luminosities L use the scaling relations from Swinbank et al. (2012a) and Livermore et al. (2015),

$$\log\left(\frac{r}{\mathrm{pc}}\right) = 1.01\log\left(\frac{\sigma}{\mathrm{km\,s^{-1}}}\right) + 0.8, \tag{6.3}$$

$$\log\left(\frac{L}{\mathrm{erg\,s^{-1}}}\right) = 3.81\log\left(\frac{\sigma}{\mathrm{km\,s^{-1}}}\right) + 34.7. \tag{6.4}$$

Finally, we include stellar continuum assuming a constant star formation history (with an integral that matches the dynamical mass after accounting for gas fraction). We use a solar metallicity Maraston (2005) SSP model with a Chabrier (2003) IMF to derive the stellar continuum and assign this uniformly to the disc according to its luminosity profile.

We ensure that appropriate cosmological dimming is applied to the flux from all components when moving to the given redshift. Starting with flux conservation,

$$\lambda_{\rm o}F_{\lambda_{\rm o}} = \lambda_{\rm e}F_{\lambda_{\rm e}} = \lambda_{\rm e}\frac{L_\lambda(\lambda_{\rm e})}{4\pi D_{\rm L}^2}, \tag{6.5}$$

where λ is the wavelength, F_λ is the flux, the subscripts o and e denote observed and emitted respectively, and $D_{\rm L}$ is the luminosity distance. We thus determine the scaling factor as a function of D_{L} and z as,

$$F_{\lambda_{\mathrm{o}}} = \frac{1}{1+z}\frac{1}{4\pi D_{\mathrm{L}}^2} L_{\lambda}\left(\frac{\lambda_{\mathrm{o}}}{1+z}\right). \tag{6.6}$$

For the purposes of this analysis, we generate these input cubes with a spatial sampling of 10×10 mas and a resolving power of $R = 10{,}000$ with narrow wavelength coverage around the Hα and nitrogen [N II] doublet.

6.2.2 Morphological templates

For the second method we take a small sample of Hα images from the SIRTF Nearby Galaxies Survey (SINGS) (Kennicutt et al., 2003) as morphological templates. SINGS is a spectroscopic and imaging survey of 75 nearby galaxies (maximum distance 30 Mpc) covering a diverse range of morphologies and luminosities. From this we select several compact galaxies with clumpy-disc morphologies observed in Hα with the CFHT. These galaxies have a complex distribution of smaller clumps, which form a disc morphology. We make the assumption that these galaxies represent morphologies that exist at higher redshifts and thus offer high resolution templates. We use the input image sampling, total image extent and galaxy initial redshift to compute the physical size in kpc. We determine the new sampling scale according to the angular diameter distance D_{A} at the output redshift,

$$D_{\mathrm{A}}(z) = \frac{x}{\theta}, \tag{6.7}$$

which, when x is in kpc and θ is converted from radians to arcsec, yields the kpc/arcsec scaling factor. We also scale the galaxies to have a radius of $r \sim 2$–2.5 kpc, which from van der Wel et al. (2014) is close to the average size at $z \sim 2$–3. We use the calculator of Wright (2006) to compute D_{A} and D_{L} for our assumed cosmology and the given redshift. For example, the (600,600) SINGS image of NGC0337 ($z_{\mathrm{in}} = 0.0055$) is sampled at 430 mas pixel^{-1} giving a total image extent of 29 kpc and galaxy radius of 7.3 kpc when $D_{\mathrm{A,z_{in}}} = 0.113$ kpc arcsec^{-1}. We then rescale the image so the galaxy radius becomes ~ 2.5 kpc and recompute the new sampling size at $z = 2$ using $D_{\mathrm{A,z=2}} = 8.37$ kpc arcsec^{-1} to give 2.0 mas pixel^{-1}. Assuming these galaxies follow the star forming galaxy main sequence

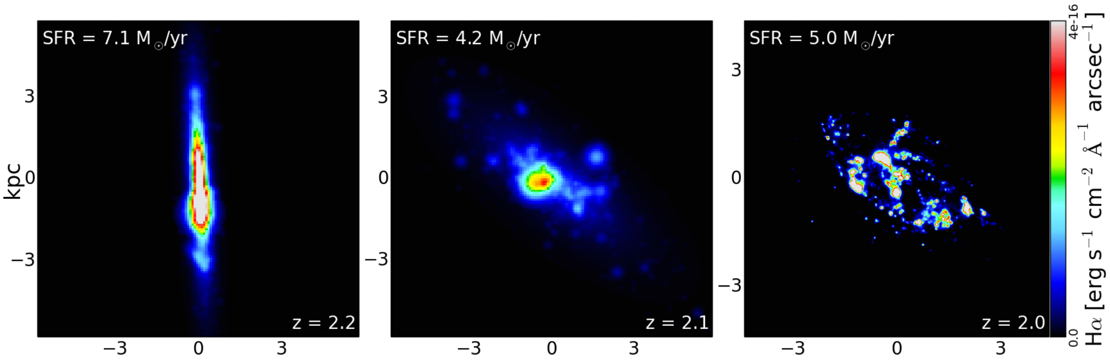

Figure 6.1: Integrated Hα flux maps from three input data cubes representing the two different generation methods. The left and middle images are disc-like and clumpy galaxies generated using analytical methods. The right-hand image is a data cube created using a SINGS Hα image (NGC0337) as a morphological template. Redshifts and SFRs for each galaxy are shown in each sub-panel. The left and middle galaxies are generated at 10 mas spaxel^{-1} and the right-hand galaxy at 2 mas spaxel^{-1}.

from Rodighiero et al. (2011) we assign stellar masses as a function of SFR.

We then add a velocity field using Equation 6.1 and an inclination from the ratio of semi-major and minor axes. The velocity dispersion distribution is added according to the clump sizes using Equation 6.3, where the clumps are determined by running CLUMPFIND on the input image (see Section 6.5). The images are scaled by the total SFR, which is converted to flux using Equation 6.2 with cosmological dimming applied using Equation 6.6. We use the same wavelength range and resolving power as with the analytical data cubes. We create a set of these input data cubes covering redshifts of $z = 2$–3 in Hα and $z = 4$ in [OII], assuming [OII] has half the line strength of Hα. We show example Hα maps of input data cubes from the two methods in Figure 6.1.

6.3 Simulation runs

We simulate a series of mock LTAO-assisted HARMONI observations of these galaxies. We adopt $T_{\mathrm{exp}} = 900\,\mathrm{s}$ per exposure and use the $R \sim 3500$ $H + K$ grating. We focus on simulations at the 20×20 mas (~ 200 pc at $z = 2$–3) scale unless otherwise stated. Both the 20 and 10 mas scales offer sufficient field of view to perform on-sky nodding and thus there is no penalty in observing time from needing separate sky exposures. The pipeline parameters (site, telescope, instrument and detector) are all set identically to those used for the sensitivity calculations (see Section 5.1.1). For the global kinematics we only look at the smooth-disc analytical data cubes. For the detailed kinematics we use clumpy galaxies from both the analytical model and template morphology methods.

6.4 Global kinematic measurements

In Figure 6.2 we show the recovered Hα flux distribution and gas kinematics for a sample of five smooth-disc galaxies assuming a 10 hour on-source integration. We use a Gaussian fitting routine to fit the Hα (and [NII]) emission lines spaxel-by-spaxel. This routine iterates over each spaxel and fits both the continuum (with a linear model) and Gaussian profiles to the spectrum. In cases where no fit is made due to insufficient S/N, we average over the surrounding spaxels to increase signal at the expense of spatial resolution. For the velocity maps, which show the global gas kinematics, we average over a 3×3 spaxel box, giving a varying resolution of 20 mas in the bright regions to 60 mas in fainter regions. We use a S/N $= 7$ threshold for detection of an emission line.

From Figure 6.2 we see that HARMONI is capable of measuring velocity profiles in $z \sim 2$ galaxies down to almost Milky Way-like star-formation rates on scales of at least ~ 200 pc (in the brightest/highest S/N regions) in this integration time. In Figure 6.3 we show the rotation curves for galaxy B (extracted along a ~ 1 kpc wide slit aligned along the semi-major axis) for the same galaxy properties, but with a star-formation rate of 3.5, 7 and 14 $\mathrm{M}_\odot\ \mathrm{yr}^{-1}$ (increasing left to right). This galaxy has the steepest rotation velocity from our sample so gives the best indication of which regions can be recovered for a small range of quiescent star-formation rates. It also shows the effect limited spatial resolution can have on tracing the inner part of the rotation curve ('beam smearing', see e.g. Davies et al., 2011). The velocity profile is traced very closely by HARMONI at 20 mas sampling through the central part of the galaxy for all SFRs. The intrinsic half-light radius of this galaxy is $r_{\mathrm{hl}} = 1.3$ kpc so the curve is recovered out to $3r_{\mathrm{hl}}$ for an SFR of 3.5 $\mathrm{M}_\odot\,\mathrm{yr}^{-1}$, which increases to $4.6r_{\mathrm{hl}}$ for a four-fold increase in SFR.

In Figure 6.3 we also show the rotation curve for a 1 hour on-source E-ELT (HARMONI) observation at the coarser 30×60 mas scale (blue squares), which has been binned up to 60×60 mas spaxels. Comparing this to the rotation curve derived from a simulated 10 hour on-source VLT (SINFONI) observation at 100 mas we see that the E-ELT offers higher resolution data at better sampling with 10× greater efficiency in observing time. For equal observing time the VLT curve underestimates the true curve at all radii and also only extends to $3r_{\rm hl}$, compared with $4.2r_{\rm hl}$ from HARMONI at 20 mas sampling. It is possible to derive a simple estimate of the dynamical mass $M(r)$ within a given radius from,

$$M(r) = \frac{v_{\rm max} r}{G}, \tag{6.8}$$

where $v_{\rm max}$ is the peak velocity and G is the gravitational constant. Deriving dynamical mass estimates from each observation gives $\sim 9 \times 10^9\,{\rm M}_\odot$ from E-ELT (HARMONI) and $\sim 4 \times 10^9\,{\rm M}_\odot$ from the VLT (SINFONI) simulation. Comparing to the input value of $8.6 \times 10^9\,{\rm M}_\odot$ this represents both an accurate estimate and a factor of two improvement by HARMONI after 10 hours observing. From these simulations we find that the E-ELT with HARMONI offers a ten fold improvement in observing efficiency compared to current telescopes, i.e. the E-ELT could observe ten times as many objects in equal on-source observing times. It also offers improved sensitivity and finer resolution, with five times more independent data points at the 20 mas scale, for equal observing times on the same object.

6.5 Detailed kinematics

The fine spatial sampling of HARMONI coupled with LTAO will allow for very detailed observations of $z \sim 2$ galaxies. In Figure 6.4 we show the observed Hα intensity and velocity dispersion maps for the clumpy galaxies in our simulations. To maintain the high spatial resolution required for detecting individual star forming regions we average over a 2×2 spaxel box where no fit is made to the emission lines, giving an effective resolution of 40 mas (~ 300 pc) in fainter regions, and again use a $\mathrm{S/N} = 7$ threshold for detection of an emission line. As Figure 6.4 shows, detailed structure is seen in both the Hα emission maps

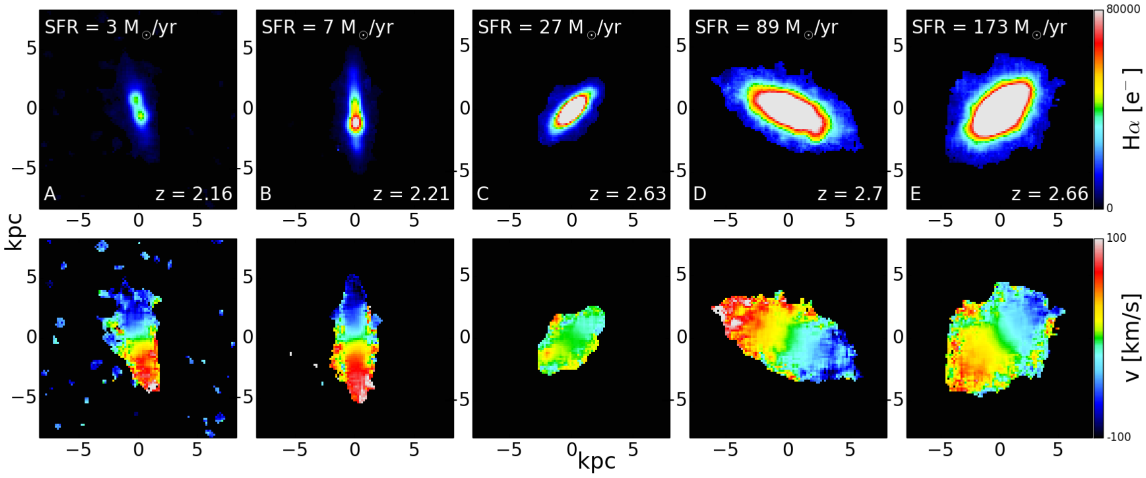

Figure 6.2: Maps of Hα flux (top row) and line-of-sight gas velocity (bottom row) for smooth disc galaxies. Galaxies are ordered in increasing SFR from left to right. Also shown is the redshift of each galaxy. All galaxies are observed for 10 hours at the 20×20 mas (~ 200 pc) scale. Velocity gradients are easily measured even for the lowest SFRs with a factor of ~ 5 improvement in resolution over existing instruments in the highest S/N regions.

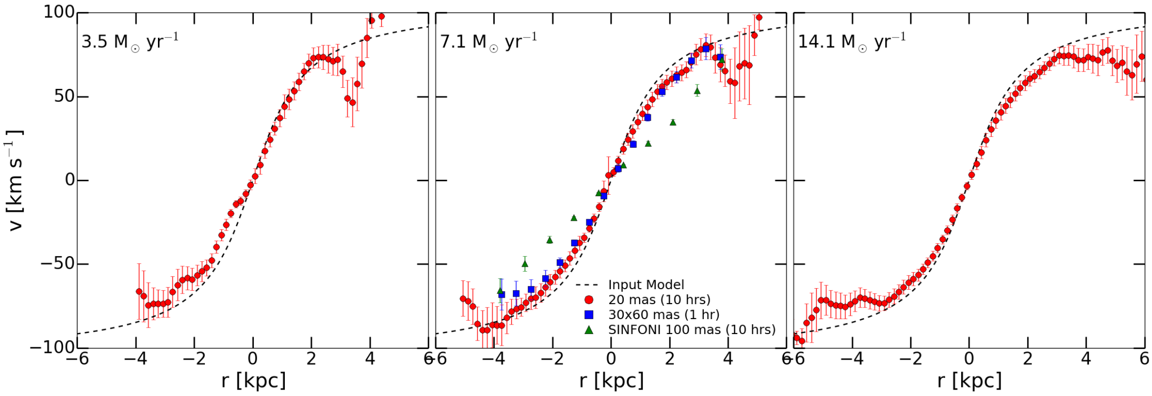

Figure 6.3: Rotation curves for smooth disc galaxy B with varying SFR (increasing left to right) at 20 mas scale (red circles) as observed by the E-ELT with HARMONI. The input model curve is shown as the dashed black line. Also plotted in the centre subplot is the rotation curve for a 1 hour observation at the 30×60 mas scale (blue squares), which has been binned up to 60 mas spaxels. We also show a simulated 10 hour VLT (SINFONI) observation at 100 mas (green triangles). All curves are extracted along a $\sim$ 1 kpc slit aligned along the semi-major axis. From these simulations the E-ELT with HARMONI offers a 10 fold improvement in observing efficiency compared to current telescopes, i.e. the E-ELT could observe 10 times as many objects in equal observing times. It also offers finer resolution, with 5× more independent data points at the 20 mas scale, and improved sensitivity for equal observing times on the same object

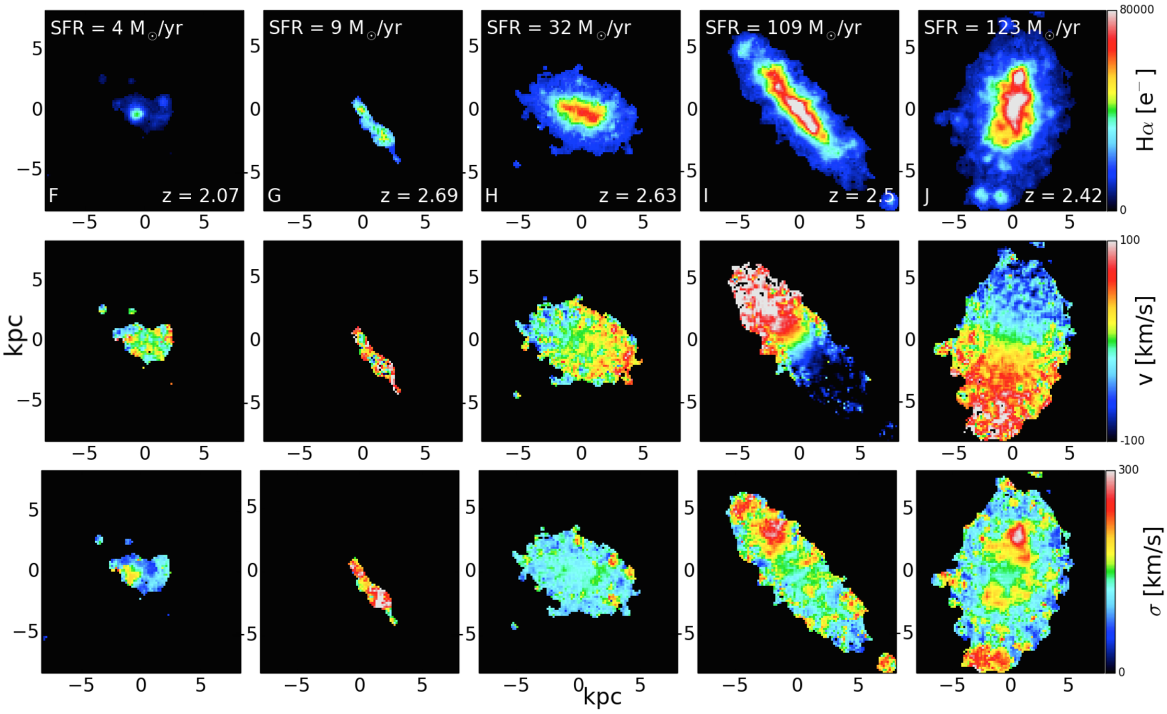

Figure 6.4: Maps of Hα flux (top row), line-of-sight gas velocity (middle row), and gas velocity dispersion (bottom row) for clumpy galaxies. Galaxies are ordered in increasing SFR from left to right. Also shown is the redshift of each galaxy. All galaxies are observed for 10 hours at the 20 × 20 mas scale. Velocity structure is evident even at the lowest SFRs and the velocity dispersion maps show internal structure of $\sim$ 5-6 spaxels diameter ($\sim$ 500 pc radius) for the faintest galaxy down to $\sim$ 3 spaxels ($\sim$ 250 pc radius) for the brightest galaxy.

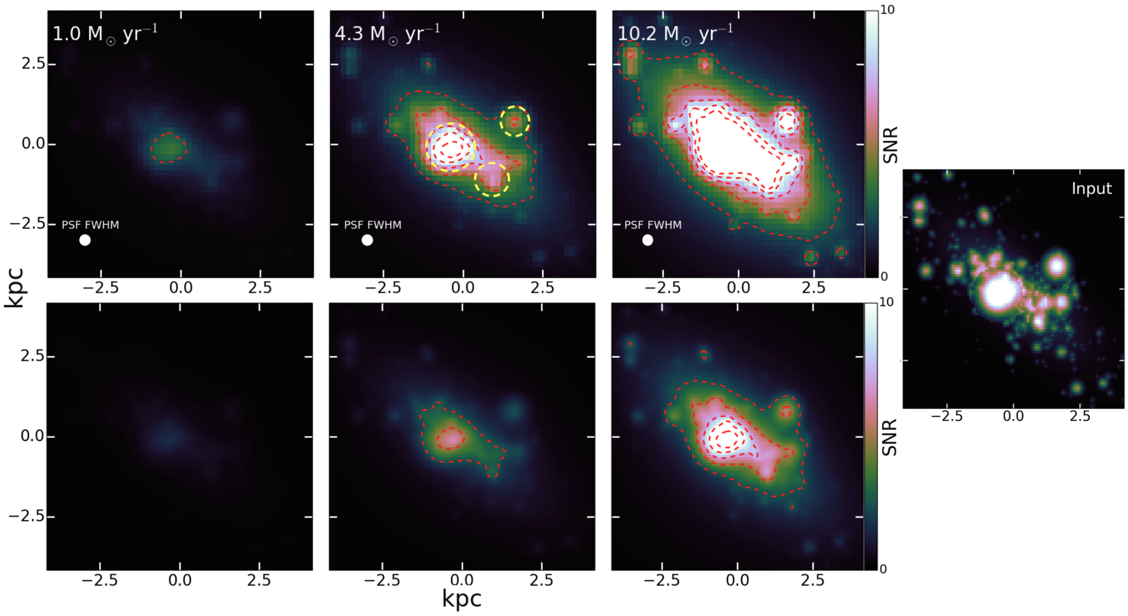

Figure 6.5: S/N maps of a model clumpy $z = 2$ galaxy for varying SFRs observed at 20×20 mas (top row) and 10×10 mas (bottom row). SFR increases from left to right and is denoted in the top left of each panel. The contours show constant S/N increasing from 2.5 to 12.5 in steps of 2.5. The size of the LTAO PSF is shown in the bottom left of the each map in the top row. The total exposure time is 10 hours on-source. The three star-forming clumps detected by CLUMPFIND are highlighted with yellow dashed circles in the central panel of the top row. For comparison we also show the input morphology (10 mas sampling) in the right hand subplot. Sub-kpc sized star forming regions are detected with S/N > 5 for SFR $\sim 4\,\mathrm{M}_\odot$ at 20mas. Similar regions are detected for SFR $\sim 10\,\mathrm{M}_\odot$ at 10mas.

and σ maps. The maps of galaxy J in Figure 6.4 (far right) show structure of ~ 3 spaxels in diameter. Thus HARMONI will be able to make very detailed measurements of galaxy substructure, even for galaxies with Milky Way star-formation rates.

To demonstrate HARMONI's ability to discern properties of individual star forming regions, we focus on the galaxy with the lowest star-formation rate from the 'clumpy' galaxy simulations (galaxy F in Figure 6.4). Figure 6.5 shows the recovered Hα S/N maps for a 10 hour on-source observation at the 20×20 mas (top row) and 10×10 mas (bottom row) scales for several SFRs, 1, 4.3 and $10.2\,\mathrm{M}_\odot\,\mathrm{yr}^{-1}$ (left to right). For star-formation rates below $10\,\mathrm{M}_\odot\,\mathrm{yr}^{-1}$ the 20 mas scale offers superior S/N, while still resolving individual clumps. However, at a star-formation rate of $1\,\mathrm{M}_\odot\,\mathrm{yr}^{-1}$ no clumps are detected with a S/N > 5 at the 20 mas scale in 10 hours.

To quantify the likely detection and properties of the clumps in a HARMONI observation we use the 2D CLUMPFIND routine by Williams et al. (1994) to determine positions and sizes of individual clumps. This method has been used previously by Livermore et al. (2012, 2015) on observations of lensed galaxies. The routine uses isophotes to define clumps starting in the brightest regions and then moving down through the isophote levels. Any isolated contours are defined as new clumps, and any which enclose an existing peak are allocated to that clump. A contour which encloses two or more existing peaks has its pixels divided between them using a 'friends-of-friends' algorithm. We follow a similar procedure as used in Livermore et al. (2015) and set the minimum threshold at 3σ and move in 1σ steps.

In galaxy F we detect three clumps (indicated by yellow circles on Figure 6.5), and proceed to calculate their luminosities and then star-formation rates by summing the pixels within the clump from the Hα map. Using Equation 6.2, we measure star-formation rates in these three clumps to be 1.46 ± 0.02, 0.26 ± 0.01 and $0.23 \pm 0.01\,\mathrm{M_\odot\,yr^{-1}}$, where the uncertainties are derived from the Hα variance map. As a crosscheck of our method we integrate the complete observed Hα map and calculate the total star-formation rate of the galaxy to be $4.12 \pm 0.03\,\mathrm{M_\odot\,yr^{-1}}$ (which is similar to the input value of $4.35\,\mathrm{M_\odot\,yr^{-1}}$).

Finally, assuming the clumps have circular symmetry, we infer a radius of each clump. We measure the radii as 980 ± 150, 500 ± 200 and $520 \pm 250\,$pc respectively. These match closely to the input clump sizes of 1000, 630 and 500 pc respectively. Comparing these measurements to observations of lensed galaxies (Figure 9 of Livermore et al. 2015) we see that HARMONI will be capable of detecting and measuring properties of clumps at least a factor of two smaller than currently possible for normal (unlensed) galaxies at $z \sim 2$ ($\sim 500\,$pc compared to $\sim 1\,$kpc). Thus, it should be possible to observe the same galaxy at the 10 mas scale for a greater number of hours and measure properties of even smaller clumps. From the S/N map of galaxy F with SFR $= 10.2\,\mathrm{M_\odot\,yr^{-1}}$ in Figure 6.5, we see there are clumps of three pixels diameter in the 20 mas scale with S/N > 5. This corresponds to $\sim 250\,$pc.

We now perform a similar analysis at the 10 mas scale on input data cubes generated using the SINGS morphological templates. These galaxies have higher initial resolutions compared with the analytical model inputs and do not have a separate disc component, as the clumps form the disc morphology. We generate mock observations of two galaxies (using the NGC0337 template shown in Figure 6.1) at $z = 2.0$, one with SFR = $5\,\mathrm{M_\odot\,yr^{-1}}$ observed for 10 hours on-source, and the other with SFR = $50\,\mathrm{M_\odot\,yr^{-1}}$ observed for 1 hour on-source. The S/N maps are shown in Figure 6.6. The maps show that star-forming regions down to around $r \sim 250\,\mathrm{pc}\,(30\,\mathrm{mas})$ in radius are detectable in both galaxies. We run CLUMPFIND again using the same procedure as before on each galaxy, and detect seven clumps in each galaxy. The smallest have $r = 350 \pm 130\,\mathrm{pc}$ and $r = 360 \pm 130\,\mathrm{pc}$, which compare closely to the input size of $r = 330\,\mathrm{pc}$. The other clumps are of size $r \sim 500\,\mathrm{pc}$. Our measurements of star-forming region sizes are consistent between the two identical morphologies at different SFRs and between two sets of input data cubes. From these simulations we can see that HARMONI will be able to probe individual large HII regions in normal (unlensed) star-forming galaxies down to the sizes currently only achievable within strongly lensed objects. This represents a huge gain in observing depth, spatial resolution and light-gathering power. From Figure 6.6, HARMONI on the E-ELT will be able to observe several high SFR ($\geq 50\,\mathrm{M_\odot\,yr^{-1}}$) galaxies in a single night. We note that HARMONI also offers the diffraction-limited 4 mas scale, which for bright galaxies will allow even greater detail to be probed. However, the $0.61'' \times 0.86''$ field of view at 4 mas means that mosaicing is required to cover an entire galaxy, so for this study we only use 10 mas where the galaxy falls entirely within the field of view.

6.6 Pushing to higher redshifts: [OII] in H-band

Pushing HARMONI to higher redshifts will yield observations spanning the full star-forming epoch from $z \sim 2 - 4$ and provide resolved kinematics of galaxies currently unaccessible with today's 8 m class telescopes. The 3727 Å [OII] doublet is the strongest emission line after Hα and falls into the H-band at $z = 3$ and 4. It traces star-forming regions similarly to Hα and thus provides a powerful diagnostic for HARMONI to probe star-forming galaxies at higher redshifts (see e.g. Kennicutt, 1998a; Kewley et al., 2004; Mouhcine et al., 2005, and references therein). We can also assess the relative advantages and disadvantages of using Hα in K-band at $z \sim 2$–2.5 compared with [OII] in H-band at $z \sim 3$.

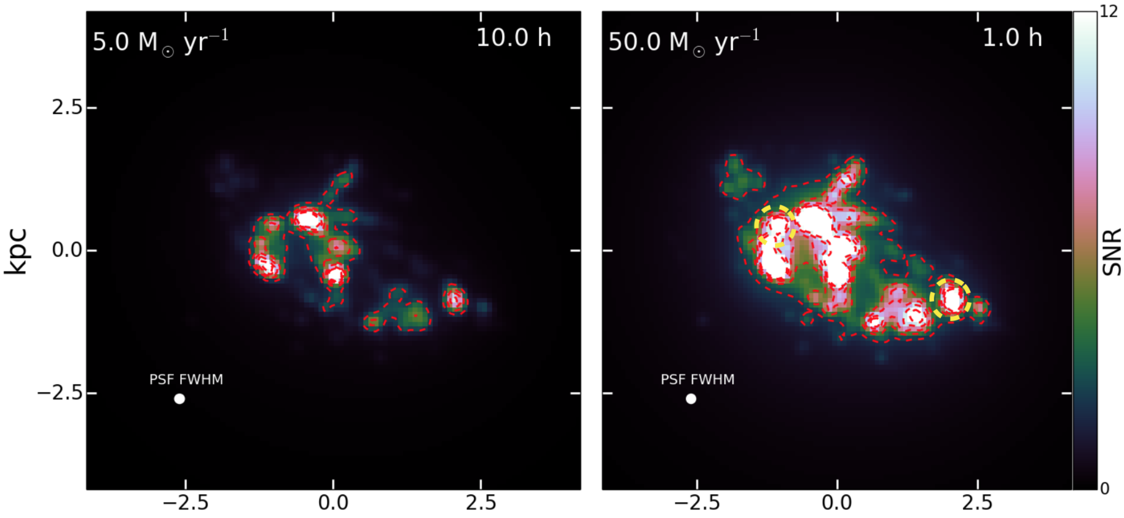

Figure 6.6: S/N maps for clumpy $z = 2$ galaxies observed at 10 mas scale. Left shows a galaxy of SFR $= 5\,\mathrm{M_\odot\,yr^{-1}}$ observed for 10 hours on-source. Right shows a SFR $= 50\,\mathrm{M_\odot\,yr^{-1}}$ galaxy observed for 1 hour on-source. The red dashed contours show constant S/N increasing from 2.5 to 12.5 in steps of 2.5. The PSF FWHM is shown in the bottom left of each subplot. The two smallest star-forming clumps detected by CLUMPFIND are highlighted with yellow dashed circles in the right hand panel. The input morphology is shown in the right hand panel of Figure 6.1. HARMONI will be capable of detecting sub-kpc regions of several bright star-forming galaxies in a single night.

We create mock data cubes at $z = 3$ and 4 using the morphological template method from Section 6.2.2 but covering the [OII] rest-frame wavelength range of 3727 Å. We assume the [OII] line strength is half that of Hα. We produce HARMONI mock observations with LTAO at the 20 mas scale. In Figure 6.7 we show a simulated clumpy $50\,\mathrm{M_\odot\,yr^{-1}}$ star forming galaxy at $z = 2$ (Hα) and $z = 3, 4$ ([OII]). The galaxy at $z = 2$ is observed for 2 hours on-source and the higher redshifts are each 10 hours on-source. The cosmological dimming with increasing redshift is evident. Also, these galaxies have the same input kinematic profiles, so comparing the velocity and dispersion maps between K-band Hα at $z = 2$ and H-band [OII] at $z = 3$ shows the effect of beam smearing by increasing the peak of the dispersion map at $z = 3$. However, at $z = 4$ where [OII] is redshifted to the K-band HARMONI offers exceptional spatial resolution and the clumpy morphology is clearly resolved at 20 mas, along with the velocity and σ maps.

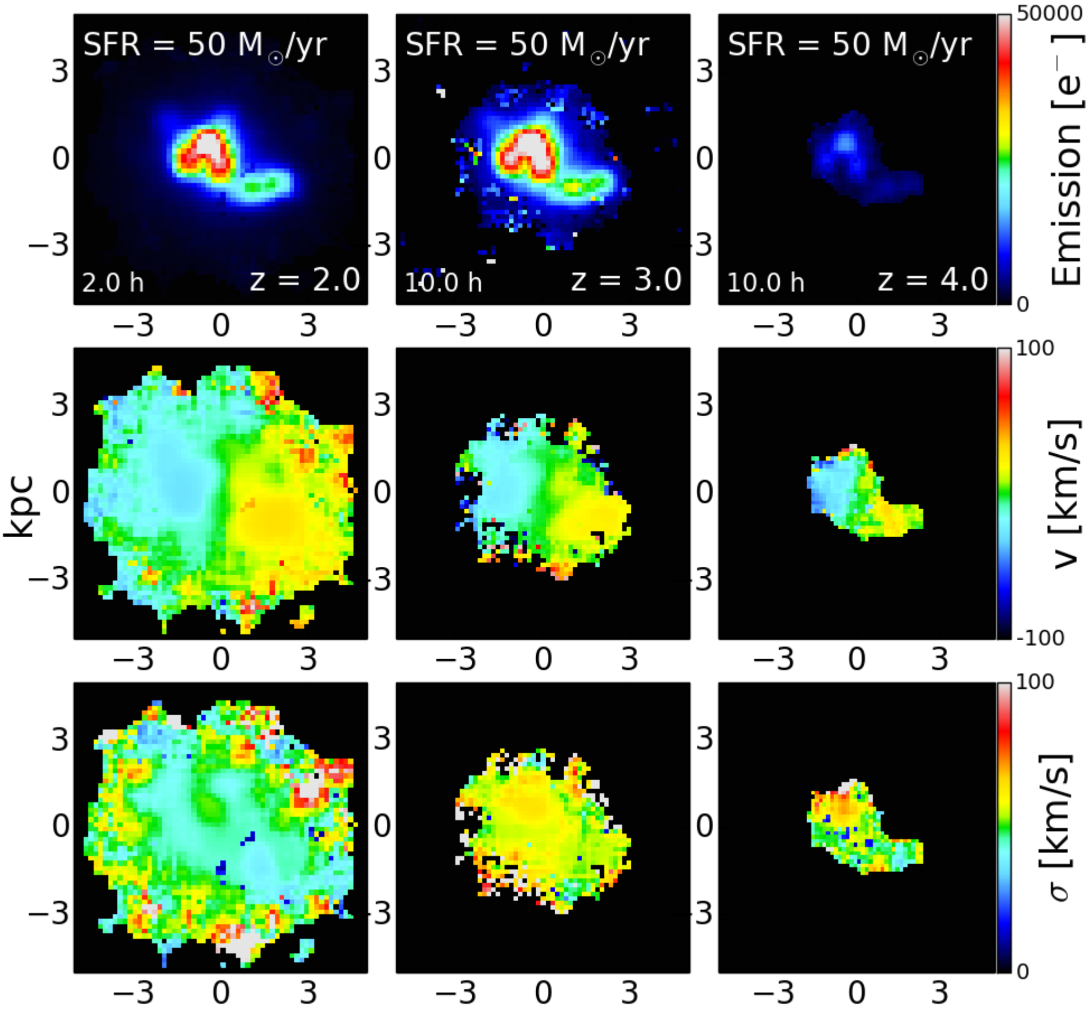

Figure 6.7: Maps of emission line flux (top row), line-of-sight gas velocity (middle row) and gas velocity dispersion (bottom row) for a clumpy $50\,\mathrm{M}_{\odot}\,\mathrm{yr}^{-1}$ star forming galaxy at increasing redshift of $z = 2$ (Hα: left) and $z = 3, 4$ ([OII]: centre and right), observed for two hours on-source at $z = 2$ and 10 hours on-source for $z = 3, 4$ at the 20 mas scale. Redshift increases from $z = 2$ (left), 3 (centre) and 4 (right). These galaxies have the same input kinematic profiles. The effect of beam smearing from the reduced spatial resolution is evident when comparing the $z = 2$ and $z = 3$ velocity dispersion maps.

6.7 Discussion and conclusions

HSIM provides a powerful tool to make quantitative predictions on the observability of star-forming galaxies at high redshift. Our simulations have shown three key results:
(i) HARMONI can fully recover gas kinematics of star-forming galaxies at $z = 2$–3 over the full galaxy main sequence, and obtain rotation profiles with a factor of ten efficiency gain compared with current generation instruments;
(ii) HARMONI offers sub-kpc resolution kinematics of galaxies over the galaxy main sequence at $z = 2$–3, from which individual star forming clumps can be detected, and this will achievable for several of the brightest galaxies in a single night;
(iii) HARMONI can perform resolved studies of the brightest star forming galaxies across the main star-forming epoch out to $z = 4$ by tracing [OII] in the H-band.

We have made use of simple analytical models, low-redshift morphological templates, and scaling relations to generate our mock, high resolution input data cubes. Therefore these simulations are not designed to test the physics of galaxy formation but allow us to make predictions about HARMONI's ability to observe these objects. A physical limitation to our input data is that there is currently limited knowledge of the internal physics of star forming galaxies at $z = 2$–4, so we do not attempt to construct physical models of galaxy sub-structure on $\sim 100\,\mathrm{pc}$ scales. Creating physically representative input data cubes offers a more robust method of testing whether HARMONI could infer physical processes on sub-kpc scales. One way to do this is via high resolution N-body cosmological simulations like RAMSES (Teyssier, 2002) and EAGLE (Schaye et al., 2015). These simulate vast cosmological volumes and evolve them through cosmic time according to detailed physical prescriptions to generate huge catalogues of galaxies at very high spatial resolution. Resolved stellar absorption-line spectroscopy at $z = 3$ with HARMONI has been investigated using this method (Kendrew et al., 2016). This method for generating input cubes allows the user to: explore limits on the spatial binning required to achieve sufficient S/N for resolved spectroscopy; test instrument effects on derived properties of the mock-observed galaxy (e.g. changing galaxy effective radius after PSF convolution); and also offers the ability to determine whether different physical prescriptions can be discerned through observations, e.g. whether two different stellar feedback models give detectable differences in the mock-observed galaxies, or whether different ages and metallicities are accurately derived from the mock-observed data.

Spatial resolution currently presents an enormous limitation in uncovering the physics behind star formation in galaxies at $z \sim 2$–3. Only a handful of strongly lensed galaxies let astronomers resolve individual star forming regions on the scales of 100s of parsecs. Thus, our results illustrate a huge gain in sensitivity and spatial resolution offered by HARMONI with LTAO on the E-ELT, and will allow the exploration of normal galaxies on the same physical scales as lensed objects but without the added complexities of strong lensing. One may then be able to determine whether star formation is driven by dynamical disturbances, triggered by outflowing winds, or fuelled by accretion and fragmentation within a rotating disc in the early Universe.

Chapter 7

Conclusions

The conclusions and future directions are presented in two parts: one for the observational work using the Oxford SWIFT, and one for the HSIM simulation pipeline for HARMONI.

7.1 Radial gradients in IMF-sensitive features with SWIFT

In the first part of this thesis we have used the Oxford SWIFT to investigate the radial variation of IMF-sensitive far red absorption indices within several galaxies covering a range of masses and morphologies. We first traced the sodium NaI doublet, calcium triplet CaT and iron-hydride FeH throughout the nucleus, bulge and disc of the nearby spiral M31, as well as within the centre of the dwarf elliptical M32. We measured a strong NaI gradient within the central $\sim 38\,\mathrm{pc}$ of M31, and flat FeH profile at all radii within both M31 and M32. From comparing to SPS models we inferred a Chabrier IMF throughout M31 and M32, and a strong sodium abundance gradient in the central 38 pc of M31. We highlighted the conflicting IMF interpretations between the FeH and NaI indices, and demonstrated that the use of sodium alone as a tracer for the IMF should be treated with caution due to the discrepant predictions between different SPS models.

We then explored radial variations within the central $\sim 5\,\mathrm{kpc}$ of the two massive BCGs in the Coma cluster, NGC4889 and NGC4874, and the BCG in the Coma south-west cluster NGC4839. We measured the IMF-sensitive features NaI, CaT and FeH, as well as titanium oxide TiO and magnesium MgI. Within NGC4889 we found strong NaI and CaT gradients but a flat FeH profile similar to M31. On comparison with SPS models, we found an old, α-enhanced population with Chabrier (or even bottom-light) IMF, in conflict with recent evidence for an increased IMF slope with increased velocity dispersion. We measured flat NaI and FeH profiles within NGC4874 and determined an old, possibly slightly α-enhanced and Chabrier IMF population. Within NGC4839 we measured both strong NaI and strong FeH, which is evidence for a bottom-heavy IMF. These findings are supported by optical index measurements and dynamical modelling results from the literature.

The galaxies we have studied cover a wide range of central velocity dispersions, from 60–400 $\mathrm{km\,s^{-1}}$, and we find no IMF variation at both lowest and highest masses, with only one galaxy showing evidence for a bottom-heavy IMF. Although there is mounting evidence for a non-universality in the form of the IMF within ETGs, independent results on individual galaxies are revealing a variety of IMFs, suggesting that the picture of galaxy formation is more complex than the simple notion of increased IMF slope with increased galaxy mass or velocity dispersion (at least for ETGs).

7.1.1 Future directions

One of the most important studies over the next few years will be accurate constraints on the stellar masses of galaxies. Many independent methods to probe the stellar component of galaxies have been actively pursued over the course of this D.Phil, including stellar absorption feature analysis from integrated spectra, dynamical modelling of galaxies using IFU data, and mass constraints of strong gravitationally lensed objects. Out of these three, only the absorption features directly probe the stellar component of galaxies and thus offer a vital handle on the distribution of stellar masses. We briefly highlight some outstanding issues and potential avenues of further research.

Combining optical and NIR IMF-sensitive absorption features: To date there has not been a comprehensive study of any galaxy covering all the known IMF-sensitive absorption features in both the optical and NIR. These include the optical TiO features (e.g. La Barbera et al., 2015) and CaH indices defined in Spiniello et al. (2014), and the far red NaI and FeH features used in this thesis and other works (e.g. van Dokkum & Conroy, 2012; Conroy & van Dokkum, 2012b). Targeting the centres of massive ellipticals (where bottom-heavy IMFs have recently been proposed) using instruments with full coverage of the optical and far red features (e.g. MaNGA: Bundy et al., 2015) will yield strong constraints on both the form of the IMF and the response of the individual absorption features. Furthermore, the absorption index results can then be combined with dynamical modelling constraints from the same data.

Understanding sodium in the centres of galaxies: The strong sodium features at 5900 Å and 8200 Å have been noted in the centres of some galaxies for several decades (also more recently a feature at $1.14\,\mu$m; Smith et al., 2015a), but there is still limited physical understanding to their prevalence. Recent interpretations of the sodium absorption as a change in the IMF have been proposed by some (e.g. van Dokkum & Conroy, 2010, 2012; Conroy & van Dokkum, 2012b) but questioned by others as only variations in the sodium abundance (e.g. Zieleniewski et al., 2015a; McConnell et al., 2015). Jeong et al. (2013) have undertaken a study of sodium excess objects, which will help quantify the prevalence of sodium within different galaxy populations. Simultaneously, further SPS modelling of sodium is required to understand its causes in stars.

Do galaxy discs and bulges have different IMFs: In M31 we traced indices through the bulge to the disc-dominated component at ~ 2.7 kpc. However, new bulge-disc decomposition techniques (e.g. Johnston et al., 2012, 2014) allow the separation of the stellar components of a galaxy to study each individually. Applying this method to IFU data cubes will allow resolved studies of the IMF separately in the bulge and disc. Any differences in IMFs would have strong implications for the overall formation of a galaxy, suggesting two distinct stellar mass growth epochs.

7.2 HSIM simulation pipeline for HARMONI on the European ELT

For the second part of this thesis we have developed HSIM, a stand-alone, modular simulation pipeline written in PYTHON, to simulate observations with HARMONI on the European ELT. HSIM takes high resolution input model data cubes and creates mock output data, folding in detailed descriptions of the sky, telescope, instrument and detector. We employed a new method of incorporating the strongly wavelength dependent AO point spread functions. HSIM provides an advancement upon traditional exposure time calculators and allows us to predict the feasibility of a given observing programme with HARMONI through the full analysis of mock data for a wide range of science cases. We provide a guide to using the HSIM software in Appendix C.

We have described the HSIM procedures in detail and used it to quantify the expected performance of HARMONI. We determined point source sensitivities and noise regimes for HARMONI's operating modes. We found that HARMONI will be predominately read-out noise limited in the R- and H-bands, but heavily background limited for the majority of K-band modes. The coarsest 30×60 mas spatial scale offers background limited observations in all bands. We also compared the visible wavelength AO performance between HARMONI and MUSE, finding that HARMONI offers improved sensitivity at $H\alpha$ and longer wavelengths. Lastly, we performed a suite of HSIM simulations of star-forming emission-line galaxies at $z \sim 2$–4. We detailed the construction of input data cubes using two separate generation methods. We showed that HARMONI will provide exquisite resolved spectroscopy of these objects, probing and deriving properties of individual star forming complexes down to at least $\sim 350\,\mathrm{pc}$ in size. It will be possible to spatially resolve the sub-kpc star-forming complexes of multiple bright galaxies in a single night, which represents a large increase in observing efficiency over current telescopes and instruments.

7.2.1 Future directions

Integral field spectroscopy has grown over the last twenty years from a niche technology to a common user facility on most of the world's largest ground-based optical/NIR telescopes.

During the course of this D.Phil many new integral field spectrographs have been commissioned and started operations, including KMOS (Sharples et al., 2013), MUSE (Bacon et al., 2010), SPHERE (Beuzit et al., 2008), SAMI (Croom et al., 2012), and MaNGA (Bundy et al., 2015; Drory et al., 2015). These are offering new insights into many areas of stellar populations, galaxy formation and evolution, and extrasolar planets.

The 'ELT' era will provide HARMONI on the E-ELT as well as equivalent instruments on the Thirty Metre Telescope (TMT) and Giant Magellan Telescope (GMT). However even before these, the NIRSpec integral field spectrograph on the James Webb Space Telescope (JWST) is due to be launched in 2018 and operate for five to ten years. Also, the Large Synoptic Survey telescope (LSST) will commence operations in 2022 and observe the southern sky, supplying a vast wealth of objects for follow-up observations. The next decade will see a huge investment in large instrumentation projects, both in developing the technology and also understanding the feasible scientific goals in order to best use the telescopes as they come online. We are in a position to utilise HSIM and make some key predictions for what HARMONI will be able to achieve over a range of science cases. A description of projects currently being pursued has been presented in Section 4.6.

Another key advantage of simulation pipelines is the ability to develop complementarities between different instruments, which will help in the optimisation of future science programmes. HARMONI will offer diffraction limited IFS between 0.47–2.5 μm on a 39 m telescope. NIRSpec on the JWST will offer 100 mas sampling IFS over a wavelength range of 0.6–5 μm on a space-based 6.5 m telescope. Developing a simulation pipeline for the NIRSpec IFU mode will enable a thorough study of how best to use these instruments over the finite lifetimes of the JWST and E-ELT, of which only up to around three years will overlap with current plans.

Appendix A

Additional plots for Chapter 2

We show here several additional plots concerning the accuracy and limitations of our telluric correction and sky subtraction techniques, as well as comparison plots between CvD12 and V12 models.

Fig. A.1 shows examples of our telluric correction around the NaI feature for M31_2 and M31_6. In each plot we use our kinematic template fits as an assumed 'telluric free' galaxy spectrum. The residuals after telluric correction are 0.8 per cent and 1 per cent rms respectively. We also check this for CaT and FeH and find residuals < 1 per cent for these features.

Fig. A.2 shows the M31_6 spectrum around the NaI feature. The second-order sky subtraction procedure has deepened the feature with extra sodium absorption, leading to a deeper feature. We checked this for all spectra to ensure systematic errors were minimised and only found this contamination in the M31_6 spectrum. We show this plot to highlight why we have used the best fit kinematic template to measure NaI for M31_6 instead of the science spectrum.

Fig. A.3 shows our M31_1, M31_5 and M31_6 science spectra around the FeH features with their best fit kinematic templates. The presence of residual sky lines after the second order sky subtraction stage in the M31_5 and M31_6 spectra leads us to use the template spectra to measure the FeH feature for these fields instead of the science spectra.

Fig. A.4 shows comparison model grids between CvD12 (left) and V12 (right) for NaI (top row), CaT (second row) and FeH (bottom; CvD12 only) features. We plot each index

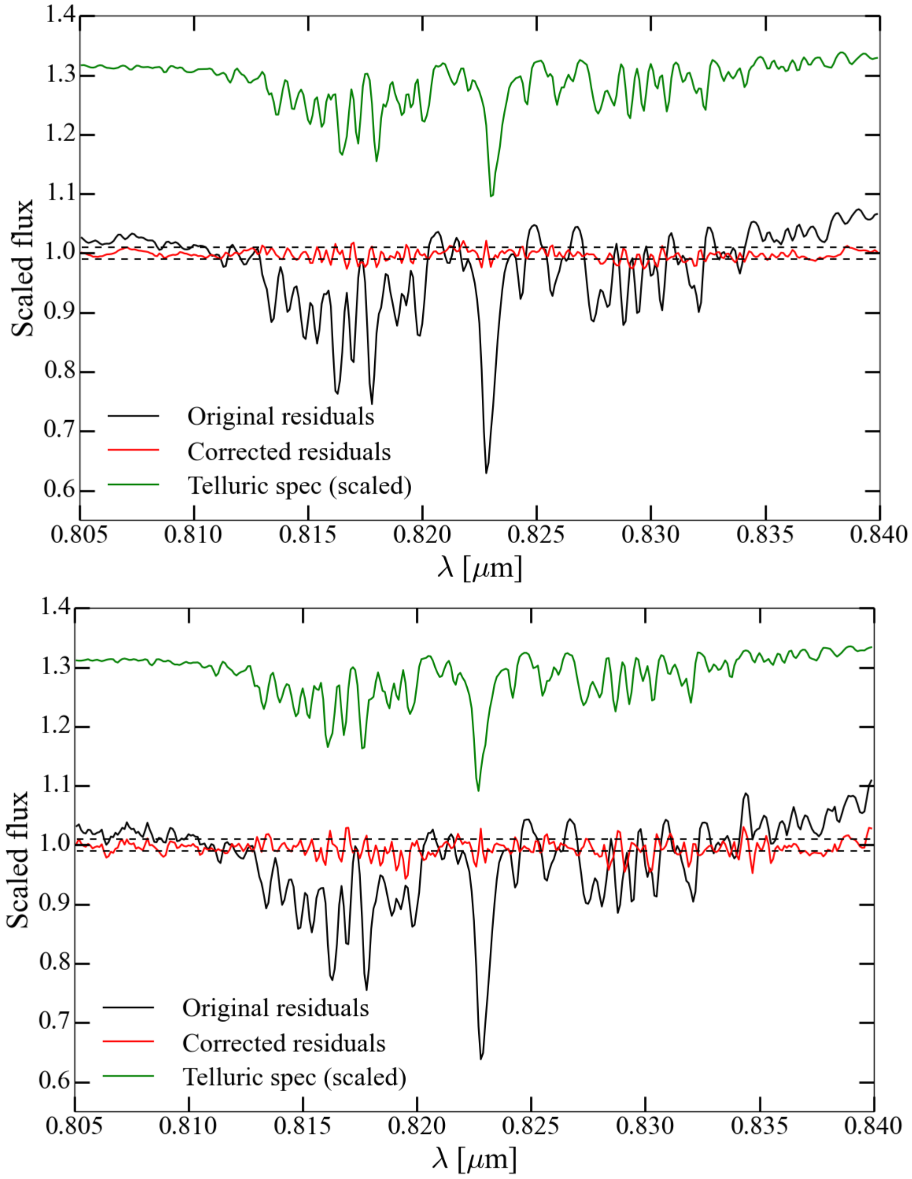

Figure A.1: Telluric correction for M31_2 (top) and M31_6 (bottom). The black line shows the ratio between original spectrum and kinematic template (assuming this is the intrinsic 'telluric free' spectrum), the red line shows the same ratio with telluric division, and the green line shows the telluric spectrum scaled by factor of 0.5 and plotted at $y = 1.3$ for clarity.

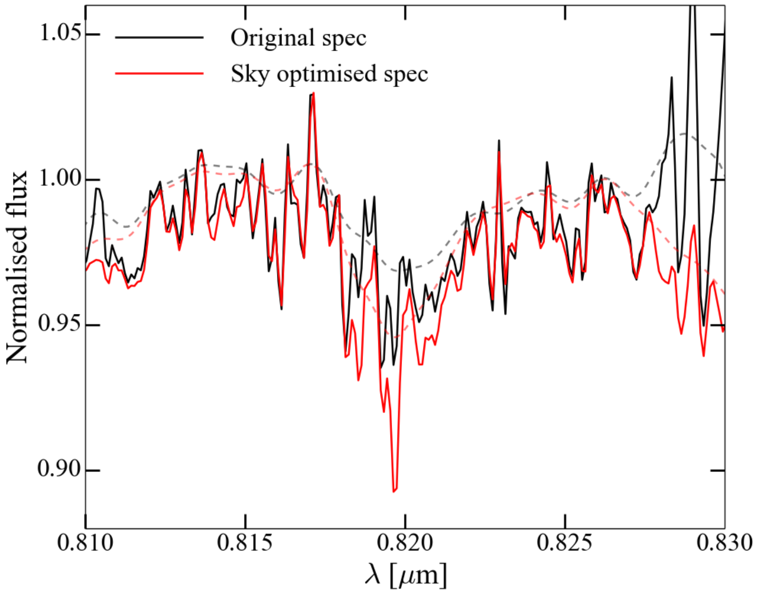

Figure A.2: Plot showing the M31_6 spectrum before (black) and after (red) the 2nd order sky subtraction routine (section 2.4). The procedure has deepened the NaI feature with (false) excess sodium absorption, which leads to a larger index value from the convolved spectra (dashed lines).

against variation in SDSS $g-r$ colour. These maps serve to show and compare the behaviour of each set of SSP models for each index within their respective model parameter spaces. Both sets of models qualitatively agree in their behaviour for variations in IMF and age. However quantitative differences exist, especially for the CaT index.

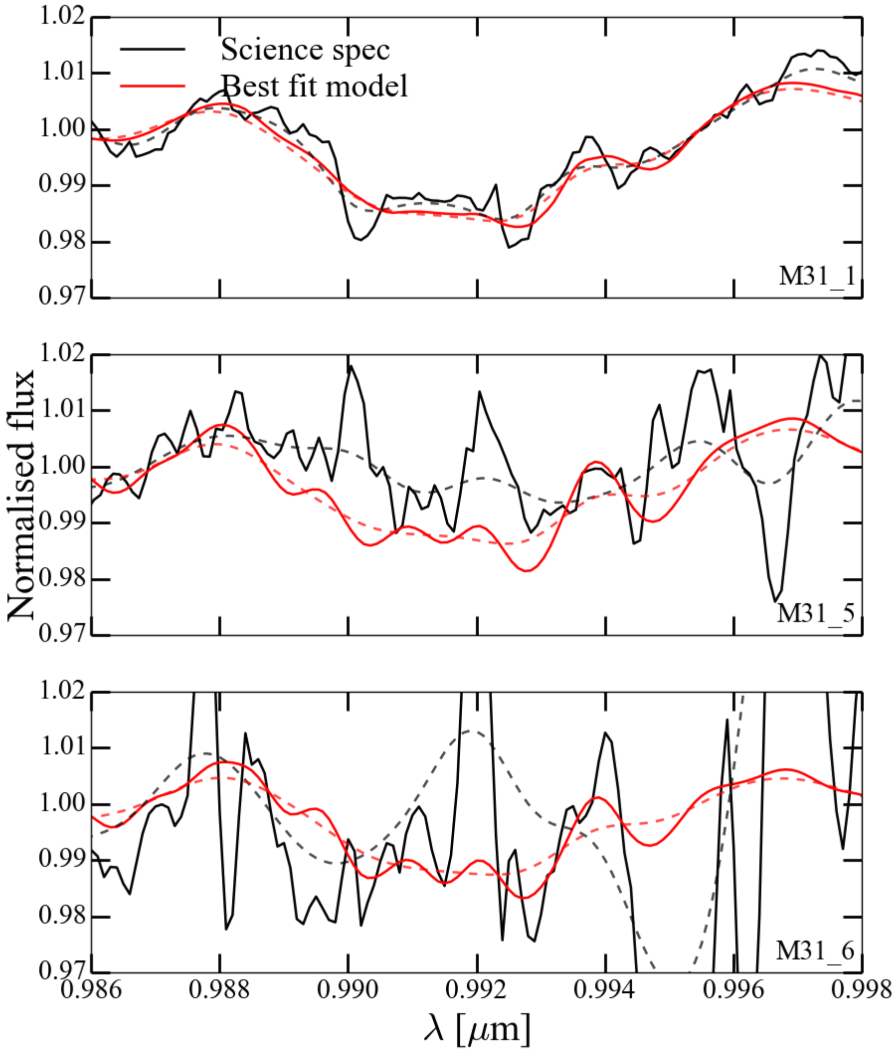

Figure A.3: Plotted spectra showing science spectra (black lines) with best fit models (red lines) for three fields, M31_1, M31_5 and M31_6. Solid lines show the spectra at their intrinsic resolution, and dashed lines show the spectra convolved up to 200 km s^{-1}. The spectra have each been normalised over the pseudo-continuum of the FeH feature.

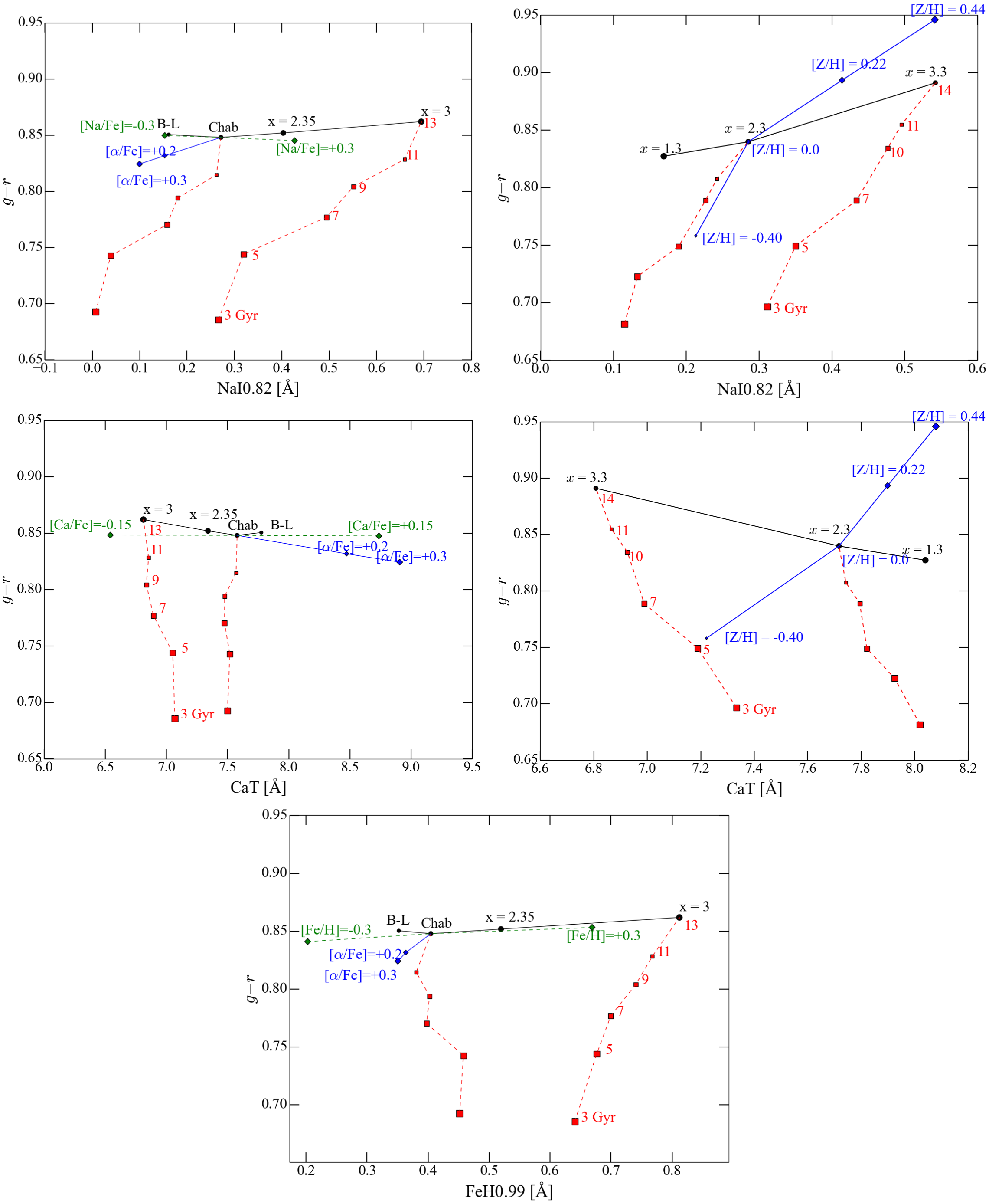

Figure A.4: Plots of NaI index (top row) and CaT (second row) against SDSS $g - r$ colour showing model variation for CvD12 (left) and V12 (right) models. Also shown is FeH (bottom) against $g - r$ for CvD12 models only, as FeH is not covered by V12. For the V12 models, black lines and circles are different IMFs at 14 Gyrs and [Z/H]=0.0, red squares are different ages, and blue diamonds are different metallicities. For the CvD12 models, black lines and circles show different IMFs, red lines and squares show different ages, blue lines and diamonds show varying [α/Fe] abundance, and green dashed lines and diamonds show varying [X/Fe].

Appendix B

Additional plots for Chapter 3

We show here additional plots concerning the accuracy of our telluric correction and sky subtraction techniques for the Coma BCG spectra. Figures B.1, B.2 and B.3 show the telluric correction around MgI (top) and the PPXF sky subtraction around FeH (bottom) for each of the BCGs; NGC4889, NGC4874 and NGC4839. For each galaxy, the MgI region is the worst affected by telluric absorption and we show the residuals for this region. We find smaller residuals around the $\mathrm{NaI_{SDSS}}$, CaT and TiO features of no worse than 0.01. We do not incur residuals around the FeH feature as we divide by a smooth fit to the throughput curve instead of by a corrected telluric spectrum. The right hand plots show the second-order sky subtraction around FeH using PPXF. Grey lines show the original spectrum, black lines show the corrected spectrum along with the best fit kinematic template (green). Blue lines show the residual sky spectrum (arbitrarily scaled and shifted in y-axis for presentation). The PPXF sky subtraction around the FeH feature is shown to be effective at minimising the prominent residual sky lines for each galaxy.

Fig. B.4 shows our measurements of the FeH index for each BCG using the spectra from our three separate data reduction processes discussed in Section 3.1.3:
(a) spectra telluric corrected and sky-subtracted using PPXF (red stars),
(b) spectra corrected by a fit to the telluric profile and sky-subtracted using PPXF (black circles),
(c) spectra corrected by a fit to the telluric profile and sky-subtracted using O-S spatial fitting (blue squares).

For all galaxies, the two different sky-subtraction methods (spectra *a* and *c*) are in good agreement. However, the telluric corrected spectrum for NGC4874 results in a much stronger FeH index compared with the telluric continuum fitting method. We therefore caution against performing telluric correction when FeH is redshifted long-ward of around $1\,\mu$m, as it moves into a region of negligible telluric absorption so any correction can introduce excess residuals.

Figure B.5 shows our index measurements for NGC4889 comparing measurements from spectra convolved to common dispersion of $\sigma = 400\,\mathrm{km\,s^{-1}}$ (black circles) with measurements corrected for radially varying dispersion (red squares). To derive the correction factors, we measure each index as a function of dispersion in a small set of the CvD12 models (9–13.5 Gyr, Chabrier and $x = 3$ IMF, [α/Fe]=$+0.0, +0.2$) and derive a multiplicative correction factor to correct each index value for the difference in dispersion between the peak value and the value at the given radius. We find good agreement between the separate methods for NGC4889 and all other galaxies, so are confident that we are not introducing any systematic effects through the convolutions, and thus trust our measurements presented in Chapter 3.

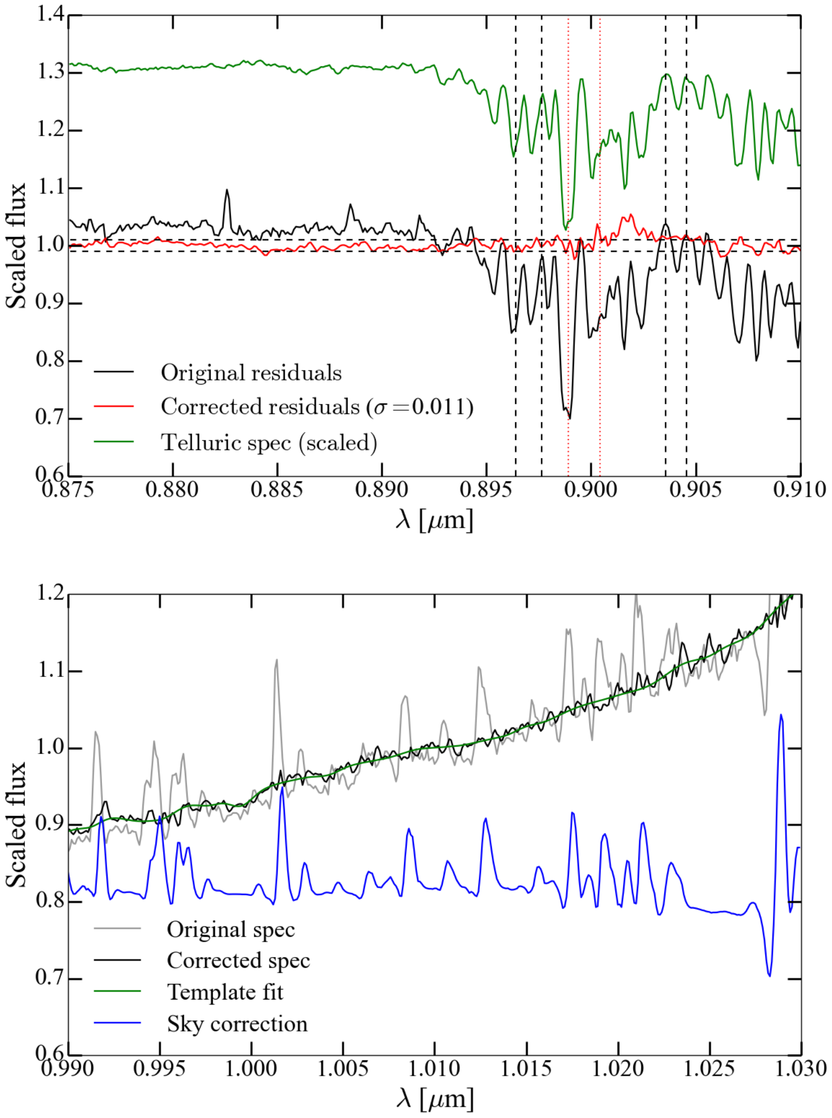

Figure B.1: Telluric correction (top) and second-order sky subtraction (bottom) for NGC4889. Top shows the telluric correction around MgI. The black line shows the ratio between original spectrum and kinematic template (assuming this is the intrinsic 'telluric free' spectrum), the red line shows the same ratio with telluric division, and the green line shows the telluric spectrum (arbitrarily scaled to fit onto plot). Bottom shows the second-order sky subtraction around FeH. Grey shows the original spectrum, black shows the corrected spectrum along with the best fit kinematic template. Blue shows the residual sky spectrum (arbitrarily scaled and shifted in y-axis for plot).

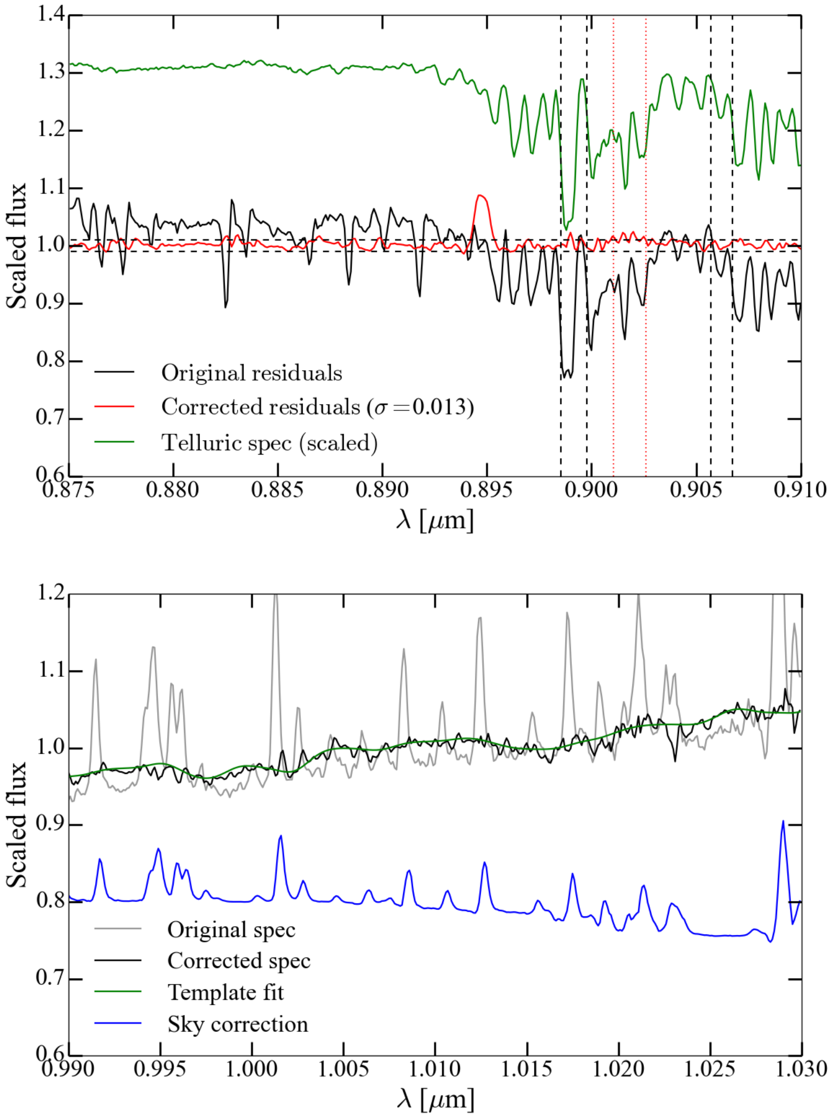

Figure B.2: Same as Figure B.1 but for NGC4874.

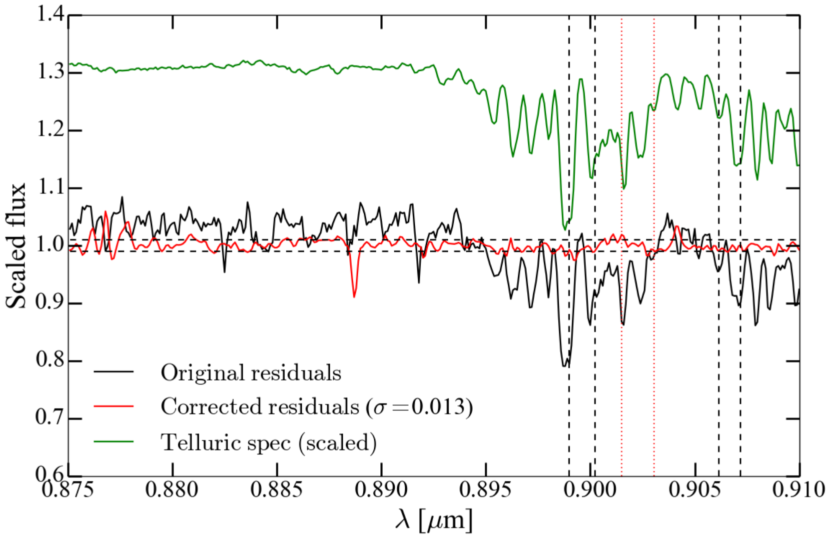

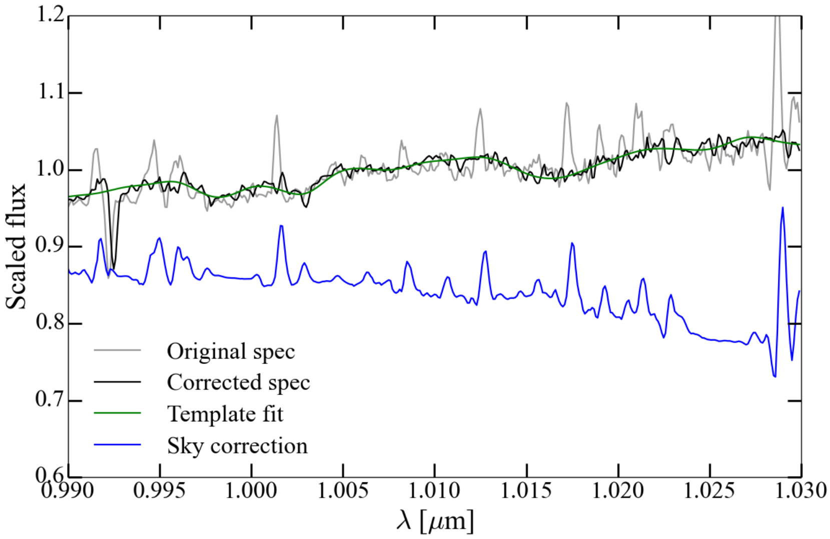

Figure B.3: Same as Figure B.1 but for NGC4839.

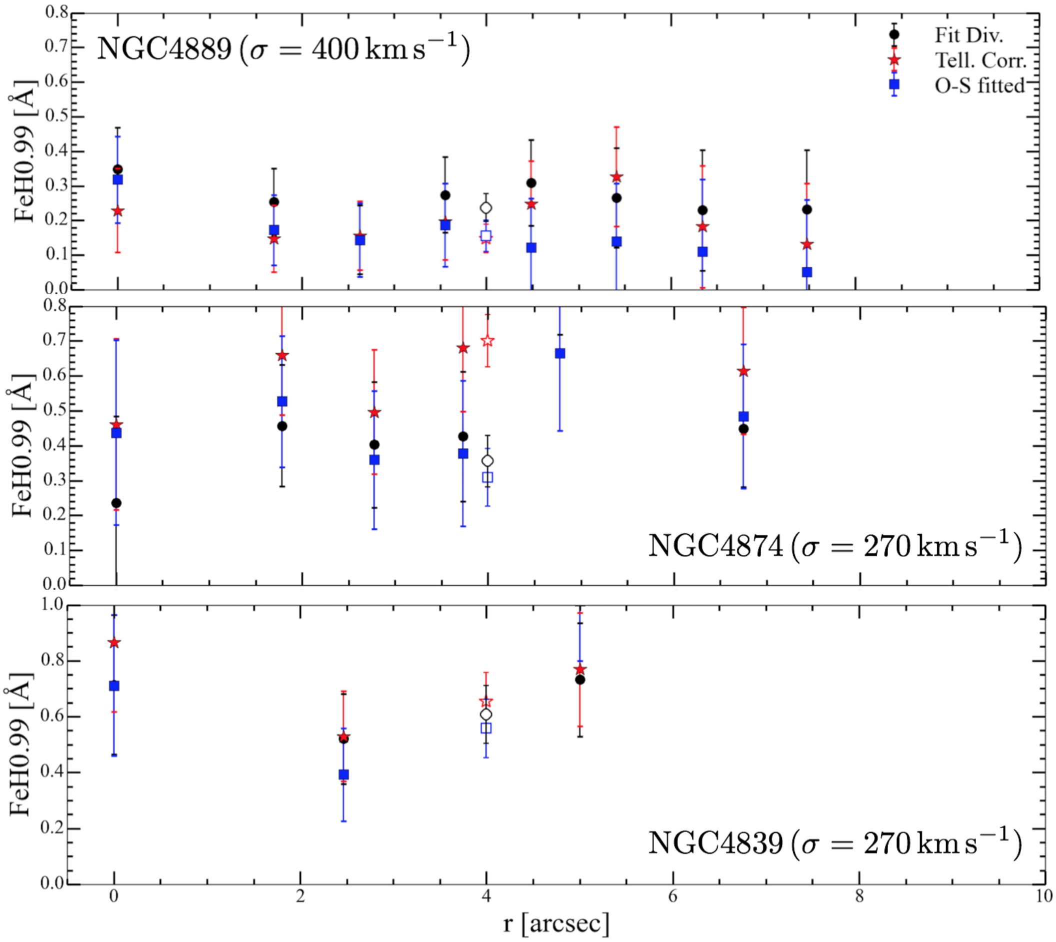

Figure B.4: Plot showing our measurements of FeH from the three separate spectra for each of the BCGs. In each subplot, black circles show our main measurements used throughout Chapter 3: telluric polynomial fit division around FeH and second order sky-subtraction using PPXF; red stars show the measurements from the telluric corrected spectra; blue squares show the measurements from the O-S data cube, Sérsic profile fitted spectra. Also shown are the optimally extracted global spectra in white-filled symbols, plotted at 4″ in each subplot.

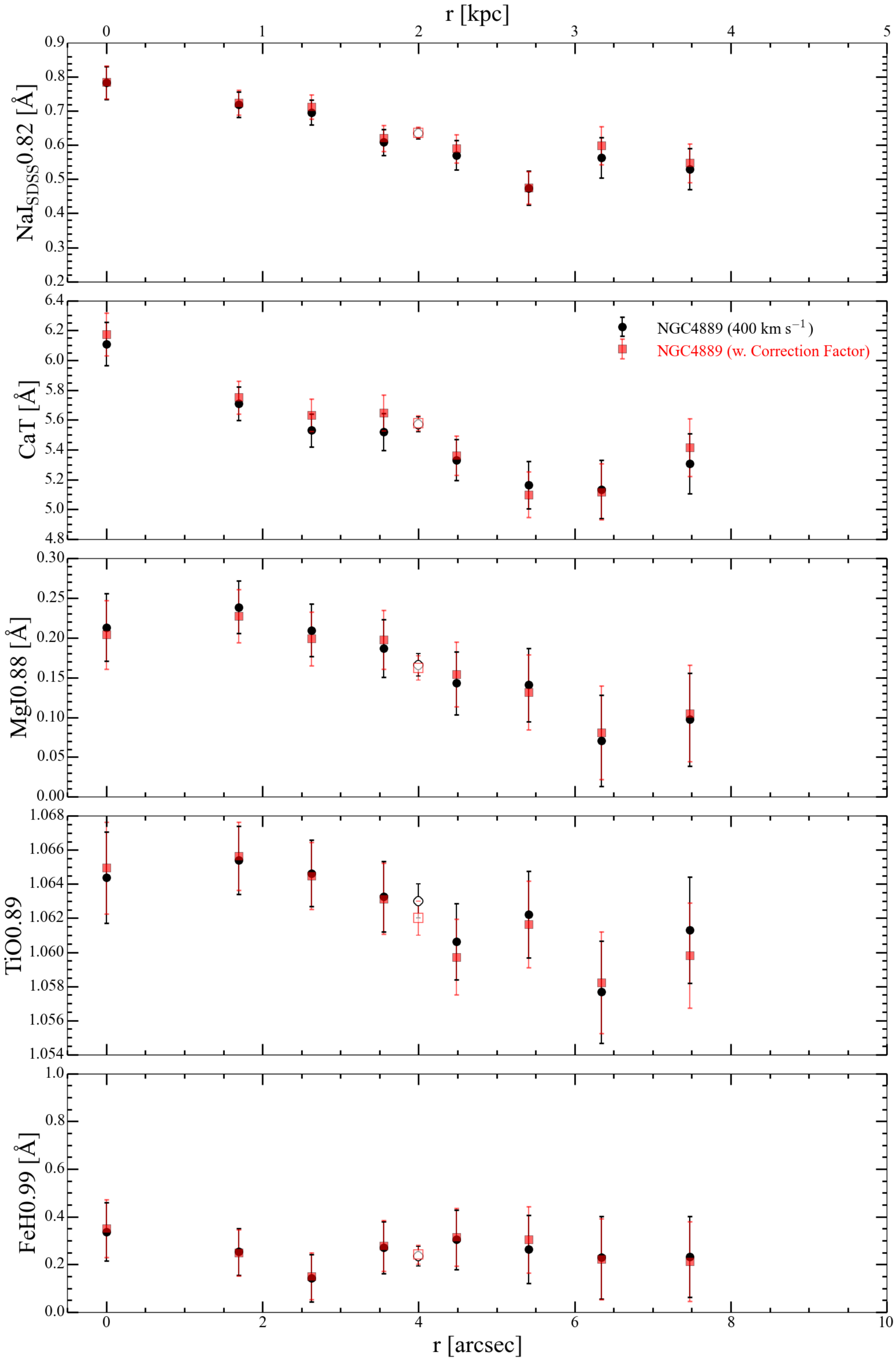

Figure B.5: Plots of index measurements as a function of radius for NGC4889, comparing measurements from spectra convolved to common dispersion of $\sigma = 400\,\mathrm{km\,s^{-1}}$ (black circles) with measurements corrected for radially varying dispersion (red squares). Plotted in white-filled symbols at 4″ are the values from the optimally extracted 'global' spectra over the full data cubes. Good consistency is found between index measurement methods.

Appendix C

HSIM user's guide

In this appendix we provide a general guide to using HSIM. We present the requirements for input data cubes and input parameter options. We then review some of the computational techniques utilised, memory considerations for input data cubes, and general speed performance when running HSIM.

The source code for HSIM is available at `https://github.com/szieleniewski/HSIM`. HSIM is written in the PYTHON (2.7.6) programming language. It requires the following external modules (version numbers used in parentheses):

- NUMPY (1.10.1): core functionality, efficient 3D array handling, FFT convolutions - `http://www.scipy.org/`
- SCIPY (0.16.1): core functionality, interpolation routines, scientific constants - `http://www.scipy.org/`
- ASTROPY: FITS file handling - `http://www.astropy.org/`
- WX (3.0.2, optional): Graphical user interface (GUI) - `http://www.wxpython.org/`
- PPROCESS (0.5.1, optional): Parallel processing routines - `http://www.boddie.org.uk/python/pprocess.html`

To use HSIM, move to the directory containing the source code and from the command line run,

```
$ python hsim.py
```

to load the GUI, or to display the list of command line options run,

```
$ python hsim.py −c
```

The required input files and parameters can then be entered either via the GUI, or listed in order on the command line.

C.1 Input parameters

The following parameters are required as input for an HSIM simulation (with options/units shown in square parentheses):

- **Input** FITS **data cube** (see Section C.2)
- **DIT** [**s**]: detector integration time (T_{exp})
- **NDIT**: number of detector integrations (N_{exp})
- **Grating** [**V+R, Iz+J, H+K, V, R, Iz, J, H, K, V-high, R-high, z, J-high, H-high, K-high, None**]: sets the wavelength range and spectral resolution. 'None' ignores spectral dimension
- $r_{\mathrm{spax,x}}$ [**mas**]: spaxel scale in x dimension
- $r_{\mathrm{spax,y}}$ [**mas**]: spaxel scale in y dimension
- **Telescope** [**E-ELT, VLT**]: Sets the aperture size and area. VLT only used for seeing-limited comparisons
- **AO** [**LTAO, SCAO, Gaussian**]: Sets the PSF
- **Zenith seeing FWHM** [**arcsec**]
- **Zenith angle** [**deg**]
- **User PSF**: upload a PSF FITS file instead of using built-in ones

- **PSF rms blur [mas]**: add additional telescope windshake jitter (adds in quadrature with any initial jitter)
- **Site temperature [K]**
- **Nyquist sample spectrum [True/False]**
- **Spectral sampling** [Å pixel^{-1}]: only used if Nyquist sampling set to False
- **Noise seed [0,1,2]**: sets noise seed for debugging purposes. 0 uses random seed, 1 or 2 take that value
- **Subtract background [True/False]**: Subtract background cube and return 'Reduced cube'
- **Return object cube [True/False]**: Returns object cubes with and without noise
- **Return transmission cube [True/False]**: Returns total throughput cube
- **Turn AR off [True/False]**: Turn atmospheric refraction off/on

C.2 Input data cubes

Input data cubes are uploaded as FITS files consisting of a 3D array (x, y, λ) and header. The required header keys are shown in Table C.1.

The pipeline input is a FITS file data cube consisting of a 3D array (x, y, λ) and associated header. Each pixel of the cube represents the flux density value at that spatial position and wavelength. Specific FITS header keys are required by the pipeline and are described in Table C.1. FITS data format has been chosen as this is the general output of 3D spectroscopic data reduction packages. The purpose of the input data cube is to quantify and represent the best understood physical mechanisms present in the astrophysical object of interest. This can include surface brightness profiles, emission lines, and detailed kinematics of specific objects. The input cubes should be higher spatial and spectral resolution than the required output in order to avoid interpolation errors. There is no field of view requirement for input data cubes. There are numerous methods for which to generate input data cubes and we give a few examples:

- **Point source:** A point source object can easily be generated using a spectrum along a single spaxel. We have used this method in Chapter 5 to measure predicted point source sensitivities of HARMONI, and it can be used for many different science cases, for example: resolved stellar populations where you create a 'field' of individual stellar spectra by populating individual spaxels; or gamma-ray bursts or supernovae at distant redshifts where a template spectrum is suitably redshifted.

- **Analytical models:** Using analytical models to describe morphologies offers a simple way to generate more spatially complex data cubes. We used this method in Chapter 6 where we used exponential profiles to create galaxy discs and added individual Gaussian star-forming 'clumps' on top of the disc. High spatial resolution data cubes can be generated but they do not provide any physical interpretation.

- **High resolution templates:** High resolution images of local objects (e.g. galaxies observed with HST, or large nearby ULIRGs) provide good morphological templates for creating higher redshift data cubes with physically motivated detail and substructure. One must be careful when moving a local object to higher redshift to ensure the spatial sampling is recalculated at the new redshift, and that cosmological dimming is applied according to the new luminosity distance. We have also utilised this method in Chapter 6 using images from the SINGS catalogue.

- **High resolution cosmological simulations:** Adaptive mesh refinement (AMR) N-body codes like RAMSES (Teyssier, 2002) can simulate large cosmological volumes and evolve them through time according to detailed physical prescriptions, creating galaxies at resolutions of $\sim 10\,\mathrm{pc}$. These provide a very promising method to generate input data cubes as the complete information on a galaxy's properties is known *a priori* from the output AMR simulation. This method has been utilised in Kendrew et al. (2016) where the authors have created an input data cube of a galaxy at $z = 3$ and assigned SSP spectra to each *star particle* from the simulation according to its age

Table C.1: FITS file header keys required for input data cubes

Header key	Description	Value
NAXIS1	x axis length	
NAXIS2	y axis length	
NAXIS3	λ axis length	
CTYPE1	Axis type (x)	x, RA
CTYPE2	Axis type (y)	y, DEC
CTYPE3	Axis type (λ)	WAVELENGTH
CUNIT1	Units of x axis	arcsec, mas
CUNIT2	Units of y axis	arcsec, mas
CUNIT3	Units of λ axis	m, microns, nm, angstroms
CDELT1	Spatial sampling [CUNIT1/pixel]	
CDELT2	Spatial sampling [CUNIT2/pixel]	
CDELT3	Spectral sampling [CUNIT3/pixel]	
CRVAL3	Value of CRPIX3 channel	
CRPIX3	Channel corresponding to CRVAL3	1
SPECRES	$\Delta\lambda_{\rm in}$ in units of CUNIT3	
FUNITS/BUNIT	Flux units for each pixel	J/s/m2/um/arcsec2 erg/s/cm2/A/arcsec2

and metallicity, to generate an input data cube with physically derived spatial and spectral properties.

There is also an option for the user to upload and use their own PSF. This file must be supplied as a FITS file containing either a 2D array or a 3D cube with header keys as shown in Table C.2. User uploaded PSFs must be normalised so the sum (of each channel in the case of a 3D cube) is equal to unity.

C.3 Output data cubes

The final outputs of an HSIM simulation are:

1. A mock observed cube: the main product of the simulation containing flux from the source and background, detector dark current, and all associated noise for each (x, y, λ) pixel of the cube (with an associated variance cube as first extension);

2. A background cube containing all background flux (with an associated variance cube as first extension);

3. A S/N cube giving the signal-to-noise ratio for each pixel.

Table C.2: FITS file header keys required for a user uploaded PSF. The file can either be a 2D image or a 3D cube. The required headers for each type are denoted by the second and third columns.

Header key	2D file	3D file	Description	Value
NAXIS1	×	×	x axis length	
NAXIS2	×	×	y axis length	
NAXIS3		×	λ axis length	
CTYPE1	×	×	Axis type (x)	x, RA
CTYPE2	×	×	Axis type (y)	y, DEC
CTYPE3		×	Axis type (λ)	WAVELENGTH
CUNIT1	×	×	Units of x axis	arcsec, mas
CUNIT2	×	×	Units of y axis	arcsec, mas
CUNIT3		×	Units of λ axis	microns, angstroms
CDELT1	×	×	Spatial sampling [CUNIT1/pixel]	
CDELT2	×	×	Spatial sampling [CUNIT2/pixel]	
CDELT3		×	Spectral sampling [CUNIT3/pixel]	
CRVAL3		×	Value of CRPIX3 channel	
CRPIX3		×	Channel corresponding to CRVAL3	1

There are also further options to return,

4. A noiseless object cube containing only source flux (with an associated variance cube as first extension);

5. A total transmission cube;

6. A 'reduced' sky-subtracted cube (observed cube - background cube, with an associated variance cube as first extension).

C.4 Computational techniques, memory usage and performance

Handling and processing 3D data cubes poses several computational problems. Firstly input cubes can become extremely large extremely quickly when trying to increase either spectral range, field of view, or spatial/spectral sampling. For example, a (2000, 2000, 300) data cube in 32-bit floating point format will total 4.8 Gb. This represents a memory challenge for most laptop or desktop computers with around 4-8 Gb of random access memory (RAM). It is possible to tailor input data cubes to specific goals of simulations. If there is a particular absorption/emission feature of interest from an object, the data cube can be cut down in wavelength around the feature. Likewise, spatial extent can be minimised if you are only interested in the flux from a point source. Furthermore, the spatial sampling can be optimised to suit specific aims. The pipeline performs spatial PSF convolutions at $1/10^{\text{th}}$ of the chosen output spatial scale, so creating more finely sampled input cubes is unnecessary. An input data cube that is spatially coarser than $1/10^{\text{th}}$ of the chosen output scale will be interpolated up to a finer scale (conserving flux), which adds computation time.

HSIM always processes the spectral dimension first and cuts the data cube to the chosen grating wavelength limits (if a grating choice has been specified), in order to reduce the number of channels in the data cube and thus decrease its memory usage.

HSIM subsequently iterates through the wavelength channels to perform the PSF convolution, AR shift and spaxel rebinning. It creates the PSF for each wavelength channel iteratively, as generating and storing in memory an entire PSF cube (at $1/10^{\text{th}}$ the input cube scale) is generally unfeasible for normal desktop and laptop computers. The python PPROCESS package gives basic parallel computing functionality to this procedure, resulting in a factor of > 2 increase in speed but is dependent on the number of available computer cores. After the wavelength iteration the output data cube size is set, and the input data cube is removed from the computer memory before any further cubes are generated. The PSF parameterisation method also offers computational efficiency over more intensive methods such as principal component analysis.

As an example, the analytical model data cubes from Chapter 6 are $(500, 250, 300) =$ 300 Mb in 64-bit floating point format and have 10 mas sampling. We run these for 10 mas output so the cubes are interpolated up to $(5000, 2500, 90)$ where they have been reduced in the spectral dimension after LSF convolution. Table C.3 shows the simulation time in minutes for two computers of different specifications. This demonstrates the ability of running HSIM in reasonable times on any modern desktop or laptop computer.

Table C.3: HSIM performance on two different computers for an input data cube of size $(500, 250, 300) = 300\,\mathrm{Mb}$ in 64-bit floating point format and 10 mas sampling, with 10 mas output sampling and final cube size $(500, 250, 90)$.

Computer cores and memory	Operating system	Time (minutes)
32×2 GHz Intel Zeon, 126 Gb RAM	Linux CentOS	6
Macbook Pro, 2×2.4 GHz Intel Core i5, 16 Gb RAM	OS X El Capitan	20

Bibliography

ALI, G. B., SHABAN, E. A., AMIN, M. Y. & RASSEM, M. A., 2014. Detailed surface photometry of the cD galaxies NGC 4839 and NGC 4874. *Astrophysics & Space Sciences*, **352**, 789–800.

ALLINGTON-SMITH, J., MURRAY, G., CONTENT, R., DODSWORTH, G., DAVIES, R., MILLER, B. W., JORGENSEN, I., HOOK, I., CRAMPTON, D. & MUROWINSKI, R., 2002. Integral Field Spectroscopy with the Gemini Multiobject Spectrograph. I. Design, Construction, and Testing. *PASP*, **114**, 892–912.

ALLINGTON-SMITH, J. R., CONTENT, R. & HAYNES, R., 1998. New developments in integral field spectroscopy. In S. D'Odorico, ed., *Optical Astronomical Instrumentation*, vol. 3355 of *Proc. SPIE*, 196–205.

ALLOIN, D. & BICA, E., 1989. A comparative study of NA I and CA II infrared lines in stars, star clusters and galaxy nuclei - an alternative to the dwarf-enriched population. *A&A*, **217**, 57–65.

ARMUS, L., MAZZARELLA, J. M., EVANS, A. S., SURACE, J. A., SANDERS, D. B. ET AL., 2009. GOALS: The Great Observatories All-Sky LIRG Survey. *PASP*, **121**, 559–576.

ASTROPY COLLABORATION, ROBITAILLE, T. P., TOLLERUD, E. J., GREENFIELD, P., DROETTBOOM, M. ET AL., 2013. Astropy: A community Python package for astronomy. *A&A*, **558**, A33.

Auger, M. W., Treu, T., Gavazzi, R., Bolton, A. S., Koopmans, L. V. E. & Marshall, P. J., 2010. Dark Matter Contraction and the Stellar Content of Massive Early-type Galaxies: Disfavoring “Light” Initial Mass Functions. *ApJ*, **721**, L163–L167.

Bacon, R., Accardo, M., Adjali, L., Anwand, H., Bauer, S. et al., 2010. The MUSE second-generation VLT instrument. In *Society of Photo-Optical Instrumentation Engineers (SPIE) Conference Series*, vol. 7735 of *Society of Photo-Optical Instrumentation Engineers (SPIE) Conference Series*, 8.

Bacon, R., Adam, G., Baranne, A., Courtes, G., Dubet, D., Dubois, J. P., Emsellem, E., Ferruit, P., Georgelin, Y., Monnet, G., Pecontal, E., Rousset, A. & Say, F., 1995. 3D spectrography at high spatial resolution. I. Concept and realization of the integral field spectrograph TIGER. *A&AS*, **113**, 347.

Bacon, R., Copin, Y., Monnet, G., Miller, B. W., Allington-Smith, J. R., Bureau, M., Carollo, C. M., Davies, R. L., Emsellem, E., Kuntschner, H., Peletier, R. F., Verolme, E. K. & de Zeeuw, P. T., 2001. The SAURON project - I. The panoramic integral-field spectrograph. *MNRAS*, **326**, 23–35.

Baraffe, I., Chabrier, G., Allard, F. & Hauschildt, P. H., 1998. Evolutionary models for solar metallicity low-mass stars: mass-magnitude relationships and color-magnitude diagrams. *A&A*, **337**, 403–412.

Bastian, N., Covey, K. R. & Meyer, M. R., 2010. A Universal Stellar Initial Mass Function? A Critical Look at Variations. *ARA&A*, **48**, 339–389.

Baugh, C. M., Lacey, C. G., Frenk, C. S., Granato, G. L., Silva, L., Bressan, A., Benson, A. J. & Cole, S., 2005. Can the faint submillimetre galaxies be explained in the Λ cold dark matter model? *MNRAS*, **356**, 1191–1200.

Bell, E. F., McIntosh, D. H., Katz, N. & Weinberg, M. D., 2003. The Optical and Near-Infrared Properties of Galaxies. I. Luminosity and Stellar Mass Functions. *ApJS*, **149**, 289–312.

BENDER, R., BURSTEIN, D. & FABER, S. M., 1992. Dynamically hot galaxies. I - Structural properties. *ApJ*, **399**, 462–477.

BERNARDI, M., SHANKAR, F., HYDE, J. B., MEI, S., MARULLI, F. & SHETH, R. K., 2010. Galaxy luminosities, stellar masses, sizes, velocity dispersions as a function of morphological type. *MNRAS*, **404**, 2087–2122.

BERTELLI, G., BRESSAN, A., CHIOSI, C., FAGOTTO, F. & NASI, E., 1994. Theoretical isochrones from models with new radiative opacities. *A&AS*, **106**.

BEUZIT, J.-L., FELDT, M., DOHLEN, K., MOUILLET, D., PUGET, P. ET AL., 2008. SPHERE: a 'Planet Finder' instrument for the VLT. In *Ground-based and Airborne Instrumentation for Astronomy II*, vol. 7014 of *Proc. SPIE*, 701418.

BOROSON, T. A. & THOMPSON, I. B., 1991. Color distributions in early type galaxies. III - Radial gradients in spectral features. *AJ*, **101**, 111–126.

BOUCHEZ, A. H., DEKANY, R. G., ANGIONE, J. R., BARANEC, C., BRITTON, M. C. ET AL., 2008. The PALM-3000 high-order adaptive optics system for Palomar Observatory. In *Society of Photo-Optical Instrumentation Engineers (SPIE) Conference Series*, vol. 7015 of *Society of Photo-Optical Instrumentation Engineers (SPIE) Conference Series*, 0.

BOWER, R. G., BENSON, A. J., MALBON, R., HELLY, J. C., FRENK, C. S., BAUGH, C. M., COLE, S. & LACEY, C. G., 2006. Breaking the hierarchy of galaxy formation. *MNRAS*, **370**, 645–655.

BRESSAN, A., CHIOSI, C. & FAGOTTO, F., 1994. Spectrophotometric evolution of elliptical galaxies. 1: Ultraviolet excess and color-magnitude-redshift relations. *ApJS*, **94**, 63–115.

BRESSAN, A., CHIOSI, C. & TANTALO, R., 1996. Probing the age of elliptical galaxies. *A&A*, **311**, 425–445.

BRILEY, M. M., SMITH, V. V., SUNTZEFF, N. B., LAMBERT, D. L., BELL, R. A. & HESSER, J. E., 1996. Sodium abundance variations in main-sequence stars of the globular cluster 47 Tucanae. *Nature*, **383**, 604–606.

Bruzual, G. & Charlot, S., 1993. Spectral evolution of stellar populations using isochrone synthesis. *ApJ*, **405**, 538–553.

Bruzual, G. & Charlot, S., 2003. Stellar population synthesis at the resolution of 2003. *MNRAS*, **344**, 1000–1028.

Bryant, J. J., Bland-Hawthorn, J., Lawrence, J., Croom, S., Fogarty, L. M., Goodwin, M., Richards, S., Farrell, T., Miziarski, S., Heald, R., Jones, H., Lee, S., Colless, M., Birchall, M., Hopkins, A. M., Brough, S. & Bauer, A. E., 2012. SAMI: a new multi-object IFS for the Anglo-Australian Telescope. In *Ground-based and Airborne Instrumentation for Astronomy IV*, vol. 8446 of *Proc. SPIE*, 84460X.

Bundy, K., Bershady, M. A., Law, D. R., Yan, R., Drory, N. et al., 2015. Overview of the SDSS-IV MaNGA Survey: Mapping nearby Galaxies at Apache Point Observatory. *ApJ*, **798**, 7.

Burstein, D., Faber, S. M., Gaskell, C. M. & Krumm, N., 1984. Old stellar populations. I - A spectroscopic comparison of galactic globular clusters, M31 globular clusters, and elliptical galaxies. *ApJ*, **287**, 586–609.

Burstein, D., Faber, S. M. & Gonzalez, J. J., 1986. Old stellar populations. III - The metallicities of M5, M71, and M67. *AJ*, **91**, 1130–1139.

Cappellari, M., 2002. Efficient multi-Gaussian expansion of galaxies. *MNRAS*, **333**, 400–410.

Cappellari, M., 2016. Structure and Kinematics of Early-Type Galaxies from Integral-Field Spectroscopy. *ArXiv e-prints*.

Cappellari, M. & Emsellem, E., 2004. Parametric Recovery of Line-of-Sight Velocity Distributions from Absorption-Line Spectra of Galaxies via Penalized Likelihood. *PASP*, **116**, 138–147.

CAPPELLARI, M., MCDERMID, R. M., ALATALO, K., BLITZ, L., BOIS, M. ET AL., 2012. Systematic variation of the stellar initial mass function in early-type galaxies. *Nature*, **484**, 485–488.

CAPPELLARI, M., SCOTT, N., ALATALO, K., BLITZ, L., BOIS, M. ET AL., 2013. The ATLAS^{3D} project - XV. Benchmark for early-type galaxies scaling relations from 260 dynamical models: mass-to-light ratio, dark matter, Fundamental Plane and Mass Plane. *MNRAS*, **432**, 1709–1741.

CARDIEL, N., GORGAS, J., CENARRO, J. & GONZALEZ, J. J., 1998. Reliable random error estimation in the measurement of line-strength indices. *A&AS*, **127**, 597–605.

CARLBERG, R. G., 1984. Dissipative formation of an elliptical galaxy. *ApJ*, **286**, 403–415.

CARTER, D., VISVANATHAN, N. & PICKLES, A. J., 1986. The dwarf star content of elliptical and lenticular galaxies. *ApJ*, **311**, 637–650.

CENARRO, A. J., CARDIEL, N. & GORGAS, J., 2008. The Calcium Triplet Gradient of M32. In J. H. Knapen, T. J. Mahoney & A. Vazdekis, eds., *Pathways Through an Eclectic Universe*, vol. 390 of *Astronomical Society of the Pacific Conference Series*, 292.

CENARRO, A. J., CARDIEL, N., GORGAS, J., PELETIER, R. F., VAZDEKIS, A. & PRADA, F., 2001. Empirical calibration of the near-infrared Ca ii triplet - I. The stellar library and index definition. *MNRAS*, **326**, 959–980.

CENARRO, A. J., CARDIEL, N., VAZDEKIS, A. & GORGAS, J., 2009. Mg and TiO spectral features at the near-IR: spectrophotometric index definitions and empirical calibrations. *MNRAS*, **396**, 1895–1914.

CENARRO, A. J., GORGAS, J., VAZDEKIS, A., CARDIEL, N. & PELETIER, R. F., 2003. Near-infrared line-strengths in elliptical galaxies: evidence for initial mass function variations? *MNRAS*, **339**, L12–L16.

CHABRIER, G., 2003. Galactic Stellar and Substellar Initial Mass Function. *PASP*, **115**, 763–795.

CHABRIER, G. & BARAFFE, I., 1997. Structure and evolution of low-mass stars. *A&A*, **327**, 1039–1053.

CHABRIER, G., HENNEBELLE, P. & CHARLOT, S., 2014. Variations of the Stellar Initial Mass Function in the Progenitors of Massive Early-type Galaxies and in Extreme Starburst Environments. *ApJ*, **796**, 75.

CIMATTI, A., DADDI, E., RENZINI, A., CASSATA, P., VANZELLA, E., POZZETTI, L., CRISTIANI, S., FONTANA, A., RODIGHIERO, G., MIGNOLI, M. & ZAMORANI, G., 2004. Old galaxies in the young Universe. *Nature*, **430**, 184–187.

CLARKE, F., THATTE, N., TECZA, M., O'BRIEN, K., HOUGHTON, R., TIEE, D., FLETCHER, L., IRWIN, P., VERMA, A., DEKANY, R., RICK, B. & ROBERTS, J., 2013. High resolution in three dimensions with SWIFT and PALM3K. In S. Esposito & L. Fini, eds., *Proceedings of the Third AO4ELT Conference*, 98.

CLAYTON, C. A., 1989. The implications of image scrambling and focal ratio degradation in fibre optics on the design of astronomical instrumentation. *A&A*, **213**, 502–515.

COCCATO, L., GERHARD, O. & ARNABOLDI, M., 2010. Distinct core and halo stellar populations and the formation history of the bright Coma cluster early-type galaxy NGC 4889. *MNRAS*, **407**, L26–L30.

COHEN, J. G., 1978. Near-infrared luminosity-sensitive features in M dwarfs and giants, and in M31 and M32. *ApJ*, **221**, 788–796.

COLE, S. & LACEY, C., 1996. The structure of dark matter haloes in hierarchical clustering models. *MNRAS*, **281**, 716.

COLE, S., LACEY, C. G., BAUGH, C. M. & FRENK, C. S., 2000. Hierarchical galaxy formation. *MNRAS*, **319**, 168–204.

CONROY, C., 2013. Modeling the Panchromatic Spectral Energy Distributions of Galaxies. *ARA&A*, **51**, 393–455.

Conroy, C. & van Dokkum, P., 2012a. Counting Low-mass Stars in Integrated Light. *ApJ*, **747**, 69.

Conroy, C. & van Dokkum, P. G., 2012b. The Stellar Initial Mass Function in Early-type Galaxies From Absorption Line Spectroscopy. II. Results. *ApJ*, **760**, 71.

Courteau, S., 1997. Optical Rotation Curves and Linewidths for Tully-Fisher Applications. *AJ*, **114**, 2402.

Couture, J. & Hardy, E., 1993. The low-mass stellar content of galaxies - Constraints through hybrid population synthesis near 1 micron. *ApJ*, **406**, 142–157.

Croom, S. M., Lawrence, J. S., Bland-Hawthorn, J., Bryant, J. J., Fogarty, L. et al., 2012. The Sydney-AAO Multi-object Integral field spectrograph. *MNRAS*, **421**, 872–893.

Cushing, M. C., Rayner, J. T., Davis, S. P. & Vacca, W. D., 2003. FeH Absorption in the Near-Infrared Spectra of Late M and L Dwarfs. *ApJ*, **582**, 1066–1072.

Davidge, T. J., 1991. Absorption line gradients in the spectrum of M32. *AJ*, **101**, 884–891.

Davidge, T. J., 1997. The Inner Bulge of M31. *AJ*, **113**, 985.

Davies, R., 2008. Adaptive optics: Observations and prospects for studies of active Galactic Nuclei. *New Astronomy Reviews*, **52**, 307–322.

Davies, R., Förster Schreiber, N. M., Cresci, G., Genzel, R., Bouché, N., Burkert, A., Buschkamp, P., Genel, S., Hicks, E., Kurk, J., Lutz, D., Newman, S., Shapiro, K., Sternberg, A., Tacconi, L. J. & Wuyts, S., 2011. How Well Can We Measure the Intrinsic Velocity Dispersion of Distant Disk Galaxies? *ApJ*, **741**, 69.

Davies, R. I., 2007. A method to remove residual OH emission from near-infrared spectra. *MNRAS*, **375**, 1099–1105.

Delisle, S. & Hardy, E., 1992. Near-infrared spectral gradients in ellipticals and bulges, and the nature of the NA feature near 8200 A. *AJ*, **103**, 711–727.

DJORGOVSKI, S. & DAVIS, M., 1987. Fundamental properties of elliptical galaxies. *ApJ*, **313**, 59–68.

DORNER, B., FERRUIT, P., PIQUÉRAS, L., LEGROS, E., PÉCONTAL, A., JARNO, A., PONS, A., GNATA, X. & PACIFICI, C., 2011. First Simulation and Data Reduction of a JWST/NIRSpec Observation. In I. N. Evans, A. Accomazzi, D. J. Mink & A. H. Rots, eds., *Astronomical Data Analysis Software and Systems XX*, vol. 442 of *Astronomical Society of the Pacific Conference Series*, 343.

DRESSLER, A., 1980. Galaxy morphology in rich clusters - Implications for the formation and evolution of galaxies. *ApJ*, **236**, 351–365.

DRESSLER, A., LYNDEN-BELL, D., BURSTEIN, D., DAVIES, R. L., FABER, S. M., TERLEVICH, R. & WEGNER, G., 1987. Spectroscopy and photometry of elliptical galaxies. I - A new distance estimator. *ApJ*, **313**, 42–58.

DRORY, N., MACDONALD, N., BERSHADY, M. A., BUNDY, K., GUNN, J. ET AL., 2015. The MaNGA Integral Field Unit Fiber Feed System for the Sloan 2.5 m Telescope. *AJ*, **149**, 77.

EISENHAUER, F., ABUTER, R., BICKERT, K., BIANCAT-MARCHET, F., BONNET, H. ET AL., 2003. SINFONI - Integral field spectroscopy at 50 milli-arcsecond resolution with the ESO VLT. In M. Iye & A. F. M. Moorwood, eds., *Instrument Design and Performance for Optical/Infrared Ground-based Telescopes*, vol. 4841 of *Society of Photo-Optical Instrumentation Engineers (SPIE) Conference Series*, 1548–1561.

EMSELLEM, E., 1999. 2-D Kinematics of Galactic Nuclei: From TIGER to OASIS. In D. R. Merritt, M. Valluri & J. A. Sellwood, eds., *Galaxy Dynamics - A Rutgers Symposium*, vol. 182 of *Astronomical Society of the Pacific Conference Series*, 45.

EMSELLEM, E., CAPPELLARI, M., KRAJNOVIĆ, D., ALATALO, K., BLITZ, L. ET AL., 2011. The ATLAS^{3D} project - III. A census of the stellar angular momentum within the effective radius of early-type galaxies: unveiling the distribution of fast and slow rotators. *MNRAS*, **414**, 888–912.

Emsellem, E., Monnet, G. & Bacon, R., 1994. The multi-gaussian expansion method: a tool for building realistic photometric and kinematical models of stellar systems I. The formalism. *A&A*, **285**.

Faber, S. M., 1973. Variations in Spectral-Energy Distributions and Absorption-Line Strengths among Elliptical Galaxies. *ApJ*, **179**, 731–754.

Faber, S. M. & French, H. B., 1980. Possible M dwarf enrichment in the semistellar nucleus of M31. *ApJ*, **235**, 405–412.

Faber, S. M., Friel, E. D., Burstein, D. & Gaskell, C. M., 1985. Old stellar populations. II - an analysis of K-giant spectra. *ApJS*, **57**, 711–741.

Ferreras, I., La Barbera, F., de la Rosa, I. G., Vazdekis, A., de Carvalho, R. R., Falcón-Barroso, J. & Ricciardelli, E., 2013. Systematic variation of the stellar initial mass function with velocity dispersion in early-type galaxies. *MNRAS*, **429**, L15–L19.

Finger, G., Dorn, R. J., Eschbaumer, S., Hall, D. N. B., Mehrgan, L., Meyer, M. & Stegmeier, J., 2008. Performance evaluation, readout modes, and calibration techniques of HgCdTe Hawaii-2RG mosaic arrays. In *Society of Photo-Optical Instrumentation Engineers (SPIE) Conference Series*, vol. 7021 of *Society of Photo-Optical Instrumentation Engineers (SPIE) Conference Series*, 0.

Fogarty, L., Thatte, N., Tecza, M., Clarke, F., Goodsall, T., Houghton, R., Salter, G., Davies, R. L. & Kassin, S. A., 2011. SWIFT observations of the Arp 147 ring galaxy system. *MNRAS*, **417**, 835–844.

Förster Schreiber, N. M., Genzel, R., Bouché, N., Cresci, G., Davies, R. et al., 2009. The SINS Survey: SINFONI Integral Field Spectroscopy of z $\sim$ 2 Star-forming Galaxies. *ApJ*, **706**, 1364–1428.

Förster Schreiber, N. M., Genzel, R., Lehnert, M. D., Bouché, N., Verma, A., Erb, D. K., Shapley, A. E., Steidel, C. C., Davies, R., Lutz, D., Nesvadba, N., Tacconi, L. J., Eisenhauer, F., Abuter, R., Gilbert, A., Gillessen, S.

& Sternberg, A., 2006. SINFONI Integral Field Spectroscopy of z ∼ 2 UV-selected Galaxies: Rotation Curves and Dynamical Evolution. *ApJ*, **645**, 1062–1075.

Förster Schreiber, N. M., Shapley, A. E., Erb, D. K., Genzel, R., Steidel, C. C., Bouché, N., Cresci, G. & Davies, R., 2011a. Constraints on the Assembly and Dynamics of Galaxies. I. Detailed Rest-frame Optical Morphologies on Kiloparsec Scale of z ∼ 2 Star-forming Galaxies. *ApJ*, **731**, 65.

Förster Schreiber, N. M., Shapley, A. E., Genzel, R., Bouché, N., Cresci, G., Davies, R., Erb, D. K., Genel, S., Lutz, D., Newman, S., Shapiro, K. L., Steidel, C. C., Sternberg, A. & Tacconi, L. J., 2011b. Constraints on the Assembly and Dynamics of Galaxies. II. Properties of Kiloparsec-scale Clumps in Rest-frame Optical Emission of z ∼ 2 Star-forming Galaxies. *ApJ*, **739**, 45.

Frenk, C. S., 1988. Galaxy formation in the cold dark matter cosmogony. In N. Kaiser & A. N. Lasenby, eds., *Post-Recombination Universe*, 367–370.

Fried, D. L., 1965. Statistics of a Geometric Representation of Wavefront Distortion. *Journal of the Optical Society of America (1917-1983)*, **55**, 1427–1431.

Frogel, J. A., Persson, S. E., Matthews, K. & Aaronson, M., 1978. Photometric studies of composite stellar systems. I - CO and JHK observations of E and S0 galaxies. *ApJ*, **220**, 75–97.

Gallazzi, A., Brinchmann, J., Charlot, S. & White, S. D. M., 2008. A census of metals and baryons in stars in the local Universe. *MNRAS*, **383**, 1439–1458.

Genzel, R., Tacconi, L. J., Eisenhauer, F., Förster Schreiber, N. M., Cimatti, A. et al., 2006. The rapid formation of a large rotating disk galaxy three billion years after the Big Bang. *Nature*, **442**, 786–789.

Girardi, L., Bressan, A., Bertelli, G. & Chiosi, C., 2000. Evolutionary tracks and isochrones for low- and intermediate-mass stars: From 0.15 to 7 M_{sun}, and from Z=0.0004 to 0.03. *A&AS*, **141**, 371–383.

Glazebrook, K., 2013. The Dawes Review 1: Kinematic Studies of Star-Forming Galaxies Across Cosmic Time. *PASA*, **30**, 56.

González Delgado, R. M. & Pérez, E., 1997. H II Region Population in a Sample of Nearby Galaxies with Nuclear Activity. II. Luminosity Function, Size, and Radial Distributions. *ApJS*, **108**, 199–228.

Gorgas, J., Faber, S. M., Burstein, D., Gonzalez, J. J., Courteau, S. & Prosser, C., 1993. Old stellar populations. IV - Empirical functions for features in the spectra of G and K stars. *ApJS*, **86**, 153–198.

Groenewald, D. N. & Loubser, S. I., 2014. Investigating the star formation histories of the brightest cluster galaxies. *MNRAS*, **444**, 808–826.

Han, M. & Mould, J. R., 1992. Peculiar velocities of clusters in the Perseus-Pisces supercluster. *ApJ*, **396**, 453–459.

Hardy, E. & Couture, J., 1988. Detection and measurement of the Wing-Ford band in the near-infrared spectra of elliptical galaxies. *ApJ*, **325**, L29–L31.

Hayward, C. C., Narayanan, D., Kereš, D., Jonsson, P., Hopkins, P. F., Cox, T. J. & Hernquist, L., 2013. Submillimetre galaxies in a hierarchical universe: number counts, redshift distribution and implications for the IMF. *MNRAS*, **428**, 2529–2547.

Heacox, W. D., 1986. On the application of optical-fiber image scramblers to astronomical spectroscopy. *AJ*, **92**, 219–229.

Hennebelle, P. & Chabrier, G., 2008. Analytical Theory for the Initial Mass Function: CO Clumps and Prestellar Cores. *ApJ*, **684**, 395–410.

Hill, J. M., Angel, J. R. P., Scott, J. S., Lindley, D. & Hintzen, P., 1980. Multiple object spectroscopy - The Medusa spectrograph. *ApJ*, **242**, L69–L72.

Hopkins, P. F., 2012a. An excursion-set model for the structure of giant molecular clouds and the interstellar medium. *MNRAS*, **423**, 2016–2036.

HOPKINS, P. F., 2012b. The stellar initial mass function, core mass function and the last-crossing distribution. *MNRAS*, **423**, 2037–2044.

HOPKINS, P. F., BUNDY, K., HERNQUIST, L., WUYTS, S. & COX, T. J., 2010. Discriminating between the physical processes that drive spheroid size evolution. *MNRAS*, **401**, 1099–1117.

HORNE, K., 1986. An optimal extraction algorithm for CCD spectroscopy. *PASP*, **98**, 609–617.

HOUGHTON, R. C. W., DAVIES, R. L., D'EUGENIO, F., SCOTT, N., THATTE, N., CLARKE, F., TECZA, M., SALTER, G. S., FOGARTY, L. M. R. & GOODSALL, T., 2013. Fast and slow rotators in the densest environments: a SWIFT IFS study of the Coma cluster. *MNRAS*, **436**, 19–33.

JARNO, A., BACON, R., FERRUIT, P. & PÉCONTAL-ROUSSET, A., 2008. Numerical Simulation of the VLT/MUSE Instrument. In R. W. Argyle, P. S. Bunclark & J. R. Lewis, eds., *Astronomical Data Analysis Software and Systems XVII*, vol. 394 of *Astronomical Society of the Pacific Conference Series*, 701.

JEE, M. J., BLAKESLEE, J. P., SIRIANNI, M., MARTEL, A. R., WHITE, R. L. & FORD, H. C., 2007. Principal Component Analysis of the Time- and Position-dependent Point-Spread Function of the Advanced Camera for Surveys. *PASP*, **119**, 1403–1419.

JEONG, H., YI, S. K., KYEONG, J., SARZI, M., SUNG, E.-C. & OH, K., 2013. On the Nature of Sodium Excess Objects. I. Data and Observed Trends. *ApJS*, **208**, 7.

JOHNSTON, E. J., ARAGÓN-SALAMANCA, A. & MERRIFIELD, M. R., 2014. The origin of S0s in clusters: evidence from the bulge and disc star formation histories. *MNRAS*, **441**, 333–342.

JOHNSTON, E. J., ARAGÓN-SALAMANCA, A., MERRIFIELD, M. R. & BEDREGAL, A. G., 2012. Spectroscopic bulge-disc decomposition: a new method to study the evolution of lenticular galaxies. *MNRAS*, **422**, 2590–2599.

Jones, A., Noll, S., Kausch, W., Szyszka, C. & Kimeswenger, S., 2013. An advanced scattered moonlight model for Cerro Paranal. *A&A*, **560**, A91.

Jones, T. A., Swinbank, A. M., Ellis, R. S., Richard, J. & Stark, D. P., 2010. Resolved spectroscopy of gravitationally lensed galaxies: recovering coherent velocity fields in subluminous z $\sim$ 2-3 galaxies. *MNRAS*, **404**, 1247–1262.

Jørgensen, I., 1999. E and S0 galaxies in the central part of the Coma cluster: ages, metal abundances and dark matter. *MNRAS*, **306**, 607–636.

Kendrew, S., Jolissaint, L., Mathar, R. J., Stuik, R., Hippler, S. & Brandl, B., 2008. Atmospheric refractivity effects on mid-infrared ELT adaptive optics. In *Adaptive Optics Systems*, vol. 7015 of *Proc. SPIE*, 70155T.

Kendrew, S., Zieleniewski, S., Houghton, R. C. W., Thatte, N., Devriendt, J., Tecza, M., Clarke, F., O'Brien, K. & Häussler, B., 2016. Simulated stellar kinematics studies of high-redshift galaxies with the HARMONI Integral Field Spectrograph. *MNRAS*, **458**, 2405–2422.

Kennicutt, Jr., R. C., 1983. The rate of star formation in normal disk galaxies. *ApJ*, **272**, 54–67.

Kennicutt, Jr., R. C., 1998a. Star Formation in Galaxies Along the Hubble Sequence. *ARA&A*, **36**, 189–232.

Kennicutt, Jr., R. C., 1998b. The Global Schmidt Law in Star-forming Galaxies. *ApJ*, **498**, 541–552.

Kennicutt, Jr., R. C., Armus, L., Bendo, G., Calzetti, D., Dale, D. A. et al., 2003. SINGS: The SIRTF Nearby Galaxies Survey. *PASP*, **115**, 928–952.

Kennicutt, Jr., R. C., Tamblyn, P. & Congdon, C. E., 1994. Past and future star formation in disk galaxies. *ApJ*, **435**, 22–36.

Kewley, L. J., Geller, M. J. & Jansen, R. A., 2004. [O II] as a Star Formation Rate Indicator. *AJ*, **127**, 2002–2030.

Kolmogorov, A., 1941. The Local Structure of Turbulence in Incompressible Viscous Fluid for Very Large Reynolds' Numbers. *Akademiia Nauk SSSR Doklady*, **30**, 301–305.

Kormendy, J. & Bender, R., 1999. The Double Nucleus and Central Black Hole of M31. *ApJ*, **522**, 772–792.

Kroupa, P., 2001. On the variation of the initial mass function. *MNRAS*, **322**, 231–246.

Kroupa, P., Weidner, C., Pflamm-Altenburg, J., Thies, I., Dabringhausen, J., Marks, M. & Maschberger, T., 2013. The Stellar and Sub-Stellar Initial Mass Function of Simple and Composite Populations. In T. D. Oswalt & G. Gilmore, eds., *Planets, Stars and Stellar Systems. Volume 5: Galactic Structure and Stellar Populations*, 115.

La Barbera, F., Ferreras, I. & Vazdekis, A., 2015. The initial mass function of early-type galaxies: no correlation with [Mg/Fe]. *MNRAS*, **449**, L137–L141.

La Barbera, F., Ferreras, I., Vazdekis, A., de la Rosa, I. G., de Carvalho, R. R., Trevisan, M., Falcón-Barroso, J. & Ricciardelli, E., 2013. SPIDER VIII - constraints on the stellar initial mass function of early-type galaxies from a variety of spectral features. *MNRAS*, **433**, 3017–3047.

Larson, R. B., 1974. Dynamical models for the formation and evolution of spherical galaxies. *MNRAS*, **166**, 585–616.

Law, D. R., Steidel, C. C., Erb, D. K., Larkin, J. E., Pettini, M., Shapley, A. E. & Wright, S. A., 2007. Integral Field Spectroscopy of High-Redshift Star-forming Galaxies with Laser-guided Adaptive Optics: Evidence for Dispersion-dominated Kinematics. *ApJ*, **669**, 929–946.

Law, D. R., Steidel, C. C., Erb, D. K., Larkin, J. E., Pettini, M., Shapley, A. E. & Wright, S. A., 2009. The Kiloparsec-scale Kinematics of High-redshift Star-forming Galaxies. *ApJ*, **697**, 2057–2082.

Livermore, R. C., Jones, T., Richard, J., Bower, R. G., Ellis, R. S., Swinbank, A. M., Rigby, J. R., Smail, I., Arribas, S., Rodriguez Zaurin, J., Colina, L., Ebeling, H. & Crain, R. A., 2012. Hubble Space Telescope Hα imaging of star-forming galaxies at z $\sim$ 1-1.5: evolution in the size and luminosity of giant H II regions. *MNRAS*, **427**, 688–702.

Livermore, R. C., Jones, T. A., Richard, J., Bower, R. G., Swinbank, A. M., Yuan, T.-T., Edge, A. C., Ellis, R. S., Kewley, L. J., Smail, I., Coppin, K. E. K. & Ebeling, H., 2015. Resolved spectroscopy of gravitationally lensed galaxies: global dynamics and star-forming clumps on $\sim$100 pc scales at $1 \leq z \leq 4$. *MNRAS*, **450**, 1812–1835.

Lorente, N. P. F., Glasse, A. C. H., Wright, G. S., Ramsay, S. K. & Evans, C. J., 2008. Specsim: A Software Simulator for Integral Field Unit Spectrometers. In A. Kaufer & F. Kerber, eds., *2007 ESO Instrument Calibration Workshop*, 295.

Loubser, S. I. & Sánchez-Blázquez, P., 2012. Stellar population gradients in brightest cluster galaxies. *MNRAS*, **425**, 841–861.

Loubser, S. I., Sánchez-Blázquez, P., Sansom, A. E. & Soechting, I. K., 2009. Stellar populations in the centres of brightest cluster galaxies. *MNRAS*, **398**, 133–156.

Loubser, S. I., Sansom, A. E., Sánchez-Blázquez, P., Soechting, I. K. & Bromage, G. E., 2008. Radial kinematics of brightest cluster galaxies. *MNRAS*, **391**, 1009–1028.

Madau, P. & Dickinson, M., 2014. Cosmic Star-Formation History. *ARA&A*, **52**, 415–486.

Maraston, C., 2005. Evolutionary population synthesis: models, analysis of the ingredients and application to high-z galaxies. *MNRAS*, **362**, 799–825.

Marigo, P., Girardi, L., Bressan, A., Groenewegen, M. A. T., Silva, L. & Granato, G. L., 2008. Evolution of asymptotic giant branch stars. II. Optical to far-infrared isochrones with improved TP-AGB models. *A&A*, **482**, 883–905.

Martin, F., Conan, R., Tokovinin, A., Ziad, A., Trinquet, H., Borgnino, J., Agabi, A. & Sarazin, M., 2000. Optical parameters relevant for High Angular Resolution at Paranal from GSM instrument and surface layer contribution. *A&AS*, **144**, 39–44.

Martín-Navarro, I., Barbera, F. L., Vazdekis, A., Falcón-Barroso, J. & Ferreras, I., 2015a. Radial variations in the stellar initial mass function of early-type galaxies. *MNRAS*, **447**, 1033–1048.

Martín-Navarro, I., La Barbera, F., Vazdekis, A., Ferré-Mateu, A., Trujillo, I. & Beasley, M. A., 2015b. The initial mass function of a massive relic galaxy. *MNRAS*, **451**, 1081–1089.

Martinez, P., Kolb, J., Sarazin, M. & Tokovinin, A., 2010. On the Difference between Seeing and Image Quality: When the Turbulence Outer Scale Enters the Game. *The Messenger*, **141**, 5–8.

McConnachie, A. W., Irwin, M. J., Ferguson, A. M. N., Ibata, R. A., Lewis, G. F. & Tanvir, N., 2005. Distances and metallicities for 17 Local Group galaxies. *MNRAS*, **356**, 979–997.

McConnell, N. J., Lu, J. R. & Mann, A. W., 2015. Radial Trends in IMF-Sensitive Absorption Features in Two Early-Type Galaxies: Evidence for Abundance-Driven Gradients. *ArXiv e-prints*.

McConnell, N. J., Ma, C.-P., Murphy, J. D., Gebhardt, K., Lauer, T. R., Graham, J. R., Wright, S. A. & Richstone, D. O., 2012. Dynamical Measurements of Black Hole Masses in Four Brightest Cluster Galaxies at 100 Mpc. *ApJ*, **756**, 179.

McKee, C. F. & Ostriker, E. C., 2007. Theory of Star Formation. *ARA&A*, **45**, 565–687.

Mehlert, D., Saglia, R. P., Bender, R. & Wegner, G., 2000. Spatially resolved spectroscopy of Coma cluster early-type galaxies. I. The database. *A&AS*, **141**, 449–468.

Mehlert, D., Thomas, D., Saglia, R. P., Bender, R. & Wegner, G., 2003. Spatially resolved spectroscopy of Coma cluster early-type galaxies. III. The stellar population gradients. *A&A*, **407**, 423–435.

Meynet, G. & Maeder, A., 2000. Stellar evolution with rotation. V. Changes in all the outputs of massive star models. *A&A*, **361**, 101–120.

Miller, G. E. & Scalo, J. M., 1979. The initial mass function and stellar birthrate in the solar neighborhood. *ApJS*, **41**, 513–547.

Moore, S. A. W., Lucey, J. R., Kuntschner, H. & Colless, M., 2002. Stellar populations in early-type Coma cluster galaxies - I. The data. *MNRAS*, **336**, 382–408.

Morris, T., Gendron, E., Basden, A., Martin, O., Osborn, J. et al., 2014. CANARY phase B: on-sky open-loop tomographic LGS AO results. In *Adaptive Optics Systems IV*, vol. 9148 of *Proc. SPIE*, 91481I.

Mouhcine, M., Lewis, I., Jones, B., Lamareille, F., Maddox, S. J. & Contini, T., 2005. The [OII]λ3727/Hα ratio of emission-line galaxies in the 2dF Galaxy Redshift Survey. *MNRAS*, **362**, 1143–1156.

Naab, T., Johansson, P. H. & Ostriker, J. P., 2009. Minor Mergers and the Size Evolution of Elliptical Galaxies. *ApJ*, **699**, L178–L182.

Narayanan, D. & Davé, R., 2012. Cosmological implications of a stellar initial mass function that varies with the Jeans mass in galaxies. *MNRAS*, **423**, 3601–3615.

Narayanan, D. & Davé, R., 2013. The cosmic evolution of the IMF under the Jeans conjecture with implications for massive galaxies. *MNRAS*, **436**, 2892–2906.

Naylor, T., 1998. An optimal extraction algorithm for imaging photometry. *MNRAS*, **296**, 339–346.

Nelan, J. E., Smith, R. J., Hudson, M. J., Wegner, G. A., Lucey, J. R., Moore, S. A. W., Quinney, S. J. & Suntzeff, N. B., 2005. NOAO Fundamental Plane

Survey. II. Age and Metallicity along the Red Sequence from Line-Strength Data. *ApJ*, **632**, 137–156.

Newton, I., 1704. *Opticks: or, a treatise of the reflexions, refractions, inflexions and colours of light. Also two treatises of the species and magnitude of curvilinear figures.*. Royal Society London.

Noll, S., Kausch, W., Barden, M., Jones, A. M., Szyszka, C., Kimeswenger, S. & Vinther, J., 2012. An atmospheric radiation model for Cerro Paranal. I. The optical spectral range. *A&A*, **543**, A92.

O'Connell, R. W., 1980. Galaxy spectral synthesis. II - M32 and the ages of galaxies. *ApJ*, **236**, 430–440.

Patat, F., 2004. Night Sky Brightness During Sunspot Maximum at Paranal. *The Messenger*, **115**, 18–21.

Peletier, R. F., 1989. *Elliptical Galaxies - Structure and Stellar Content*. Ph.D. thesis, , University of Groningen, The Netherlands, (1989).

Peletier, R. F., 2013. Stellar Populations. In J. Falcón-Barroso & J. H. Knapen, eds., *Secular Evolution of Galaxies*, 353. Cambridge University Press.

Piquéras, L., Legros, E., Pons, A., Legay, P.-J., Ferruit, P., Dorner, B., Pécontal, A., Gnata, X. & Mosner, P., 2010. The JWST/NIRSpec instrument performance simulator software. In *Society of Photo-Optical Instrumentation Engineers (SPIE) Conference Series*, vol. 7738 of *Society of Photo-Optical Instrumentation Engineers (SPIE) Conference Series*, 12.

Planck Collaboration, Ade, P. A. R., Aghanim, N., Armitage-Caplan, C., Arnaud, M., Ashdown, M., Atrio-Barandela, F., Aumont, J., Baccigalupi, C., Banday, A. J. & et al., 2014. Planck 2013 results. XVI. Cosmological parameters. *A&A*, **571**, A16.

Planck Collaboration, Ade, P. A. R., Aghanim, N., Arnaud, M., Ashdown, M., Aumont, J., Baccigalupi, C., Banday, A. J., Barreiro, R. B., Bartlett, J. G. & et al., 2015. Planck 2015 results. XIII. Cosmological parameters. *ArXiv e-prints*.

Pope, B., Tuthill, P., Hinkley, S., Ireland, M. J., Greenbaum, A., Latyshev, A., Monnier, J. D. & Martinache, F., 2016. The Palomar kernel-phase experiment: testing kernel phase interferometry for ground-based astronomical observations. *MNRAS*, **455**, 1647–1653.

Puech, M., Flores, H., Lehnert, M., Neichel, B., Fusco, T., Rosati, P., Cuby, J.-G. & Rousset, G., 2008. Coupling MOAO with integral field spectroscopy: specifications for the VLT and the E-ELT. *MNRAS*, **390**, 1089–1104.

Puech, M., Rosati, P., Toft, S., Cimatti, A., Neichel, B. & Fusco, T., 2010a. Simulating the physics and mass assembly of distant galaxies out to z ˜ 6 with the E-ELT. *MNRAS*, **402**, 903–922.

Puech, M., Yang, Y. B. & Flores, H., 2010b. Web-based scientific simulation tools for E-ELT instruments. In *Society of Photo-Optical Instrumentation Engineers (SPIE) Conference Series*, vol. 7735 of *Society of Photo-Optical Instrumentation Engineers (SPIE) Conference Series*, 5.

Ragazzoni, R., Ghedina, A., Baruffolo, A., Marchetti, E., Farinato, J., Niero, T., Crimi, G. & Ghigo, M., 2000. Testing the pyramid wavefront sensor on the sky. In P. L. Wizinowich, ed., *Adaptive Optical Systems Technology*, vol. 4007 of *Proc. SPIE*, 423–430.

Renzini, A., 2006. Stellar Population Diagnostics of Elliptical Galaxy Formation. *ARA&A*, **44**, 141–192.

Renzini, A. & Ciotti, L., 1993. Transverse Dissections of the Fundamental Planes of Elliptical Galaxies and Clusters of Galaxies. *ApJ*, **416**, L49.

Robertson, J. G., 1986. Optimal extraction of single-object spectra from observations with two-dimensional detectors. *PASP*, **98**, 1220–1231.

Roddier, F., 1981. The effects of atmospheric turbulence in optical astronomy. *Progress in optics. Volume 19. Amsterdam, North-Holland Publishing Co., 1981, p. 281-376.*, **19**, 281–376.

Roddier, F. & Roddier, C., 1988. Curvature Sensing and Compensation: A New Concept in Adaptive Optics. In M.-H. Ulrich, ed., *European Southern Observatory Conference and Workshop Proceedings*, vol. 30 of *European Southern Observatory Conference and Workshop Proceedings*, 667.

Rodighiero, G., Daddi, E., Baronchelli, I., Cimatti, A., Renzini, A. et al., 2011. The Lesser Role of Starbursts in Star Formation at z = 2. *ApJ*, **739**, L40.

Roe, H. G., 2002. Implications of Atmospheric Differential Refraction for Adaptive Optics Observations. *PASP*, **114**, 450–461.

Rose, J. A., Arimoto, N., Caldwell, N., Schiavon, R. P., Vazdekis, A. & Yamada, Y., 2005. Radial Age and Metal Abundance Gradients in the Stellar Content of M32. *AJ*, **129**, 712–728.

Saglia, R. P., Fabricius, M., Bender, R., Montalto, M., Lee, C.-H., Riffeser, A., Seitz, S., Morganti, L., Gerhard, O. & Hopp, U., 2010. The old and heavy bulge of M 31 . I. Kinematics and stellar populations. *A&A*, **509**, A61.

Salpeter, E. E., 1955. The Luminosity Function and Stellar Evolution. *ApJ*, **121**, 161.

Sánchez, S. F., Rosales-Ortega, F. F., Marino, R. A., Iglesias-Páramo, J., Vílchez, J. M. et al., 2012. Integral field spectroscopy of a sample of nearby galaxies. II. Properties of the H ii regions. *A&A*, **546**, A2.

Sánchez-Blázquez, P., Gorgas, J., Cardiel, N. & González, J. J., 2006. Stellar populations of early-type galaxies in different environments. II. Ages and metallicities. *A&A*, **457**, 809–821.

Sarajedini, A. & Jablonka, P., 2005. The Metallicity Distribution Function of Field Stars in M31's Bulge. *AJ*, **130**, 1627–1634.

SARAZIN, M. & RODDIER, F., 1990. The ESO differential image motion monitor. *A&A*, **227**, 294–300.

SCALO, J. M., 1986. The stellar initial mass function. *Fundam. Cosm. Phys.*, **11**, 1–278.

SCHALLER, G., SCHAERER, D., MEYNET, G. & MAEDER, A., 1992. New grids of stellar models from 0.8 to 120 solar masses at Z = 0.020 and Z = 0.001. *A&AS*, **96**, 269–331.

SCHAYE, J., CRAIN, R. A., BOWER, R. G., FURLONG, M., SCHALLER, M. ET AL., 2015. The EAGLE project: simulating the evolution and assembly of galaxies and their environments. *MNRAS*, **446**, 521–554.

SCHIAVON, R. P., BARBUY, B., ROSSI, S. C. F. & MILONE, A., 1997a. The Near-Infrared Na I Doublet Feature in M Stars. *ApJ*, **479**, 902–906.

SCHIAVON, R. P., BARBUY, B. & SINGH, P. D., 1997b. The FeH Wing-Ford Band in Spectra of M Stars. *ApJ*, **484**, 499–510.

SCHUBERT, G. & WALTERSCHEID, R. L., 2000. Earth. In A. N. Cox, ed., *Allen's Astrophysical Quantities*, 239. 4th ed.; New York: AIP.

SCOTT, N., HOUGHTON, R., DAVIES, R. L., CAPPELLARI, M., THATTE, N., CLARKE, F. & TECZA, M., 2012. An Oxford SWIFT integral field spectroscopy study of 14 early-type galaxies in the Coma cluster. *MNRAS*, **425**, 1521–1526.

SEARLE, L., SARGENT, W. L. W. & BAGNUOLO, W. G., 1973. The History of Star Formation and the Colors of Late-Type Galaxies. *ApJ*, **179**, 427–438.

SÉRSIC, J. L., 1963. Influence of the atmospheric and instrumental dispersion on the brightness distribution in a galaxy. *Boletin de la Asociacion Argentina de Astronomia La Plata Argentina*, **6**, 41.

SHARPLES, R., BENDER, R., AGUDO BERBEL, A., BEZAWADA, N., CASTILLO, R. ET AL., 2013. First Light for the KMOS Multi-Object Integral-Field Spectrometer. *The Messenger*, **151**, 21–23.

Smith, R. J., Alton, P., Lucey, J. R., Conroy, C. & Carter, D., 2015a. The IMF-sensitive 1.14-μm Na I doublet in early-type galaxies. *MNRAS*, **454**, L71–L75.

Smith, R. J. & Lucey, J. R., 2013. A giant elliptical galaxy with a lightweight initial mass function. *MNRAS*, **434**, 1964–1977.

Smith, R. J., Lucey, J. R. & Carter, D., 2012. The stellar initial mass function in red-sequence galaxies: 1-μm spectroscopy of Coma cluster galaxies with Subaru/FMOS. *MNRAS*, **426**, 2994–3007.

Smith, R. J., Lucey, J. R. & Conroy, C., 2015b. The SINFONI Nearby Elliptical Lens Locator Survey: discovery of two new low-redshift strong lenses and implications for the initial mass function in giant early-type galaxies. *MNRAS*, **449**, 3441–3457.

Spiniello, C., Koopmans, L. V. E., Trager, S. C., Czoske, O. & Treu, T., 2011. The X-Shooter Lens Survey - I. Dark matter domination and a Salpeter-type initial mass function in a massive early-type galaxy. *MNRAS*, **417**, 3000–3009.

Spiniello, C., Trager, S., Koopmans, L. V. E. & Conroy, C., 2014. The stellar IMF in early-type galaxies from a non-degenerate set of optical line indices. *MNRAS*, **438**, 1483–1499.

Spiniello, C., Trager, S. C. & Koopmans, L. V. E., 2015. The Non-universality of the Low-mass End of the IMF is Robust against the Choice of SSP Model. *ApJ*, **803**, 87.

Spinrad, H. & Taylor, B. J., 1969. Scanner Abundance Studies. I. an Investigation of Supermetallicity in Late-Type Evolved Stars. *ApJ*, **157**, 1279.

Spinrad, H. & Taylor, B. J., 1971. The Stellar Content of the Nuclei of Nearby Galaxies. I. M31, M32, and M81. *ApJS*, **22**, 445.

Stephens, A. W., Frogel, J. A., DePoy, D. L., Freedman, W., Gallart, C., Jablonka, P., Renzini, A., Rich, R. M. & Davies, R., 2003. The Stellar Content of the Bulge of M31. *AJ*, **125**, 2473–2493.

SWINBANK, A. M., SMAIL, I., SOBRAL, D., THEUNS, T., BEST, P. N. & GEACH, J. E., 2012a. The Properties of the Star-forming Interstellar Medium at z = 0.8-2.2 from HiZELS: Star Formation and Clump Scaling Laws in Gas-rich, Turbulent Disks. *ApJ*, **760**, 130.

SWINBANK, A. M., SOBRAL, D., SMAIL, I., GEACH, J. E., BEST, P. N., MCCARTHY, I. G., CRAIN, R. A. & THEUNS, T., 2012b. The properties of the star-forming interstellar medium at z = 0.84-2.23 from HiZELS: mapping the internal dynamics and metallicity gradients in high-redshift disc galaxies. *MNRAS*, **426**, 935–950.

TEMPEL, E., TUVIKENE, T., TAMM, A. & TENJES, P., 2011. SDSS surface photometry of M 31 with absorption corrections. *A&A*, **526**, A155.

TEYSSIER, R., 2002. Cosmological hydrodynamics with adaptive mesh refinement. A new high resolution code called RAMSES. *A&A*, **385**, 337–364.

THATTE, N., TECZA, M., CLARKE, F., DAVIES, R. L., REMILLIEUX, A. ET AL., 2010. HARMONI: a single-field wide-band integral-field spectrograph for the European ELT. In *Society of Photo-Optical Instrumentation Engineers (SPIE) Conference Series*, vol. 7735 of *Society of Photo-Optical Instrumentation Engineers (SPIE) Conference Series*, 2.

THATTE, N., TECZA, M., CLARKE, F., GOODSALL, T., LYNN, J., FREEMAN, D. & DAVIES, R. L., 2006. The Oxford SWIFT integral field spectrograph. In *Society of Photo-Optical Instrumentation Engineers (SPIE) Conference Series*, vol. 6269 of *Society of Photo-Optical Instrumentation Engineers (SPIE) Conference Series*, 3.

THOMAS, D., MARASTON, C. & BENDER, R., 2003. New clues on the calcium underabundance in early-type galaxies. *MNRAS*, **343**, 279–283.

THOMAS, D., MARASTON, C., BENDER, R. & MENDES DE OLIVEIRA, C., 2005. The Epochs of Early-Type Galaxy Formation as a Function of Environment. *ApJ*, **621**, 673–694.

Thomas, J., Saglia, R. P., Bender, R., Thomas, D., Gebhardt, K., Magorrian, J., Corsini, E. M. & Wegner, G., 2007. Dynamical modelling of luminous and dark matter in 17 Coma early-type galaxies. *MNRAS*, **382**, 657–684.

Thomas, J., Saglia, R. P., Bender, R., Thomas, D., Gebhardt, K., Magorrian, J., Corsini, E. M., Wegner, G. & Seitz, S., 2011. Dynamical masses of early-type galaxies: a comparison to lensing results and implications for the stellar initial mass function and the distribution of dark matter. *MNRAS*, **415**, 545–562.

Tinsley, B. M., 1968. Evolution of the Stars and Gas in Galaxies. *ApJ*, **151**, 547.

Tinsley, B. M., 1972. Stellar Evolution in Elliptical Galaxies. *ApJ*, **178**, 319–336.

Tokovinin, A., 2002. From Differential Image Motion to Seeing. *PASP*, **114**, 1156–1166.

Toomre, A., 1977. Mergers and Some Consequences. In B. M. Tinsley & R. B. G. Larson, D. Campbell, eds., *Evolution of Galaxies and Stellar Populations*, 401.

Toomre, A. & Toomre, J., 1972. Galactic Bridges and Tails. *ApJ*, **178**, 623–666.

Trager, S. C., Faber, S. M. & Dressler, A., 2008. The stellar population histories of early-type galaxies - III. The Coma cluster. *MNRAS*, **386**, 715–747.

Trager, S. C., Worthey, G., Faber, S. M., Burstein, D. & González, J. J., 1998. Old Stellar Populations. VI. Absorption-Line Spectra of Galaxy Nuclei and Globular Clusters. *ApJS*, **116**, 1–28.

Treu, T., Auger, M. W., Koopmans, L. V. E., Gavazzi, R., Marshall, P. J. & Bolton, A. S., 2010. The Initial Mass Function of Early-Type Galaxies. *ApJ*, **709**, 1195–1202.

van der Wel, A., Franx, M., van Dokkum, P. G., Skelton, R. E., Momcheva, I. G. et al., 2014. 3D-HST+CANDELS: The Evolution of the Galaxy Size-Mass Distribution since z = 3. *ApJ*, **788**, 28.

van Dokkum, P. G., 2001. Cosmic-Ray Rejection by Laplacian Edge Detection. *PASP*, **113**, 1420–1427.

van Dokkum, P. G., 2008. Evidence of Cosmic Evolution of the Stellar Initial Mass Function. *ApJ*, **674**, 29–50.

van Dokkum, P. G. & Conroy, C., 2010. A substantial population of low-mass stars in luminous elliptical galaxies. *Nature*, **468**, 940–942.

van Dokkum, P. G. & Conroy, C., 2012. The Stellar Initial Mass Function in Early-type Galaxies from Absorption Line Spectroscopy. I. Data and Empirical Trends. *ApJ*, **760**, 70.

Vanderriest, C., 1980. A fiber-optics dissector for spectroscopy of nebulosities around quasars and similar objects. *PASP*, **92**, 858–862.

Vazdekis, A., Casuso, E., Peletier, R. F. & Beckman, J. E., 1996. A New Chemo-evolutionary Population Synthesis Model for Early-Type Galaxies. I. Theoretical Basis. *ApJS*, **106**, 307.

Vazdekis, A., Cenarro, A. J., Gorgas, J., Cardiel, N. & Peletier, R. F., 2003. Empirical calibration of the near-infrared CaII triplet - IV. The stellar population synthesis models. *MNRAS*, **340**, 1317–1345.

Vazdekis, A., Ricciardelli, E., Cenarro, A. J., Rivero-González, J. G., Díaz-García, L. A. & Falcón-Barroso, J., 2012. MIUSCAT: extended MILES spectral coverage - I. Stellar population synthesis models. *MNRAS*, **424**, 157–171.

Vivès, S. & Prieto, E., 2006. Original image slicer designed for integral field spectroscopy with the near-infrared spectrograph for the James Webb Space Telescope. *Optical Engineering*, **45**(9), 093001.

Weijmans, A.-M., Cappellari, M., Bacon, R., de Zeeuw, P. T., Emsellem, E., Falcón-Barroso, J., Kuntschner, H., McDermid, R. M., van den Bosch, R. C. E. & van de Ven, G., 2009. Stellar velocity profiles and line strengths out to four effective radii in the early-type galaxies NGC3379 and 821. *MNRAS*, **398**, 561–574.

WESTMOQUETTE, M. S., EXTER, K. M., CHRISTENSEN, L., MAIER, M., LEMOINE-BUSSEROLLE, M., TURNER, J. & MARQUART, T., 2009. The integral field spectroscopy (IFS) wiki. *ArXiv e-prints*.

WHITFORD, A. E., 1977. The Wing-Ford band as a constraint on the mass function in old galaxy populations. *ApJ*, **211**, 527–538.

WILLIAMS, J. P., DE GEUS, E. J. & BLITZ, L., 1994. Determining structure in molecular clouds. *ApJ*, **428**, 693–712.

WING, R. F. & FORD, JR., W. K., 1969. The Infrared Spectrum of the Cool Dwarf Wolf 359. *PASP*, **81**, 527–529.

WISNIOSKI, E., FÖRSTER SCHREIBER, N. M., WUYTS, S., WUYTS, E., BANDARA, K. ET AL., 2015. The KMOS^{3D} Survey: Design, First Results, and the Evolution of Galaxy Kinematics from $0.7 \leq z \leq 2.7$. *ApJ*, **799**, 209.

WORTHEY, G., FABER, S. M. & GONZALEZ, J. J., 1992. MG and Fe absorption features in elliptical galaxies. *ApJ*, **398**, 69–73.

WORTHEY, G., FABER, S. M., GONZALEZ, J. J. & BURSTEIN, D., 1994. Old stellar populations. 5: Absorption feature indices for the complete LICK/IDS sample of stars. *ApJS*, **94**, 687–722.

WRIGHT, E. L., 2006. A Cosmology Calculator for the World Wide Web. *PASP*, **118**, 1711–1715.

ZIELENIEWSKI, S., HOUGHTON, R. C. W., THATTE, N. & DAVIES, R. L., 2015a. The initial mass functions of M31 and M32 through far red stellar absorption features. *MNRAS*, **452**, 597–606.

ZIELENIEWSKI, S. & THATTE, N., 2013. Parameterising E-ELT AO PSFs for detailed science simulations for HARMONI. In S. Esposito & L. Fini, eds., *Proceedings of the Third AO4ELT Conference*. INAF - Osservatorio Astrofisico di Arcetri, Firenze. ISBN 978-88-908876-0-4.

Zieleniewski, S., Thatte, N., Kendrew, S., Houghton, R., Tecza, M., Clarke, F., Fusco, T. & Swinbank, M., 2014. Simulating observations with HARMONI: the integral field spectrograph for the European Extremely Large Telescope. In *Society of Photo-Optical Instrumentation Engineers (SPIE) Conference Series*, vol. 9147 of *Society of Photo-Optical Instrumentation Engineers (SPIE) Conference Series*, 93.

Zieleniewski, S., Thatte, N., Kendrew, S., Houghton, R. C. W., Swinbank, A. M., Tecza, M., Clarke, F. & Fusco, T., 2015b. HSIM: a simulation pipeline for the HARMONI integral field spectrograph on the European ELT. *MNRAS*, **453**, 3754–3765.